High pressure investigations on carbides, oxides and nitrides

By

BHABYADARSAN SAHOO
Enrolment No.: PHYS01201204005

Bhabha Atomic Research Centre, Mumbai, India

A thesis submitted to the

Board of Studies in Physical Sciences

In partial fulfillment of requirements
for the Degree of

DOCTOR OF PHILOSOPHY

of

HOMI BHABHA NATIONAL INSTITUTE

January, 2016

Homi Bhabha National Institute[1]

Recommendations of the Viva Voce Committee

As members of the Viva Voce Committee, we certify that we have read the dissertation prepared by **Shri Bhabyadarsan Sahoo** entitled "**High pressure investigations on carbides, oxides and nitrides**" and recommend that it may be accepted as fulfilling the thesis requirement for the award of Degree of Doctor of Philosophy.

Dean Physical & Mathematical Sciences - Dr. Saibal Basu **Date:** 19/12/2016

Chairman-Dr. S.M. Sharma **Date:**

Guide / Convener - Dr. Satish C. Gupta Satish C Gupta **Date:** 19.12.2016

Co-guide - Dr. S.L. Chaplot S. L. Chaplot **Date:** 19-12-2016

Examiner - Dr. G.D. Mukherjee **Date:** 19/12/16

Member-Dr. P. Ch. Sahu **Date:**

Tech. Adviser- Dr. K.D. Joshi **Date:** 19.12.16

Final approval and acceptance of this thesis is contingent upon the candidate's submission of the final copies of the thesis to HBNI.

I/We hereby certify that I/we have read this thesis prepared under my/our direction and recommend that it may be accepted as fulfilling the thesis requirement.

Date: 19.12.2016

Place:

Signature
Co-guide (if applicable)

Satish C Gupta
Signature
Guide

---

[1] This page is to be included only for final submission after successful completion of viva voce.

Version approved during the meeting of Standing Committee of Deans held during 29-30 Nov 2013

STATEMENT BY AUTHOR

This dissertation has been submitted in partial fulfillment of requirements for an advanced degree at Homi Bhabha National Institute (HBNI) and is deposited in the Library to be made available to borrowers under rules of the HBNI.

Brief quotations from this dissertation are allowable without special permission, provided that accurate acknowledgement of source is made. Requests for permission for extended quotation from or reproduction of this manuscript in whole or in part may be granted by the Competent Authority of HBNI when in his or her judgment the proposed use of the material is in the interests of scholarship. In all other instances, however, permission must be obtained from the author.

Bhabyadarsan Sahoo

DECLARATION

I, hereby declare that the investigation presented in the thesis has been carried out by me. The work is original and has not been submitted earlier as a whole or in part for a degree / diploma at this or any other Institution / University.

Bhabyadarsan Sahoo

List of Publications arising from the thesis

Journal

1. "Prediction of new high pressure structural sequence in thorium carbide: A first principles study " B. D. Sahoo, K. D. Joshi and Satish C. Gupta, **,** J. Appl. Phys.117, 185903 (2015).

2. " Pressure effect on elastic, lattice dynamic and superconducting behavior of yttrium sulfide: A first principle study " B.D. Sahoo, K.D. Joshi and Satish C. Gupta, J. Appl. Phys., 115, 123502-8 (2014).

3. "On equation of state , elastic, and lattice dynamic stability of bcc bismuth under high pressure :Ab-initio calculations" D. Mukherjee, B.D. Sahoo, K.D. Joshi and Satish C. Gupta, J. Appl. Phys., 115, 053702-7 (2014).

4. " Structural, elastic and lattice dynamic stability of yttrium selenide (YSe) under pressure: A first principle study " , B. D. Sahoo, K. D. Joshi and Satish C. Gupta, **,** J. Appl. Phys.116, 193504 (2014).

5. "Theoretical prediction of high pressure phase transition in ScC and YC: Ab initio calculations" B.D. Sahoo, K.D. Joshi and Satish C. Gupta, J. Appl. Phys 114, 053516 (2013).

6. "On Structural Stability of LaN Under High Pressure: ab-initio calculations" D. Mukherjee, B.D. Sahoo, K.D. Joshi and Satish C. Gupta, High Pres. Res., 33, 563 (2013).

7. "On the structural stability of CeN at high Pressure: Ab-initio calculations" B.D. Sahoo, K.D. Joshi and Satish C. Gupta, J. Appl. Phys., 113, 1935121-7 (2013).

8. "Ab-initio study on structural stability of uranium carbide" B.D. Sahoo, K.D. Joshi and Satish C. Gupta, J. Nucl. Mater, 437, 81 (2013).

9. "Ab-initio Calculations on structural, elastic and dynamic stability of CdO at high pressures" B.D. Sahoo, K.D. Joshi and Satish C. Gupta, J. Appl. Phys., 112, 0935231-6 (2012).

10."Thermo-physical properties of LiH at high pressures by ab initio calculations", D. Mukherjee, B. D. Sahoo, K. D. Joshi, S. C. Gupta, and S. K. Sikka, J. Appl. Phys., 109, 103515 (2011).

Conferences

11. "On structural and lattice dynamic stability of LaF_3 under high pressure: A first principle Study " B.D. Sahoo, K.D. Joshi and Satish C. Gupta, AIP Conference Proceedings, Vol. 1665, pp. 030028-030031 (2015).

12. "Structural elastic and lattice dynamic stability of TaC under high pressure-high temperature: Ab-intio study" B.D. Sahoo, K.D. Joshi and Satish C. Gupta, ICEMP-2014 ISBN 978-81-928552-1-9 (2014)

13. "High Pressure phase transformation in yttrium sulphide : A first principle study" B.D. Sahoo, K.D. Joshi and Satish C. Gupta, AIP Conference Proceedings, AIP Conference Proceedings, Vol. 1591, pp. 50-52 (2014).

14. "High Pressure phase transformation in uranium carbide: A first principle study", B.D. Sahoo, K.D. Joshi and Satish C. Gupta, AIP Conference Proceedings, Vol. 1512, pp. 78-79 (2013).

15. "High Pressure phase transformation in thorium carbide: A first principle study", B.D. Sahoo, K.D. Joshi and Satish C. Gupta, AIP Conference Proceedings, Vol. 1536, pp. 937-938 (2013).

16. "Lattice dynamic calculations on LiH", D. Mukherjee, B.D. Sahoo, K.D. Joshi and Satish C. Gupta, AIP Conference Proceedings, Vol. 1536, pp. 403-404 (2013).

17."On Dynamic and Elastic Stability of Lanthanum Carbide" B.D. Sahoo, D. Mukherjee, K.D. Joshi and Satish C. Gupta, J. Phys: Conf. Series. 377, 120871 (2012).

18. "On Dynamic and Elastic Stability of Group IIIB Metal Carbides: ab-initio Calculations", B.D. Sahoo, D. Mukherjee, K.D. Joshi and Satish C. Gupta, AIP Conference Proceedings, Vol. 1447, pp. 803-804 (2012).

Bhabyadarsan Sahoo

To

ALL MY FAMILY AND FRIENDS

ACKNOWLEDGEMENTS

I would like to thank all people who have helped me in different aspects and inspired me during my doctoral work.

I would like to express my sincere gratitude to my adviser Prof. Satish C. Gupta Sir, for his invaluable guidance, keen interest, constant encouragement, inspiration and good wishes. His wide knowledge and his logical way of thinking on critical scientific problems have been of great value for me.

This thesis would not have been possible without the guidance, help, support, critical analysis and valuable suggestions from Dr. K. D. Joshi Sir who has been truly invaluable to me both on an academic and a personal level, for which I am extremely grateful. I am also thankful to him for sharing his excellent knowledge and scientific understanding with me.

It gives me immense pleasure to thank the members of the doctoral committee Prof. S.M. Sharma (Chairman), Prof. S. L. Chaplot (Co-Guide) and Prof. P. Ch. Sahu (Member) for their critical review and suggestions during the progress review and pre-synopsis viva-voce.

I am grateful to all the members of Applied Physics Division. Specially, I would like to thank to my division head Prof T .C. Koushik to give enough encouragement and valuable time and motivatations to do calculations during my last time of my research period. I also acknowledge the assistance provided by Dr. D. Mukherjee for various fruitful discussions, preparation of the thesis.

I owe my heartfelt gratitude and indebtedness to my father, mother, my sister and my brothers for the constant appreciation and courage.

Finally, I would like to thank my friends for her continuous encouragement
Lastly, I beg apology to all the people whom I have missed to mention in this page.

CONTENTS

1. Introduction

2. Structural Stability Analysis of CdO under High Pressure

3. High Pressure Phase Transition in Transition Metal Carbides ScC, YC and TaC

4. Structural Stability Analysis of CeN under High Pressure

5. Structural Stability Analysis of ThC and UC under High Pressure

High pressure investigations on carbides, oxides and nitrides

(SYNOPSIS)

High pressures, capable of generating high compressions in materials can alter the interatomic interactions drastically which may lead to several interesting phenomena such as phase transitions and chemical reactions [1-5]. The effect of pressure on materials can be classified into two categories, namely, the lattice effect and the electronic structural change. However, these two changes are not totally independent, but one is associated with the other. The decrease in interatomic distances or equivalently increase in the density leading to changes in the lattice dynamical properties (phonon spectra), free energy and often causing the phase transitions to the compact structures characterized by significant changes in the physical properties falls under the category of lattice effects. As the inter atomic distance decreases, the overlap of outer electronic orbital's increases, which affects the width of the energy bands, the extent of hybridization of the outer electronic orbital's and position of the energy bands, etc. All these electronic effects lead to interesting changes in the physical and chemical properties of materials. For example, the pressure induced metallization of hydrogen and oxygen [6-8], metal to insulator transition in sodium around 200 GPa [9], crystalline to amorphous and amorphous to crystalline phase transformations in porous silicon [10, 11] and the high pressure superconductivity of lithium and silane above 20 GPa and 90GPa, respectively [12-14] are some of popular high pressure studies reported in past.

Experimentally, the high pressures in the materials are generated either by static compression methods or by dynamic compression (shock compression) methods. In the static compression technique [4], material is compressed slowly; for which, temperature inside the sample during the experiment remains constant *i.e.* the static compression is an isothermal process. In static method one can compress the material hydrostatically by selecting a suitable (fluid or gas) pressure transmitting medium surrounding the sample [4, 15]. On the other hand, in shock loading methods, materials are compressed uniaxially with very high rate of pressurization (rise times ~ few tens of nanoseconds), leading to the increase in both temperature and entropy of the materials. Under static compression, the duration of the pressure on the material can be as long as we desire whereas, in case of shock compression the duration of pressure pulse is of order of few microseconds depending upon the size of the sample. These differences in two compression techniques sometimes lead to different results on the materials. For example, tantalum (Ta) having bcc structure at ambient conditions has been reported to remain stable in this phase up to ~ 170 GPa in static compression experiments [16], whereas it transform to ω phase at ~ 45 GPa under shock loading [17].

The diamond anvil cell (DAC) apparatus is widely used to generate static pressures in the materials [4, 15]. The modern diamond anvil cell (DAC) apparatus can generate high static pressures of multimegabar. Apart from the high pressure studies the modern DACs equipped with laser heating techniques have facilitated the investigation of material behaviour under high pressure-high temperature environment [18]. The advent of third stage synchrotron sources and neutron spallation sources have added the new dimensions to the diagnostics required for characterization of the behaviour of material subjected to high pressure [19-21]. The significant progress has also been made in development of dynamic pressure generation techniques. Development of two stage guns, laser shock techniques and electromagnetic launchers has made it possible to generate extreme state of high transient pressure and temperature in materials [22-29]. The combination of static and dynamic pressure studies of materials have made it possible to access the new regimes of equation of state of materials.

Apart from the experiments, the modern *ab-initio* electronic band structure calculation methods based on the density functional approach have also been proved useful to not only reproduce the experimental results but also to predict the behaviour of materials under high pressure and high temperature [9-37]. For example, in case of sodium, high pressure experiment revealed that it becomes optically transparent around ~200GPa [9] but the quality of the XRD pattern for the transparent phase was insufficient to find the exact structure solution hence theoretical calculations have been employed as a tool to identify the high pressure phase, which confirmed it to be hexagonal phase (Na-hP4).This insulating state is formed due to p-d hybridizations of valence electrons and their repulsion by core electrons into the interstices of the six-coordinated highly distorted double-hexagonal close-packed structure. Atomic structure is the most important piece of information about crystalline solids: Just from the knowledge of topology of the structure, a precise structural model and many physical properties of crystals can be determined with state of the-art quantum-mechanical methods. In some cases, where it is not possible to solve crystal structure from experimental data, the theoretical structure prediction becomes crucially important. For example, when experimental data are of poor quality for structure solution (defective or small samples, especially at high pressures and temperatures) theory provides the last hope to this. Apart from this, theory is the only way of investigating matter at extreme conditions which are inaccessible with today's experimental techniques. Even with so much advancement in the experimental methods both in synthesis technique as well as measurements techniques still it is difficult to understand the structural changes at ambient as well as under high pressure conditions in many cases [38]. For example, in simple metal calcium, the *ab-initio* calculations of Oganov *et al.* [39] predicted a β-tin type tetragonal structure (space group $I4_1/amd$) to be more favorable above 33 GPa. However, the high pressure x-ray diffraction measurements by Mao *et al.* [40] reported a phase transition around 32 GPa and indexed this as rhombohedral structure (space group R-3m) at 300 K and orthorhombic structure (space group C*mmm*) below 30 K. This discrepancy between theory and experiment, latter solved by Li *et al.* [41] repeating the experiment on this material. In this new experimental study authors have reported that the high pressure phase formed around 35 GPa is indeed a β-tin type tetragonal structure, consistent with theoretical prediction. Also with the evolution of structural prediction methods such as Universal Structure Predictor: Evolutionary Xtallography (USPEX) it has been possible to predict the unusual stoichiometries in many compounds under high pressure. For example, in sodium chloride using USPEX algorithm in conjunction with *ab-initio* electronic band structure method, the stable $NaCl_3$ and Na_3Cl have been predicted under high pressure [42]. Interestingly, these predictions have been realized experimentally in recent studies [42] . Similarly, in xenon oxide various stoichiometries such as XeO, XeO_2, XeO_3 have been predicted to be stable at different pressures [43].

The *ab-initio* electronic structure calculations can be carried out using two approaches, one in which, the ions are assumed to be fixed rigidly at their location (adiabatic approximation) and other in which the corrections due to atomic vibrations are also taken into account. The calculations limited to the rigid periodic arrangement of atoms (ions) in the solid are termed as static lattice calculations. Under this approximation the interaction energy between the ions depends on their separation or equivalently on atomic position. The interactions are categorised as (i) long-range Coulomb interactions and (ii) short-range interactions. However, in lattice dynamic calculations, using quasi harmonic approximation (QHA), one proceeds a step further by calculating the phonon spectra from the knowledge of forces and structures obtained from static lattice model calculations. The study of lattice vibrations in condensed matter is of considerable interest because several physical properties of crystals like the specific heat, thermal conductivity, thermal expansion, sound velocity etc. are related to the vibrations of atoms in solids [44, 45]. The lattice vibration spectra basically relate the energy of the thermal motions of the atoms to the corresponding wavelength. The collective motions of atoms in solids forming travelling waves are quantized in terms of ‘‘phonons” and these are determined from the knowledge of the interatomic interactions. The resulting vibrational spectra act as a sensitive probe for the local bonding and chemical structure. Further, very low-frequency modes can be associated with phase transformations, and imaginary frequencies provide an indication that the calculated structure is not the stable one. So lattice dynamics (phonons) play a dominant role in deciding the structural stability of the materials.

The present thesis attempts to understand various aspects of material behavior under high pressure – high temperature by resorting *ab-initio* static lattice and lattice dynamic calculations as a tool for investigations. The high pressure- high temperature behavior of binary compounds reported in the present thesis includes the oxides, carbides and nitrides of transition and actinide metals. The oxide includes CdO, the carbides include ScC, YC, TaC, ThC and UC, and the nitrides include CeN. The main goal was to add further understanding to the high pressure structural, elastic and lattice dynamic stability of these binary compounds formed by combining the transition metals or actinide metals to simple elements of group IV, V and VI of the periodic table. Apart from structural stability analysis, the thermo-physical properties like equilibrium volume, bulk modulus, specific heat, entropy, vibrational free energy and thermal expansion as a function of temperature have also been derived. All these binary compounds exist in rocksalt structure (B1) at ambient conditions and have attracted attention of researchers due to their technical as well as academic importance. For example, in case of UC and ThC having high stiffness and high melting point, the major interest is due to their importance as nuclear fuel materials in the generation

IV nuclear reactors [46, 47]. In order to develop the technologies for the nuclear cycle based on carbide fuels, it is important to understand structural, thermo-physical and mechanical properties of these compounds. As far as transition metal carbides ScC, YC and TaC are concerned, the extreme hardness, good strength even at elevated temperatures and high melting point exhibited by these carbides makes them important scientifically as well as technologically [48-59]. Some of the potential technological applications are in cutting tools and optoelectronics. The academic interest on these materials comes due to the existence of mixed bonding (both metallic and covalent) which is believed to be responsible for high hardness and high melting points of these materials. The CeN which is one of the mono nitride of rare earth metal shows anomalous physical properties such as unusually small lattice parameters [60- 62]. The anomalous physical properties of this mono nitride are attributed to the peculiar behavior of 4*f* electron of Ce ion. The unusual physical properties make this compound interesting both academically and industrially. Transition metal oxides are systems with large variability of structures and chemical bonding which brings about different magnetic, electrical and optical properties. These unique properties make these compounds suitable for applications like new memories smaller transistors and smart-sensors in different semiconductor industries. The technological applications have attracted the interest on the high pressure behavior of these materials. The cadmium oxide is one of the attractive semiconductor materials. It has many industrial applications such as in the production of solar cells, liquid-crystal displays, electro chromic devices, light-emitting diodes, etc.[63-66]. So, in order to fully exploit this semiconductor material, it is necessary to obtain a good understanding of the physical properties of CdO, and in particular, its structural and thermodynamic properties under high pressure [67-73].

The first chapter gives a brief description to the basic concepts and scopes of the high pressure research, and outlines of the research work to be presented in the successive chapters of the thesis. Besides this it also describes the different methods used to generate high pressure in materials and various characterization techniques utilized to understand the behavior of materials under high pressure. Also, a brief description of modern DFT based *ab-initio* electronic band structure methods employed for understanding the material response under high pressures has been presented in this chapter. The brief description of the structural prediction method used for the pressure induced phase transformations and the outline of the methodology used for determination of elastic property and lattice dynamics have been described.

The Second chapter deals with the theoretical calculations carried out on CdO. In CdO, the main focus was to analyze the structural stability under high pressure and to determine the pressure dependent elastic and vibrational properties (lattice-dynamics). For this purpose, first the *ab-initio* calculations at 0 K have been performed to analyze structural stability by choosing the structures namely B1, primitive orthorhombic (Pmmn) and CsCl type (B2). The 0 K calculations have been utilized to derive the 300 K isotherm after adding finite temperature corrections within quasi harmonic approximations. Additionally, employing the theoretically determined thermal equation of state in conjunction with Rankine Hugoniot relation, the Hugoniot of B1 phase of this material has been derived. Additional calculations have been performed to determine the shear elastic moduli and phonon dispersions as a function of hydrostatic compression. The structural stability analysis suggests that the B1 phase will transforms to B2 phase at ~ 87 GPa in good agreement with experimental value of 90.6 GPa [68]. The inclusion of finite temperature corrections determined from lattice dynamic calculations within quasi harmonic approximation to the 0 K calculations lowers this transition pressure by ~1GPa at 300 K. The 300 K isotherm agrees reasonably with the experimental data. Various thermo physical properties such as atomic volume, bulk modulus, its pressure derivative, Debye temperature, thermal expansion coefficient and specific heat at ambient conditions derived from theoretical calculations are $27.59(A^0)^3$/atom, 111 GPa , 4.94, 273 K, 4.445×10^{-5}/K and 7.564×10^{-23} J/K/formula unit as compared to the experimental data of $26.05(A^0)^3$/atom, 129 GPa, 4.71, 255 K , 4.2×10^{-5}/K and 7.195×10^{-23} J/K/formula unit, respectively [74-77]. The pressure dependent elastic constants have been determined for both B1 and B2 phase. For the B1 phase, the elastic constants C_{11}, C_{12}, and C_{44} of 168.29 GPa, 76.02 GPa and 46.13 GPa determined at zero pressure compare well with the other theoretical values of 183.99 GPa, 76.02 GPa and 45.78 GPa, respectively [69]. For B2 these values are determined to be 303.09 GPa, 48.15 GPa and -25.99 GPa. The negative value of the shear modulus C_{44} for B2 phase indicates elastic instability of B2 structure at ambient conditions. Further, the elastic stability of these structures has been examined up to 160

GPa. The C_{44} modulus of B1 phase displayed a monotonic decrease with increasing pressure and vanished at ~ 126 GPa, suggesting the development of elastic instability in B1 phase around this pressure. In contrast the B2 phase was found to remain elastically unstable up to a pressure of ~ 38 GPa and beyond this pressure it emerged as an elastically stable structure. To know the dynamical stability of B1 and B2 phase, the phonon dispersion curves (PDC) have been calculated for both the phases at ambient conditions and at various high pressures. Up to 116 GPa, the phonon dispersion for B1 phase displays the positive vibrational frequency in all symmetry directions of Brillouin zone confirming the dynamic stability of this structure up to this pressure. For the B2 phase the imaginary frequencies persists up to 56 GPa and thereafter all the frequencies become positive making the structure dynamically stable beyond this pressure. The analysis of elastic and dynamic stability as a function of hydrostatic compression suggested that the pressure induced B1 to B2 transition in CdO is driven by soft transverse acoustic phonon mode at the Brillouin zone boundary.

The third chapter of the thesis reports the detailed theoretical investigations carried out in transition metal carbides ScC, YC and TaC. The theoretical work includes the analysis of structural stability, determination of equation of state, elastic and lattice dynamic properties as a function of hydrostatic compression. The comparison of enthalpies of B1 structure, Primitive orthorhombic (Pmmn) and B2 phase at various pressures suggested that the ambient pressure B1 phase of ScC will transform to the Pmmn phase at ~80 GPa. In case of YC the same transition occurs at ~ 30 GPa. In TaC instead of Pmmn phase, the B2 structure becomes stable around 472 GPa. This theoretical prediction is open for experimental confirmation. Various thermo physical and elastic properties such as volume, bulk modulus, its pressure derivative and elastic constants C_{11}, C_{12}, and C_{44} have been determined at zero pressure. For ScC in B1 phase, these are determined to be 25.43$(A^0)^3$/atom, 161.9 GPa, 4.18, 304.4 GPa 72.5 GPa and 46 GPa, respectively. These quantities for YC are evaluated be 33.23 $(A^0)^3$/atom, 125.2 GPa, 4.14, 226.5 GPa, 74.5 GPa and 53.7 GPa, respectively. In case of TaC these parameters are found to be 22.4$(A^0)^3$/atom, 342 GPa, 3.93, 723 GPa 151 GPa and 178 GPa, respectively**.** Further, these quantities compare well with the available experimental data [48, 59, 78-81]. The examination of elastic behavior along the hydrostatic compression path revealed that the B1 structure will become elastically unstable at ~ 210 GPa in ScC and at ~ 180 GPa in YC, much beyond the B1 to Pmmn transition pressure. In TaC also, the B1 phase remains elastically stable much beyond the B1 to B2 transition pressure. The phonon dispersion relations determined at various pressures from lattice dynamic calculations showed that the phonon frequencies for B1 phase become imaginary around 110 GPa in ScC and around 28 GPa in YC, suggesting that the B1 to Pmmn transition in these materials is driven by phonon softening. In case of TaC it has been found that the B1 phase remains dynamically stable even beyond the B1 to B2 transition pressure (up to ~ 600 GPa). Besides this for ScC and YC, the phonon frequencies (ω), their pressure derivative coefficients and Gruneisen parameter (γ) of several modes at high symmetry points Γ, X and L of Brillouin zone in B1 phase have also been calculated. The negative TA Gruneisen parameter at X point for both the materials indicates that the frequency at this point decreases with increasing pressure. Additionally the frequencies of various modes calculated in our work have been compared with other published data [59] for both the materials.

The fourth chapter presents the theoretical high pressure investigations on CeN. In high pressure energy dispersive X-ray diffraction measurements it has been reported that the B1 phase of this material transforms to B2 structure at ~ 65 GPa [82]. This transition observed in this material is in contrast to that observed in mononitrides of left and right nearest neighbors of Ce in periodic table i.*e.* LaN and PrN [83,84]. In these two materials the observed high pressure phase was low symmetry tetragonal (P4/nmm) (B10) structure. This distinct high pressure behaviour shown by CeN led us to perform the high pressure theoretical investigations on this material. The comparison of enthalpies calculated as a function of hydrostatic pressure for B1, B10 and B2 structures suggests that the B1 phase will transform to B10 structure at 53 GPa, which upon further compression will transform to B2 phase at 200 GPa. This theoretical prediction is in contrast to the existing experimental report and opens for experimental confirmation. In order to understand the discrepancy between the theory and experiment, the theoretical X-ray diffraction pattern have been calculated for both the B10 and B2 phases around 75 GPa (well above the transition pressure) and it was observed that most of the intense peaks, except few weak peaks (211, 301) of the calculated B10 phase coincide either with that of B1 or with B2 phase. In the experimental EDXRD pattern recorded at ~ 77 GPa, many peaks *e.g.* (222) and (400) of B1 phase and (210) B2 phase which displayed a good strength in theoretical pattern were hardly visible in the experimental pattern. These observations suggest the need for more experiments up to still higher pressures to develop these peaks significantly if at all present in the experiment. Further, the elastic stability of B1structure has been examined upto 160 GPa. The $C_{11}$and C_{12} elastic constants displayed a monotonic increase while C_{44} modulus displayed a monotonic decrease with increasing pressure and vanished at ~ 100 GPa *i.e.* much beyond the B1 to B10 transition pressure. Additionally, the lattice dynamic stability of CeN has also been analysed. To know the dynamical stability of B1 B10 and B2 phases we have calculated the PDC and phonon density of states (PDOS) at ambient conditions as well as with higher compression. At zero pressure the positive frequencies in all symmetry directions of Brillouin zone of B1 phase showed the stability of this phase at ambient conditions. With increasing pressure the transverse acoustic (TA) frequency in the midway of Γ-X direction decreases and becomes imaginary at the transition pressure (53 GPa) whereas B10 phase emerges as a dynamical stable phase at this pressure , in agreement with the static calculations. The B2 phase, however, still remains dynamical unstable but at higher pressure of around 200 GPa it shows positive frequencies in all symmetry directions of Brillouin zone, confirming its dynamical stability. These results of lattice dynamic calculations support outcome of our static lattice calculations. Various physical properties such as volume, bulk modulus and its pressure derivative, at ambient conditions derived from theoretical calculations are 31.85$(A^0)^3$/atom, 168.2 GPa and 4.02 as compared to the experimental values of 31.71$(A^0)^3$/atom, 156 GPa and 4.0, respectively. For B10 and B2 these parameters are calculated to be 30.55$(A^0)^3$/atom, 99.1GPa and 4.90, and 28.39$(A^0)^3$/atom, 159.3GPa and 4.47, respectively.

The theoretical investigation on carbides materials is extended to monocarbides of light actinides *i.e.* UC and ThC. The experimental studies [85-87] on these carbides have reported that the UC undergoes B1 to primitive orthorhombic transition (Pmmn) at ~ 27 GPa, whereas, the ThC remains stable in B1 phase even up to 50 GPa. Theoretical studies have been performed to analyze structural stability of these two materials under hydrostatic pressure. In agreement with the experiment in UC our calculations have shown that the B1 phase will transform to Pmmn structure around 20 GPa. The static lattice calculations have been substantiated by lattice dynamic calculations, which displayed that the B1 phase will become dynamically unstable around transition pressure due to vanishing of long wavelength TA phonons. This outcome of the lattice dynamic calculations has been supported by the behavior of C_{44} shear elastic modulus examined as a function of pressure. It has been found that this modulus fails around the transition pressure, indicating that the B1 to Pmmn phase transition in UC is shear driven. Various thermo physical quantities such as atomic volume, bulk modulus, its pressure derivative and Debye temperature of $29.77(A^0)^3$/atom,185.2 GPa ,3.59 and 206 K, respectively are in good agreement with the experimental values of $30.5(A^0)^3$/atom,160 GPa , 3.6 and 366 K, respectively [101]. In ThC, however, our theoretical results are not in agreement with the experimental reports [86, 87]. The comparison of enthalpies, derived for various phases from 0 K total energy calculations at several hydrostatic compressions, yielded a high pressure structural sequence of B1 $\rightarrow$ Pnma $\rightarrow$ Cmcm $\rightarrow$ B2 with transition pressures of ~ 19 GPa, 36 GPa and 200 GPa, respectively. The discrepancy between the theory and the experiments could be due to the substoichiometry of the thorium monocarbide samples used in the experimental study. The theoretical finding opens scope for conducting more experiments with varying substiochiomerty of ThC samples to understand the role of this on the structural stability of ThC under high pressure. Further, in order to substantiate the results of static lattice calculations, the phonon dispersion relations for these structures have been derived from lattice dynamic calculations. The theoretically calculated phonon spectrum reveal that the B1 phase fails dynamically at ~ 33.8 GPa whereas the Pnma phase appears as dynamically stable structure around this pressure. Similarly, the Cmcm structure also displays dynamic stability in the regime of its structural stability. The B2 phase becomes dynamically stable much below the Cmcm to B2 transition pressure. Apart from this, various thermophysical properties such as zero pressure equilibrium volume, bulk modulus, its pressure derivative, Debye temperature, thermal expansion coefficient and Gruneisen parameter at 300K have been derived and compared with available experimental data [88-93]. Further, the behavior of zero pressure bulk modulus, heat capacity and Helmholtz free energy has been examined as a function temperature and compared with the experimental data of Danan [91]. All these results are discussed in details in chapter five of the thesis.

The thesis will be concluded in the sixth chapter giving a discussion and summary of results of the overall work presented followed by further research scope open and theoretical problem in the present field.

References

[1] F. R. Boyd, *Science*, **145**, 3627 (1964).

[2] D. J. Stevenson, *Annu. Rev. Earth Planet. Sci.*, **10**, 257 (1982).

[3 S.K. Sikka, Current Science, 67, 874, (1994).

[4] A. Jayaraman, *Rev. Mod. Phys*., **55**, 65 (1983); *Rev. Sci. Instrum.,* **57**, 1013 (1986).

[5] P. W. Bridgman, *Proc. Am. Acad. Arts Sci.*, **47**, 321-43 (1911); *Proc. Am. Acad. Arts Sci.*, **47**, 441 (1911).

[6] S.T. Weir, A.C. Mitchell and W.J. Nellis *Phys. Rev. Lett*. **76**, 1860 (1996); W.J. Nellis, *Phil. Mag.* B79, 655 (1999), *High Press. Res*., **24**, 87 (2004).

[7] Y. Akahama, H. Kawamura, D. Hausermann, M. Hanfland, and O. Shimomura, *Phys. Rev. Lett.*, **74**, 4690 (1995).

[8] S. Desgreniers, Y. K. Vohra, and A. L. Rouff, *J. Phys. Chem.*, **94**, 1117 (1990).

[9] Y. Ma, M. Eremets, A. R. Oganov, Y. Xie, I. Trojan, S. Medvedev, A. O. Lyakhov, M. Valle and V. Prakapenka, *Nature***, 458**, 182 (2009).

[10] S. K. Deb, M. C. Wilding, M. Somayazulu, and P. F. McMillan, *Nature (London)* **414**, 528 (2001).

[11] Nandini Garg, K.K. Pandey, K.V. Shanavas, C. A. Betty and Surinder M Sharma, *Phys. Rev. B*, **83**, 115202 (2011).

[12] K. Shimizu, H. Ishikawa, D. Takao, T. Yagi, and K. Amaya, *Nature (London*) **419**, 597 (2002).

[13] V. Struzhkin, M. I. Eremets, W. Gan, H.-K. Mao, and R. J. Hemley, *Science* **298**, 1213 (2002).

[14] M. I. Eremets, I. A. Trojan, S. A. Medvedev, J. S. Tse, and Y. Yao, *Science* **319**, 1506 (2008).

[15] H.K. Mao and P.M. Bell, *Science*, 200, 1145, (1978);.K.A. Goettel, H.K. Mao and P.M. Bell, *Rev. Sci. Instrum.,*56, 1420 (1985).

[16] H. Cynn and C. Yoo, *Phys. Rev. B*, **59,** 8526 (1998).

[17] L. M. Hsiung and D. H. Lassila, *Scripta Matter.*, **39,** 603 (1998).

[18] Jung-Fu Lin, Mario Santoro, Viktor V. Struzhkin, Ho-kwang Mao, and Russell J. Hemley, *Rev. Sci. Instr*., **75**, 3302 (2004).

[19] F. Elder, A.M. Gurewitsch, R.V. Langmuir, H.C Pollock, *Phys. Rev.* **71**, 829 (1947).

[20] G. **S.** Knapp, M. A. Beno, and H. You, *Annu. Rev. Mater. Sci.*, 1996. **26**, 693 (1996).

[21] Donald H Bilderback, Pascal Elleaume and Edgar Weckert, J. *Phys. B: At. Mol. Opt. Phys*. **38**, S773 (2005).

[22] J.R. Asay, *Int. J. Impact Engg*. **20**, 27 (1997).

[23] M. D. Furnish, L.C. Chhabildas, and W.D. Reinhart, *International Journal of Impact Engineering* **2**3, 261 (1999).

[24] Satish C. Gupta, R.G. Agarwal, J.S. Gyanchandani, S. Roy, N. Suresh, S.K. Sikka, A. Kakodkar and R. Chidambaram, *in Shock Compression of Condensed Matter*-1991 (Ed. S.C Schmidt, R.D. Dick, J.W. Forbes and D.G. Tasker), p. 839.

[25] J. Osher, R. Gathers, H. Chau, R. Lee, G. Pomykal, and R. Weingart, *Int. J. Impact Eng*. **10**, 439 (1990).

[26] T. C. Kaushik *et al*, *IEEE Transaction in Plasma Science*, **30**, 2133 (2002).

[27] C.A. Hall, J.R. Asay, M.D. Knudson, W.A. Stygar, R.B. Spielman, T.D. Pointon, D.B. Reisman, A. Toor and R.C. Cauble, *Rev. Sci. Instrum*., **72**, 3587 (2001).

[28] M. D. Knudson, D. L. Hanson, J. E. Bailey, C. A. Hall, and J. R. Asay, *Phys. Rev. Lett*., **87**, 225501-1 (2001).

[29] D.B. Reisman et al., *J. Appl. Phys*., **89**, 1625 (2001).

[30] M. B. Boisen, G. V. Gibbs, M. S. T. Bukowinski, *Phys. Chem. Minerals* **21**, 269 (1994).

[31] S. Gödecker, *J. Chem. Phys.* **120**, 9911 (2004).

[32] R. Martonak, A. Laio, and M. Parrinello, *Phys. Rev. Lett***.** **90**, 075503 (2003).

[33] R. Martonak, A. Laio, M. Bernasconi, C. Ceriani, P. Raiteri, F. Zipoli, and M. Parrinello, *Z. Krist.* **220**, 489 (2005).

[34] R. Martoňák, D. Donadio, A. R. Oganov, M. Parrinello, *Nature Materials* **5**, 623 (2006).

[35] A. R. Oganov, C. W. Glass, S. Ono, *Earth Planet. Sci. Lett***.** **241**, 95 (2006).

[36] A. R. Oganov, C. W. Glass, *J. Chem. Phys.* **124**, 244704 (2006).

[37] C. W. Glass, A. R. Oganov, N. Hansen, *Comp. Phys. Comm.* **175**, 713 (2006).

[38] Zerr A, Miehe G, Serghiou G, Schwarz M, Kroke E, Riedel R, Fuess H, Kroll P and Boehler R *Nature* (London) **400** ,340 (1999)

[39] A. R. Oganov, Y. Ma, Y. Xu, I. Erread, A. Bergarad, and A. O. Lyakhov, *PNAS*, **107**, 7646 (2010).

[40] W. L. Mao, L. Wang, Y. Ding, W. Yangd, W. Liu, D. Y. Kimg, W. Luo, R. Ahuja, *PNAS*, **107**, 9965 (2010).

[41] B. Li,Y. Ding, W. Yang, L. Wang, B. Zou, J. Shu, S. Sinogeikin, C. Park, G. Zou and H. Mao, *PNAS*, **109**, 16459 (2012).

[42] W.W. Zhang, A.R. Oganov, A.F. Goncharov, Q. Zhu, S.E. Boulfelfel, A.O. Lyakhov, E. Stavrou, M . Somayazulu, V.B. Prakapenka and Z. Konopkova, *Science* **342**, 1502 (2013).

[43] Q. Zhu, D.Y. Jung, A.R. Oganov, C. Gatti, C.W Glass., A.O. Lyakhov, *Nature Chemistry* **5**, 61 (2013).

[44] S.L. Chaplot, N. Choudhury, S Ghose, M.N. Rao, R. Mittal, P. Goel, *Eur J Mineral* **14**,291 (2002).

[45] G Venkataraman, L Feldkamp, VC. Sahni, *Dynamics of perfect crystals. Cambridge: MIT Press*; (1975).

[46] D. Petti, D. Crawford, and N. Chauvin, *MRS Bull*. **34** , 40 (2009).

[47] D. C. Crawford, D. L. Porter, and S. L. Hayes, *J. Nucl. Mater.* **371**, 202 (2007)

[48] Aleksandra Vojvodic and Carlo Ruberto, J. Phys. Cond. Matter **22**, 3755011 (2010).

[49] Zengtao Lv, HaiquanHu, Cheng Wu, Shouxin Cui, Guiqing Zhang and Wenxia Feng *Physica B* **406**, 2750 (2011).

[50] Hui Li, Litong Zhang, Qingfeng Zeng, Haitao Ren, Kang Guan, Qiaomu Liu, Laifei Cheng *Solid. State Comm.* **151**, 61(2011).

[51] H. G. Smith and W. Gläzer, *Phys. Rev. Lett*. **25,** 1611 (1970).

[52] H. G. Smith, *Phys. Rev. Lett*. **29**, 353 (1972).

[53] H. G. Smith and W. Gläzer, in Proceedings of the International Conference on Phonons, Rennes, France, July 1971, edited by M. A. Nusimovici, Flammaron Sciences, Paris, (1971).

[54] J.F. Alward, C.Y. Fong, M. El-Batanouny, F. Wooten, *Phys. Rev.* B**, 12,** 1105 (1975).

[55] H. Wipf, M.V. Klein, W.S. Williams, *Phys. Status Solidi B***408,** 489 (1981).

[56] F.A. Modine, T.W. Haywood, C.Y. Allison, *Phys. Rev. B***, 32,** 7743 (1985).

[57] L. Pintschovius, W. Reichardt, B. Scheerer, *J. Phys. C* **11,** 1557 (1978).

[58] A.M. Nartowski, I.P. Parkin, M. Mackenzie, A.J. Craven, I. MacLeod, J. Mater. Chem. **9,** 1275 (1999).

[59] E. I. Isaev, S. I. Simak, I. A. Abrikosov, R. Ahuja., Yu. Kh. Vekilov, M. I. Katsnelson, A. I. Lichtenstein and B. Johansson, *J. Appl. Phys*. **101**, 123519 (2007).

[60] Anna Delin, P. M. Oppeneer, M. S. S. Brooks, T. Kraft, J. M. Wills, Borje Johansson and Olle Eriksson, *Phys. Rev. B* **55**, R10173 (1997).

[61] V. Kanchana, G. Vaitheeswaran, Xinxin Zhang, Yanming Ma, A. Svane, and O. Eriksson, *Phys. Rev.B* **84**, 205135-1(2011).

[62] S.K. De and S. Chatterjee, *J. Phys. C: Solid State Phys.* **21**, 3261 (1988).

[63] S. Kose, F. Atay, V. Bilgin and I. Akyuz, *Int. J. Green,Energy* **1**, 353(2004).[52] R. Kondo, H. Okimura and Y. Sakai, *Jpn. J. Appl.Phys.* **10**, 1547 (1971).

[64] F. A. Benko and F. P. Koffyberg, *Solid State Commun.* **57,** 901 (1986).

[65] A., Shiori *Jpn. Pat., No*. **7**, 909 (1997).

[66] D. R. Lide (Editor), *CRC Handbook of Chemistry and Physics*, 77th edition (CRC Press, Boca Raton) (1996-1997)

[67] Roberto J. Guerrero-Moreno and Noboru Takeuchi,*Phys. Rev.* **B. 66**, 2052051 (2002).

[68] Haozhe Liu, Ho-kwang Mao, Maddury Somayazulu, Yang Ding, Yue Meng, and Daniel Häusermann, *Phys. Rev.* **B 70**, 0941141 (2004).

[69] Feng Penga, Qiang Liu, Hongzhi Fu and Xiangdong Yang, *Solid State Comm.* **148**, 6 (2008).

[70] M. Durandurdu, *EPL* **84**, 66003 (2008).

[71] Wenxia Feng, Shouxin Cui, Haiquan Hu, Guiqing Zhang, Zengtao Lv and Zizheng Gong, *Phys. Status Solidi* **B 247**, 2202 (2010).

[72] W. Martienssen and H. Warlimont (eds.), Springer Handbook of Condensed Matter and Materials Data (Springer,Berlin, 2005).

[73] Gen-Quan Li, Cheng Lu, Xing-QiangYang, Shao-Wu Xiao, Ai-HuaWang, LiWang and Xiao-Ming Tan, *High Press. Res.* **30**, 679 (2010).

[74] H.Z. Liu, J.S. Tse, and H.K. Mao, *J. Appl. Phys.* **100**, 093509-1 (2006).

[75] W. Martienssen and H. Warlimont, *Hand Book of Condensed matter and Materials data,* Springer, Germany 2005

[76] H.P. Singh and B. Dayal, *Solid State Commun*. **7**, 725 (1969)

[77] O. Madelung, U. Rossler and M. Schulz (eds.), Cadmium Oxide (CdO) Debye temperature, heat capacity, melting point, density, in Landolt-Bornstein Group III, Vol. 41B:II-VI and I-VII Compounds, Semimagnetic Compounds (Springer-Verlag, Berlin, 1999).

[78] C. K. Jun and P. T. B. Shaffer *J. Less-Common Metals***, 23**. 367 (1971).

[79] H.P. Liermann, A.K. Singh, B. Manoun, S.K. Saxena, C.S. Zha, *Int. J. Refractory Metals & Hard Materials,* **23**,.109 (2005).

[80] Laura Lo´pez-de-la-Torre, Bjo¨rn Winkler, Ju¨rgen Schreuer, Karsten Knorr, Miguel Avalos-Borja, *Solid State Comu.,* **134,** 245 (2005)

[81] S.P. Dodd, M. Cankurtaran and B. James *J. Materials Sci*., **38** , 1107 (2003).

[82] J. Staun Olsen, J.-E. Jørgensen, L. Gerward, G. Vaitheeswaran, V. Kanchana, A. Svane*, J. Alloys and Compounds*, **533**, 29 (2012).

[83] Sebastian B. Schneider, Dominik Baumann, Ashkan Salamat and Wolfgang Schnick, J. Appl. Phys., **111**, 093503-1 (2012).

[84] Hyunchae Cynn, Magnus Lipp, William Evans and Yasuo Ohishi, *J. Phys.: Conference Series* **215,** 012010 (2010).

[85] J. S. Olsen, L. Gerward, U. Benedict, J.P. ITIE and K. Richter, *J. Less Comn. Metals* **121,** 445 (1986).

[86] L. Gerward, J. Stalin Olsen, U. Benedict, J.-R. Itie and J.C. Spirlet, *J.Appl.Cryst.***19**, 308 (1986).

[87] L. Gerward, J. Stalin Olsen, U. Benedict and H. Luo, *J. Less Common Metals* **161**, L11, (1990)

[88] H. M. Tütüncü and G. P. Srivastava*, High Press. Res*. **87**, 4109 (2007).

[89] L. Gerward, J. Stalin Olsen, U. Benedict, J.-R. Itie and J.C. Spirlet, *J.Appl.Cryst.***19**, 308 (1986)

[90] L. Gerward, J. Stalin Olsen, U. Benedict and H. Luo, *J. Less Common Metals* **161**, L11 (1990)

[91] J. Danan, J. Nucl. Mater **57**, 280 (1975)

[92] R.S. Street, T.N. Water, *The Thermal Expansion of the ThC and ThN*, UKAEA Report AERE-1115, (1962)

[93] P. Chiotti and R.W. White, J. Nucl. Mater. **23**, 37 (1967)

List of Figures

List of Tables

Chapter 1

Introduction

1.1 Preface

Pressure is a thermodynamical variable which leads to very large change in volume and interatomic distances, which can be an order of magnitude higher than the change possible with temperature variation. The effect of pressure is to decrease the interatomic distances causing the increased overlapping or mixing of outer electronic orbitals. This increased overlapping leads to shifting and broadening of the energy bands resulting in interesting changes in the physical and chemical properties of materials including the structural phase transformations, solid to liquid transitions, metal to insulator transitions, formation of new stoichiometric compounds etc [1-5]. Discovery of various important pressure induced phase transitions and measurement of high pressure equation of state (EOS), shock Hugoniot, pressure dependent elastic constants and strength properties of materials have been proved very important in both applied and basis sciences. For example, in applied science the high pressure EOS, shock Hugoniot, elastic constants and pressure induced phase transitions serve as key inputs for hydrodynamic codes used for simulation of various situations such as reactor accidents, effect of missile attacks and shock propagation through geological media, fission/fusion energy systems and analysis of many problems related to geophysics, astrophysics. On basic sciences, many new phase transformations have been discovered for example, the pressure induced metallization of fluid molecular hydrogen and in oxygen around 140GPa and 96 GPa [6, 7-8], metal to insulator transition in sodium around 200 GPa [9]. Other interesting pressure induced phase transitions occurs in porous silicon (π-Si) where it undergoes a crystalline phase transition from diamond type structure to a primitive hexagonal structure around ~20 GPa during compression whereas, upon decompression, it first undergoes amorphization [10, 11] and then this amorphous phase again transforms to hexagonal phase under further increase of pressure showing a kind of memory effect. Similarly, the pressure induced superconductive transition in lithium above 30 GPa and in silane above 90 GPa [12-14] are some of popular high pressure studies reported in past.

Experimentally, the high pressures in the materials are generated either by static compression methods or by shock compression methods. In the static compression technique [4], material is compressed slowly and the temperature inside the sample during the experiment remains constant *i.e.* the static compression is an isothermal process. In static method one can compress the material hydrostatically by selecting a suitable (fluid or gas) pressure transmitting medium surrounding the sample [4, 15]. On the other hand, in shock loading methods, materials are compressed uniaxially with very high rate of pressurization (rise times ~ few tens of nanoseconds), leading to the increase in both temperature and entropy of the materials.

Apart from the experiments, the modern *ab-initio* electronic band structure calculation methods based on the density functional approach have also been proved useful to not only reproduce the experimental results but also to predict the behaviour of materials under high pressure and high temperature [9-30]. In recent years, new theoretical techniques have become available to explore the energy landscape of different chemical systems [30-38]. It has been possible to predict new phases in many compounds under high pressure. For example, in simple metal calcium using Universal Structure Predictor:Evolutionary Xtallography (USPEX) algorithm in conjunction with *ab-initio* electronic band structure method Oganov *et al.* [39] predicted a β-tin type tetragonal structure (space group $I4_1/amd$) to be more favorable above 33 GPa. However, in contrast to this theoretical prediction, Mao *et al.* [40], in high pressure x-ray diffraction measurements reported a phase transition to rhombohedral structure (space group R-3m) around 32 GPa at 300 K which upon cooling to 30K at the constant pressure transformed to orthorhombic structure (space group C*mmm*). This discrepancy between theory and experiment has been solved by Li *et al.* [41] later by repeating the experiment on this material and confirming the occurrence of β-tin type tetragonal structure around 35GPa. Similarly, it has been also possible to predict the unusual stoichiometries in many compounds under high pressure. For example, in sodium chloride the stable $NaCl_3$ and Na_3Cl have been predicted under high pressure [42] which have been realized experimentally also [42].

In view of the important role played by pressure induced structural phase transitions, high pressure EOS, pressure dependent elastic constants and dynamical stability of materials, it is important to determine these properties for understanding the several aspects of the material behaviour under high pressures. The present thesis deals with such studies carried out on some binary carbides, oxides and nitrides materials. The oxide includes CdO, the carbides include ScC, YC, TaC, ThC and UC, and the nitride includes CeN. All these binary compounds exist in rocksalt structure (B1) at ambient conditions and have attracted attention of researchers due to their technical as well as academic importance. For example, in case of UC and ThC having high stiffness and high melting point, the major interest is due to their importance as nuclear fuel materials in the generation IV nuclear reactors [43, 44]. In order to develop the technologies for the nuclear cycle based on carbide fuels, it is important to understand structural, thermo-physical and mechanical properties of these compounds. As far as transition metal carbides ScC, YC and TaC are concerned, the extreme hardness, good strength even at elevated temperatures and high melting point exhibited by these carbides makes them important scientifically as well as technologically [45-56]. Some of the potential technological applications are in cutting tools and optoelectronics. The academic interest on these materials comes due to the existence of mixed bonding (both metallic and covalent) which is believed to be responsible for high hardness and high melting points of these materials. The CeN which is one of the mono nitride of rare earth metal shows anomalous physical properties such as unusually small lattice parameters [57-59]. The anomalous physical properties of this mono nitride are attributed to the peculiar behaviour of 4*f* electron of Ce ion. The unusual physical properties make this compound interesting both academically and industrially. Transition metal oxides are systems with large variability of structures and chemical bonding which brings about different magnetic, electrical and optical properties. These unique properties make these compounds suitable for applications like new memories smaller transistors and smart-sensors in different semiconductor industries. The technological applications have attracted the interest on the high pressure behaviour of these materials. The cadmium oxide is one of the attractive semiconductor materials. It has many industrial applications such as in the production of solar cells, liquid-crystal displays, electro chromic devices, light-emitting diodes, etc.[60-63]. So, in order to fully exploit this semiconductor material, it is necessary to obtain a good understanding of the physical properties of CdO, and in particular, its structural and thermodynamic properties under high pressure [64-70]. The main goal of the present work is to add further understanding to the high pressure structural, elastic and lattice dynamic stability of these binary compounds formed by combining the transition metals or actinide metals to simple elements of group IV, V and VI of the periodic table. Apart from structural stability analysis, the thermo-physical properties like equilibrium volume, bulk modulus, specific heat, entropy, vibrational free energy and thermal expansion as a function of temperature have also been derived.

The thesis to be presented is divided into six chapters. The present chapter provides the outline of the work to be presented in the subsequent chapters along with the current status of high pressure research including the basics of high pressure, the methods of generation of high pressure and various diagnostic techniques utilized for determining the behaviour of the materials under pressure. Also discussed are the theoretical methods (*ab-initio* calculations) available to simulate the high pressure response of the materials.

The second chapter deals with the theoretical calculations carried out on CdO. In CdO, the main focus was to analyze the structural stability under high pressure and to determine the pressure dependent elastic and vibrational properties (lattice-dynamics). For this purpose, first the *ab-initio* calculations at 0 K have been performed to analyze structural stability by choosing the structures namely B1 and CsCl type (B2). The 0 K calculations have been utilized to derive the 300 K isotherm after adding finite temperature corrections within quasi harmonic approximations. Additionally, employing the theoretically determined thermal equation of state in conjunction with Rankine Hugoniot relation, the Hugoniot of B1 phase of this material has been derived. Further calculations have been performed to determine the shear elastic moduli and phonon dispersions as a function of hydrostatic compression. The structural stability analysis suggests that the B1 phase will transforms to B2 phase at ~87 GPa in good agreement with experimental value of 90.6 GPa [65]. The pressure dependent elastic constants have been determined for both B1 and B2 phase upto ~200 GPa. All the elastic moduli of B1 phase at zero pressure have positive values and upon compression all of these, except the shear modulus (C_{44}), display increasing trend with pressure. The C_{44} modulus displaying opposite trend with increasing pressure decreases monotonically with increasing pressure and vanishes at ~126 GPa, suggesting the development of elastic instability in B1 phase around this pressure. In contrast, for the B2 phase, all the elastic moduli at zero pressure have been found to be negative and remain negative up to the pressure of ~ 38GPa, suggesting that this structure is elastically unstable up to this pressure and emerges as an elastically stable structure thereafter. The dynamical stability of B1 and B2 phase has been tested by calculating the phonon dispersion curves (PDC) at ambient conditions and at higher pressures. For B1 phase, all the phonon frequencies below the pressure of 116 GPa have been found to be positive, but for pressures ≥ ~116 GPa all the phonon frequencies become imaginary making the structure unstable dynamically beyond this pressure. The situation for the B2 phase is different; it shows imaginary frequencies up to 56 GPa and thereafter all the frequencies become positive making the structure dynamically stable beyond this pressure. The analysis of elastic and dynamic stability as a function of hydrostatic compression suggests that the pressure induced B1 to B2 transition in CdO is driven by soft transverse acoustic phonon mode at the Brillouin zone boundary.

In the third chapter of the thesis the detailed theoretical investigations carried out in transition metal carbides ScC, YC and TaC have been reported. The theoretical work includes the analysis of structural stability, determination of equation of state, elastic and lattice dynamic properties as a function of hydrostatic compression. The comparison of enthalpies of B1 structure, Primitive orthorhombic (Pmmn) and B2 phase at various pressures suggested that the ambient pressure B1 phase of ScC will transform to the Pmmn phase at ~80 GPa. In case of YC the same transition occurs at ~ 30 GPa. In TaC instead of Pmmn phase, the B2 structure becomes stable around 472 GPa. This theoretical prediction is open for experimental confirmation. Various thermophysical and elastic properties such as volume, bulk modulus, its pressure derivative, elastic constants have been determined. The phonon dispersion relations determined at various pressures from lattice dynamic calculations show that the phonon frequencies for B1 phase in ScC are positive at zero pressure and remain positive upto 110 GPa. For YC, however, this phase displays positive phonon frequencies up to 28 GPa. These results suggest that the B1 phase in ScC and YC will become dynamically unstable beyond 110 GPa and 28 GPa, respectively. Further, this also suggests that the B1 to Pmmn transition in these materials is driven by phonon softening. In case of TaC it has been found that the B1 phase remains dynamically stable much beyond the B1 to B2 transition pressure upto maximum pressure 600 GPa. Besides this for ScC and YC, the phonon frequencies (ω), their pressure derivative coefficients and Gruneisen parameter (γ) of several modes at high symmetry points Γ, X and L of Brillouin zone in B1 phase have also been calculated. The negative TA Gruneisen parameter at X point for both the materials indicates that the frequency at this point decreases with increasing pressure. Additionally the frequencies of various modes calculated in our work have been compared with other published data [56] for both the materials. In TaC, the calculations have been extended to determine the temperature effect on volume and bulk modulus of B1 phase using quasiharmonic approximation (QHA). Apart from the phonon dispersion relations, the pressure dependent elastic constants have also been calculated for both B1 and B2 phase upto 200 GPa in both the materials.

The fourth chapter presents the theoretical high pressure investigations CeN one of the mono nitride of rare earth metal. In high pressure energy dispersive X-ray diffraction measurements it has been reported that the B1 phase of this material transforms to B2 structure at ~ 65 GPa [71]. This transition reported in this material is in contrast to that observed in mononitrides of nearest neighbors of Ce in periodic table i.*e.* LaN and PrN [72, 73]. In these two materials the observed high pressure phase is a low symmetry tetragonal (P4/nmm) (B10) structure. The distinct high pressure behavior of CeN as compared to that shown by LaN and PrN led us to perform the high pressure theoretical investigations on this material. Our calculations on CeN suggest that the B1 phase in this material will also transform to B10 structure at ~53 GPa which upon further compression will transform to B2 phase at 200 GPa. So, according to our theoretical analysis instead of direct B1 to B2 transition, the CeN will undergo transition sequence of B1 to B10 to B2 phase at 53 GPa and at 200 GPa, respectively. In order to further support our results, the theoretical X-ray diffraction pattern have been calculated for both the B10 and B2 phases around 75 GPa (well above the transition pressure) and it has been found that most of the intense peaks, except few weak peaks (211, 301) of the calculated B10 phase coincide either with that of B1 or with B2 phase. In the experimental EDXRD pattern recorded at ~ 77 GPa, many peaks *e.g.* (222) and (400) of B1 phase and (210) B2 phase which display a good strength in theoretical pattern are hardly visible in the experimental pattern, suggesting the need for more experiments to either confirm the existence of B2 phase or rule out its occurrence. Further, the elastic stability analysis of the B1 structure up to 160 GPa, suggests that the B1 to B10 transition in this compound is not related to elastic failure. However, the lattice dynamic simulations carried out at different pressures indicate that this transition is related to the lattice dynamic instability occurring around the transition pressure due to vanishing of transverse acoustic (TA) frequency in the midway of Γ-X direction. Additionally, it is found from present theoretical analysis that the B2 phase is dynamically unstable below the 200 GPa and acquires dynamical stability only around 200 GPa. These results of lattice dynamic calculations support outcome of the static lattice calculations.

The theoretical investigation on carbides materials is extended to monocarbides of light actinides *i.e.* UC and ThC and presented in fifth chapter of the thesis. The experimental studies [74-76] on these carbides have reported that the UC undergoes B1 to primitive orthorhombic transition (Pmmn) at ~ 27 GPa, whereas, the ThC remains stable in B1 phase even up to 50 GPa. Theoretical studies have been performed to analyze structural stability of these two materials under hydrostatic pressure. In agreement with the experiment in UC the present calculations have shown that the B1 phase will transform to Pmmn structure around 20 GPa. The static lattice calculations have been substantiated by lattice dynamic calculations, which displayed that the B1 phase will become dynamically unstable around transition pressure due to vanishing of long wavelength TA phonons. This outcome of the lattice dynamic calculations has been supported by the behavior of C_{44} shear elastic modulus examined as a function of pressure. It has been found that this modulus fails around the transition pressure, indicating that the B1 to Pmmn phase transition in UC is shear driven. In ThC, however, our theoretical results do not agree with the experimental reports [75,76]. The comparison of enthalpies, derived for various phases from 0 K total energy calculations at several hydrostatic compressions, yielded a high pressure structural sequence of B1 → Pnma → Cmcm → B2 with transition pressures of ~ 19 GPa, 36 GPa and 200 GPa, respectively. The discrepancy between the theory and the experiments could be due to the substoichiometry of the thorium monocarbide samples used in the experimental study. The theoretical finding opens scope for conducting more experiments with varying substiochiomerty of ThC samples to understand the role of this on the structural stability of ThC under high pressure. Further, in order to substantiate the results of static lattice calculations, the phonon dispersion relations for these structures have been derived from lattice dynamic calculations. The theoretically calculated phonon spectrum reveal that the B1 phase fails dynamically at ~ 33.8 GPa whereas the Pnma phase appears as dynamically stable structure around this pressure. Similarly, the Cmcm structure also displays dynamic stability in the regime of its structural stability. The B2 phase becomes dynamically stable much below the Cmcm to B2 transition pressure.

The last chapter of the thesis summarises and conclude the overall work presented in the thesis. The summary and conclusion is followed by the further research scopes open in these areas.

Though, the present thesis deals with high pressure theoretical investigations on the materials, it is worth to give a brief account of the available modern high pressure experimental methods and diagnostic techniques also for sake of completeness. Therefore, the following section describes briefly the various experimental methods used to generate high pressures in materials and diagnostic techniques used to characterize the state of material under high pressures. Following to this is presented the modern *ab-initio* electronic band structure methods available for simulation of material behaviour under high pressure. The methods used for the simulations of materials to be presented in this thesis are described with greater length.

1.2 Experimental methods for high pressure generation

Experimentally, the high pressures in the materials are generated either by static compression methods or by dynamic compression (shock compression) methods. In the static compression technique [4], material is compressed slowly; for which, temperature inside the sample during the experiment remains constant *i.e.* the static compression is an isothermal process. In static method one can compress the material hydrostatically by selecting a suitable (fluid or gas) pressure transmitting medium surrounding the sample [4, 15]. On the other hand, in shock loading methods, materials are compressed uniaxially with very high rate of pressurization (rise times ~ few tens of nanoseconds), leading to the increase in both temperature and entropy of the materials. Under static compression, the duration of the pressure on the material can be as long as we desire whereas, in case of shock compression the duration of pressure pulse is of order of few microseconds depending upon the size of the sample. These differences in two compression techniques sometimes lead to different results on the materials. A brief description of two compression techniques is provided in following sections.

1.2.1 Static Compression Techniques

1.2.1.1 Method of Generation of Static High Pressure

Static compression technique was first introduced by Nobel Laureate P. W. Bridgman. He built the piston-cylinder device where the sample is compressed in a cylinder by two opposed pistons [75]. This basic apparatus was improvised later. This was followed by the invention of Bridgman anvil cell where the material under examination is sandwiched between two anvils of tungsten carbide. The quest for still higher pressures led to the invention of the diamond anvil cell (DAC) [77-83] (a sketch is shown in Fig. 1.1) which works on the same principle as the Bridgman cell; the only difference being the material used for the anvils is the hardest material known so far. The sample, here, is squeezed between two opposing single crystals of diamond. Various diagnostic techniques used to analyze the state of sample under high pressure include the measurement of electrical resistance, Mossbauer spectroscopy, x-ray diffraction, Raman and Brillouin spectroscopy, optical absorption spectroscopy etc.

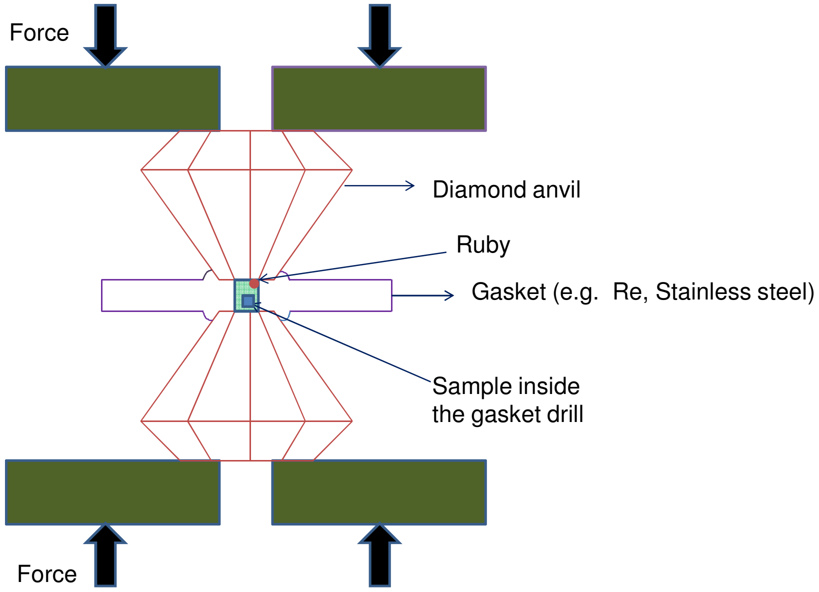

Figure 1.1: Schematic diagram of Diamond anvil apparatus used for generating high static pressures in samples.

As shown in the figure 1.1, the material to be squeezed is placed in the hole of metal gasket made of hard material rhenium or stainless steel, which is fixed on the flat tip (size ~ 200-500 μm) of the bottom anvil. The pressure in the material is generated by compressing the anvils against each other. In order to generate hydrostatic compression the sample is surrounded by a fluid pressure transmitting medium. The commonly used pressure transmitting mediums are 4:1 methanol-ethanol mixture, Xe, Ar, He and H_2 [4]. The methanol-ethanol mixture is used up to 10 GPa, however, the gases Xe, Ar, He and H_2 are used up to higher pressures of ~ 100 GPa. The DAC developed by Mao and Bell can generate static pressure of about 200 GPa in samples [82, 83]. Still higher pressures of more than 500 GPa are reported to be achieved by using improved DAC [84]. Very recently, the micro-semi-balls of nano-crystalline diamonds have been used as second stage of conventional diamond anvil cell and this extends the achievable pressure in this device to above 600 GPa [85]. To study high pressure behaviour of materials at elevated temperatures the new version of diamond anvil cell known as LHDAC has been developed [86]. This DAC uses laser heating arrangements and can generate high temperatures and pressures > 3000 K and >100 GPa, respectively. This instrument is useful for understanding the state of material in the conditions existing in the interior of the earth.

1.2.1.2 Diagnostic Techniques in Static High Pressure Experiments

The commonly used microscopic techniques for characterization of pressurized sample are x-ray diffraction [87], inelastic x-ray spectroscopy [88], extended x-ray absorption fine-structure (EXAFS) [89], X-ray fluorescence (XRF) [90], Mössbauer spectroscopy (SMS) [91], nuclear forward and inelastic scattering (NFS and NIS) [92], neutron diffraction, Raman scattering, IR scattering and Brillouin scattering [4, 93-99] commonly used for online characterization of the pressurized sample in DAC.

The x-ray diffraction technique is one of the microscopic techniques used widely for characterization of samples subjected to high pressures in DAC. A significant advancement has been made in this technique after the birth of synchrotron radiation sources around the world. The European Synchrotron Radiation Source (ESRF), the Advanced Photon Source (APS) in the United States, the Japanese source SPRING-8 and National Synchrotron Light Source (NSLS) at Brookhaven National Laboratory are examples of some of the third generation synchrotron sources. The synchrotron radiation generated from such sources spans a broad spectrum from the far infrared to hard x-rays; it is pulsed and naturally polarized; and it is ~ 10^3 -10^4 times brilliant than the beams from conventional x-ray machines. The high brilliance along with the possibility to tune the wavelength of the x-rays, to control their polarization, and to choose between a single wavelength or a range of wavelengths makes this radiation an excellent probe for normal and magnetic materials, biomolecules, polymers and allowing to explore phase diagram, chemical reactivity, properties of elements and compounds [100]. The high brilliance of synchrotron radiation makes it a very powerful tool for characterizing the low Z elements (*e.g.* H_2, Li) or materials composed of low Z elements (*e.g.* hydrogen storage material $NaBH_4$) and quantitative analysis of phase composition specially for phases present in extremely low concentration < 1%. For example, in Li the occurrence of new rhombohedral phase and cubic polymorph with 16 atoms per unit cell under high pressure could be confirmed through sufficiently intense synchrotron radiation diffraction (SRD) [101]. In nominal high purity α-alumina ceramic, the SRD could clearly establish the presence of trace levels of β- alumina and anorthite ($CaAl_2Si_2O_8$), which was inconclusive from conventional x-ray diffraction [102]. The synchrotron radiation has been used for Mossbauer spectroscopy also. For example, the detection of the antiferromagnetic to paramagnetic transition in $SrFe_2As_2$ at 4.2 GPa and 13 K could be done through Mossbauer spectroscopy using SRD [103].

The measurement of pressure generated in the sample due to static compression is carried out using either the internal pressure markers or pressure dependence of ruby fluorescence. In first method the pressure generated in the sample is determined by adding internal pressure marker material (whose EOS is known) such as Mo, Cu, Pd or Ag with the sample in DAC [4]. The compression generated in the sample and pressure marker material is determined from collected x-ray diffraction data of sample and marker. The corresponding pressure in the sample is then inferred from the known EOS of marker material. In the second method the pressure dependence of R1 (6943Å) line of Ruby fluorescence is used to determine the pressure generated in the sample at a given compression [4]. The calibration of ruby fluorescence pressure scale for this purpose is carried out using isothermal EOS of marker materials derived from shock wave experiments [4]. The calibration so obtained relates the pressure and the shift in R1 line as follows [83]:

$$P(Mbar) = \frac{A}{B}\left\{\left[1+\frac{\Delta\lambda}{\lambda}\right]^{B} - 1\right\}$$

with $\Delta\lambda$ is the ruby R-line shift (= 0.365 Å/kbar) and A = 19.04 Mbar and B = *7.665.*

The detection of pressure induced structural phase transitions and determination of their mechanisms is carried out by performing x-ray diffraction; Raman or IR spectroscopy in the compressed state, and electron diffraction and electron microscopy measurements on samples retrieved after pressurization. The continuous monitoring of the evolution of the new structure in the sample material in DAC experiments through x-ray diffraction or Raman, IR spectroscopy is carried out in in-situ mode as a function of applied pressure. Further, the in-situ measurements are useful to detect the reversible phase transitions in the materials. For example, the reversible cubic to amorphous phase transitions in negative thermal expansion materials $ZrMo_2O_8$ and $HfMo_2O_8$ [104], scheelite phase to fergusonite phase transition in $BaWO_4$ [105] could be detected by in-situ x-ray diffraction measurements. Though both the x-ray diffraction, and spectroscopy measurements are equally important for detecting the structural transitions in materials sometimes the sub structural changes that remain undetected through x-ray diffraction are observed only through Raman measurements *e.g.* sub-structural amorphization in $Co(OH)_2$ [106], where the Co-O substructure remains intact but O-H substructure gets disordered under pressure. In this case, the x-ray diffraction which is sensitive to only change in Co-O substructure, does not see any change in the structure of $Co(OH)_2$, however, the Raman measurements which are sensitive to location of H atom also, could reveal disordering of O-H substructure manifested by broadening of the peak width of the O-H stretch mode. The electron microscopy measurements are useful for not only to detect the pressure induced irreversible phase transitions but also to determine the lattice correspondence between the parent and product phases, which in turn is used to understand the mechanism of the phase transition. For example, the lattice correspondence between the parent α (hcp) phase and product ω phase derived from electron diffraction patterns obtained from partially ω (three atom simple hexagonal) transformed samples of group IV transition elements and their alloys subjected to high static and dynamic pressures has been used to understand the mechanism of this transition [107-113].

Apart from these microscopic techniques, the macroscopic method of electrical resistance measurements is very useful in detecting the pressure induced phase transitions, *e.g.* in Ti and Yb through continuous monitoring of the electrical resistances under pressure, Singh [114, 115] has not only detected the $\alpha \rightarrow \omega$ transition in Ti and fcc → bcc transition in Yb but also investigated the kinetics of these transitions.

The pressure dependent elastic moduli of materials are determined through high pressure x-ray diffraction measurements in DAC experiments [116-118]. Singh *et al.* [116] have developed a formalism to determine the elastic moduli at high pressures through x-ray diffraction measurements performed under non-hydrostatic conditions. To generate non-hydrostatic stresses the samples are directly compressed between diamond anvils *i.e.* no pressure transmitting medium is used. Employing this formalism, Singh *et al.* [116] determined the elastic moduli for bcc Fe at 4.6 GPa, its high pressure hexagonal phase at 52 GPa, and fcc FeO at 8.3 GPa. Through same formalism and similar measurements, the pressure dependence of elastic moduli in Mo up to 25 GPa has been determined by Duffy *et al.* [117]. In niobium, the pressure dependence of elastic compliances was determined up to 145 GPa [118] using x– ray diffraction in transmission geometry. In addition to x-ray diffraction, various other methods such as ultrasonic pulse echo experiments and Brillouin scattering [119-122] are also used to determine the elastic constants of materials. In the ultrasonic methods, an ultrasound transducer generates an ultrasonic pulse and receives its echo after reflection from sample free surface. The velocity of the sound in the sample is determined from the measured time lapse between the pulse and its echo and known thickness of the sample which in turn is related to the elastic modulus. In order to determine all the elastic constants, sound waves with longitudinal and transverse polarization are propagated in various crystallographic directions in single crystals [119]. The Brillouin scattering, where the incident monochromatic light photon interacts with the acoustic phonon of the material and either it absorbs a phonon or it emits a phonon, which causes a decrease or increase in wavelength of the scattered photon. By measuring the wavelength of incident and scattered photon and applying the conservation of energy and crystal momentum one can determine the sound velocity and hence the corresponding elastic modulus. All the elastic moduli, or equivalently elastic constants, of a material can be determined by performing Brillouin scattering from single crystal samples of different orientation. For example, the three independent elastic constants namely C_{11}, C_{12} and C_{44} of a material having cubic structure can be determined by performing Brillouin scattering from [100] and [110] or [100] and [111] oriented single crystals [120, 121]. These methods are limited to low pressures < 25 GPa.

1.2.2 Shock Compression Techniques

1.2.2.1 Basic Concepts of Shock Compression

A shock wave is said to be generated in the material when a sudden deposition of high energy on a material by some means causes an impulse of compression in the material which travels with supersonic speed with respect to the uncompressed material ahead of it and produces a near-discontinuous changes in density and pressure across the wave front [123]. This is in sharp contrast to subsonic sound waves, where all thermodynamic quantities vary continuously through the medium. The formation of shock wave in a medium can be understood as follows:

Suppose a sudden deposition of energy on a material surface introduces a compression wave into it. This compressive disturbance travels in the interior of the material as a broad stress wave as displayed in Fig.1.2a. Every point in this profile travels with a velocity

$$\frac{dx}{dt} = C + u \tag{1.1}$$

Where C represents the sound velocity and u corresponds to the material velocity at a pressure P. As the compressibility of most of the materials decreases with increasing pressure, so both C and u increase with increasing pressure, thus making the point near to the crest to travel faster than that away from the same *i.e.* starting from foot to the crest of the profile the velocity goes on increasing (shown by the vectors in Fig 1.2a), which in turn sharpens the wave front. This sharpening effect arising due to dependence of sound speed on amplitude of pressure is opposed by the spreading effects due to viscosity and thermal conductivity of the material. Hence at some latter time $t = t_1$, when the two opposing effects start balancing each other the steady shock wave front with finite constant width (Fig. 1.2b) propagates in to the material. For a steady shock wave the conservation of mass, momentum and energy across the discontinuity can be written as a set of differential equations [123, 124], which lead directly to the Rankine-Hugoniot relationships between the specific volume V, the stress (shock pressure) *P*, the particle velocity u the shock velocity D and the specific internal energy E :

$$\rho_0 D = \rho(D-u) \text{(Mass Conservation)} \tag{1.2}$$

$$P - P_0 = \rho_0 D u \text{ (Momentum Conservation)} \tag{1.3}$$

$$\mathrm{E} - \mathrm{E}_0 = \frac{1}{2}(\mathrm{P} + \mathrm{P}_0)(\mathrm{V}_0 - \mathrm{V}) \text{(Energy Conservation)} \tag{1.4}$$

where, the subscript ‘0’ refers to the initial values in front of the advancing shock wave. Further, the following useful relationships can be deduced from Eqs. (1.2) and (1.3).

$$(P - P_0) = \frac{D^2}{V_0^2}(V_0 - V) \tag{1.5}$$

$$u^2 = V_0^2\left[(P - P_0)/(V_0 - V)\right] \tag{1.6}$$

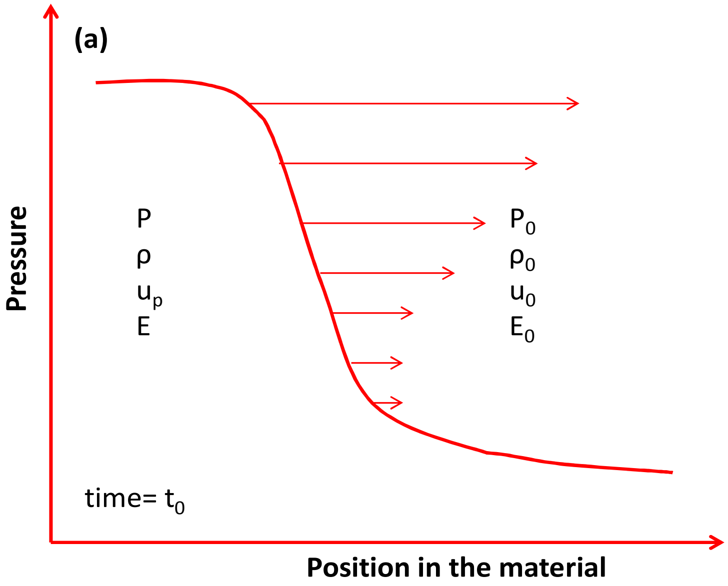

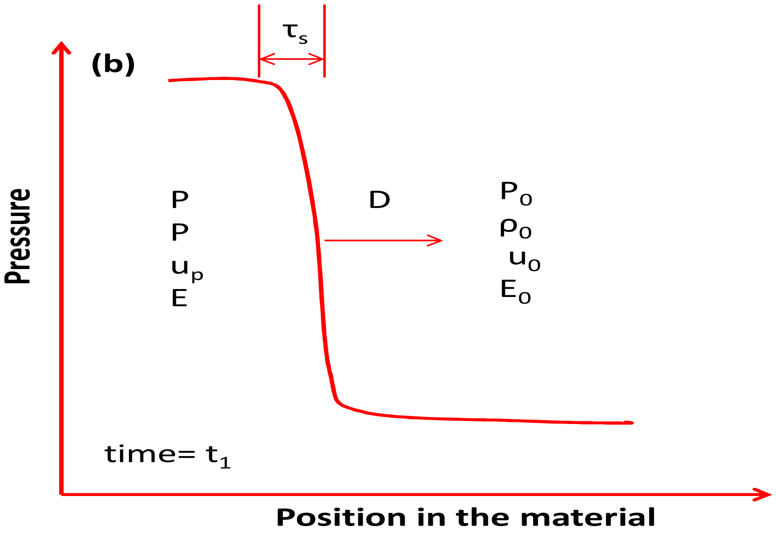

Fig.1.2: **(a)** Hypothetical broad stress wave profile at initial time = t_0. The length of the vector indicates the speed of the point in the profile, which increases with stress at that point. **(b)** At some instant t_1 the wavefront attains a finite constant width (τ_s) due to balancing of sharpening effect caused by non linearity and spreading effect from viscosity and thermal conductivity of material for which a steady shock wave with constant front width (τ_s) propagates into the material

Under shock compression the thermodynamic path followed by material while going from initial state (P_0, V_0) to a final state (P, V) is a line known as Rayleigh line having slope D^2/V_0^2 and represented by Eq. (1.5). Only the initial and final states on this line are the equilibrium states and can be measured *i.e.* in a shock process it is possible to achieve only one P, V data point. Therefore, to generate various P, V data of a material under shock compression a number of shock wave experiments, each with different shock velocity need to be conducted. The curve connecting these P, V data (reached from the same initial P_0, V_0 state) is known as shock adiabat or Hugoniot. In other words, the Hugoniot of a material is the locus of all the possible equilibrium states that can be achieved from a given initial state, but the successive states along which cannot be achieved one from another by a shock process.

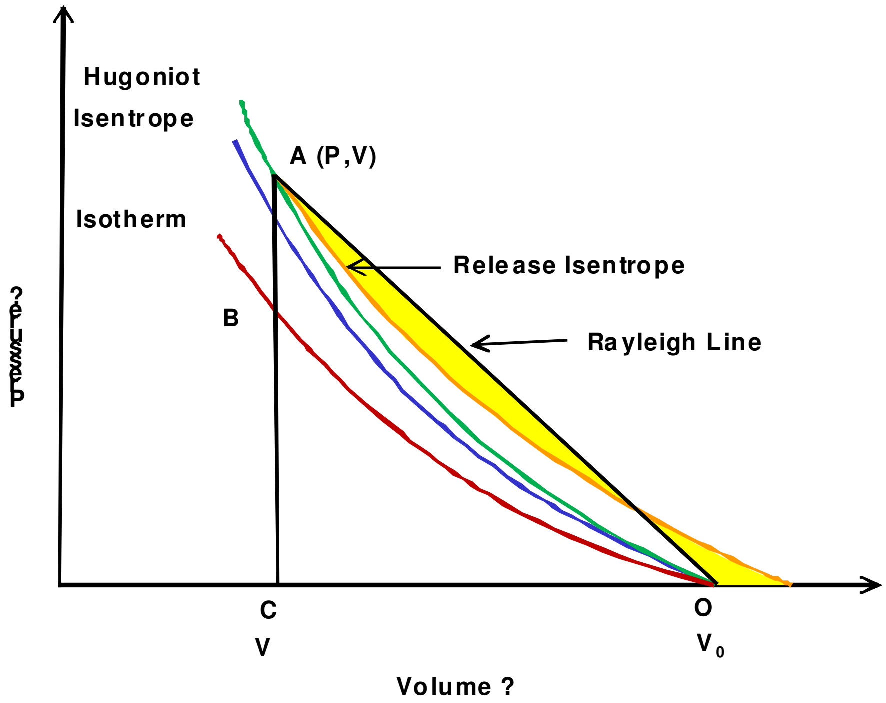

Fig 1.3 Schematic P-V diagram showing the compression curves. The Hugoniot lies above the isentrope which lies above the isotherm. For isentrope and isotherm, the thermodynamic path coincides with the locus of end states. For Hugoniot which is the locus of shock states, the thermodynamic path is a straight line (Rayleigh line) from (P = 0, V = 0) to (P, V) state on the Hugoniot curve. The magenta colured curve is the release isentrope. The difference of yellow shaded areas below and above the Rayleigh line indicates the residual heat upon unloading from peak shocked state.

Fig. 1.3 displays the differences between the isotherm, isentrope and Hugoniot passing through the common initial state. The red, blue and green curves represent the isotherm, isentrope and Hugoniot, respectively, starting from the same initial state (P_0, V_0). Isotherm and isentrope are thermodynamic paths *i.e.* during isothermal or isentropic compression; the material actually passes through each successive point along the isotherm or isentrope as it approaches the final state. Unlike isotherm or isentrope, the Hugoniot is not a thermodynamic path that is followed during shock compression; instead a state on Hugoniot can be reached from a given initial state via Rayleigh line as shown in Fig.1.3.

The process of shock compression is irreversible in nature and is accompanied by increase in entropy. Also, the temperature of the shock recovered sample is more than that of the initial unshocked state. Further, it is clear in Fig. 1.3 if the compression to volume V is carried out isothermally, then the increase in internal energy will be the area of the curved triangle OBC below the isotherm. However, under shock loading, the internal energy deposited on the compressed material is the area of the triangle OAC. The difference of the area OAC and OBC corresponds to the heat energy deposited by the shock on compressed material, which results in the thermal pressure. It may be noted that a small fraction of supplied energy goes in to generation of defects also. Fig. 1.3 clearly shows that with increasing, compression more and more energy goes into generation of thermal pressure. After passage of the shock, the material unloads through the release isentrope as shown in the figure 1.3. The difference of the area of triangle OAC and curved triangle under release isentrope represents the heat deposited on the terminal material.

1.2.2.2 Techniques of Shock Wave Loading

Shock wave in a material can be generated by rapid deposition of energy or by high velocity impact. Different forms of energy like chemical, mechanical, electrical, magnetic and radiation have been used for producing shock waves in materials. These can be classified as explosive driven systems, pulse radiation (laser, electron, X-ray, neutron, ion beam, photons etc.), gas guns, electric guns, rail guns and magnetic flux compression [124, 125-136].

The shock compression in materials can be achieved by several techniques such as gas guns, explosive systems, pulse radiation and electromagnetic launchers. The gas guns working on the principle of single stage, double stage or three stage acceleration of the projectile use hydrogen, helium or nitrogen as the propelling gases [128-130]. Apart from the gas guns the propellant derived guns known as propellant guns are also used to accelerate the projectile. The chemical explosives can be used to generate high shock pressures of several megabars in the materials by impacting the stationary target plate by a flyer plate propelled by gases generated due to detonation of the explosive. Electric gun is one of the examples of the electromagnetic launchers in which the thin flyer of light insulating material such as Mylar can be propelled to a velocity of several km/s by the hot vapours of metallic foil exploded by rapid electrical discharge. The maximum velocity of the flyer plate achieved so far using such system is more than ~30 km s^{-1} [133-135]. The electric gun developed in our laboratory at Bhabha Atomic Research Centre has the ability of launching a 0.5 g flyer up to a velocity of 6.6 km/s [132]. Extremely high shock pressures have been generated by direct irradiation of high intensity laser light (10^{12} to 10^{14} Wcm^{-2}). In such experiments, the thickness of the sample is of a few hundred μm and diameter is less than ~ 1mm. The temporal shape of the laser beam is often variable to produce shock waves [136].

The magnetic flux compressions method is another class of high pressure generation methods which can be used to generate isentropic compression in the materials [133, 134]. As Hugoniot of a material is a curve in EOS surface that is generated from a series of shock compression experiments, similarly, compression isentrope is a class of curve that explores another region of EOS surface. Unlike in shock compression experiments where single datum is obtained in one experiment, in isentropic compression experiment (ICE) one can generate a full isentrope in a single experiment. Recently, Sandia National Laboratory has developed a Z accelerator facility to produce 0.5 Mbar isentropic compressions in solids [135]. In magnetic compression techniques high magnetic fields (more than 100 Tesla) are generally produced in pulsed form using capacitor banks. These fields may be further enhanced through compression of metallic liners (cylindrical shells) in which initial magnetic field may be trapped and then compressed using secondary energy source such as another capacitor bank or chemical explosives. Apart from the isentropic compression these devices have been used to generate shock compressions also by accelerating the flyer plates to velocities of several km/s. The Z-accelerator of Sandia National Laboratory has been used to launch flyer plates of aluminium with thickness ~ 1 mm with ultrahigh velocities up to ~ 34 km/s not achievable with conventional gas guns [137]. Recently, the combination of static and dynamic compressions methods have been used with laser irradiation to achieve pressures of order of TPa on the samples [138]. Here, a sample is compressed inside a diamond anvil cell and laser induced shock wave further pressurizes this pre-compressed sample to generate the pressures of ~ 10-100 TPa.

1.2.2.3 Diagnostic Techniques in Shock Wave Experiments

In shock wave experiments the measurements technique can be broadly classified in two categories namely macroscopic (continuum) measurement techniques and microscopic measurement techniques depending upon the nature of properties to be measured. The macroscopic measurement techniques include impact velocity measurement, shock arrival measurement, time resolved stress profile and particle/free surface velocity history measurements. The impact velocity can be measured using electrical pins or optical technique. The shock velocity in the target material is generally measured using electrical and optical transducers. For measurement of shock velocity, the electrical sensors are placed at various known depths in the target from the impact surface and shock arrival timings at sensor locations is recorded, which is then used to determine the shock velocity in the target material [139-140]. The piezoresistive manganin gauges [141] have been mostly used to record the time resolved stress profile [142-143]. The interferometery techniques [144-149] such as velocity interferometer system for any reflector (VISAR) [144-145] and optically recording velocity interferometer system (ORVIS) [146] are used for measuring particle/free surface velocity history of the shock loaded target plate. ORVIS employs a streak camera to record the interference data with subnanosecond time resolution. Later, line imaging variations on these techniques [147-149] have been extended to encode spatial information from streak camera detectors. Adapting these techniques to the context of laser-driven targets has enabled precise measurement of the motion of a variety of shock-related phenomena in laser-driven targets, including the motion of free surfaces, of shocked interfaces, and of ionizing shock fronts in a wide variety of transparent media. These macroscopic (continuum) techniques can provide quantitative information about shock induced phase transitions (both reversible and irreversible), mechanical failure (fracture strength, Hugoniot elastic limit (HEL) and yield strength) at high strain rates and melting. These techniques however, do not provide the atomic level scale of such phenomena.

Though in-situ microscopic measurements in shock wave experiments are not easy, still there are some laboratories in the world that have recently developed capabilities of Raman measurements and real time x-ray diffraction measurements in shock wave experiments [150-155]. In polycrystalline magnesium, Milathianaki *et al.* [150] have detected the shock induced hcp to bcc phase transformation using online x-ray diffraction measurements. Similarly, in shock loaded iron Kalantar *et al.* [151] have detected the bcc to hcp structural transformation through in-situ x-ray diffraction measurements. Sub-nanosecond temporal resolution of X ray diffraction has been used to show that single crystal of silicon can sustain very high elastic strain [152]. More recently, Dolan et al. using real time optical transmission and imaging measurements in multiple shock wave compression up to peak pressure of 5GPa, have reported the solidification of water on nanosecond time scale [155].

1.3 Computational methods for high-pressure research

The past few decades have seen dramatic improvements in the ability to simulate complicated physical systems using computers. For example, there is a significant advancement in the computational simulations methods used to calculate the electronic band structure of solids. The knowledge of electronic band structures in turn has been utilized to examine structural stability, to determine equation of state, elastic properties of materials, dynamical (phonon) properties as a function of pressure. The predictive capabilities of modern electronic band structure methods have facilitated the determination of structural phase transitions, equation of state and pressure dependent elastic and mechanical properties of materials prior to experiments.

Properties of a material *e.g.*, EOS, elastic moduli, phonon frequencies etc. depend upon the crystal structure it acquires. Therefore, for proper understanding of material behavior under pressure it is essential first to analyze the structural stability. For a material, at a given thermodynamic condition (pressure, temperature and specific volume), the thermodynamically favourable structure is the one which has the lowest free energy and it is found by determining and comparing the free energies for various plausible structures. Depending upon the thermodynamic condition the different forms of free energy are used for structural stability analysis. For example, for constant volume and temperature condition the thermodynamically favorable structure is the one for which the Helmholtz free energy (*F*) is lowest. However, for constant pressure and temperature condition it is the minimum Gibbs free energy (*G*) which is used to determine the possible stable crystal structure. These free energies are defined as follows:

The Helmholtz free energy, which is function of thermodynamic variables *T* and *V* is:

$$F = E - TS \tag{1.7}$$

With *E*, *T* and *S* are total internal energy, temperature and entropy, respectively. Further, the total internal energy is expresses as $E(V,T) = E_c(V) + E_T(V,T) + E_e(V,T)$, with E_c, E_T and E_e are 0 K energy, Lattice thermal energy and electronic excitation energy, respectively.

Similarly, the Gibbs free energy which is function of thermodynamic variables T and P is:

$$G = F + PV \tag{1.8}$$

With *P* and *V* are the pressure and volume thermodynamic variables.

It may be noted that for $T = 0$, the Helmholtz free energy reduces to total internal energy at 0 K and the Gibbs free energy reduces to $H = E_c + PV$, where *H* is defined as enthalpy. The term E_c can be determined through electronic band structure methods, however, the lattice thermal energy, electronic excitation energy and the entropy contribution can be determined by using the physical quantities such as elastic moduli and density of electronic states obtained from *ab-initio* calculations in the continuum model like Debye model. In other approach one can also use quasi harmonic approximation to determine the vibrational free energy due to phonons by taking both acoustic as well as optic mode contribution from the phonon density of states.

The pressure from the total energy is determined as

$$P = -\frac{\partial E}{\partial V} \tag{1.9}$$

Thus the equation of state can be drawn by calculating the pressure at various compressions. The total energy calculations can be performed on specifically deformed lattice and by calculating the energy of the deformed lattice the elastic constants can be calculated.

The Hartree-Fock [156-158] method, density functional theory (DFT) [159,160] and quantum Monte Carlo [161] approaches are the three most popular *ab initio* methodologies used for calculations of electronic band structure and 0K total energy E_c. Apart from this there are a number of models and approximations *e.g.* nearly free electron model, tight binding model, muffin-tin approximation and k-p model, developed to calculate the electronic band structures of solids.

In the nearly free electron model, the interactions among electrons are completely ignored. The wave function is periodic in wave vector space which is given by:

$$\Psi_{\mathrm{n},\mathbf{k}}(\boldsymbol{r}) = e^{i\boldsymbol{k}.\boldsymbol{r}} u_n(\boldsymbol{r}) \tag{1.10}$$

Where, n is the n^th^ energy band, wavevector $\boldsymbol{k}$ is related to the direction of electron motion, $\boldsymbol{r}$ is the position in the crystal and the $u_n(\boldsymbol{r})$ is periodic over the lattice vector ***R:***

$$u_n(\boldsymbol{r}) = u_n(\boldsymbol{r} - \boldsymbol{R}) \tag{1.11}$$

Here the interaction between the ion cores and the conduction electrons are modelled as ‘weak’ perturbing potentials.

Other opposite extreme to this model is the tight binding model where the electrons stay most of the time to the constituent atoms. Here $\Psi(\boldsymbol{r})$ is approximated by a linear combination of atomic orbitals. $\psi_n(\boldsymbol{r})$

$$\Psi(\boldsymbol{r}) = \sum_{n,\boldsymbol{R}} \boldsymbol{b}_{n,\boldsymbol{R}}\, \psi_n(\boldsymbol{r} - \boldsymbol{R}) \tag{1.12}$$

Further improvement of the tight binding model is the well known Hubbard model, where the Hamiltonian of the interacting particles in the lattice consists of two terms: a kinetic energy term which describes the tunneling (hopping) of particles between sites of the lattice and a potential term for the on-site interaction. If interaction between particles of different sites of the lattice is considered, the model is referred as the extended Hubbard model.

Various electronic band structure methods such as Korringa-Kohn-Rostoker approximation (KKR), augmented plane wave (APW), linearized muffin-tin orbital (LMTO) and Green’s function methods use the muffin-tin approximation. The muffin-tin approximation basically is shape approximation of the potential around an electron in the solid. In the methods using this approximation, the lattice is divided in two parts. Around the atom the potential is approximated to be spherically symmetric and electron wavefunction spanned as a linear combination of spherical harmonics multiplied by a radial wavefunction. Outside this spherically symmetric potential, the potential is assumed to be flat *i.e.* constant or zero and linear combination of plane waves are used to span the wavefunction of the electron.

In the k.p perturbation theory (p=momentum operator) the term $\boldsymbol{k.p}$ is taken as perturbation in the Hamiltonian. The total Hamiltonian is represented as:

$$H_T = H_0 + H_K' \tag{1.13}$$

Where $H_0 = \frac{p^2}{2m} + V$ is the unperturbed Hamiltonian and

$H_K' = \frac{\hbar^2 k^2}{2m} + \frac{\hbar\, \boldsymbol{k.p}}{m}$ is the perturbation term.

The perturb energy to the unperturbed Hamiltonian (which is the exact Hamiltonian for the $\boldsymbol{k}$ = *0, i.e.,* at the Gamma point) is calculated.

The starting point of *ab-initio* electronic band structure methods is the Hartree –Fock theory [156-158]. This method is based on determining the exact wave function for any state of the many electron system and then finding the total energy at that state by solving the Schrödinger equation. Further, the ground state energy of the system is calculated by variationally minimizing the energy with respect to the wave function *i.e.* the ground state wave function is the one which minimizes the total energy. The accuracy here depends upon the exactness of the state wave function which is approximated to be the single determinant (Slater's determinant) wave function constructed out of individual electron wave function that takes into account the antisymmetry requirement. The antisymmetry requirement incorporated in the many electron wave function introduces an additional potential energy term known as exchange energy which is purely due to Pauli exclusion principle and is different from the conventional Coulomb repulsive term. The Hatree Fock method gives quite accurate results for small systems like atoms or molecules but fails when applied for solids *i.e.* systems containing a large number ~ 10^{23} of electrons. The reason for this could be associated to following facts: (i) The potential energy due to exchange effects is taken in full, however, in many electron systems the exchange interaction should be screened by the correlation hole (defined as the region around the electron of particular spin depleted of the other electron of the same spin). In other words the separation between electrons with parallel spins and that between the electrons with antiparallel spin is assumed to be same in Hatree –Fock method, however, in practical this is not so as due to Pauli principle the electrons with parallel spin cannot approach each other as closely as do electrons with antiparallel spin, therefore the exchange energy calculated using this method is more than the actual value. (ii) The binding between the correlation hole and electron has been ignored. Additionally, the assumption that many electron wave function can be expressed in terms of linear combination of the products of many single electron wave functions, which is not necessarily true; in fact an adequate wave function must involve ~ 10^{23} parameters *i.e.* as many parameters as the number of electrons in the solid. Because of these problems it is difficult to work with this method for large systems. This difficulty gave birth to the well known density functional theory.

As all the theoretical analysis on various materials presented in the subsequent chapters of the thesis have used the band structure calculation methods based on the well established density functional approach, a separate section has been provided to describe the density functional theory.

1.4 Density Functional Theory

In first-principles (*ab initio*) methods, an attempt is made at solving the Schrödinger equation without any empirical system specific parameters. Such simulations give, in principle, all relevant information on the atomic, electronic and magnetic structure of materials. However, they are computationally very demanding (~10^3 times more expensive than atomistic simulations) and cannot be done without approximations. As mentioned above, for solids there are three most popular *ab initio* methodologies Hartree-Fock method [156], density functional theory (DFT) [159-160] and quantum Monte Carlo [161] approach. It is also worth to mention that the hybrid density-functional approaches [162], which are mostly used in molecular chemistry related simulations, have become very popular in recent days. The methods based on density-functional approach are mostly employed in condensed matter research due to the computational efficiency and comparatively good accuracy offered by these.

Density functional theory is a quantum mechanical description of the electronic band structure of many body system particularly atoms, molecules and the condensed phase. The theory deals with the calculation of total energy of the many body system from the first principle by solving the Schrodinger equation without taking any approximation on the potential of the system under consideration. With this theory the properties of the system under consideration can be determined from the total ground state energy functional *i.e.* the energy is a function of density which itself is a function of position co-ordinate. As it is not dependent on any particular parameters, these calculations are more reliable than any model calculations where many parameters are used to optimize the potential of the system and then predict the properties of the system. In the present thesis, the problems addressed stem ultimately from the calculations involving how matter behaves under pressure. A brief outline of the basic principle of the theory is given below.

The central concept of DFT is to describe the total energy of many-body interacting system via its particle density and not via its many-body wavefunction. Its main aim is to reduce the 3N degrees of freedom of the N-body system to only three spatial coordinates through its particle density. Its basis is the well known Hohenberg-Kohn (HK) theorem [159], which claims that all ground state properties of a system can be considered to be unique functionals of its ground state density and the exact ground state will be found when the exact density is found. Together with the Born-Oppenheimer (BO) approximation [163] and Kohn-Sham (KS) ansatz [164], practically accurate DFT calculations have been made possible via approximations for the so called exchange-correlation (XC) potential, which describes the effects of the Pauli principle and the Coulomb potential beyond a pure electrostatic interaction of the electrons. Since it is impossible to calculate the exact XC potential (by solving the many-body problem exactly), two common approximations, the so-called local density approximation (LDA) and generalized gradient approximations (GGA), are implemented to get the XC energy contribution towards the total energy.

In many cases the results of DFT calculations for condensed-matter systems agreed quite satisfactorily with experimental data, especially with better approximations for the XC energy functional since the 1990s. Also, the computational costs were relatively low compared to traditional ways which were based on the complicated many-electron wavefunction, such as Hartree-Fock theory [156-158] and quantum Monte Carlo (QMC) [161].

1.4.1 Born-Oppenheimer (BO) Approximation

The significance of the BO approximation is to separate the movement of electrons and nuclei. Since the nuclei are much heavier than electrons (the mass of a proton is about 1836 times the mass of an electron), the nuclei move much slower (about two order of magnitude slower) than the electrons. For example, even for the lighter material say helium, its ion is ~ 10^4 times heavier than the electron. For the same momentum the speed of ion will be much less as compared to that of electron (~1/10000 of speed of electron).This assumption is appropriate as long as temperatures are not high enough Therefore we can separate the movement of nuclei and electrons. The underlying theory is given below which is the first step of DFT approximation.

The Hamiltonian of a many-body condensed-matter system consisting of nuclei and electrons can be written as:

$$H_{tot} = -\sum_{I} \frac{\hbar^2}{2M_I} \boldsymbol{\nabla}^2_{\boldsymbol{R}_I} - \sum_{i} \frac{\hbar^2}{2m_e} \boldsymbol{\nabla}^2_{\boldsymbol{r}_i} + \frac{1}{2} \sum_{\substack{I,J \\ I \neq j}} \frac{Z_I Z_J e^2}{|\boldsymbol{R}_I - \boldsymbol{R}_J|} + \frac{1}{2} \sum_{\substack{i,j \\ i \neq j}} \frac{e^2}{|\boldsymbol{r}_i - \boldsymbol{r}_j|} - \sum_{I,i} \frac{Z_I e^2}{|\boldsymbol{R}_I - \boldsymbol{r}_i|} \quad (1.14)$$

where the indexes *I*, *J* run on all nuclei of the system, i and j on all the electrons, $\boldsymbol{R}_I$ and M_I are positions and masses of the nuclei, $\boldsymbol{r}_i$ and m_e of the electrons, Z_I the atomic number of nucleus *I*. The first two terms are the kinetic energies of the nuclei and the electrons respectively, the third term is the potential energy of nucleus-nucleus Coulomb interaction, the fourth term is the potential energy of electron-electron Coulomb interaction and the last term is the potential energy of nucleus-electron Coulomb interaction. The time-independent Schrödinger equation for the system reads:

$$H_{tot} \Psi(\{\boldsymbol{R}_\mathrm{I}\}, \{\boldsymbol{r}_i\}) = E\, \Psi(\{\boldsymbol{R}_\mathrm{I}\}, \{\boldsymbol{r}_i\}) \quad (1.15)$$

where $\Psi(\{\boldsymbol{R}_\mathrm{I}\}, \{\boldsymbol{r}_i\})$is the total wave function of the system. In principle, everything about the system is known if one can solve the above Schrödinger equation. However, it is impossible to solve it in practice as it is a partial differential equation entangled with large number of variables. A so-called Born-Oppenheimer (BO) approximation made by Born and Oppenheimer [163] in 1927 comes here for rescue. When we consider the movement of electrons, it is reasonable to consider the positions of nuclei are fixed, thus the total wavefunction of the electrons and nuclei can be decoupled in the following way:

$$\Psi(\{\boldsymbol{R}_{\mathrm{I}}\},\{\boldsymbol{r}_i\}) = \Theta(\{\boldsymbol{R}_{\mathrm{I}}\})\phi(\{\boldsymbol{r}_i\};\{\boldsymbol{R}_{\mathrm{I}}\}) \tag{1.16}$$

where $\Theta(\{\boldsymbol{R}_I\})$ describes the nuclei and $\varphi(\{\boldsymbol{r}_i\}$; $\{\boldsymbol{R}_I\})$ the electrons (depending parametrically on the positions of the nuclei). With the BO approximation, Eqn. (1.15) can be divided into two separate Schrödinger equations:

$$H_e\,\phi(\{\boldsymbol{r}_i\};\{\boldsymbol{R}_{\mathrm{I}}\}) = V(\{\boldsymbol{R}_{\mathrm{I}}\})\,\phi(\{\boldsymbol{r}_i\};\{\boldsymbol{R}_{\mathrm{I}}\}) \tag{1.17}$$

Where

$$H_e = -\sum_i \frac{\hbar^2}{2m_e}\boldsymbol{\nabla}^2_{\boldsymbol{r}_i} + \frac{1}{2}\sum_{\substack{I,J\\ I\neq j}}\frac{Z_I Z_J e^2}{|\boldsymbol{R}_I-\boldsymbol{R}_J|} + \frac{1}{2}\sum_{\substack{i,j\\ i\neq j}}\frac{e^2}{|\boldsymbol{r}_i-\boldsymbol{r}_j|} - \sum_{I,i}\frac{Z_I e^2}{|\boldsymbol{R}_I-\boldsymbol{r}_i|} \tag{1.18}$$

and

$$\left[-\sum_I \frac{\hbar^2}{2M_I}\boldsymbol{\nabla}^2_{\boldsymbol{R}_I} + V(\{\boldsymbol{R}_{\mathrm{I}}\})\right]\Theta(\{\boldsymbol{R}_{\mathrm{I}}\}) = E'\Theta(\{\boldsymbol{R}_{\mathrm{I}}\}) \tag{1.19}$$

Eqn. (1.17) is the equation for the electronic problem with the nuclei positions fixed. The eigenvalue of the energy $V(\{\boldsymbol{R}_I\})$ depends parametrically on the positions of the nuclei. After solving Eq. (1.17), $V(\{\boldsymbol{R}_I\})$ is known and by applying it to Eqn. (1.19), which has no electronic degrees of freedom, the motion of the nuclei is obtained. Eqn. (1.19) is sometimes replace by a Newton equation, *i.e.*, to move the nuclei classically, equating $\boldsymbol{\nabla}$V with the forces.

Now we can consider that the electrons are moving in a static external potential $V_{ext}(\boldsymbol{r})$ formed by the nuclei, which is the starting point of DFT. The BO approximation was extended by Bohn and Huang known as Born-Huang (BH) approximation [165] to take into account more non-adiabatic effect in the electronic Hamiltonian than in the BO approximation.

1.4.2 Kohn-Sham Ansatz

It is the Kohn-Sham (KS) ansatz [164] that puts Hohenberg-Kohn theorems into practical use and makes DFT calculations possible with even a single personal computer. This is part of the reason that DFT became the most popular tool for electronic structure calculations. The KS ansatz was so successful that Kohn was honoured the Nobel Prize in chemistry in 1998.

The KS ansatz is to replace the original many-body system by an auxiliary independent-particle system and assume that the two systems have exactly the same ground state density. It maps the original interacting system with real potential onto a fictitious non-interacting system whereby the electrons move within an effective Kohn-Sham single-particle potential $V_{KS}(\boldsymbol{r})$.For the auxiliary independent-particle system, the auxiliary Hamiltonian is

$$\hat{\mathrm{H}}_{KS} = -\frac{1}{2}\boldsymbol{\nabla}^2 + V_{KS}(\boldsymbol{r}) \tag{1.20}$$

in atomic units.

For a system with N independent electrons, the ground state is obtained by solving the N one-electron Schrodinger equations,

$$\left(-\frac{1}{2}\boldsymbol{\nabla}^2 + V_{KS}(\boldsymbol{r})\right)\psi_i(\boldsymbol{r}) = \varepsilon_\mathrm{i}\,\psi_i(\boldsymbol{r}) \tag{1.21}$$

where there is one electron in each of the N orbitals $\psi_i(\boldsymbol{r})$ with the lowest eigenvalues ε_i. The density of the auxiliary system is constructed from:

$$n(\boldsymbol{r}) = \sum_{i=1}^{N} |\psi_i(\boldsymbol{r})|^2 \tag{1.22}$$

which is subject to the conservation condition:

$$\int n(\boldsymbol{r})\,d\boldsymbol{r} = N \tag{1.23}$$

The non-interacting independent-particle kinetic energy $T_S[n(\boldsymbol{r})]$ is given by,

$$T_S[n(\boldsymbol{r})] = -\frac{1}{2}\sum_{i=1}^{N}\int \psi_i^*(\boldsymbol{r})\,\boldsymbol{\nabla}^2\psi_i(\boldsymbol{r})\,d\boldsymbol{r} \tag{1.24}$$

Now a new quantity, the universal functional *F[n(**r**)]* ,can be rewritten as

$$F[n(\boldsymbol{r})] = T_S[n(\boldsymbol{r})] + E_H[n(\boldsymbol{r})] + E_{XC}[n(\boldsymbol{r})] \tag{1.25}$$

where $E_H[n(\boldsymbol{r})]$ is the classic electrostatic (Hartree) energy of the electrons,

$$E_H[n(\boldsymbol{r})] = \frac{1}{2}\iint \frac{n(r)n(\boldsymbol{r}')}{|\boldsymbol{r}-\boldsymbol{r}'|}\,d\boldsymbol{r}\,d\boldsymbol{r}' \tag{1.26}$$

and $E_{XC}[n(\boldsymbol{r})]$ is the exchange correlation energy, which contains the difference between the exact and non-interacting kinetic energies and also the non-classical contribution to the electron-electron interactions, of which the exchange energy is a part. Since the ground state energy of a many-electron system can be obtained by minimizing the energy functional $E[n(\boldsymbol{r})] = F[n(\boldsymbol{r})] + \int n(\boldsymbol{r})V_{ext}(\boldsymbol{r})d\boldsymbol{r}$, subject to the constraint that the number of electrons N is conserved,

$$\delta\{F[n(\boldsymbol{r})] + \int n(\boldsymbol{r})V_{ext}(\boldsymbol{r})d\boldsymbol{r} - \mu(\int n(\boldsymbol{r})\,d\boldsymbol{r} - N)\} = 0 \tag{1.27}$$

and the resulting equation is

$$\mu = \frac{\delta F[n(\boldsymbol{r})]}{\delta n(\boldsymbol{r})} + V_{ext}(\boldsymbol{r}) \tag{1.28}$$

$$= \frac{\delta T_S n(\boldsymbol{r})}{\delta n(\boldsymbol{r})} + V_{KS}(\boldsymbol{r})$$

where μ is the chemical potential,

$$V_{KS}(\boldsymbol{r}) = V_{ext}(\boldsymbol{r}) + V_H(\boldsymbol{r}) + V_{XC}(\boldsymbol{r}) \tag{1.29}$$

$$= V_{ext}(\boldsymbol{r}) + \frac{\delta E_H[n(\boldsymbol{r})]}{\delta n(\boldsymbol{r})} + \frac{\delta E_{XC}[n(\boldsymbol{r})]}{\delta n(\boldsymbol{r})}$$

is the KS one-particle potential with the Hartree potential $V_H(\boldsymbol{r})$

$$V_H(\boldsymbol{r}) = \frac{\delta E_H[n(\boldsymbol{r})]}{\delta n(\boldsymbol{r})} \tag{1.30}$$

$$= \int \frac{n(\boldsymbol{r}')}{|\boldsymbol{r} - \boldsymbol{r}'|}\, d\boldsymbol{r}'$$

and the XC potential $V_{XC}(\boldsymbol{r})$

$$V_{XC}(\boldsymbol{r}) = \frac{\delta E_{XC}[n(\boldsymbol{r})]}{\delta n(\boldsymbol{r})} \tag{1.31}$$

Eqns. (1.21), (1.22), (1.29) together are the well-known KS equations, which must be solved self-consistently because $V_{KS}(\boldsymbol{r})$ depends on the density through the XC potential. In order to calculate the density, the N equations in Eqn. (1.21) have to be solved in KS theory as opposed to one equation in the TF approach. However an advantage of the KS method is that as the complexity of a system increases, due to N increasing, the problem becomes no more difficult, only the number of single-particle equations to be solved increases. Although exact in principle, the KS theory is approximate in practice because of the unknown XC energy functional $E_{XC}[n(\boldsymbol{r})]$. An implicit definition of $E_{XC}[n(\boldsymbol{r})]$ can be given as:

$$E_{XC}[n(\boldsymbol{r})] = T[n(\boldsymbol{r})] - T_S[n(\boldsymbol{r})] + E_{int}[n(\boldsymbol{r})] - E_H[n(\boldsymbol{r})] \tag{1.32}$$

where $T[n(\boldsymbol{r})]$ and $E_{int}[n(\boldsymbol{r})]$ are the exact kinetic and electron-electron interaction energies of the interacting system respectively. It is crucial to have an accurate XC energy functional $E_{XC}[n(\boldsymbol{r})]$ or potential $V_{XC}(\boldsymbol{r})$ in order to give a satisfactory description of a realistic condensed-matter system. The most widely used approximations for the XC potential are the local density approximation (LDA) and the generalized-gradient approximation (GGA).

1.4.3 Local Density Approximation (LDA)

The Local Density Approximation (LDA) was firstly proposed by Kohn and Sham, and used in the early works. Although the exact XC energy functional $E_{XC}[n(\boldsymbol{r})]$ should be very complicated, but simple approximations to it have been successful not only to predict various properties of many systems reasonably well but also greatly reduce computational costs, leading to the wide use of DFT for electronic structure calculations. Of these approximations, the local density approximation (LDA) is the most widely used one. In LDA, the XC energy per electron at a point $\boldsymbol{r}$ is considered the same as that for a homogeneous electron gas (HEG) that has the same electron density at the point $\boldsymbol{r}$. The total exchange-correlation functional $E_{XC}[n(\boldsymbol{r})]$ can be written as,

$$E_{XC}^{LDA}[n(\boldsymbol{r})] = \int n(\boldsymbol{r})\epsilon_{XC}^{hom}(n(\boldsymbol{r}))d\boldsymbol{r} \tag{1.33}$$

$$= \int n(\boldsymbol{r})[\epsilon_{X}^{hom}(n(\boldsymbol{r})) + \epsilon_{C}^{hom}(n(\boldsymbol{r}))]d\boldsymbol{r}$$

$$= E_{X}^{LDA}[n(\boldsymbol{r})] + E_{C}^{LDA}[n(\boldsymbol{r})]$$

for spin unpolarized systems and

$$E_{XC}^{LDA}[n_\uparrow(\boldsymbol{r}), n_\downarrow(\boldsymbol{r})] = \int n(\boldsymbol{r})\epsilon_{XC}^{hom}(n_\uparrow(\boldsymbol{r}), n_\downarrow(\boldsymbol{r}))d\boldsymbol{r} \tag{1.34}$$

for spin polarized systems[14], where the XC energy density $\epsilon_{XC}^{hom}(n(\boldsymbol{r}))$ is a function of the density alone, and is decomposed into exchange energy density $\epsilon_{X}^{hom}(n(\boldsymbol{r}))$ and correlation energy density $\epsilon_{C}^{hom}(n(\boldsymbol{r}))$ so that the XC energy functional is decomposed into exchange energy functional $E_{X}^{LDA}[n(\boldsymbol{r})]$ and correlation energy functional $E_{C}^{LDA}[n(\boldsymbol{r})]$ linearly.

The LDA is very simple, where corrections to the exchange-correlation energy due to the in homogeneities in the electronic density are ignored. The LDA approximations it tends to underestimate atomic ground state energies and ionization energies, while overestimating binding energies. It makes large errors in predicting the energy gaps of some semiconductors. Different approximations like generalized gradient approximations (GGA) has been proposed for $E_{XC}[n(\boldsymbol{r})]$ like Perdew and Zunger [166] Its success and limitations lead to approximations of the XC energy functional beyond the LDA, through the addition of gradient corrections to incorporate longer range gradient effects. The LDA has also been extended to LDA+U method to account for the strong correlations of the *d* electrons in transition elements and *f* electrons in lanthanides and actinides.

1.4.4 Generalized Gradient Approximation

The LDA is restricted to be applied to systems with slowly varying density. As mentioned above, the LDA neglects the in-homogeneities of the real charge density which could be very different from the HEG. The XC energy of inhomogeneous charge density can be significantly different from the HEG result. This leads to the development of various generalized-gradient approximations (GGA) which include density gradient corrections and higher spatial derivatives of the electron density and may give better results than LDA in many cases.

The definition of the XC energy functional of GGA is the generalized form of Eqn. (1.42) of LDA to include corrections from density gradient $\nabla n(\boldsymbol{r})$ as

$$E_{XC}^{GGA}[n_\uparrow(\boldsymbol{r}), n_\downarrow(\boldsymbol{r})] = \int n(\boldsymbol{r}) \epsilon_{XC}^{hom}(n_\uparrow(\boldsymbol{r}), n_\downarrow(\boldsymbol{r}), \nabla n_\uparrow(\boldsymbol{r}), \nabla n_\downarrow(\boldsymbol{r})) d\boldsymbol{r} \qquad (1.35)$$

GGA improves the shortcomings of LDA's poor description of strong inhomogeneous system. Many different reformulations and extensions of GGA have been proposed and tested over the years. Traditionally, physicists favor a non-empirical approach, deriving approximations from quantum mechanics and avoiding fitting to specific finite systems. One of the physics type of GGA functionals is the Perdew-Burke-Ernzerhof (PBE) [167], which is widely used in material sciences. On the other hand, chemists typically use a few or several dozen parameters to improve the accuracy on a limited class of molecules, like LYP [168] and its revised version BLYP functional [169], which has smaller errors for main-group organic molecule energetic than PBE, but does badly for the correlation energy of metals. GGA generally works better than LDA, in predicting bond length and binding energy of molecules, crystal lattice constants, and so on, especially in systems where the charge density is rapidly varying. However GGA sometimes overcorrects LDA results in ionic crystals where the lattice constants from LDA calculations fit well with experimental data but GGA will overestimate it. Nevertheless, both LDA and GGA perform badly in materials where the electrons tend to be localized and strongly correlated such as transition metal oxides and rare-earth elements and compounds. This drawback leads to approximations beyond LDA and GGA.

1.4.5 Semi-local functional

Universal GGAs such as PBE work for a wide range of systems, but they are still limited in accuracy. One approach is to devise GGAs that are specialized for certain classes of compounds. PBEsol [170] GGA is an example: it recovers the original gradient expansion for exchange, and its correlation piece is adjusted to reproduce surface energies accurately. Due to its diminished gradient dependence, PBEsol is biased towards solids and yields better lattice constants and other equilibrium properties of densely packed solids than PBE. However, it is generally less accurate for molecular bond energies.

1.4.6 Orbital-dependent functional

Another major problem of standard LDAs and GGAs is that they could not describe the system when the electrons tend to be localised and strongly interacting, such as transition metal oxides, rare earth elements and compounds. In order to properly describe these strongly correlated systems, orbital-dependent potentials should be used for *d* and *f* electrons. There are several approaches available nowadays to incorporate the strong electron-electron correlations between *d* electrons and *f* electrons. Of these methods including the self-interaction correction (SIC) method [171], Hartree-Fock (HF) method [172], and GW approximation [173], LDA+U method [174] is the most widely used one.

In the LDA+U method, the electrons are divided into two classes: delocalized *s*, *p* electrons which are well described by LDA (GGA) and localized *d* or *f* electrons for which an orbital-dependent term $\frac{1}{2}\, U \sum_{i \neq j} n_i\, n_j$ should be used to describe Coulomb $d - d$ or $f - f$ interaction, where n_i are *d*- or *f*- orbital occupancies. The total energy in LDA+U method is given as[164]:

$$E_{tot}^{LDA+U}[\rho_\sigma(\boldsymbol{r}), \{n_\sigma\}] = E^{LSDA}[\rho_\sigma(\boldsymbol{r})] + E^U[\{n_\sigma\}] - E_{dc}[\{n_\sigma\}] \tag{1.36}$$

$$E_{tot}^{LDA+U}[\rho_\sigma(\boldsymbol{r}),\{n_\sigma\}] = E^{LSDA}[\rho_\sigma(\boldsymbol{r})] + \frac{1}{2}U\sum_{i\neq j} n_i n_j + UN(N-1)/2 \quad (1.37)$$

And

$$N=\sum_i n_i \quad (1.38)$$

where σ denotes the spin index, $\rho_\sigma(\boldsymbol{r})$ is the electron density for spin- σ electrons and $\{n_\sigma\}$ is the density matrix of *d* or *f* electrons for spin-σ, the first term is the standard LDA energy functional, the second term is the electron-electron Coulomb interaction energy [171]. The last term in Eqn. (1.37) is the double counting term such that which removes an averaged LDA energy contribution of these *d* or *f* electrons from the LDA energy.

1.4.7 Dispersion corrections

DFT is widely known to poorly describe long-range dispersion effects. Due to their dependence on the local density, the semi-local functionals cannot account for XC effects due to the presence of electrons in remote parts of a molecule. There are many attempts to correct this by adding a Van Der Waals (vdW) attraction between the nuclei to the nuclear potential energy ($E_{\text{dispersion}}$)

$$E_{DFT-D} = E_{KS} + E_{dispersion} \quad (1.39)$$

and $E_{\text{dispersion}}$ can be derived from a empirical force field in DFT-D2 and DFT-D23 methods of Grimme [175], DFT with dispersion functional usually gives accurate results for a restricted class of compounds. But the accuracy strongly depends on the quality of the force fields, thus it cannot be transferable. A fully non-local non-empirical dispersion correction to GGAs was proposed as so called vdW-DF functional [176]. However, its original formulation requires large computational cost. It was recently improved by using the algorithm of Roman-Perez and Soler which transforms the double real space integral to reciprocal space and therefore could largely reduce the computational effort [177, 178].

1.4.8 Basis set

To solve the KS equation without any information from the experiments, a set of functions is required to create the wavefuction, which is called basis set. There are three types of basis sets, plane wave, atomic orbital and atomic spheres which are generally used.

1.4.8.1 Plane Waves

In this method, the wavefunctions (eigenfunctions of the KS equations) are expanded in a complete set of plane waves $e^{ik.r}$ and the external potential of nuclei are replaced by pseudopotentials which include effects from core electrons. Such pseudopotentials have to satisfy certain conditions. Most widely used pseudopotentials nowadays include norm-conserving pseudopotentials [179] (NCPPs) and ultrasoft pseudopotentials [180] (USPPs).

Plane waves have played an important role in the early orthogonalized plane wave (OPW) calculations [181-183] and are generalized to modern projector augmented wave (PAW) method [184-186]. Because of the simplicity of plane waves and pseudopotentials, computational load is significantly reduced in these methods and therefore it is most suitable for calculations of large systems. However, results from plane wave methods using pseudopotentials are usually less accurate than results from all-electron full potential methods. And great care should be taken when one generates pseudopotential and it should be tested to match results from all-electron calculations. The most widely used codes using plane waves and pseudopotentials are plane wave self-consistent field (now known as Quantum ESPRESSO) [187] (PWscf), ABINIT [188], VASP [189] (which uses PAW method too).

Plane wave basis set is the most natural solution for periodic crystals where they provide good understanding and simple algorithms for practical calculations. Its main disadvantage is that a huge number of plane waves might be required to describe the dramatic change of the wavefunction (for instance, the wavefunction from the deep core electrons to valence electrons). There are several ways to overcome this problem - the LAPW method, Projector Augmented Wave method, pseudopotential method. Plane wave is perfect fit for periodic boundary conditions. Molecules and surfaces can be treated in an approximate model by inserting vacuum layers. However, a very large number of plane waves will be spent. Therefore, a more economical way is to consider another type of basis set based on localized orbitals.

1.4.8.2 Localized Atomic(-like) Orbitals

The most well-known methods in this category are linear combination of atomic orbitals (LCAO) [190], also called tight-binding (TB) [190] and full potential non-orthogonal local orbital (FPLO) [191]. The basic idea of these methods is to use atomic orbitals as the basis set to expand the one-electron wavefunction in KS equations. LCAO defines atom centred orbitals as a product of the angular (Y_{lm}) and radial (R(r)) parts:

$$\psi_i(r) = Y_{lm} R(r) \tag{1.40}$$

where the radial part is a linear combination of Slater-type functions or Gaussian-type functions. Slater oribtals are more accurate but requires much more computational cost. Gaussian functions are usually preferred.

1.4.8.3 Atomic Sphere Methods

Methods in the class can be considered as a combination of plane wave method and localized atomic orbitals. It uses localized atomic orbital presentation near the nuclei and plane waves in the interstitial region. The most widely used methods are (full potential) linear muffin-tin orbital[192] (LMTO) as implemented in LMTART[193] by Savrasov and (full potential) linear augment plane wave[193, 194] (LAPW) as implemented in WIEN2K[195].

1.4.9 Pseudopotentials

A very important idea for efficient implementation of DFT is the pseudopotential. In practice, electrons are usually separated into core and valence electrons. The core electrons are usually chemically inert, and do not contribute to bonding. There is no need to treat them explicitly. Therefore, pseudopotential can be constructed to freeze the core electrons while only consider the chemically active valence electrons. A good pseudopotential should satisfy the following rules:

1) The pseudo wave functions (Ψ^{PP}(r)) should be identical to the all-electron wavefunctions (Ψ^{AE} (r)) outside the cut-off radius (r_c), as shown in Fig.1.4.

$$\Psi^{AE}(r) = \Psi^{PP}(r)\,,\ \ r > r_c \qquad (1.41)$$

2) The eigenvalues should be conserved.

$$\varepsilon_i^{AE} = \varepsilon_i^{PP} \qquad (1.42)$$

3) The total charge of each pseudo wave function should be equal the charge of the all-electron wave function.

$$\int_0^{r_c} |\Psi^{AE}(r)|^2 dr = \int_0^{r_c} |\Psi^{PP}(r)|^2 dr \qquad (1.43)$$

4) The scattering properties of the pseudopotential should be conserved.

$$\frac{d}{dr}\ln\{\Psi^{AE}(r)\}_{r=r_{logD}} = \frac{d}{dr}\ln\{\Psi^{PP}(r)\}_{r=r_{logD}} \qquad (1.44)$$

According norm-conserving condition, the pseudopotential $V_i(r)$ can be split into a local part, long-ranged and behaving like $-Ze^2/r$ for $r \to \infty$, and a short-ranged semi local term:

$$V^{PP} = V_{loc} + V_{SL}$$

where $V_{loc}(r)$ is a radial function, and V_{SL} (r) the semi-local part is the deviation from the all-electron potential inside the core region, The pseudopotential reproduces the true potential outside the core region, but is much smoother inside the core. The oscillations of the electron wave function inside the core region are eliminated by the pseudopotential. This is a great advantage for numerical calculations. A further approximation, the ultrasoft pseudo-potential [180], uses more than one projector for each momentum, and further smoothes the electron wave function. The projector augmented wave (PAW) method [196] is a general approach for solution of the electronic structure. The PAW approach introduces projectors and auxiliary localized functions, like ultrasoft type method. However, it also keeps the full all-electron wavefunction in a form similar to the general OPW expression.

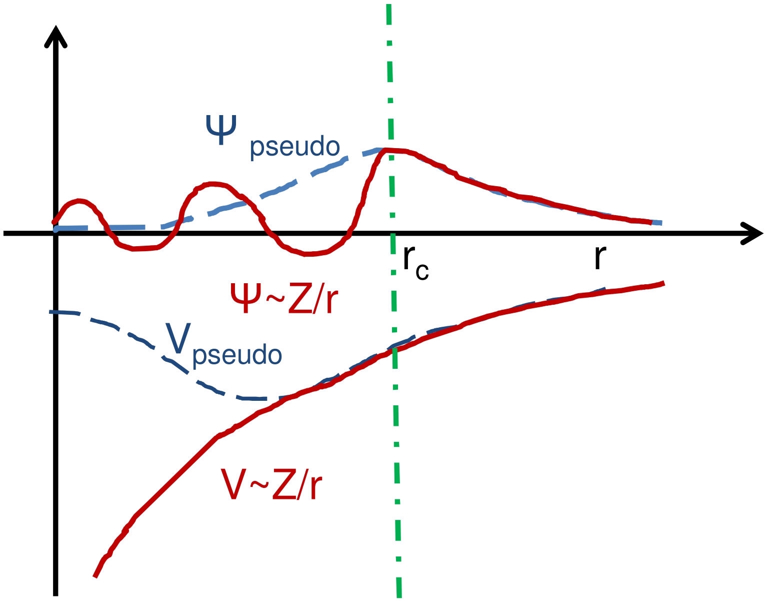

Fig. 1.4 Comparison of a wave function in the Coulomb potential of the nucleus (red) to the one in the pseudopotential

1.5 Lattice Dynamics and Phonons

Specific heat, thermal conductivity, thermal expansion, sound velocity etc. are related to the vibrations of atoms in solids, So the study of lattice vibrations plays an important role in condensed matter physics [197,198].Vibrational frequencies are routinely and accurately measured mainly using infrared and Raman spectroscopy, as well as inelastic neutron scattering. The lattice vibration spectra basically relate the energy of the thermal motions of the atoms to the corresponding wavelength. The collective motions of atoms in solids forming travelling waves are quantized in terms of ‘‘phonons” and these are determined from the knowledge of the interatomic interactions. The resulting vibrational spectra are a sensitive probe of the local bonding and chemical structure. Further, very low-frequency modes can be associated with the phase transformations, and imaginary frequencies provide an indication of the dynamical instability of the structure. So lattice dynamics (phonons) play a dominant role in deciding the structural stability of the materials. Accurate calculations of frequencies and displacement patterns can thus yield a very good of information on the atomic and electronic structure of materials. Forces in DFT can thus be calculated from the knowledge of the electron charge-density. In general, the Inter atomic force constants can be calculated as finite differences of Hellmann–Feynman forces for small finite displacements of atoms around the equilibrium positions. For finite systems (molecules, clusters) this technique is straightforward, but it may also be used in other technique in solid state physics (*frozen phonon*) [199]. An alternative technique is the direct calculation of inter atomic force constants (IFC) using density-functional perturbation theory (DFPT) [200]. Practically, one can build one super cell to give phonons at all wave vectors. The results are limited to small super cells. For instance, one only needs a primitive cell to calculate the gamma-point. If we want the entire dispersions for all vectors in BZ, a more accurate model should be proposed, for instance density functional perturbation theory. So in the next section we have given the theoretical overview of DFPT.

1.5.1 Density Functional perturbation Theory (DFPT)

Born-Oppenheimer adiabatic approximation allows one to decouple the vibrational from electronic degrees of freedom. lattice dynamical properties of a system are determined by the eigen value ϵ eigen function Θ of the schordinger equation :

$$\left[-\sum_I \frac{\hbar^2}{2M_I} \boldsymbol{\nabla}^2_{\boldsymbol{R_I}} + E(R)\right] \Theta(R) = \epsilon\, \Theta(R) \qquad (1.45)$$

Where $\boldsymbol{R_I}$ is the coordinate of the I_{th} nucleus, $\boldsymbol{M_I}$ its mass, $\boldsymbol{R} = \{\boldsymbol{R_I}\}$ the set of all the nuclear coordinates, and $E(R)$ is the ion electron energy of the system , in general $E(R)$ is the ground state energy of a system of interacting electrons moving in the field of fixed nuclei, whose Hamiltonian – which acts onto the electronic variables and depends parametrically upon $\boldsymbol{R}$-reads

$$H_{BO}(\boldsymbol{R}) = -\sum_I \frac{\hbar^2}{2m_i} \boldsymbol{\nabla}^2_{\boldsymbol{r_i}} + \frac{1}{2} \sum_{\substack{i,j \\ i \neq j}} \frac{e^2}{|\boldsymbol{r_i} - \boldsymbol{r_j}|} - \sum_{I,i} \frac{Z_I e^2}{|\boldsymbol{R_I} - \boldsymbol{r_i}|} + E_N(R) \qquad (1.46)$$

Where Z_I is the charge of the I_{th} nucleus, e is the electron charge, and $E_N(R)$ is the electrostatic interactions between different nuclei:

$$E_N = \frac{1}{2} \sum_{\substack{I,J \\ I \neq j}} \frac{Z_I Z_J e^2}{|\boldsymbol{R_I} - \boldsymbol{R_J}|} \qquad (1.47)$$

The equilibrium geometry of the system is given by the condition that the forces acting on individual nuclei vanish:

$$F_I = -\frac{\partial E(\boldsymbol{R})}{\partial \boldsymbol{R_I}} = 0 \tag{1.48}$$

Whereas the vibrational frequencies ω are determined by the eigenvalues of the Hessian of the Born Oppenheimer energy {E(**R**)}, scaled by the nuclear masses.

1

$$det\left|\frac{1}{\sqrt{M_I M_J}}\frac{\partial^2 E(R)}{\partial R_I \partial R_J} - \omega^2\right| = 0 \tag{1.49}$$

The calculation of the equilibrium geometry and of the vibrational properties of a system thus requires to compute the first and second derivatives of its Born Oppenheimer energy surface.

In the Born Oppenheimer approximation, nuclear coordinates act as parameters in the electronic Hamiltonian by eq 1.46 .The force acting on the I^{th} nucleus in the electronic ground state is thus

$$F_I = -\frac{\partial E(\boldsymbol{R})}{\partial \boldsymbol{R_I}} = -\left\langle \psi(\boldsymbol{R}) \left| \frac{\partial H_{\boldsymbol{BO}}}{\partial \boldsymbol{R_I}} \right| \psi(\boldsymbol{R}) \right\rangle \tag{1.50}$$

Where $\psi(\boldsymbol{R})$ is the electronic ground state wave function of the Born Oppenheimer Hamiltonian. This Hamiltonian depends on **R** via the electron-ion interaction that is associated with the electronic degrees of freedom by the electron charge density. The Hellmann-Feynman theorem states in this case that

$$F_I = \int n_R(r)\frac{\partial V_R(r)}{\partial \boldsymbol{R_I}}dr - \frac{\partial E_N(\boldsymbol{R})}{\partial \boldsymbol{R_I}} \tag{1.51}$$

$$V_R(r) = -\sum_{I,i}\frac{Z_I e^2}{|\boldsymbol{R_I} - \boldsymbol{r_i}|} \tag{1.52}$$

Where $V_R(r)$ is the electron-nucleus interaction, and $n_R(r)$ is the ground state electron charge density to the nuclear configuration **R**. The Hessian of the Born Oppenheimer energy surface appearing in eq 1.49 is obtained by differentiating the Hellmann-Feynman forces with respect to nuclear coordinates ,

$$\frac{\partial^2 E(R)}{\partial R_I \partial R_J} = -\frac{\partial F_I}{\partial \boldsymbol{R_J}} = \int \frac{\partial V_R(r)\partial n_R(r)}{\partial \boldsymbol{R_I}\partial \boldsymbol{R_J}}dr + \int n_R(r)\frac{\partial^2 V_R(r)}{\partial \boldsymbol{R_I}\partial \boldsymbol{R_J}}dr \tag{1.53}$$

This equation states that the calculation of Hessian of the Born Oppenheimer energy surface requires the calculation of the ground state electron charge density $n_R(r)$ as well as of its linear response to the distortion of the nuclear geometry ,. $\frac{\partial n_R(r)}{\partial \boldsymbol{R_I}}$

Where $V_R(r)$ is the electron-nucleus interaction, and $n_R(r)$ is the ground state electron charge density to the nuclear configuration **R**. The Hessian of the Born Oppenheimer energy surface appearing in eq 1.49 is obtained by differentiating the Hellmann-Feynman forces with respect to nuclear coordinates. The Hessian matrix is usually termed as interatomic force constants.

1.5.2 Quasi-Harmonic Approximations

The *ab-initio* electronic structure calculations can be carried out using two approaches one in which the ions are assumed to be fixed rigidly at their location (adiabatic approximation) other in which the corrections due to atomic vibrations are also taken into account. The calculations limited to the rigid periodic arrangement of atoms (ions) in the solid are termed as static lattice calculations. Under this approximation the interaction energy between the ions depends on their separation or equivalently on atomic position. The interactions are categorised as (i) long-range Coulomb interactions and (ii) short-range interactions. However, in lattice dynamic calculations, using quasi harmonic approximation (QHA), one proceeds a step further by calculating the phonon spectra from the knowledge of forces and structures obtained from static lattice model calculations. From the classical statistical mechanics, it is known that the heat capacity of a system of harmonic oscillators does not depend on temperature or on its spectrum. Debye theory of heat capacity of solids is one of the landmarks of modern solid-state physics. This model naturally explains the low temperature specific heat of solids in terms of the statistical mechanics of an ensemble of harmonic oscillators, which can in turn be pictorially described as a gas of non interacting quasi-particles obeying the Bose-Einstein statistics. In the Born-Oppenheimer approximation, the vibrational properties of solids are determined by their electronic structure through the dependence of the ground-state energy on the positional coordinates of the atomic nuclei. At low temperature the amplitudes of atomic vibrations are much smaller than interatomic distances, and one can assume that the dependence of the ground-state energy on the deviation from equilibrium of the atomic positions is quadratic. In this, so called harmonic, approximation (HA) energy differences can be calculated from electronic-structure theory. In the HA, vibrational frequencies do not depend on interatomic distances, so that the vibrational contribution to the crystal internal energy does not depend on volume. As a consequence, constant pressure (C_P) and constant-volume specific heats (Cv) coincide in this approximation, and the equilibrium volume of a crystal does not depend on temperature. Prediction of an infinite thermal conductivity, infinite phonon lifetimes, and the independence of vibrational spectra on temperature, are the other shortcomings of the HA. A proper account of anharmonic effects on the static and dynamical properties of materials would require the calculation of phonon-phonon interaction coefficients for all modes in the BZ. The simplest generalization of the HA, which corrects for most of the above mentioned deficiencies, while not requiring any explicit calculation of anharmonic interaction coefficients, is the QHA. As a practical application the constant-volume specific heat, the entropy, the phonon contributions to internal energy and Helmholtz free energy, and the atomic temperature factors of any crystal can be calculated as a function of temperature from ab initio phonon band structures.

For a lattice, the Helmholtz free energy F in the QHA is,

$$F(T,V) = U(V) - TS(T,V) \tag{1.54}$$

where U is the internal lattice energy, T is the absolute temperature, V is the volume and S is the entropy due to the vibrational degrees of freedom. This entropy term is from lattice vibration.

$$F(V,T) = \sum_{q,j} \frac{1}{2} \hbar \omega_j(q,V) + k_B T \sum_{q,j} \ln \left[1 - \exp\left(\frac{-\hbar \omega_j(q,V)}{k_B T} \right) \right] \tag{1.55}$$

Where $\omega_j(q,V)$ is the frequency of j_{th} phonon band at the point q in the Brillouin zone

The Gibbs free energy of the system is a function of temperature and pressure.

$$G(T,P) = min[F(T,V) + PV]$$

Since volume dependencies of energies in electronic and phonon structures are different, volume giving the minimum value of the energy function in the square brackets shifts from the value calculated only from electronic structure at 0 K. The increase in temperature can change the volume dependence of phonon free energy, and then the equilibrium volume. This is considered as thermal expansion under QHA. The volume thermal expansion coefficient α(T) from $V(T)$ is then obtained using expression:

$$\alpha(T) = \frac{1}{V_0}\left(\frac{\partial V(T)}{\partial T}\right) \qquad (1.56)$$

V_0 is the equilibrium volume at 0 K. Further, the zero pressure bulk modulus at a given temperature is obtained by finding the [$V(\partial^2F/\partial V^2)$] at that temperature. Repeating this process for several temperatures yielded the zero pressure bulk modulus $B_0(T)$ as a function of temperature

1.6 Computational codes used

In this thesis different codes such as Quantum Espresso [187], VASP [189,201] and WIEN2K [195,202] have been used in the present study. Qunatum Espresso and VASP are plane wave codes while WIEN2K which could support all-electron calculation. Both Quantum Espresso and VASP use pseudopotentials for calculation. Quantum Espresso is available under the GNU General Public License (GPL), often referred to as a "Copyleft". Under this licensing scheme [203], the user receives four freedoms: (i) unlimited use of the package for any purpose; (ii) the freedom to study the sources and modify them to match his/her needs; (iii) the freedom to copy the package and (iv) freedom to distribute modified versions. The license also protects these four freedoms by requiring that they must come with any transmitted copy of the program. These intentionally constructed to let everybody benefit from and contribute to the project. Most of the calculations reported in this thesis have been performed using Quantum Espresso code whose main features are given below:

(i) Quantum Espresso is based on a plane-wave expansion of the electronic wavefunctions, with a periodic representation of the system in a box (primitive unit cell) under periodic boundary conditions.

(ii) It uses the standard Kohn-Sham self-consistent density functional method in the local density (LDA) or generalized gradient (GGA) approximations.

(iii) It uses both norm-conserving and Ultra-soft pseudopotentials.

(iv) It calculates the dynamical matrices at any point in the Brillouin zone, by Fourier interpolation of the dynamical matrices provided in the data-base, and thus the corresponding eigenvectors and eigenvalues, the latter forming the phonon band structure.

(v) It produce thermodynamical properties (such as free energy, heat capacity and entropy), in the quasi-harmonic approximation, obtained by the integration of the phonon degrees of freedom over the Brillouin zone.

(vi) It computes the forces and stresses, using Hellmann Feynman theorem or the stress theorem within DFT in all the cases in which the total energy can be computed, except in the spin-orbit case.

In some of the calculations within this thesis, structure relaxations are performed using DFT within PBE functional in the framework of PAW method as implemented in the VASP code. And the conjugate-gradient algorithm are mostly used (IBRION = 2) during structure relaxation stage.

1.7 Crystal structure prediction and evolutionary algorithm

In some cases where it is not possible to solve crystal structure from experimental data, theoretical structure prediction becomes crucially important. For example, when experimental data are of poor quality for structure refinement (defective or small samples, especially at high pressures and temperatures) theory provides the last hope to this. Apart from this theory is the only way of investigating matter at extreme conditions which are inaccessible with today's experimental techniques. Under equilibrium conditions, most materials form crystalline states, which can possess long range order and symmetry. Understanding the structure of materials is fundamental to being able to understand their physical properties. However, the prediction of crystal structure used to be a long-term challenge in physical and chemical science. Back in 1988, Maddox summarized this problem as it is general impossible to predict the structure of even the simplest crystalline solids from knowledge of their chemical composition [204]. After some years, programs started developed that attempted to do just this and, in 1994, Gavezzotti [205] addressed the fundamental questions about the predictive capability of crystal structure. The answer was again safely concluded as "No". This happens because, for each chemical composition, there are an infinite number of possible atomic arrangements that can, in principle, exist, which correspond to all possible local minima of the free energy surface. Crystal structure prediction requires us to find the global minimum on the free-energy landscape for system of a given compositions. Each point on this free energy landscape represents a crystal structure with certain atomic positions and lattice vectors. Evolutionary algorithms is one step to this to find stable and metastable structures.The name of the approach - evolutionary - indicates that it uses mechanisms similar to biological evolution: reproduction, mutation, recombination, and selection. One of the features of evolutionary algorithms, which is very helpful for the crystal structure prediction problem, is their capability to find metastable states – good local minima on the energy landscape that are easily separated from the global minimum. Naturally, the free energy would be the relevant fitness function for a crystal structure prediction algorithm.

The basic steps of the evolutionary technique (see Figure 1.5) are as follows: The evolutionary approach starts by choosing the adequate representation for the problem: a one-to-one correspondence between the point in the search space and a set of numbers. Initialization of the first generation, that is, a set of points in the search space that satisfy the problem constrains.

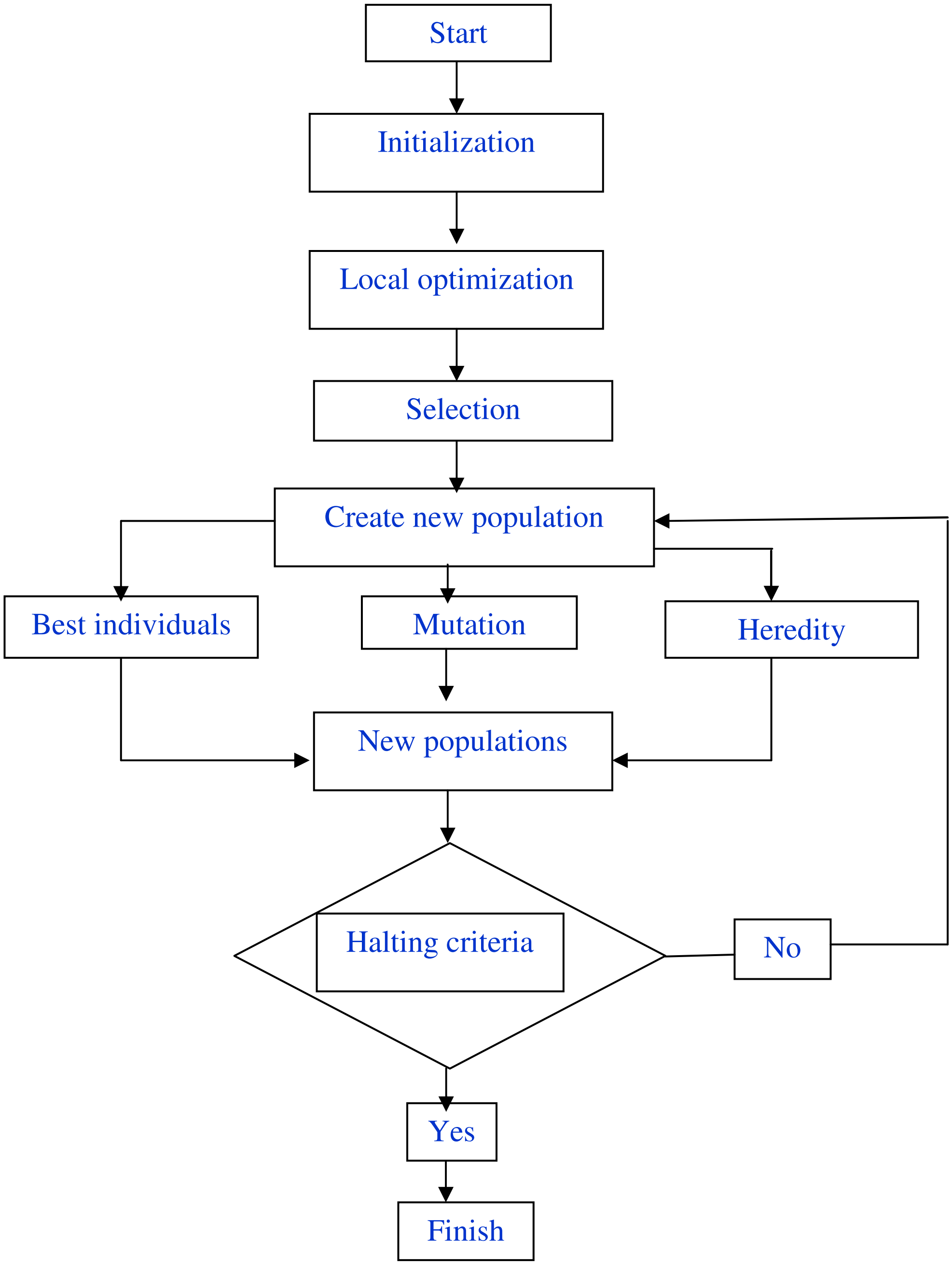

Fig. 1.5 Illustration of the evolutionary algorithm for crystal structure prediction.

1) The distance between any two atoms is smaller than threshold determined by user (e.g.,No bonds should not be shorter than 0.5 A°). One can use different thresholds for different pair of atom types separately; for example, the sum of correspondent atom radii.

2) One of the lattice vectors is too small. User can determine the threshold value; for example, it can be set to the diameter of the largest atom present in the system.

3) The angle between two lattice vectors is too small or the angle between the lattice vector and the diagonal of the parallelogram formed by other two lattice vectors is too small, One can always choose the lattice vectors in such a way that the angle between any of them is in the (60°, 120°) range.

Selection of the ‘‘best’’ members from the current generation as parents from which the algorithm creates new points (offspring) in the search space by applying specially designed variation operators to them. Evaluation of the best member (individual) of each population (group of individual) and selecting best member for new generation of the population continues till some halting criteria (when the same structure repeated many times) is achieved.

1.7.1 Variation Operators

The choice of variation operators plays an important role in the evolutionary process. Mutation operators usually randomly distort the numbers from the set that represents the solution, while heredity operators combine different parts of these sets from different parent solutions into one child solution. There are two different types of mutation operators – lattice mutation and atom permutation. Lattice mutation applies strain matrix to the lattice vectors: Lattice mutation is shown in Figure 1.6. The position of atoms (their fractional coordinates within the lattice) remains unchanged. Lattice mutation operator increases the diversity of the lattices in the population. Atom permutation operator swaps chemical identities of atoms in randomly selected pairs, see Figure 1.7, while lattice remains unchanged. Heredity operators are vital part of any evolutionary algorithm. Heredity operators are responsible for utilizing and refining the information about the system that we gather during the execution of the algorithm.

Since properties of the crystal are determined by spatial arrangement of atoms in the unit cell, the most physically meaningful way to build a heredity operator is to conserve the information from parents by using spatially coherent pieces (spatial heredity). To create a child from two parents, the algorithm first randomly chooses the lattice vector and a point on that vector. Then the unit cells of the parent structures are cut by the plane parallel to other vectors that goes through this point. Planar slices are matched, see Figure 1.8, and the number of atoms of each kind is adjusted. For big cells, it is possible to use more than two structures as parents and combine slices from all of them into a single child structure. Altogether three variation operators described above explore the search space .while preserving and refining the good spatial features through generations. It can be visualized by comparing the best structures from different generations.

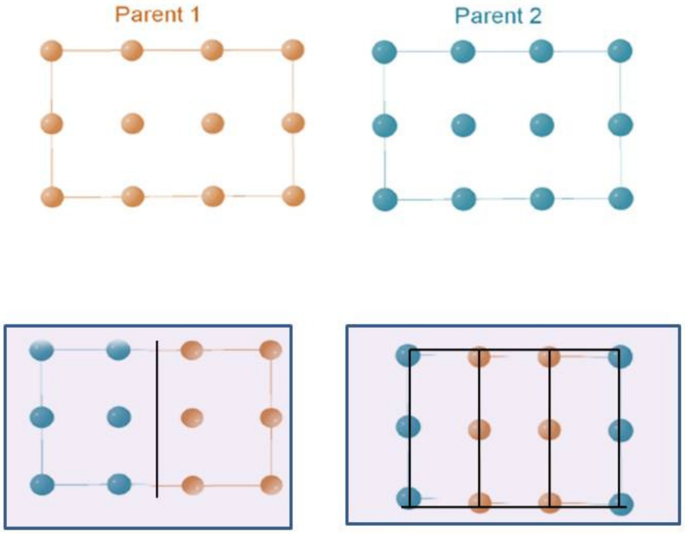

Fig. 1.6 Heredity operator combines spatial slices from different parent structures to form an offspring structure.

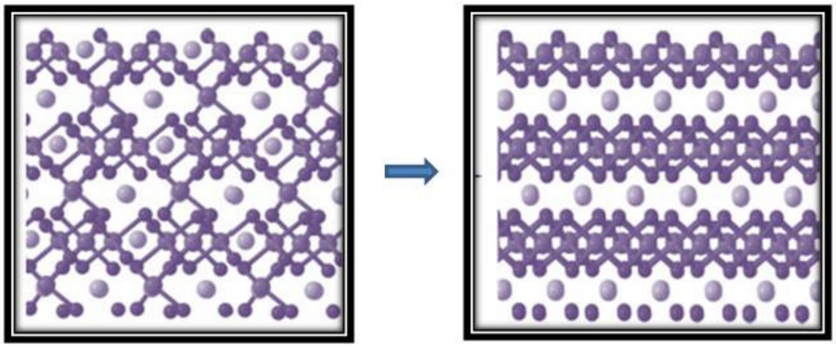

Fig. 1.7 Permutation operator produces from parent structure to permuted structure by swapping atom pairs.

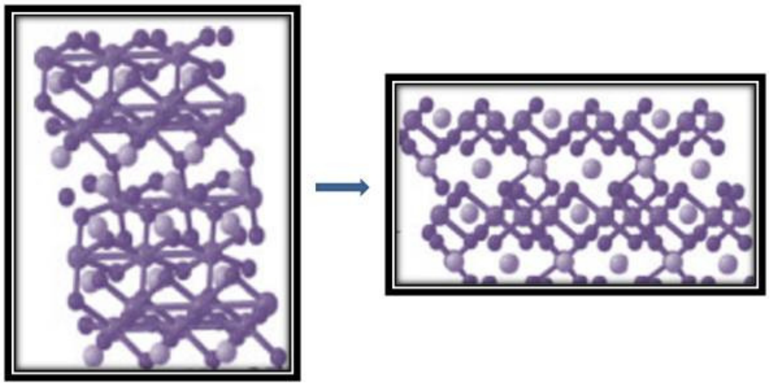

Fig.1.8 Mutation operator produces from parent structure to muted structure by using strains to lattice vectors.

1.8 Summary

In this chapter a brief description of the work to be presented in the subsequent chapters of the thesis is provided. This description is followed by an overview of the available experimental techniques for carrying out high pressure experiments and various diagnostic techniques used to understand the response of the material to high pressures. Also, the basic principle of the modern electronic band structure theoretical methods used for analyzing the high pressure behaviour of materials has been introduced.

References

1. F. R. Boyd, *Science* **145**, 3627 (1964).
2. D. J. Stevenson, *Annu. Rev. Earth Planet. Sci.* **10**, 257 (1982).
3. S.K. Sikka, *Current Science* **67**, 874 (1994).
4. A. Jayaraman, *Rev. Mod. Phys*. **55**, 65 (1983); *Rev. Sci. Instrum.,* **57**, 1013 (1986).
5. P. W. Bridgman, *Proc. Am. Acad. Arts Sci.*, **47**, 321 (1911); *Proc. Am. Acad. Arts Sci.*, **47**, 441 (1991)
6. S.T. Weir, A.C. Mitchell and W.J. Nellis, *Phys. Rev. Lett*. **76**, 1860 (1996).
7. Y. Akahama, H. Kawamura, D. Hausermann, M. Hanfland, and O. Shimomura, *Phys. Rev. Lett.* **74**, 4690 (1995).
8. S. Desgreniers, Y. K. Vohra, and A. L. Rouff, *J. Phys. Chem.* **94**, 1117 (1990).
9. Y. Ma, M. Eremets, A. R. Oganov, Y. Xie, I. Trojan, S. Medvedev, A. O. Lyakhov, M. Valle and V. Prakapenka, *Nature* **458**, 182 (2009).
10. S. K. Deb, M. C. Wilding, M. Somayazulu, and P. F. McMillan, *Nature (London)* **414**, 528 (2001).
11. Nandini Garg, K.K. Pandey, K.V. Shanavas, C. A. Betty and Surinder M Sharma, *Phys. Rev. B* **83**, 115202 (2011).
12. K. Shimizu, H. Ishikawa, D. Takao, T. Yagi, and K. Amaya, *Nature (London*) **419**, 597 (2002).
13. V. Struzhkin, M. I. Eremets, W. Gan, H.-K. Mao, and R. J. Hemley, *Science* **298**, 1213 (2002).
14. M. I. Eremets, I. A. Trojan, S. A. Medvedev, J. S. Tse, and Y. Yao, *Science* **319**, 1506 (2008).
15. H.K. Mao and P.M. Bell, *Science*, 200, 1145, (1978);.K.A. Goettel, H.K. Mao and P.M. Bell, *Rev. Sci. Instrum,***56**, 1420 (1985).
16. H. Cynn and C. Yoo, *Phys. Rev. B* **59,** 8526 (1998).
17. L. M. Hsiung and D. H. Lassila, *Scripta Matter.* **39,** 603 (1998).
18. Jung-Fu Lin, Mario Santoro, Viktor V. Struzhkin, Ho-kwang Mao, and Russell J. Hemley, *Rev. Sci. Instr*. **75**, 3302 (2004).
19. F. Elder, A.M. Gurewitsch, R.V. Langmuir, H.C Pollock, *Phys. Rev.* **71**, 829 (1947).
20. G. **S.** Knapp, M. A. Beno, and H. You, *Annu. Rev. Mater. Sci*. 1996. **26**, 693 (1996).

21. Donald H Bilderback, Pascal Elleaume and Edgar Weckert, J. *Phys. B: At. Mol. Opt. Phys*. **38**, S773 (2005).
22. J.R. Asay, *Int. J. Impact Engg*. **20**, 27 (1997).
23. M. D. Furnish, L.C. Chhabildas, and W.D. Reinhart, *International Journal of Impact Engineering* **2**3, 261 (1999).
24. Satish C. Gupta, R.G. Agarwal, J.S. Gyanchandani, S. Roy, N. Suresh, S.K. Sikka, A. Kakodkar and R. Chidambaram, *in Shock Compression of Condensed Matter*-1991 (Ed. S.C Schmidt, R.D. Dick, J.W. Forbes and D.G. Tasker), p. 839.
25. J. Osher, R. Gathers, H. Chau, R. Lee, G. Pomykal, and R. Weingart, *Int. J. Impact Eng*. **10**, 439 (1990).
26. T. C. Kaushik *et al*, *IEEE Transaction in Plasma Science* **30**, 2133 (2002).
27. C.A. Hall, J.R. Asay, M.D. Knudson, W.A. Stygar, R.B. Spielman, T.D. Pointon, D.B. Reisman, A. Toor and R.C. Cauble, *Rev. Sci. Instrum*.**72**, 3587 (2001).
28. M. D. Knudson, D. L. Hanson, J. E. Bailey, C. A. Hall, and J. R. Asay, *Phys. Rev. Lett*. **87**, 225501 (2001).
29. D.B. Reisman et al., *J. Appl. Phys*. **89**, 1625 (2001).
30. M. B. Boisen, G. V. Gibbs, M. S. T. Bukowinski, *Phys. Chem. Minerals* **21**, 269 (1994).
31. S. Gödecker, *J. Chem. Phys.* **120**, 9911 (2004).
32. R. Martonak, A. Laio, and M. Parrinello, *Phys. Rev. Lett***. 90**, 075503 (2003).
33. R. Martonak, A. Laio, M. Bernasconi, C. Ceriani, P. Raiteri, F. Zipoli, and M. Parrinello, *Z. Krist.* **220**, 489 (2005).
34. R. Martoňák, D. Donadio, A. R. Oganov, M. Parrinello, *Nature Materials* **5**, 623 (2006).
35. A. R. Oganov, C. W. Glass, S. Ono, *Earth Planet. Sci. Lett.* **241**, 95 (2006).
36. A. R. Oganov, C. W. Glass, *J. Chem. Phys.* **124**, 244704 (2006).
37. C. W. Glass, A. R. Oganov, N. Hansen, *Comp. Phys. Comm.* **175**, 713 (2006).
38. Zerr A, Miehe G, Serghiou G, Schwarz M, Kroke E, Riedel R, Fuess H, Kroll P and Boehler R *Nature* (London) **400** ,340 (1999)
39. A. R. Oganov, Y. Ma, Y. Xu, I. Erread, A. Bergarad, and A. O. Lyakhov, *PNAS* **107**, 7646 (2010).
40. W. L. Mao, L. Wang, Y. Ding, W. Yangd, W. Liu, D. Y. Kimg, W. Luo, R. Ahuja, *PNAS* **107**, 9965 (2010).

41. B. Li,Y. Ding, W. Yang, L. Wang, B. Zou, J. Shu, S. Sinogeikin, C. Park, G. Zou and H. Mao, *PNAS* **109**, 16459 (2012).
42. W.W. Zhang, A.R. Oganov, A.F. Goncharov, Q. Zhu, S.E. Boulfelfel, A.O. Lyakhov, E. Stavrou, M . Somayazulu, V.B. Prakapenka and Z. Konopkova, *Science* **342**, 1502(2013).
43. D. Petti, D. Crawford, and N. Chauvin, *MRS Bull*. **34** , 40 (2009).
44. D. C. Crawford, D. L. Porter, and S. L. Hayes, *J. Nucl. Mater.* **371**, 202 (2007)
45. Aleksandra Vojvodic and Carlo Ruberto, *J. Phys. Cond. Matter.* **22**, 3755011 (2010).
46. Zengtao Lv, HaiquanHu, Cheng Wu, Shouxin Cui, Guiqing Zhang and Wenxia Feng *Physica B* **406**, 2750 (2011).
47. Hui Li, Litong Zhang, Qingfeng Zeng, Haitao Ren, Kang Guan, Qiaomu Liu, Laifei Cheng *Solid. State Comm*. **151**, 61(2011).
48. H. G. Smith and W. Gläzer, *Phys. Rev. Lett*. **25,** 1611 (1970).
49. H. G. Smith, *Phys. Rev. Lett*. **29**, 353 (1972).
50. H. G. Smith and W. Gläzer, in Proceedings of the International Conference on Phonons, France, July 1971, edited by M. A. Nusimovici, Flammaron Sciences, Paris, (1971).
51. J.F. Alward, C.Y. Fong, M. El-Batanouny, F. Wooten, *Phys. Rev. B* **12,** 1105 (1975).
52. H. Wipf, M.V. Klein, W.S. Williams, *Phys. Status Solidi B* **408,** 489 (1981).
53. F.A. Modine, T.W. Haywood, C.Y. Allison, *Phys. Rev. B* **32,** 7743 (1985).
54. L. Pintschovius, W. Reichardt, B. Scheerer, *J. Phys. C* **11,** 1557 (1978).
55. A.M. Nartowski, I.P. Parkin, M. Mackenzie, A.J. Craven, I. MacLeod, *J. Mater. Chem*. **9,** 1275 (1999).
56. E. I. Isaev, S. I. Simak, I. A. Abrikosov, R. Ahuja., Yu. Kh. Vekilov, M. I. Katsnelson, A. I. Lichtenstein and B. Johansson, *J. Appl. Phys*. **101**, 123519 (2007).
57. Anna Delin, P. M. Oppeneer, M. S. S. Brooks, T. Kraft, J. M. Wills, Borje Johansson and Olle Eriksson, *Phys. Rev. B* **55**, R10173 (1997).
58. V. Kanchana, G. Vaitheeswaran, Xinxin Zhang, Yanming Ma, A. Svane, and O. Eriksson, *Phys. Rev.B* **84**, 205135 (2011).
59. S.K. De and S. Chatterjee, *J. Phys. C: Solid State Phys.* **21**, 3261 (1988).
60. S. Kose, F. Atay, V. Bilgin and I. Akyuz, *Int. J. Green,Energy* **1**, 353(2004).[52] R. Kondo, H. Okimura and Y. Sakai, *Jpn. J. Appl.Phys.* **10**, 1547 (1971).
61. F. A. Benko and F. P. Koffyberg, *Solid State Commun.* **57,** 901 (1986).

62. A., Shiori *Jpn. Pat., No.* **7**, 909 (1997).
63. D. R. Lide (Editor), *CRC Handbook of Chemistry and Physics*, 77th edition (CRC Press, Boca Raton) (1996-1997)
64. Roberto J. Guerrero-Moreno and Noboru Takeuchi,*Phys. Rev. B*. **66**, 2052051 (2002).
65. Haozhe Liu, Ho-kwang Mao, Maddury Somayazulu, Yang Ding, Yue Meng, and Daniel Häusermann, *Phys. Rev. B* **70**, 0941141 (2004).
66. Feng Penga, Qiang Liu, Hongzhi Fu and Xiangdong Yang, *Solid State Comm.* **148**, 6 (2008).
67. M. Durandurdu, *EPL* **84**, 66003 (2008).
68. Wenxia Feng, Shouxin Cui, Haiquan Hu, Guiqing Zhang, Zengtao Lv and Zizheng Gong, *Phys. Status Solidi B* **247**, 2202 (2010).
69. W. Martienssen and H. Warlimont (eds.), Springer Handbook of Condensed Matter and Materials Data (Springer,Berlin, 2005).
70. Gen-Quan Li, Cheng Lu, Xing-QiangYang, Shao-Wu Xiao, Ai-HuaWang, LiWang and Xiao-Ming Tan, *High Press. Res.* **30**, 679 (2010).
71. J. Staun Olsen, J.-E. Jørgensen, L. Gerward, G. Vaitheeswaran, V. Kanchana, A. Svane*, J. Alloys and Compounds*, **533**, 29 (2012).
72. Sebastian B. Schneider, Dominik Baumann, Ashkan Salamat and Wolfgang Schnick, J. Appl. Phys. **111**, 093503 (2012).
73. Hyunchae Cynn, Magnus Lipp, William Evans and Yasuo Ohishi, *J. Phys.: Conference Series* **215,** 012010 (2010).
74. D. C. Crawford, D. L. Porter, and S. L. Hayes, *J. Nucl. Mater.* **371**, 202 (2007)
75. L. Gerward, J. Stalin Olsen, U. Benedict, J.-R. Itie and J.C. Spirlet, *J.Appl.Cryst.***19**, 308 (1986).
76. L. Gerward, J. Stalin Olsen, U. Benedict and H. Luo, *J. Less Common Metals* **161**, L11, (1990)
77. P. W. Bridgman, Collected Experimental Papers, seven volumes (1964)(Cambridge, MA: Harvard University Press).
78. P. W. Bridgman, *The Physics of High Pressure*, (Bell, London, 1952).
79. F. P. Bundy, in *Modern High Pressure Research*, (Ed: R.H. Wentorf Jr. Butterworths, Washington, DC, 1962), Vol. 1.

80. H. T. Hall, *Rev. Sci. Instr.* **33**, 1278 (1962).
81. M. B. Weinberger, S. H. Tolbertand A. Kavner, *Phys. Rev. Lett.* **100**, 0455061 (2008).
82. H. K. Mao and P. M. Bell, *Science* **200**, 1145, (1978);.K. A. Goettel, H. K. Mao and P. M. Bell, *Rev. Sci. Instrum.* **56**, 1420 (1985).
83. H. K. Mao, P. M. Bell, J. W. Shaner and D. J. Steinberg, *J. Appl. Phys*. **49**, 3276 (1978).
84. L. Ruoff and H. Luo, in Recent Trends in High Pressure Research, Proceedings of XIII AIRAPT Int. Conf. On High Pressure Sciences and Technology(Ed: A.K. Singh, Oxford and IBH New Delhi 1992), p. 779.
85. L. Dubrovinsky, N. Dubrovinskaia, V. B. Prakapenka, and A. M. Abakumov, *Nat. Commun.* **3**, 1163 (2012). http://dx.doi.org/10.1038/ncomms2160
86. Jung-Fu Lin, Mario Santoro, Viktor V. Struzhkin, Ho-kwang Mao, and Russell J. Hemley, *Rev. Sci. Instr*., **75**, 3302 (2004).
87. M. Murakami, K. Hirose, K. Kawamura, N. Sata, Y. Ohishi, *Science* **304**, 855 (2004).
88. J. F. Lin, W. Sturhahn, J. Y. Zhao, G. Y. Shen, H. K. Mao, R. J. Hemley, *Science* **308**, 1892 (2005).
89. D. Andrault, M. Munoz, N. Bolfan-Casanova, N. Guignot, J.P. Perrillat, G. Aquilanti, S. Pascarelli, *Earth Planet. Sci. Lett.* **293**, 90 (2010).
90. D. Andrault, S. Petitgirard, G. Lo Nigro, J. L. Devidal, G. Veronesi, G. Garbarino, M. Mezouar, *Nature* **487**, 354 (2012).
91. V. Potapkin, C. McCammon, K. Glazyrin, A. Kantor, I. Kupenko, C. Prescher, R. Sinmyo, G. V. Smirnov, A. I. Chumakov, R. Ruffer, L. Dubrovinsky, *Nat. Commun.* **4**, 1427 (2013).
92. C. McCammon, L. Dubrovinsky, O. Narygina, I. Kantor, X. Wu, K. Glazyrin, I. Sergueev, A. I. Chumakov, *Phys. Earth Planet. Inter.* **180**, 215 (2010).
93. A. K. Singh, H. K. Mao, J. Shu, R. J. Hemley, *Phys. Rev. Lett.* **80**, 2157 (1998).
94. T. S. Duffy, G. Shen, J. Shu, H. K. Mao, R. J. Hemley and A. K. Singh, *J. Appl. Phys*. **86**, 6729 (1999).
95. A. K. Singh and T. Kenichi, *J. Appl. Phys*. **90**, 3269 (2001).
96. D. C. Hurley, R. S. Gilmore and W. F. Banholzer, *J. Appl. Phys*. **76**, 7726 (1994).
97. R. Vogelgesang A. K. Ramdas, and S. Rodriguez, M. Grimsditch, T. R. Anthony, *Phys. Rev. B* **54**, 3989 (1996).

98. E. S. Zouboulis, M. Grimsditch., A. K. Ramdas and S. Rodriguez, *Phys. Rev. B,* **57**, 2889 (1998).
99. M. Grimsditch, E.S. Zouboulis, A. Polian, *J. Appl. Phys.* **76**, 832 (1994).
100. F. P. Bundy, in *Modern High Pressure Research*, (Ed: R.H. Wentorf Jr. Butterworths, Washington, DC, 1962), Vol. 1.
101. M. Hanfland, K. Syassen, N. E. Christensen and D. L. Noviko, *Nature* **408**, 174 (2000
102. Latella A. Bruno and O' Connor H. Brian, *J. Am. Ceram. Soc*., **80**, 2941 (1997).
103. J. J. Wu et al., *Scientific Reports* **4,** 3685 (2014).
104. C. Lind, D. G. VanDerveer, A. P. Wilkinson, J. Chen, M. T. Vaughan, and D. J. Weidner, *Chem. Mater.* **13**, 487 (2001).
105. Vinod Panchal, Nandini Garg, A.K. Chauhan, Sangeeta, Surinder M. Sharma, *Solid State Comm.* **130**, 203 (2004).
106. J. H. Nguyen, M.B. Kruger and R. Jeanloz, *Phys. Rev. Lett.,* 78, 1936 (1997); Sean R. Shieh and Thomas S. Duffy, *Phys. Rev. B*. **66**, 134301 (2002)
107. M.P. Usikov and V.A. Zilbershtein, *Phys. Stat. Sol.(a,* **19**, 53 (1973).
108. A.R. Kutsar, I.V. Lyasotski, A.M. Podurits and A.F. Sanches-Bolinches, *High Press. Res.* **4**, 475 (1990).
109. S. Song and G.T. Gray III, *High Pressure Science and Technology-1993* (Eds: S.C. Schmidt, J.W. Fowles, G.S. Samara and M. Ross), AIP Press, New York, 251 (1994).
110. G. Jyoti, K.D. Joshi, Satish C. Gupta, S.K. Sikka, G.K. Dey and S. Banerjee, *Phil. Mag. Lett*. **75**, 291 (1997).
111. S.K. Sikka, Y.K. Vohra, and R. Chidambaram, *Prog. Mater. Sci.* **27,** 245 (1982).
112. H. Xia, S.J. Duclos, A.L. Ruoff and Y.K. Vohra, *Phys. Rev. Lett.* **64**, 204 (1990).
113. H. Xia, G.Parthsarthy, H. Luo, Y.K. Vohra and A. Ruoff, *Phys. Rev. B* **42**, 6736 (1990).
114. A. K Singh, *Bull. Mater. Sci.* **5**, 219 (1983).
115. A K Singh, *Mater. Sci. Forum* **3**, 291 (1985)
116. Anil K. Singh, H.K. Mao, J. Shu, Russel J. Hemley, *Phys. Rev. Lett,* **80**, 2157 (1998).
117. Thomas S. Duffy, Guoyin Shen, Jinfu Shu, H.K. Mao, R.J. Hemley and Anil K. Singh, *J. Appl. Phys*. **86**, 6729 (1999).
118. Anil K. Singh and Takemura Kenichi, *J. Appl. Phys*. **90,** 3269 (2001).
119. D.C. Hurley, R.S. Gilmore and W.F. Banholzer, *J. Appl. Phys*. **76,** 7726 (1994).

120. R. Vogelgesang A. K. Ramdas, and S. Rodriguez, M. Grimsditch, T. R. Anthony, *Phys. Rev. B* **54**, 3989 (1996).

121. E.S. Zouboulis, M. Grimsditch., A. K. Ramdas and S. Rodriguez, *Phys. Rev. B* **57**, 2889 (1998).

122. M. Grimsditch, E.S. Zouboulis, A. Polian, *J. Appl. Phys.,* 76, 832 (1994).

123. Lee Davison, *Fundamentals of shockwave propagation in solids*, Springer Verlag, 2008, p. 38.

124. G.E. Duval and R.A. Graham, *Rev. of Modern Phys*., 49, 523 (1977); G.E. Duvall and G R. Fowles 1963 *Shock Waves in High Pressure Physics and Chemistry* Vol 2, (Ed: R S Bradley) New York: Academic, p. 2

125. W.J. Nellis, J.A. Morarity, A.C. Mitchell and N.C. Holmes, *J. Appl. Phys*. 82, 2225 (1997)

126. Y.M. Gupta, *Shock Compression of Condensed Matter-1999*, (Eds. M.D. Furnish, L.C. Chhabildas and R.S. Hixson, AIP, 2000) p. 3.

127. A. Benuzzi-Mounaix, M. Koenig, G. Huser, B. Faral, D. Batani, E. Henry, B. Marchet, T.A. Hall, M. Boustie, Th. De Resseguier, M. Hallouin, G. Guyot, D. Andrault and Th. Charpin, *Phys. Plasma* **9**, 2466 (2002).

128. J.R. Asay, *Int. J. Impact Engg*. **20**, 27 (1997).

129. M. D. Furnish, L.C. Chhabildas, and W.D. Reinhart, *International Journal of Impact Engineering* **23**, 261 (1999).

130. Satish C. Gupta, R.G. Agarwal, J.S. Gyanchandani, S. Roy, N. Suresh, S.K. Sikka, A. Kakodkar and R. Chidambaram, *in Shock Compression of Condensed Matter*-1991 (Ed. S.C Schmidt, R.D. Dick, J.W. Forbes and D.G. Tasker), p. 839.

131. J. Osher, R. Gathers, H. Chau, R. Lee, G. Pomykal, and R. Weingart, *Int. J. Impact Eng*. **10**, 439 (1990).

132. T. C. Kaushik *et al*, *IEEE Transaction in Plasma Science* **30**(6), 2133 (2002).

133. C.A. Hall, J.R. Asay, M.D. Knudson, W.A. Stygar, R.B. Spielman, T.D. Pointon, D.B. Reisman, A. Toor and R.C. Cauble, *Rev. Sci. Instrum.***72**, 3587 (2001).

134. M. D. Knudson, D. L. Hanson, J. E. Bailey, C. A. Hall, and J. R. Asay, *Phys. Rev. Lett.* **87,** 225501 (2001).

135. D.B. Reisman et al., *J. Appl. Phys*. **89**, 1625 (2001).

136. L. D. Da Silva *et al.*, *Phys. Rev. Lett.* **78**, 483(1997).

137. R. W. Lemke, M. D. Knudson, C. A Hall, and T. A. Haill, P. M. Desjarlais, J. R. Assay and T. A. Mehlhorn, *Phys. Plasmas* **10**, 1092 (2003).

138. R. Jeanloz et al., *PNAS* **104**, 22 (2007).

139. G. Jyoti, N. Suresh, K. D. Joshi and S. C. Gupta, *Solid State Physics, India* (Ed: R. Mukhopadhyay, B.K. Godwal and S.M. Yusuf), vol. 42, p. 272(1999).

140. A. S. Rav, K. D. Joshi and S. C. Gupta, in 12th National Seminar on Physics and Technology of Sensors, (2007).

141. S. C. Gupta and Y. Gupta, *J. Appl. Phys.***57**, 2464 (1985).

142. S. C. Gupta, *Indian J. of Pure & App. Phys.* **34**, 651 (1996).

143. S. C. Gupta and S. K. Sikka, *Shock Waves* **6**, 345 (1997).

144. G. I. Kanel, S. V. Razorenov and V. E. Fortov, *J. Phys Cond. matter* **16**, S1007 (2004).

145. L. M. Barker and R. E. Hollenbach, *J. Appl. Phys.* **43**, 4669 (1972).

146. D. D. Bloomquist and S. A. Sheffield, *J. Appl. Phys.* **54**, 1717 (1983).

147. W. Hemsing, A. Mathews, R. Warnes, M. George, and G. Whittemore, in Shock Compression of Condensed Matter, edited by S. Schmidt, R. Dick, J. Forbes, and D. Tasker (Elsevier, New York),pp. 767(1992).

148. K. Baumung, J. Singer, S. Razorenov, A. Utkin, in Shock Compression of Condensed Matter, edited by S. Schmidt and W. Tao (AIP, Woodbury, NY), p. 1015(1996).

149. P. Celliers, G. Collins, L. DaSilva, D. Gold, and R. Cauble, *Appl. Phys. Lett.* **73**, 1320 (1998).

150. D. Milathianaki et al., *Phys. Rev. B* **86**, 014101(2012).

151. D. H. Kalantar et al., *Phys. Rev. Lett.* **95**, 075502 (2005).

152. A. Loveridge-Smith, A. Allen, J. Belak, T. Boehly, A. Hauer, B. Holian, D. Kalantar, G. Kyrala, R. W. Lee, P. Lomdahl, M. A. Meyers, D. Paisley, S. Pollaine, B. Remington, D. C. Swift, S. Weber, J. S. Wark, *Phys. Rev. Lett.* **86**, 2349 (2001).

153. G. I. Pangilinan and Y. M. Gupta, *High Pressure Shock Compression of Solids III*, ed. L. Davison and M. Shahinpoor (Springer Verlag–New York 1998) p. 81.

154. K. G. Nakamura, K. Wakabayashi, Y Hironaka and K Kondo, *J. Phys. Cond. Matter* **14**, 10817 (2002).

155. D. H. Dolan and Y. M. Gupta, *J. Chem. Phys.* **121**, 9050 (2004).

156. D.R. Hartree, *Proc. Cambridge Philos. Soc*. **24**, 89 (1928).

157. V.Z. Fock, *Physik* **62**, 126 (1930).

158. J.C. Slater, *Phys. Rev. B* **35**, 210 (1930).

159. P.C. Hohenberg and W. Kohn, *Phys. Rev.* **136**, B864 (1964).

160. W. Kohn and L.J. Sham*,* *Phys. Rev. A* **140**, 1133 (1965).

161. D. M. Ceperley and B. J. Alder, *Phys. Rev. Lett.* **45**, 566 (1980).

162. A.D. Becke (1993). *J. Chem. Phys.* **98**, 5648(1993)

163. M. Born and R. Oppenheimer, *Annalen der Physik* **84**, 457 (1927).

164. W. Kohn and L. J. Sham, *Phys. Rev. A* **140**, 1133 (1965).

165. M. Born and K. Huang, *Dynamic Theory of Crystal Lattices.* Oxford: Oxford University Press (1954).

166. J. P. Perdew and A. Zunger. *Phys. Rev. B* **23**,5048 (1981).

167. J. P. Perdew, K. Burke, and M. Ernzerhof. *Phys. Rev. Lett*. **77,** 3865 (1996).

168. C. Lee, W. Yang, and R. G. Parr. *Phys.Rev. B* **37**,785 (1988).

169. A. D. Becke. *Phys. Rev. A* **38**,3098, (1988).

170. J. P. Perdew, A. Ruzsinszky, G. I. Csonka, O. A. Vydrov, G. E. Scuseria, L. A. Constantin, X. Zhou, and K. Burke. *Phys. Rev. Lett*. **100**,136406, (2008)

171. A. Svane and O. Gunnarsson, *Phys. Rev. Lett.* **65**, 1148 (1990).

172. S. Massida, M. Posternak and A. Baldereschi, *Phys. Rev. B* **48**, 5058 (1993).

173. L. Hedin, *Phys. Rev.* **139**, A796 (1965).

174. V. I. Anisimov, F. Aryasetiawan and A. I. Lichtenstein, *J. Phys. Cond. Matter* **9**, 767 (1997).

175. S. Grimme, *J. Comp. Chem.*, **27** 1787(2006) .

176. M. Dion, H. Rydberg, E. Schr□oder, D. C. Langreth, and B. I. Lundqvist. *Phys. Rev. Lett.,* **92**,246401 (2004).

177. G. Roman-Perez and J. M. Soler. *Phys. Rev. Lett.* **103**,096102(2009).

178. J. Klimes, D. R. Bowler, and A. Michaelides. *Phys. Rev. B*, **83**,195131 (2011).

179. D. R. Hamann, M. Shluter, and C. Chiang, *Phys. Rev. Lett.* **43**, 1494 (1979).

180. D. Vanderbilt, *Phys. Rev. B* **41**, 7892 (1990).

181. W. C. Herring, *Phys. Rev.* **57**, 1169 (1940).

182. W. C. Herring and A. G. Hill, *Phys. Rev.* **58**, 132 (1940).

183. F. Herman, *Rev. Mod. Phys.* **30**, 102 (1958).

184. P. E. Blochl, *Phys. Rev. B* **50**, 17953 (1994).

185. G. Kresse and D. Joubert, *Phys. Rev. B* **59**, 1758 (1999).

186. N. A. W. Holzwarth, G. E. Matthews, A. R. Tackett, and R. B. Dunning, *Phys. Rev.B* **55**, 2055 (1997).

187. http://www.quantum-espresso.org/

188. http://www.abinit.org/

189. http://cms.mpi.univie.ac.at/vasp/

190. J. C. Slater and G. F. Koster, *Phys. Rev.* **94**, 1498 (1954).

191. K. Koepernik and H. Eschrig, *Phys. Rev. B* **59**, 1743 (1999).

192. O. K. Anderson, *Phys. Rev B* **12**, 3060 (1975).

193. S. Y. Savrasov, *Phys. Rev. B* **54**, 16470 (1996); S. Y. Savrasov, D. Y. Savrasov, *ibid* **54** 16487 (1996).

194. D.J. Singh, *Plane Waves, Pseudopotentials and the LAPW Method*, Kluwer Academic Publishers, Boston, Dordrecht, London (1994).

195. P. Blaha, K. Schwarz, G. K. H. Madsen, D. Kvasnicka and J. Luitz, WIEN2K, (K. Schwarz, Techn. Univ. Wien, Austria, 2001).

196. P. E. Blochl, *Phys. Rev. B* **50**, 17953, (1994).

197. S.L. Chaplot, N. Choudhury, S Ghose, M.N. Rao, R. Mittal, P. Goel, *Eur J Mineral* **14**,291 (2002).

198. G Venkataraman, L Feldkamp, VC. Sahni, *Dynamics of perfect crystals. Cambridge: MIT Press*; (1975).

199. A. Togo, F. Oba, and I. Tanaka, *Phys. Rev. B* **78**,134106 (2008).

200. S. Baroni, S. Gironcoli, A. Corso, and P. Giannozzi, *Rev. Mod. Phys*.**73**,515 (2001).

201. G. Kresse and J. Furthmuller, *Phys. Rev. B* **54**, 11169 (1996).

202. K. Schwarz and P. Blaha, *Comput. Mater. Sci*.**28**,259(2003).

203. http://www.gnu.org/copyleft/gpl.txt

204. J Maddox, *Nature* **335**, 201 (1988).

205. A. Gavezzotti ,*Acc. Chem. Res*. **27** , 309 (1994).

Chapter 2

Structural Stability Analysis of CdO under High Pressure

2.1 Introduction

The Transition metal oxides (TMO) are systems with large variability of structures and chemical bonding, which brings about different magnetic electrical and optical properties. The high quality electrical and optical properties of these compounds are useful in designing of new memories smaller transistors and smart sensors in different semiconductor industries. These technological applications have attracted the interest on the high pressure behavior of these materials. Cadmium oxide (CdO) is an attractive semiconductor material. It has many industrial applications such as in the production of solar cells, liquid-crystal displays, electro-chromic devices, light-emitting diodes, etc.[1-5]. So, in order to fully exploit this semiconductor material, it is necessary to obtain a good understanding of the thermo physical properties of CdO, and in particular, its structural and thermodynamic properties under high pressure [6-13].

At ambient pressure CdO differs from the other IIB–VIA semiconductors and it crystallizes in the NaCl-type (B1) phase rather than zinc blende (B3) or wurtzite (B4) type structures. In spite of structural differences, the electronic properties such as band structure and optical band gaps etc of CdO are closely related to those of the other IIB–VIA semiconductors. With the rapid development of high-pressure techniques, extensive experimental work has been done to address the high-pressure behaviour of CdO in the past few years [6-12]. In first principles theoretical investigations using full potential linearized augmented plane wave (FPLAPW) method as implemented in the WIEN97 code, Moreno and Takeuchi [6] have predicted rocksalt type (B1) to CsCl (B2) structural phase transition in CdO at ~ 89GPa. This prediction was confirmed by Liu *et al.* [7] in a high pressure x-ray diffraction measurements carried out in a diamond anvil cell, where the B1 phase of CdO was observed to transforms to B2 structure at ~90.6GPa. Subsequently, in recent past, some other theoretical studies on structural stability analysis of CdO under high pressure have also been published. [8–12]. For example, in an ab-initio study carried out using plane wave pseudo potential method implemented in CASTEP code, Penga et al. [8] have examined the structural stability and calculated the pressure dependent elastic constants of CdO in B1 phase. Their study showed that the B1 phase undergoes transition to B2 phase at ~83GPa. Durandurdu [9] has performed molecular dynamics (MD) simulations and suggested the B1 to B2 structural phase transition in CdO around 100GPa. Subsequently, Feng et al. [10] suggested this phase transition to occur around ~86 GPa. Further, these authors, on the basis of their electronic band structure calculation suggested that both the B1 and B2 phases are metallic in nature, which is in contrast with the experimental observations [11]. Apart from the high pressure phase transition studies, the work on the determination of the thermodynamic properties, such as bulk modulus, shear elastic moduli, sound speed, and Debye temperature as a function of pressure up to 160GPa has also been reported in past [12].

All the above mentioned theoretical studies, except the MD simulations by Durandurdu [9], address issues related to structural stability of CdO on the basis of static lattice calculations, however, it is well established that the lattice dynamic stability plays a crucial role in stabilizing the different structures. Hence it is essential to test the lattice dynamic stability of both the B1 and B2 phases as a function of pressure. We have performed a detailed *ab-intio* band structure calculation under hydrostatic compressions on these two phases of CdO. The investigations included static as well as lattice dynamical calculation. Results of these calculations are presented in this chapter.

2.2 Methodology Employed for Present Calculations

All the calculations have been performed employing plane wave pseudo potential method within the framework of Density Functional Theory (DFT) [13] implemented in QUANTUM ESPRESSO package [14]. The structural and elastic stability analysis has been carried out from static lattice calculations. The *ab-initio* total energy calculations required for structural stability analysis have been performed within both generalized gradient approximation (GGA) [15] and local density approximation (LDA) [16] for the exchange correlation potential. Since the pressure for B1 to B2 transition from GGA approximation better matches with the experimental transition pressure, all the further calculations are performed within GGA only. The ultrasoft pseudo potential having valence configurations of $4d^{10}5s^2$ and $2s^22p^4$ has been used for Cd and O respectively. For generation of pseudo potential, the cut off radius in Cd are taken to be 2.1 Bohr for 4d and 5s orbitals, and 2.5 Bohr for 5p orbitals, whereas these in O are taken to be 1.2 Bohr for both 2s and 2p orbitals. Also, non-linear core correction to the exchange-correlation energy functional for Cd has been added. For GGA, we have used PW91 [15] potential, however, for LDA, the Troullier-Martins [16] norm-conserving pseudo potential has been used for both the atoms. Electronic wave functions are expanded in a plane wave basis set (PWs) with energy cut off of 60 Ry and charge density is represented in PWs with energy cut off of 600 Ry. Energy convergence of 10^{-6} Ry has been met by using the 12x12x12 Monkhorst–Pack (MP)[17] grid of k-points in the full Brillouin zone (BZ). The dynamic stability of B1 and B2 phase has been analyzed from the phonon spectra determined from self consistent density functional perturbation theory (DFPT) using linear response method [18]. For phonon dispersion calculations a 4×4×4 q mesh in the first BZ has been used.

2.2.1 Determination of Isotherm at 300 K and shock Hugoniot

To analyze the structural stability under hydrostatic compression, the total energy for B1and B2 phases of CdO at 0 K have been computed as a function of volume up to about 150 GPa. The total energy at 0 K is used to generate pressure-volume relation for each phase and which finally is utilized to determine the enthalpies of these phases at various pressures. In order to derive the pressure-volume relation, a polynomial fit of total energy with volume is used and the pressure is determined using the negative volume derivative of total energy dependence on unit cell volume. The enthalpies have been compared at various pressures and the stable structure is obtained. After examining the structural stability at various pressures, the 0K isotherm of the CdO is determined. To determine bulk modulus at zero pressure (B_0) and the pressure derivative of bulk modulus at zero pressure ($B_0^{'}$), the 0K theoretical P-V data are fitted to the third order Birch-Murnaghan (B-M) equation of state:

$$P = \frac{3}{2}B_0\left[\left(\frac{V}{V_0}\right)^{-7/3} - \left(\frac{V}{V_0}\right)^{-5/3}\right]\left[1 + \frac{3}{4}\left(B_0^{'} - 4\right)\left\{\left(\frac{V}{V_0}\right)^{-2/3} - 1\right\}\right] \tag{2.1}$$

where, V and V_0 are volume at a compressed state and volume at zero pressure, respectively. The B_0 and $B_0^{'}$ are derived from the above fit. The bulk modulus B and its pressure derivative B' at different pressures are then determined as follows:

$$B = V\frac{\partial^2 E_c}{\partial V^2} = -V\frac{\partial P}{\partial V} \text{ and } B^{'} = \frac{\partial B}{\partial P} = -\frac{V}{B}\frac{\partial B}{\partial V} \tag{2.2}$$

In order to derive the 300K isotherm and the temperature dependence of volume (V) and bulk modulus (B) of B1 phase, the Helmholtz free energy F (V,T) has been computed using quasiharmonic approximation (QHA) [19-20] as follows:

$$F(V,T) = F_{static}(V) + F_{phonon}(V,T) = E_c(V,0) + E_{phonon}(V,T) - TS_{phonon}(V,T) \tag{2.3}$$

Here $F_{phonon}(V,T)$, $E_{phonon}(V,T)$ and $S_{phonon}(V,T)$, respectively, are the free energy, internal energy and entropy contribution from phonons. Further, $F_{phonon}(V,T)$ can be expressed as:

$$F_{phonon}(V,T) = \sum_{q,n}\frac{1}{2}\hbar\omega_n(q,V) + k_B T\sum_{q,n}\ln\left[1 - \exp\left(\frac{-\hbar\omega_n(q,V)}{k_B T}\right)\right] \tag{2.4}$$

With $\omega_n(q,V)$ is the frequency of n_{th} phonon band at the point q in the Brillouin zone. Here the entropy contribution from phonons is defined as:

$$S_{phonon}(V,T) = -k_B \sum_{q,n} \ln\left[1-\exp\left(\frac{-\hbar\omega_n(q,V)}{k_B T}\right)\right] + \sum_{q,n} k_B \frac{\hbar\omega_n(q,V)}{k_B T}\left[\exp\left(-\frac{\hbar\omega_n(q,V)}{k_B T}\right)-1\right]^{-1} \tag{2.5}$$

The equilibrium volume and bulk modulus at a given temperature T = T_1 is determined by calculating the F(V,T_1) as a function of volume at that temperature and finding the volume corresponding to zero pressure *i.e.* volume at which the - $\partial F/\partial V = 0$. This process has been repeated at various temperatures and equilibrium volumes as a function of temperature *i.e.* *V (T)*, has been determined. The volume thermal expansion coefficient α(T) from *V (T)* is then obtained using expression:

$$\alpha(T) = \frac{1}{V_0}\left(\frac{\partial V}{\partial T}\right) \tag{2.6}$$

V_0 is the equilibrium volume at 0 K. The bulk modulus at a given temperature T_1 is obtained by using the expression:

$$B = V\left(\frac{\partial^2 F(V,T_1)}{\partial V^2}\right) \tag{2.7}$$

To determine the shock Hugoniot and 300K isotherm the thermal lattice contributions and thermal electronic excitation contributions to the total energy has also been calculated and added to the 0K energy. The total energy *E(V,T)* and pressure *P(V,T)* at given temperature *T* and volume *V* have been expressed as [21-22]:

$$E(V,T) = E_c(V) + E_T(V,T) + E_e(V,T) \tag{2.8}$$

$$P(V,T) = -\frac{\partial F(V,T)}{\partial V} = -\frac{\partial F_c}{\partial V} - \frac{\partial F_T(V,T)}{\partial V} - \frac{\partial F_e(V,T)}{\partial V} \tag{2.9}$$

Here *F(V,T)* is the Helmholtz free energy at temperature *T* and volume *V* with F_c, denoting the free energy at 0 K, and $F_T(V,T)$ and $F_e(V,T)$ are the free energies corresponding to the thermal lattice vibrations and thermal electronic excitations contributions, respectively.

The Eqn. (2.9) can equivalently be put in different way as [28-30]

$$P(V,T) = -\frac{\partial E_c(V)}{\partial V} + \frac{\gamma E_T}{V} + \gamma_e \frac{E_e}{V} \tag{2.10}$$

where E_T is vibrational energy contribution of the ions including zero point vibration energy and E_e thermal electronic contribution to the total energy. γ and γ_e are the thermal and electronic Grüneisen parameters, respectively. The E_T is calculated from lattice dynamic calculations using QHA. At 300 K the electronic excitation energy contributions are very small (of order of 10^{-2} mRy/atom) hence to determine the 300 K isotherm these terms in Eqn. (2.8) and (2.10) are neglected. The thermal Grüneisen parameter is determined using the definition:

$$\gamma = V\left(\frac{\partial P}{\partial E}\right)_V = \frac{\alpha B_T V}{C_V} \tag{2.11}$$

Finally the 300 K isotherm is evaluated by substituting the value of γ, E_T at 300 K in Eqn. (2.10).

The shock Hugoniot is determined using Eqn. (2.8) and (2.10) in conjunction with the Rankine–Hugoniot relation (the energy conservation equation for a shock-wave travelling through a material) [27-28]:

$$E(V,T_H) - E(V_0,T_0) = \frac{1}{2}\left[P(V,T_H) + P(V_{0,}T_0)\right]\left[V_0 - V\right] \qquad (2.15)$$

Here T_H is the temperature rise along shock Hugoniot and T_0 is the room temperature.
As temperatures generated during shock compressions are high so contribution of electronic excitations also becomes significant. The electronic contributions E_e to total energy is evaluated using the expression $E_e = \frac{1}{2}\beta T^2$ where β is defined as [29, 30]:

$$\beta = \pi^2 k_B^2 N(E_f)/3 \qquad (2.16)$$

Where $N(E_f)$ is the density of states at Fermi level, which is determined at various unit cell volume from pseudo potential calculations. The γ_e required for determination of pressure is defined as [29, 30]:

$$\gamma_e = \frac{\partial \ln \beta}{\partial \ln V}. \qquad (2.17)$$

Finally, using the expression of energy $E(V,T)$ and the corresponding pressure $P(V,T)$ calculated according to Eqn. (2.8) and (2.10), the Hugoniot point for a particular compression is evaluated by finding the temperature (T_H) for which the Rankine – Hugoniot relation (Eqn. 2.15) is satisfied. Putting the value of T_H in the expression of $P(V,T)$ the Hugoniot pressure is calculated.

2.2.2 Determination of elastic constants and phonon dispersion

For the CdO single crystal having cubic structure, there are only three independent elastic constants, C_{11}, C_{12} and C_{44} or equivalently three independent elastic moduli namely bulk modulus (B) and two shear moduli C'= (C_{11} - C_{12})/2 and C_{44}. To determine the shear moduli C' and C_{44} at a particular volume, the total energy is calculated as a function of different kinds of distortions and the shear elastic moduli are then calculated from the second order derivative of the total energy with respect to strain e_i (with i= 1to 6) as described below:

Total energy of the strained lattice is related to the deformation tensor by the following relation [31]:

$$E_c(V,\underline{\varepsilon}) = E_c(V,0) + \frac{1}{2} V \sum_i \sum_j C_{ij} e_i e_j \tag{2.18}$$

Where e_i are the components of the deformation tensor $\underline{\varepsilon}$ represented in matrix notation as follows:

$$\underline{\varepsilon} = \begin{bmatrix} e_1 & \frac{1}{2}e_6 & \frac{1}{2}e_5 \\ \frac{1}{2}e_6 & e_2 & \frac{1}{2}e_4 \\ \frac{1}{2}e_5 & \frac{1}{2}e_4 & e_3 \end{bmatrix} \tag{2.19}$$

The total energy variation of the lattice is calculated using volume conserving deformation [30, 32]. The volume conserving deformations used for the calculations of the shear elastic moduli C' and C_{44}, respectively are (in matrix notation):

$$\begin{bmatrix} e & 0 & 0 \\ 0 & -e & 0 \\ 0 & 0 & \frac{e^2}{1-e^2} \end{bmatrix} \quad \text{and} \quad \begin{bmatrix} 0 & e & 0 \\ e & 0 & 0 \\ 0 & 0 & \frac{e^2}{1-e^2} \end{bmatrix} \tag{2.20}$$

When these two deformation matrices (Eqn. 2.20) are used in Eqn. (2.18), the relation between the total energies of the strained lattice and the elastic constants becomes:

$$E_c(V,\underline{\varepsilon}) = E(V,0) + V(C_{11} - C_{12})e^2 + O(e^4) \qquad (2.21)$$

$$E_c(V,\underline{\varepsilon}) = E(V,0) + 2VC_{44}e^2 + O(e^4) \qquad (2.22)$$

At each unit cell volume V, the total energy $E_c(V,\underline{\varepsilon})$ of the strained lattice is computed and then Eqn. (2.21) and Eqn. (2.22) are used to determine the moduli C_{11} - C_{12} and C_{44}. Again, the bulk modulus (B) calculated using equation of state (Eqn. 2.2) is related to the C_{11} and C_{12} elastic constants by the following relation

$$B = \frac{1}{3}(C_{11} + 2C_{12}) \qquad (2.23)$$

The independent elastic constants C_{11} and C_{12}, and C_{44} are evaluated by solving Eqn. (2.21) through Eqn. (2.23).

Besides static lattice calculations, the lattice dynamic calculations have also been performed using plane wave pseudopotential method as implemented in the Quantum ESPRESSO software package [33] and phonon spectra at various pressures have been determined. The lattice dynamical calculations have been carried out within the framework of self consistent perturbation theory with 4×4×4 q points and 8×8×8 k-mesh used for integration over the Brillouin zone do determine phonon dispersion curve. The calculations are carried out within GGA and the electronic wave functions are expanded in a plane wave (PW) basis set with energy cut off of 60 Ry and charge density is represented in PWs with energy cut off of 600 Ry.

2.3 Results and Discussions

2.3.1 Structural stability, equation of state and shock Hugoniot

In order to determine equation of state, the knowledge of structural stability as a function of pressure is necessary. Therefore analysis of structural stability of CdO under hydrostatic compression has been carried out as a first step. For this purpose the total energy at 0 K has been calculated at various unit cell volumes for the B1, B2 structures. The enthalpy of both the structures has been determined from the energy volume data. Also, Gibbs free energy of both B1 and B2 phases has been determined using the quasiharmonic approximation. Fig.2.1 shows the enthalpy (H) of the B2 phase relative to that of the B1 phase as a function of hydrostatic pressure. The inset of Fig. 2.1, compares the Gibbs free energy (ΔG) of B2 phase relative to B1 phase at 300 K. As is depicted in the figure, the calculations performed within GGA suggest that at 0 K, the B1$\rightarrow$ B2 phase transition will occur at a pressure of ~ 87 GPa, however, at 300 K it will occur at ~86 GPa as compared to experimental value of ~ 90.6 GPa of Liu *et al.* [7]. This transition within LDA, at 0 K, is found to occur at ~74 GPa, indicating that the pressure for B1$\rightarrow$B2 transition determined within GGA agrees better with experiment [7] as well as other theoretical studies [6, 8, 10, 12] than that obtained from LDA. So, further calculations have been restricted within GGA only. The calculated 300 K isotherm is plotted in Fig. 2.2 along with the experimental data [7, 34]. The volume discontinuity of 7% at the transition pressure shows the first order nature of this phase transition. Additionally, employing the theoretically determined thermal equation of state in conjunction with Rankine Hugoniot relation, the Hugoniot of B1 phase of CdO has been derived. For this purpose the prescription of Luo *et al* [39] has been used. At each volume, the temperature has been adjusted until the obtained pressure and energy satisfied Rankine Hugoniot equation. This yielded Hugoniot in pressure - volume and pressure - temperature plane. The Hugoniot curve so obtained is plotted in Fig. 2.3. The shock velocity (*D*) and particle velocity *(u)* at various volumes could be obtained from the pressure –volume Hugoniot curve in conjunction with the mass and momentum conservation equations as mentioned in chapter 1. As depicted in Fig 2.3 c the *D* and *u* exhibit a linear relationship:

$$D = C_b + su \tag{2.24}$$

where, the constant C_b. represents the bulk sound velocity. The constant C_b is approximately related to the bulk modulus and the s parameter to pressure derivative of the bulk modulus through following expressions:

$$C_b = \sqrt{\frac{B_0}{\rho_0}} \tag{2.25}$$

$$B_0^{'} = 4s - 1 \tag{2.26}$$

The value of C_b and slope (s) determined from linear D – u relation is 3.65 km/s and 1.62, respectively.

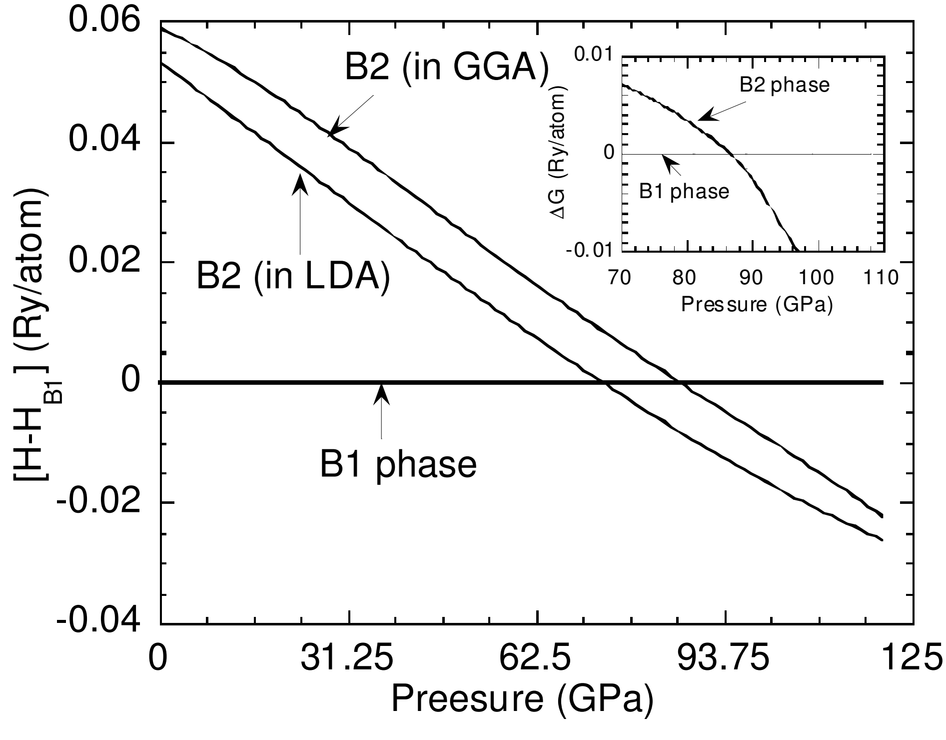

Fig. 2.1 Enthalpy of B2 phase relative to that of B1 phase for CdO at various pressures. The inset displays the Gibbs free energy of B2 phase relative to B1 phase at 300 K.

In Table 2.1, compares various physical quantities for B1 phase derived from present calculations with the experimental data and theoretical values available from other sources [6-10, 12, 34, 35]. The calculated zero pressure volume, bulk modulus and its pressure derivative at zero pressure obtained from GGA calculations agree within 7%, 14% and 5%, respectively with experimental values [7, 34, 35]. Further, as depicted in the Table 2.1, for B2 phase the zero pressure volume, bulk modulus and its pressure derivative at zero pressure derived from present calculations agree with experimental values within 1.7%, 4.6% and 0.2% [35]. The Gruneisen parameter (γ) of B1 phase at 300 K is estimated to be ~ 1.79. The value of α, B_T and C_V used for this purpose are 4.445×10^{-5}/K, 111 GPa and 7.564×10^{-23} J/K/formula unit, respectively, taken from present calculations. In Table 2.2 these quantities have been compared with the available theoretical and experimental data [36-37].

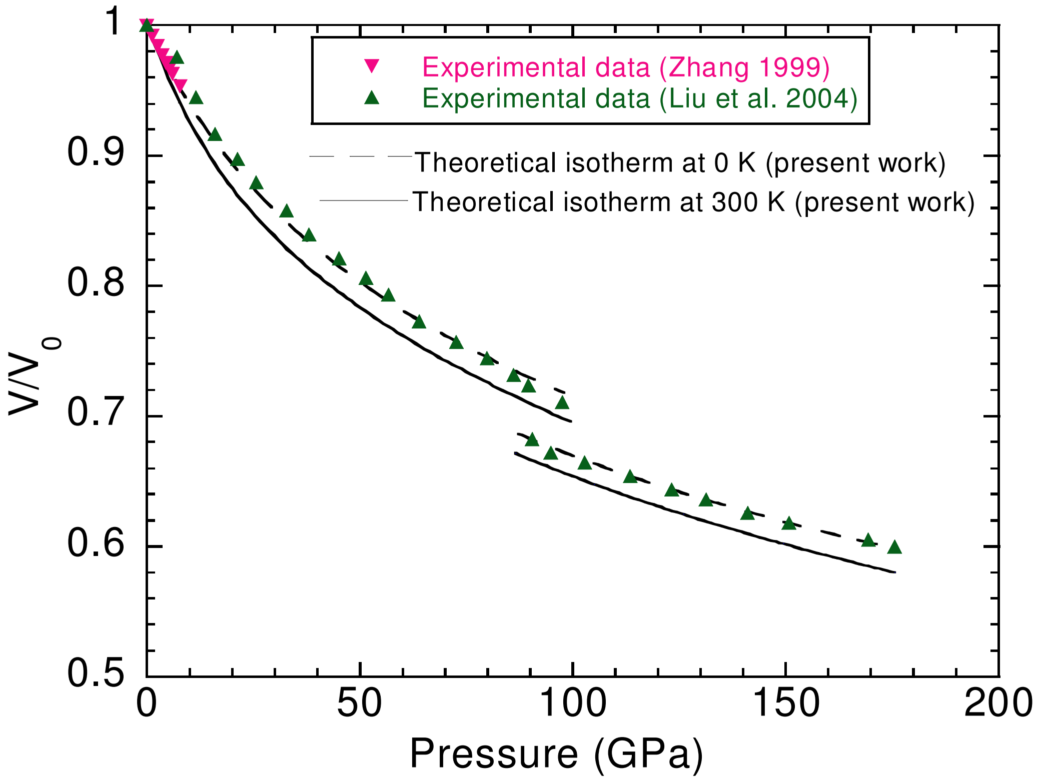

Fig. 2.2 Comparison of theoretical isotherm at 300K of CdO with experimental data of Liu *et al.* and Zhang *et al.*

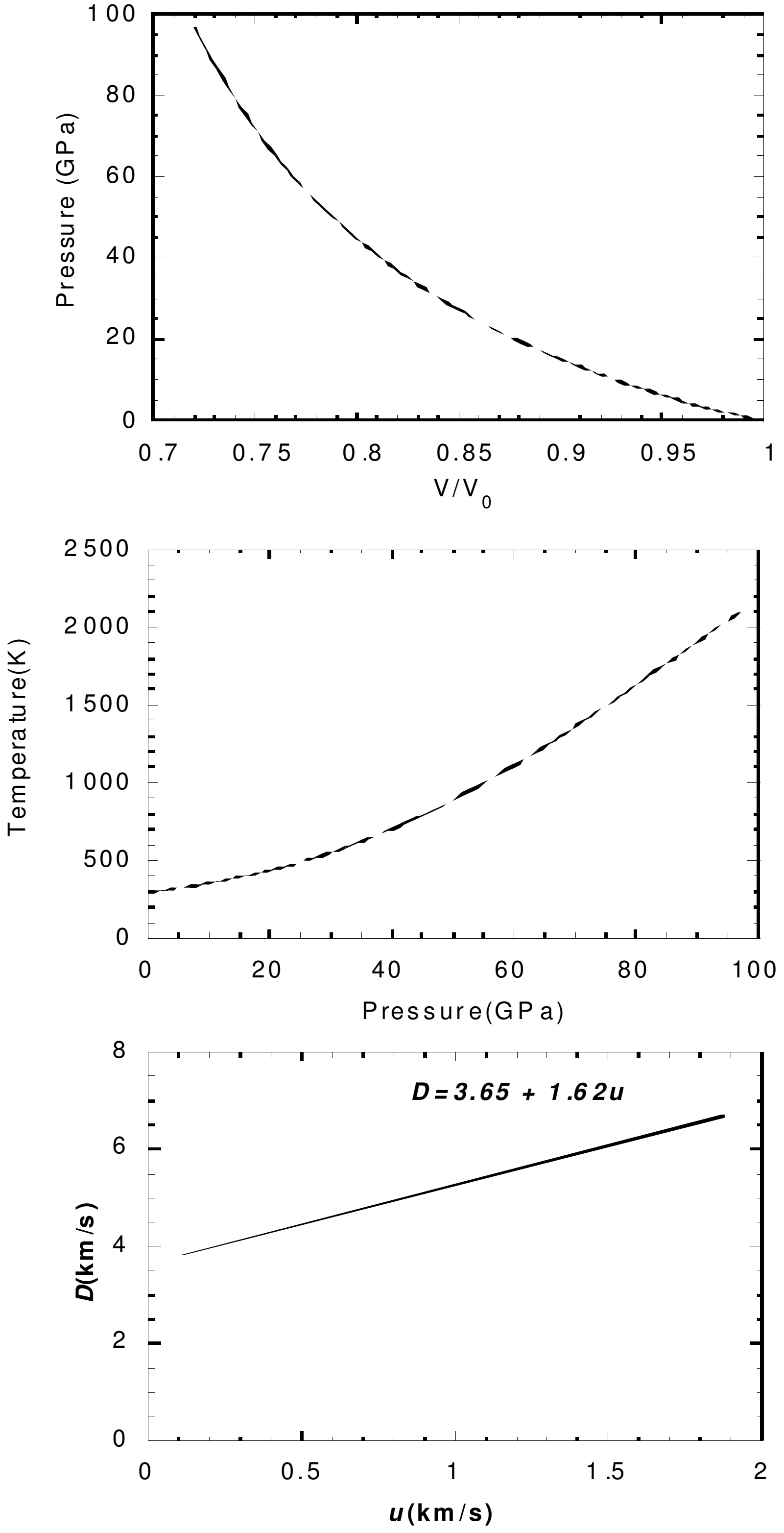

Fig. 2.3 Theoretically determined Hugoniot of CdO in B1 phase.

Table 2.1: Comparison of theoretical and experimental values of equation of state parameters of B1 and B2 phases of CdO at zero pressure.

Properties at Equilibrium Volume	Present Theoretical Work	Theoretical (Other sources)	Experimental
B1 Phase:			
V_0 (Å^3/formula unit)	26.90, 27.59(300K)	27.15[6], 27.28[8], 27.20[9], 26.96[10] 27.59[12]	25.88[7] 25.89[34] 26.05[35]
B_0 (GPa)	129, 111(300K)	130[6], 125[8], 118[9], 133.8[10], 125.5[12]	147[7] 148[34] 129[35]
B_0'	4.59, 4.94(300K)	4.13[6], 4.91[8], 5.23[9], 4.79[10], 4.90[12]	4.2[7], 4[34] 4.71[35]
B2 Phase:			
V_0 (Å^3/atom)	24.87	25.41[6], 25.65[8], 24.82[9], 25.10[10], 25.65[12]	25.3[35]
B_0 (GPa)	134	114[6], 128[8], 141[9], 134.2[10], 128.1[12]	169[7] 128[35]
B_0'	4.67	4.66[6], 4.92[8], 5.16[9] , 4.93 [10], 4.97 [12]	4.66[7] 4.98[35]

Table 2.2: Thermodynamic properties of CdO for B1 phase at zero pressure.

Properties at Equilibrium Volume	Present Theoretical Work	Theoretical (Other sources)	Experimental
$\alpha(10^{-5}/K)$	4.445	--	4.2[36], 3.99[37]
C_v (10^{-23}J/K/f. unit)	7.564	7.987[38]	7.195[36],
γ	1.79	--	--

Table 2.3: Elastic Constants of CdO for B1 and B2 phases at zero pressure.

Properties at Equilibrium Volume	Present Theoretical Work	Theoretical (Other sources)	Experimental
B1 Phase:			
C_{11}(GPa)	190.3	183.99 [8], 190.9[10] 184.48[12]	--
C_{12}(GPa)	98.33	96.01[8], 101.94[10] , 96.05[12]	--
C_{44} (GPa)	46.13	45.78[8] , 48.06[10] 45.77[12]	--
θ_D (K)	273	336[8] , 341[10] 413[12] , 260[38]	255±6[40]
B2 Phase:			
C_{11}(GPa)	303.09	290.21[8] , 285.12[12]	--
C_{12}(GPa)	48.85	47.53[8], 49.64[12]	--
C_{44} (GPa)	-25.99	-25.03[8] ,-25.01[12]	--

2.3.2 Elastic Properties and activation barrier

Table 2.3 compares elastic constants determined theoretically in present work for B1 and B2 phases at zero pressure with those reported in other theoretical studies [8, 10, 12]. The $C' = (C_{11}-C_{12})/2$ and C_{44} modulus at zero pressure calculated in the present work are almost equal suggesting that CdO in B1 phase is elastically isotropic [$A= 2C_{44}/(C_{11}-C_{12})$] at zero pressure. The Debye temperature (θ_D) calculated for B1 phase from elastic constants turns out to be 273 K as compared to the experimental value of 255±6 K [40] and theoretical value of 260 K [38] derived from calculation using CASTEP code. The value of Debye temperature calculated in present work is more close to the experimental value as compared to those reported by other theoretical studies [8, 10, 12]. Further, the elastic stability of B1 phase was analyzed by calculating the elastic moduli as a function of hydrostatic compression and examining the stability conditions throughout the compression path. Fig.2.4 shows the three independent elastic moduli of CdO in B1 phase at various pressures. No comparison with experiments could be done due to unavailability of experimental data. As can be seen from the figure, the bulk modulus and the tetragonal shear modulus C′ increase monotonically with increasing pressure, however, the shear modulus C_{44} displays opposite behavior *i.e.* it decreases monotonically with increasing pressure and vanishes at ~126 GPa, in close agreement with theoretical findings of Peng *et al.*[8] and Feng *et al.*[10]. It may be noted that though C_{44} in B1 phase decreases monotonically with compression, it does not soften completely at the B1 to B2 transition pressure. Also, the monotonic increase of C′ and decrease of C_{44} with increasing pressure indicates that the initially elastically isotropic CdO becomes anisotropic under pressure and this anisotropy continues to increases with increasing compression. Fig.2.5, displays these quantities for B2 phase of CdO. The figure clearly shows that the C_{44} modulus which is negative (-25.99 GPa) agrees with other theoretical values [8, 12] at zero pressure, increases monotonically with increasing pressure and acquires positive values beyond 38 GPa. This suggests that the B2 phase will become elastically stable above 38 GPa *i.e.* much before the B1 → B2 transition pressure.

Additionally, the activation barrier between the B1 and B2 structures has been determined at various compressions. For this purpose, the total energy calculations at a given compression have been carried out on a rhombohedral cell as a function of rhombohedral angel (α). It may be noted that the B1 and B2 structures are special cases of rhombohedral cell *i.e.* for $\alpha = 60°$ the rhombohedral cell reduces to B1 structure and for $\alpha = 90°$ it corresponds to B2 structure. Fig. 2.6 shows the total energy of rhombohedral cell as a function of angle α relative to that for the $\alpha = 60$. The figure correctly depicts that at ambient pressure ($V/V_0 = 1.0$) the B1 phase is stable structure, whereas, the B2 structure is unstable. Upon compression at $V/V_0 \sim 0.79$ the B2 emerges as a metastable phase and appears as a stable structure at $V/V_0 \sim 0.71$ with corresponding pressure 87 GPa. At this pressure both B1 and B2 have same energy and are separated by a barrier of height ~ 2 mRy/formula unit. Above this pressure, the B2 phase displays the global minima and B1 phase becomes unstable.

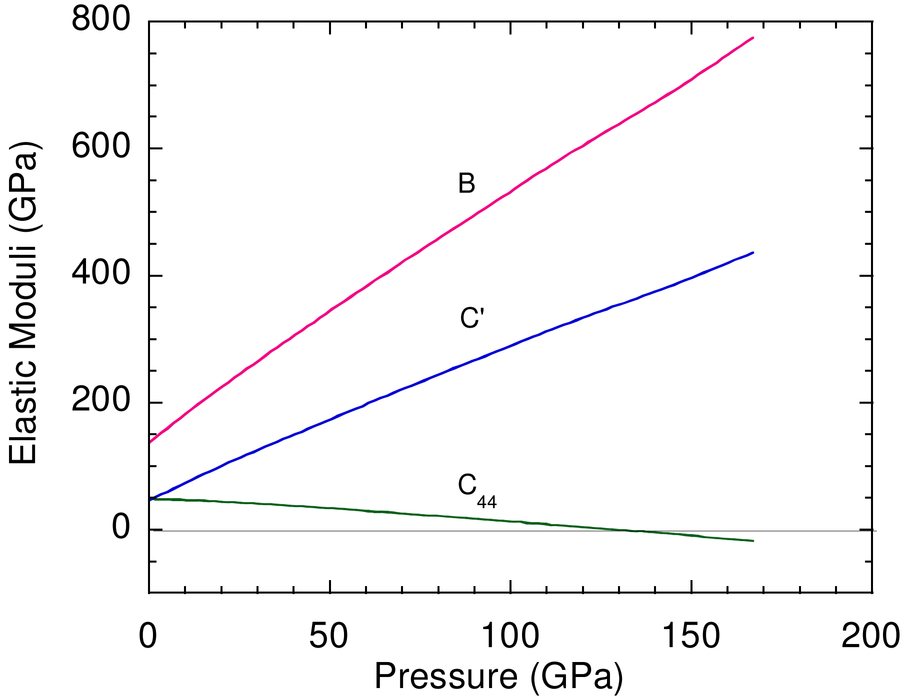

Fig. 2.4 Theoretically calculated elastic moduli of CdO single crystal in B1 phase as a function of pressure. Here B is bulk modulus, $C' = (C_{11}-C_{12})/2$ and C_{44} are shear moduli.

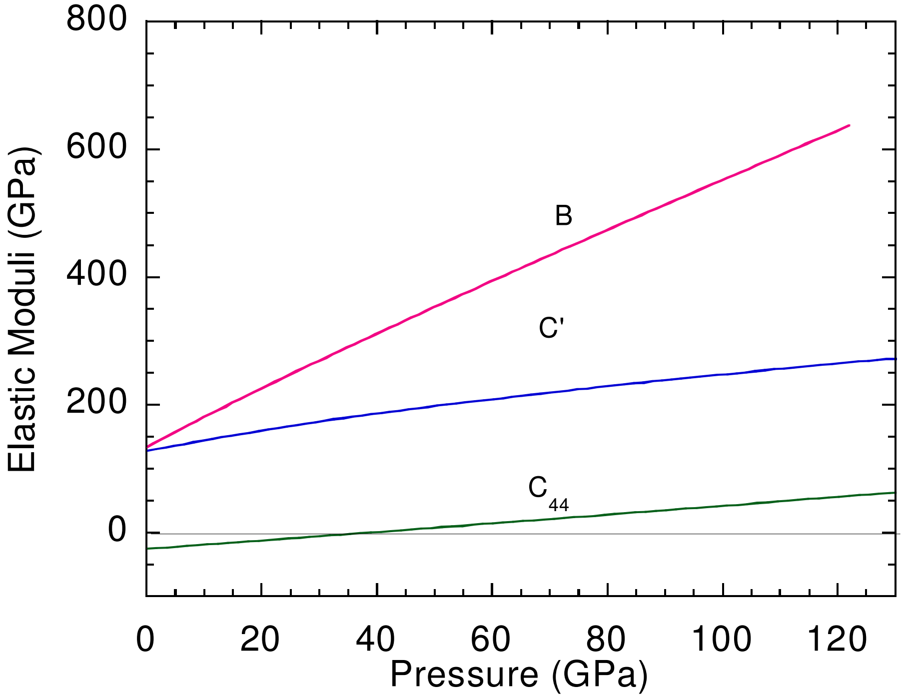

Fig. 2.5 Pressure dependent elastic moduli of CdO in B2 phase.

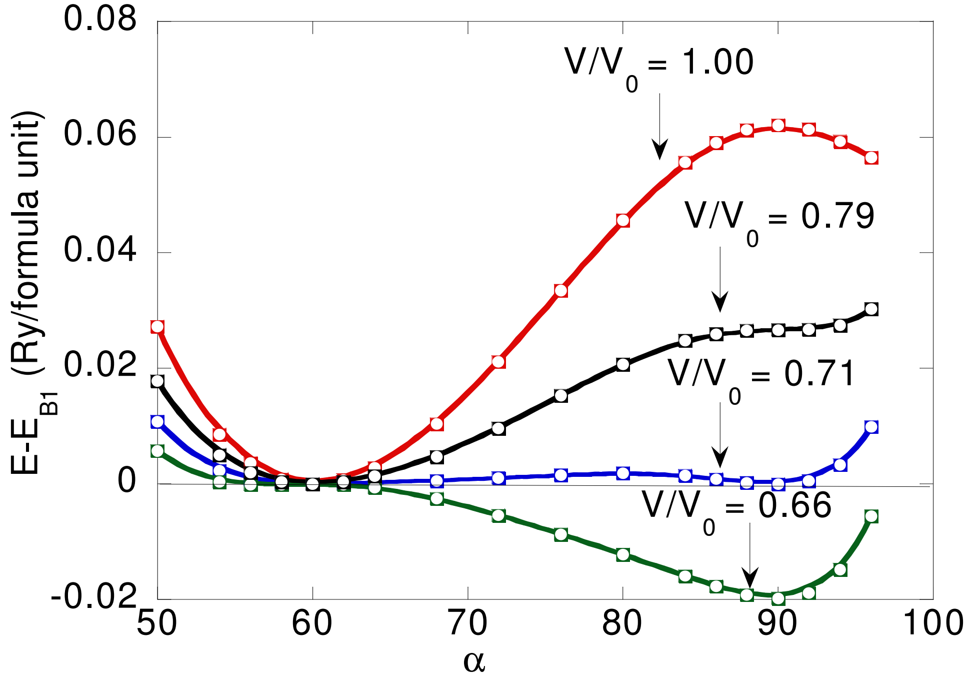

Fig. 2.6 Total energy of rhombohedral cell relative to that of B1 phase as a function of α at various compressions.

2.3.3 Dynamic stability analysis

The phonon spectrum of a solid is useful to get insight into lattice dynamical stability of the material which in turn is related to structural stability of the material. Additionally, it is useful for evaluating various thermodynamic quantities such as specific heat, thermal expansion coefficients etc. So the calculations have been extended to examine the dynamic stability of B1 and B2 phases. For this purpose the phonon dispersion relations and vibrational density of states for B1 and B2 phases at various pressures have been calculated. Fig. 2.7 displays phonon spectrum and corresponding phonon density of states for B1 phase at zero pressure, 87 GPa (transition pressure), 118 GPa and 140 GPa. As expected, the projected phonon density of states plotted along with the total density of states in this figure, show that the high frequency vibrations are dominated by the O atom due to its relatively lower atomic mass whereas the low frequency vibrations are dominated by Cd atom due to its higher mass. Additionally, the

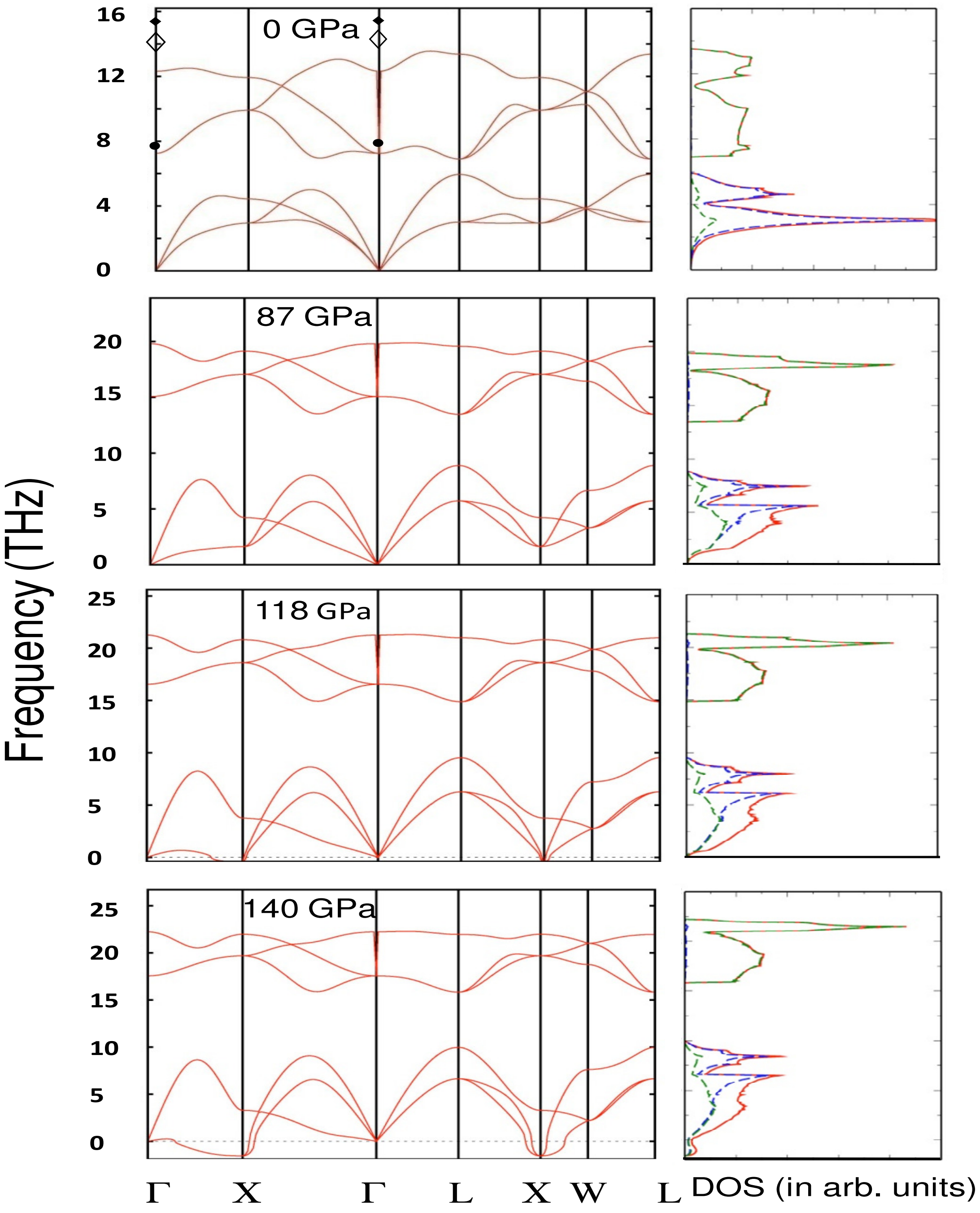

Fig. 2.7 Theoretically calculated phonon spectra and phonon density of states of CdO in B1 phase at transition pressure.

theoretical transverse optic (TO) phonon frequency of 7.76 THz at zone centre (Γ point) shows an excellent agreement with the experimental values of 7.85 THz and 7.95 THz measured in two separate Raman experiments.[41,42] However, that for longitudinal optic (LO) mode is calculated to be 12.6 THz as compared to the experimental values of 15.83 THz and 14.1 THz [29, 30]. The reason for this underestimation in theory might be due to the insufficient splitting of TO and LO at zone center resulted by the overestimation of the equilibrium lattice constant. As shown in Fig.2.7, the TO, LO and LA phonon branches along Γ- X and L - X- W directions become stiffer with increasing compression, however, the TA phonon branches along the same directions soften monotonically with increasing pressure, indicating a negative mode Grüneisen parameter $\gamma_j(q)= - \partial \ln \upsilon_j(q) / \partial \ln V$ for a particular mode j (here q is wave vector, υ is frequency, and V is volume). The continuous softening of TA branch with increasing pressure results in the imaginary phonon frequencies along Γ-X and L-X-W directions at pressure around 118 GPa, making the B1 phase dynamically unstable near this pressure. This also suggests that the B1 phase remains dynamically stable even at B1 to B2 transition pressure. In order to find the exact pressure at which the B1 phase becomes dynamically unstable, the square of frequency of transverse acoustic phonon at X point with pressure has been plotted in Fig. 2.8. Also, plotted is the C_{44} modulus in the same figure. It is clear from the figure that the onset of dynamic instability in B1 phase occurs at ~ 116 GPa, however, the pressure at which this phase becomes elastically unstable due to complete softening of C_{44} is 126 GPa. Though the dynamic instability is close in pressure with elastic instability (the difference between the pressures for the two instabilities is ~ 10 GPa), the phonon instability occurring at points away from the center of the BZ and before the elastic instability is indicative of phonon driven B1 → B2 phase transition under pressure. The situation is somewhat similar to that found in CaO by Zhang and Kuo [43], where authors report the B1 to B2 transition to occur at ~ 67 GPa and TA phonon at X point soften completely around 158 GPa as compared to the C_{44} modulus which vanishes around 180 GPa. Based on these results the authors conclude that the transition is driven by phonon instability. Further, a near perfect linear relation between υ^2 and P (Fig. 2.8) further supports this argument, consistent with the Landau theory of pressure-induced soft mode phase transitions [44].

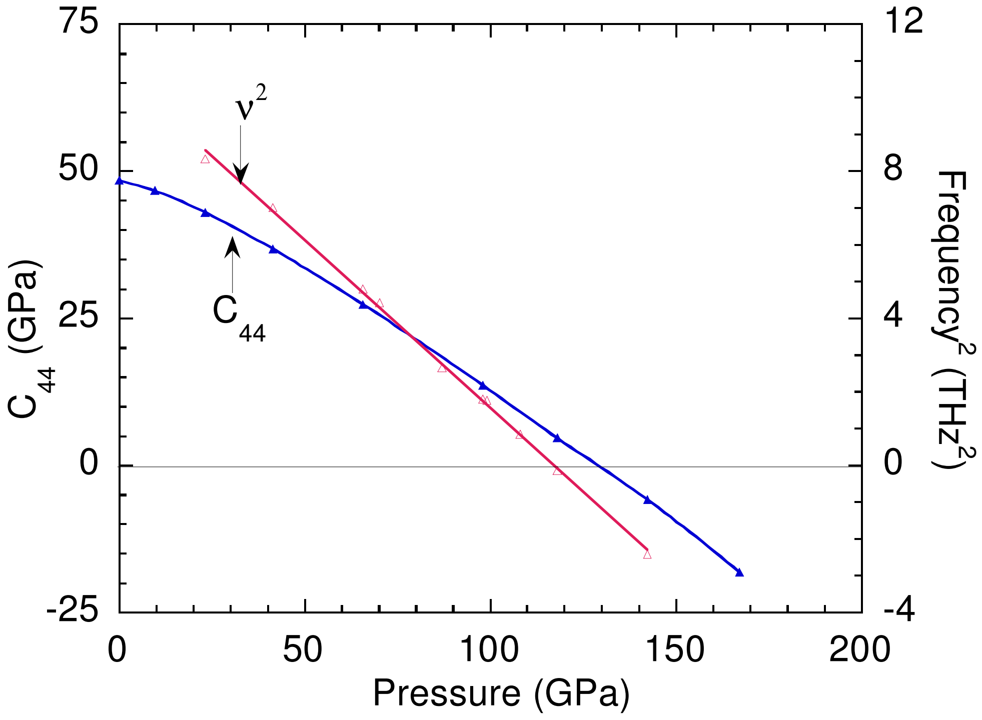

Fig.2.8 The square of the acoustic phonon frequency at X point in the Brilouin zone of B1 phase as function of pressure. Also, plotted is the pressure dependent shear elastic modulus C_{44}

The phonon spectra and corresponding density of phonon states at zero pressure and transition pressure (87 GPa) for B2 structure is displayed in Fig.2.9. Unlike that for B1 phase, in B2 phase at zero pressure itself, the acoustic phonon frequencies in several directions of Brillouin zone are imaginary, indicating dynamic instability of this phase at ambient conditions. Upon compression these phonon frequencies shift towards positive direction and become real at transition point confirming the existence of B2 phase at high pressure which is consistent with the experimental results [7]. To determine the exact pressure for onset of dynamical stability of B2 phase, we have plotted the frequency of TA phonon at M point in Fig. 2.10. It is clear from the figure that the B2 phase emerges as dynamically stable structure at a pressure of ~ 55 GPa *i.e.* much before it gets stabilized energetically.

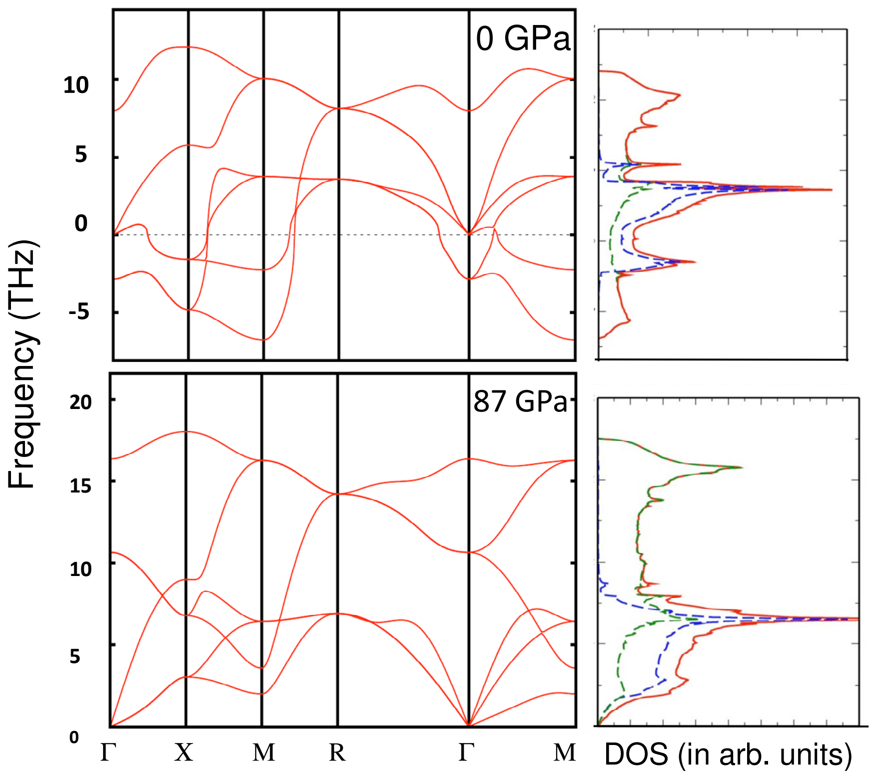

Fig.2.9 Theoretically calculated phonon spectra and phonon density of states of CdO in B2 phase at zero pressure and B1 → B2 transition pressure.

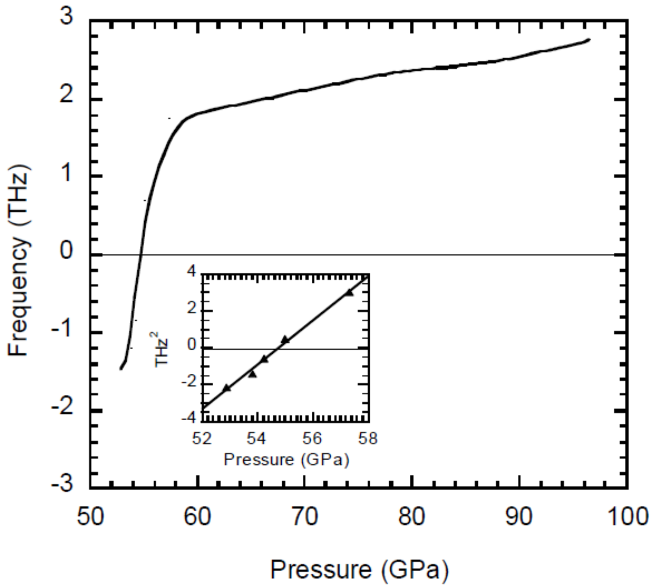

Fig. 2.10 Pressure dependence of phonon frequency of lowest acoustic branch of CdO at M point in B2 phase. The inset displays the square of this frequency as a function of pressure.

2.4 Summary

Ab-initio total energy calculations have been performed on the phases B1 and B2 of CdO as a function of hydrostatic compression to examine the structural stability. Apart from this, the calculations have been carried out to determine the equation of state and pressure dependent elastic constants and lattice dynamic stability of CdO. Various thermophysical parameters have been determined from theoretical equation of state and elastic constants. The structural stability analysis suggests that B1 phase of CdO will transform to B2 phase at a pressure of ~ 87 GPa at 0K, which reduces to 86 GPa at 300 K. The 300K isotherm determined theoretically after adding the thermal lattice energies to the cold energies agrees closely with experimental P-V data. The equation of state derived from calculations within GGA agrees better with experimental data than that obtained from the LDA approximations. The calculated equilibrium lattice parameter, bulk modulus and pressure derivative of bulk modulus at zero pressure derived from theoretical equation of state are in good agreement with the experimental findings. Various physical quantities such as elastic moduli at ambient pressure, the Debye temperature, the Grüneisen parameter, bulk sound speed, the Hugoniot parameter '*s*' compare well with the available experimental data.

The ambient pressure elastic constants C_{11}, C_{12} and C_{44} of 168.29 GPa, 76.02 GPa and 46.13 GPa for the B1 phase of CdO determined in the present work are in reasonable agreement with theoretical values reported in different works [8, 10, 12]. With increasing pressure, the C_{11} and C_{12} increase monotonically, whereas, the C_{44} decreases and becomes negative around ~126 GPa. The elastic anisotropy parameter ($A=2C_{44}/(C_{11}-C_{12})$) at zero pressure is found to be ~ 1.00. Further, this parameter has been found to increase monotonically with increasing pressure. From the lattice dynamic calculation it is confirmed that B1 structure is dynamically stable and its zone center phonon frequency agrees with experimental findings, whereas for B2 phase it shows imaginary frequency in all directions of reciprocal space. Under compressions TA phonon modes at the X point for B1 show softening and seize to zero around ~ 116 GPa. For B2 phase however, the phonon frequency at the M point accuires positive around ~55GPa. From the above analysis of elastic and dynamic stability suggests that pressure induced B1 →B2 transition could be driven by phonon softening.

References

1. S. Kose, F. Atay, V. Bilgin and I. Akyuz, *Int. J. Green,Energy* **1**, 353(2004).
2. R. Kondo, H. Okimura and Y. Sakai, *Jpn. J. Appl.Phys.* **10**, 1547 (1971).
3. F. A. Benko and F. P. Koffyberg, *Solid State Commun.* **57,** 901 (1986).
4. A., Shiori Jpn. Pat., No. 7, 909 (1997).
5. D. R. Lide (Editor), CRC Handbook of Chemistry and Physics, 77th edition (CRC Press, Boca Raton) 1996-1997
6. Roberto J. Guerrero-Moreno and Noboru Takeuchi, *Phys. Rev. B* **66**, 2052051 (2002).
7. Haozhe Liu, Ho-kwang Mao, Maddury Somayazulu, Yang Ding, Yue Meng, and Daniel Häusermann, *Phys. Rev. B* **70**, 0941141 (2004).
8. Feng Penga, Qiang Liu, Hongzhi Fu and Xiangdong Yang, *Solid State Comm.* **148**, 6 (2008).
9. M. Durandurdu, *EPL* **84**, 66003 (2008).
10. Wenxia Feng, Shouxin Cui, Haiquan Hu, Guiqing Zhang, Zengtao Lv and Zizheng Gong, *Phys. Status Solidi B* **247**, 2202 (2010).
11. W. Martienssen and H. Warlimont (eds.), Springer Handbook of Condensed Matter and Materials Data (Springer,Berlin, 2005).
12. Gen-Quan Li, Cheng Lu, Xing-QiangYang, Shao-Wu Xiao, Ai-HuaWang, LiWang and Xiao-Ming Tan, *High Press. Res.* **30**, 679 (2010).
13. S. Baroni, P. Giannozzi and A. Testa, *Phys. Rev. Lett*. **58,** 1861 (1987).
14. S. Baroni, A. Corso Dal, S. de Gironcoli, P. Giannozzi, C. Cavazzoni, G. Ballabio, S. Scandolo, G. Chiarotti, P. Focher, A. Pasquarello, K. Laasonen, A. Trave, R. Car, N. Marzari and A. Kokalj, http://www.pwscf.org
15. J.P. Perdew and Y. Wang, *Phys. Rev. B* **45**, 13244 (1992).
16. N. Troullier and J.L. Martins, *Phys. Rev. B* **43**, 1991(1993).
17. H J Monkhorst and J D Pack, *Phys. Rev.* ***B*** **13**, 5188 (1976).
18. P. Giannozzi, S. de Gironcoli, P. Pavone and S. Baroni, *Phys. Rev.* ***B*** **43,** 7231(1991)
19. S. Baroni, P. Giannozzi, and E. Isaev, *Rev. Mineral. Geochem*. **71**, 39 (2010)
20. B. D. Sahoo, K. D. Joshi, and Satish C. Gupta, *J. Appl. Phys*. **115**, 123502 (2014)
21. B. K. Godwal and R. Jeanloz, *Phys. Rev. B* **40**, 7501 (1989).
22. S. C. Gupta, K. D. Joshi, S. Banerjee, *Metall. Materials Trans. A* **39**, 1593 (2008).

23. G. Valentin, *ArXiv: Cond-Matt/*99114072-v2 [Cond-mat.mtrl-sci], (1999).
24. C. Kittel, *Introduction to Solid State Physics* (John Wiley & Sons, NewYork 1996).
25. W. Voigt, *Lehrbuch der Kristallphysik* (Taubner, Leipzig, 1928).
26. A. Reuss, Z. Angew. *Math. Mech.* **9**, 49 (1929).
27. W. Band and G. E. Duvall, *Am. J. Phys.* **29**, 780 (1961).
28. 28.G. E. Duvall and G. R. Fowles, *Shock Waves in High Pressure Physics and Chemistry*, vol 2, (ed R. S. Bradley, New York: Academic) 209 (1963).
29. F. Birch, *J. Geophys. Res.* **83**, 1257 (1978).
30. K. D. Joshi, S. C. Gupta and S. Banerjee, *J. Phys. Cond. Matter* **21**, 415402 (2009).
31. J. F. Nye, *Physical Properties of Crystals*, Oxford University Press, London (1957).
32. R. E. Cohen, L. Sixtrude and E. Wasserman, *Phys. Rev B* **56**, 8575 (1997).
33. S. Baroni et al.,Quantum ESPRESSO package, 2005, www.pwscf.org/
34. J. Zhang, *Phys. Chem. Minerals* **26**, 644 (1999).
35. H.Z. Liu, J.S. Tse, and H.K. Mao, *J. Appl. Phys.* **100**, 093509 (2006).
36. W. Martienssen and H. Warlimont, Hand Book of Condensed matter and Materials data, Springer, Germany 2005.
37. H.P. Singh and B. Dayal, Solid State Commun. **7**, 725 (1969).
38. Liping Yao, Feng Peng, Hongzhi Fu and Xinlu Cheng, *Phys. Stat. Sol.(b)* **245**, 1113 (2008)
39. Fen Luo, Ling Cang Cai, Xiang Rong Chen, Fu Qian Jing and Dario Alfe, *J. Appl. Phys.* **111**, 053503 (2012)
40. O. Madelung, U. Rossler and M. Schulz (eds.), Cadmium Oxide (CdO) Debye temperature, heat capacity, melting point, density, in Landolt-Bornstein Group III, Vol. 41B:II-VI and I-VII Compounds, Semimagnetic Compounds (Springer-Verlag, Berlin, 1999).
41. Z.V. Popovic, G. Stanisic, D. Stojakovic and R. Rostic, *Phys. Stat. Sol.(b)* **165**, K109 (1991).
42. R. Cuscó, J. Ibáñez, N. Domenech-Amador, L. Artús, J. Zúñiga-Pérez, and V. Muñoz-Sanjosé, *J. Appl. Phys*. **107**, 063519(2010).
43. Jingyun Zhang and Jer-Iai Kuo, *J. Phys. Cond. Matter*, **21**, 015402 (2009).
44. W.V.D. Osten, B. Dorner, *Solid State Commun*. **16**, 431 (1975).

Chapter 3

High Pressure Phase Transition in Transition Metal Carbides ScC, YC and TaC

3.1 Introduction

The extreme hardness, good strength even at elevated temperatures and high melting point exhibited by the carbides of transition metals make these materials important scientifically as well as technologically [1-6]. For instance, the melting temperature (about 4200 ^{0}C) of TaC is the highest among known materials. Besides this, transition metal carbides are chemically very stable and have high corrosion resistance. Due to these characteristics, they find wide applications in various industrial applications such as cutting tools, in information storage technology for coating of magnetic sheets, high power energy industry and optoelectronics. The academic interest on these materials comes due to the existence of mixed bonding (both metallic and covalent) which is believed to be responsible for high hardness and high melting points of these materials [7-9].The carbides of group IIIB elements (Sc, Y and La) and group VB are among some of the transition metal carbides which have been of current interest [10-12]. In present chapter the high pressure theoretical investigations carried out in three transition metal carbides ScC, YC and TaC will be presented.

The crystal structure adopted by these three carbides at ambient conditions is NaCl type (B1) structure. The lattice dynamic simulations of Isaev *et al.* [11] show that at ambient conditions the B1 phase in ScC and YC is dynamically stable. Further, through the static lattice calculations employing full potential linearized augmented plane wave (FP-LAPW) method, Soni *et al* [12] have found that at ambient conditions, this phase is stable elastically also. These theoretical findings in ScC and YC are in line with the experimentally observed B1 phase at ambient conditions. Recently, Soni et al. [12] through electronic band structure calculations on ScC and YC have predicted that the B1 phase of these carbides will transform to CsCl type (B2 phase) structure at hydrostatic pressure of ~ 127 GPa and 80 GPa, respectively. But these predictions were lacking the support of lattice dynamic stability test as these authors have not performed lattice dynamic calculations.

In TaC, various experimental as well as theoretical investigations pertaining to determination of elastic properties, understanding the lattice dynamics and the equation of state of this material have been reported in past [13-19]. For instance, Jun and Shaffer [13] using sonic resonance technique have measured the elastic constants of TaC in B1 phase as a function of temperature up to 1500K. Subsequent to this, Dodd *et al.* [14] have performed the measurements of electrical resistivity and elastic properties as a function of temperature up to 1300 K using four point probe dc technique and ultrasonic technique, respectively. Additionally, these authors have measured the pressure dependence of longitudinal and shear stiffness up to maximum pressure of ~ 20GPa and reported that this material exhibits strong atomic bonding and offers high resistance to shear deformations. In yet another experimental study, Torre *et al.* [15] have determined the elastic constants of TaC by performing ultrasonic measurements on a (100) cut single crystal. Further, these authors have calculated the elastic constants through the model calculations also and reported that the theoretical values agree with the experimental data within ~ 8%. Apart from studies related to elastic properties, the phonon spectra measurements at room temperature and at the low temperature of ~ 4.2 K have also been reported in past [16, 17]. Smith and Glaser, employing inelastic neutron scattering, have measured the phonon dispersion curves of TaC along [001] and [110] directions of Brillouin zone in B1 phase. Subsequent to this Smith [14] has experimentally demonstrated the anomaly in transverse acoustic (TA) branch in the [110] direction, supporting the prediction by Weber *et al.* [18]. Apart from these elastic and lattice dynamic studies at room pressure, the experimental work to understand high pressure behavior and determine the equation of state of TaC has also been reported by Liermann *et al.* [19]. In this work authors have performed high pressure angle dispersive x-ray diffraction measurements on TaC sample compressed statically in diamond anvil cell (DAC) and shown that the B1 phase remains stable up to ~ 76 GPa (the maximum pressure achieved in the experiment).

In theoretical front most of the studies are on the elastic and lattice dynamic stabilities of B1 phase of TaC at ambient pressure [20-23]. In first principle plane wave pseudopotential method based calculations Peng *et al.* [24] have reported the equation of state and elastic properties of

B1 phase of TaC up to ~ 60 GPa. Additionally, these authors have investigated pressure – temperature behavior of bulk modulus and thermal expansion up to 60 GPa and ~ 1500K. In recent past, Srivastava *et al.* [25] on the basis of first principles static lattice calculations performed using pseudopotential method have predicted the B1 to B2 structural phase transition in TaC at a pressure of ~ 640 GPa. Again in this material too, the lattice dynamic stability under pressure remained to be investigated.

This chapter of the thesis presents a detailed theoretical investigation carried out on ScC, YC and TaC under high pressure. The high pressure work includes the examination of structural satiability, elastic stability and dynamic stability of ScC, YC and TaC under pressure. For this purpose the enthalpies of plausible structures has been calculated as a function of pressure and compared. The plausible structures for ScC and YC have been chosen to be B1, Pmmn and B2 phases. For TaC however, the B1, B2, zincblende type (B3), wurtzite type (B4) and NiAs type (B8) structures have been considered as candidate structures. In TaC, the Pmmn structure reduces to B1 phase at lower pressures and to B2 phase at pressures ≥ the B1 to B2 transition pressure. The 0 K isotherms have been determined from the theoretically calculated total energies and converted to 300 K isotherm after adding finite temperature contributions. The elastic stability has been examined by evaluating the single crystal elastic constants as a function of pressure using energy strain method. The lattice dynamic stability has been analyzed by calculating the phonon spectra at different pressures.

3.2 Methodology Employed for Present Calculations

3.2.1 Calculation details for structural and lattice dynamic stability analysis

To analyze the structural stability of ScC and YC, theoretical investigations have been performed on three phases namely B1, Pmmn and B2, whereas for TaC the B1, B2, B3, B4 and B8 structures have been examined. The detailed analysis of structural stability included both the static lattice calculations and lattice dynamic calculations. All the calculations have been performed employing plane wave pseudopotential method within the framework of Density Functional Theory (DFT) [26] implemented in Quantum ESPRESSO package [27]. The total energy of B1, Pmmn and B2 phases has been calculated as a function of hydrostatic compression within the generalized gradient approximation (GGA) [28] for the exchange correlation potential. The ultrasoft pseudopotential having valence configurations of $3s^2 3p^6 4s^2 3d^1$ for Sc, $4s^2 4p^6 4d^1 5s^2$ for Y, $5s^2 5p^6 5d^3 6s^2$ for Ta and $2s^2 2p^2$ for C has been used. In Sc, the cut off radius chosen for generating the pseudopotential is 1.8 Bohr for 3s and 4s, 2.2 Bohr for 3p and 2.4 for 3d orbitals, whereas that in Y is taken as 1.8 Bohr for 4s and 5s, 2.0 Bohr for 4p, and 2.2 for 4d orbitals. In Ta, the cut off radius chosen for generating the pseudopotential is 2.4 Bohr for 5p and, 2.2 Bohr for 5s ,6s and 5d orbitals. For C the cut off radius is taken to be 1.1 Bohr for both 2s and 2p orbitals. For Sc, Y and Ta the non-linear core correction to the exchange-correlation energy functional has also been added. For GGA, the PW91 (ref 28) potential has been used for both the atoms. Electronic wave functions have been expanded in a plane wave basis set (PWs) with energy cut off of 60 Ry and charge density is represented in PWs with energy cut off of 600 Ry. In ScC and Y, the energy convergence of 10^{-6} Ry has been met by using the 12x12x12, 9x6x9 and 16x16x16 Monkhorst–Pack (MP)[29] grid of k-points in the full Brillouin zone (BZ) of B1, Pmmn and B2 structures. Whereas in TaC this criteria is met by using the 12x12x12, 16x16x16, 11x11x11, 9x9x6 and 11x11x9 Monkhorst–Pack (MP) [29] grid of k-points in the full Brillouin zone (BZ) for B1,B2,B3,B4 and B8 structures, respectively.

The dynamic stability of different phases in ScC, YC and TaC has been analyzed from the phonon spectra determined using self consistent density functional perturbation theory within linear response approximation [30]. For phonon dispersion calculations a 4×4×4, 3×2×3 and 4×4×4 q mesh in the first BZ of B1, Pmmn and B2 structure has been used for ScC and YC. Similarly, for TaC, the 4×4×4 q mesh have been used for both the B1 and B2 structures. In TaC, only B1 and B2 structures have been analyzed for lattice dynamic stability as static lattice calculations predicted only B1 to B2 transition under pressure.

3.2.2 Details of structures used for analysis

In ScC and YC, to analyze the structural stability under hydrostatic compression, the total energy for B1, Pmmn and B2 phases at 0 K have been computed as a function of volume. In the Pmmn structure which is a primitive orthorhombic cell, the atomic species Sc or Y is located at

2a (0 0 z_1, ½ ½ -z_1) and C is located at 2b (0 ½ z_2, ½ 0 –z_2) (international table of Crystallography, Vol. 2). It may be noted that the Pmmn structure is as a distorted B1 phase (Fig.3.1) which for *b/a* =√2, *c/a* =1 and z_1=z_2=1/4 becomes identical to B1 phase. In other words, the B1 and Pmmn structure are related by group-subgroup relation. Further, if axial ratios and internal parameters of Pmmn cell are changed such that *b/a* =1, z_2=0.0, it represents a primitive tetragonal structure with space group P_4/nmm and if *b/a* =√2, *c/a* =1, z_1=0.5, z_2=0 Pmmn structure reduces to B2 structure. In the calculations, both the axial ratios (*c/a* and *b/a*) and internal parameters z_1 and z_2 of Pmmn structure have been optimized at all volumes. The optimum *c/a, b/a,* z_1 and z_2 at a given volume is the one for which the total energy is minimum.

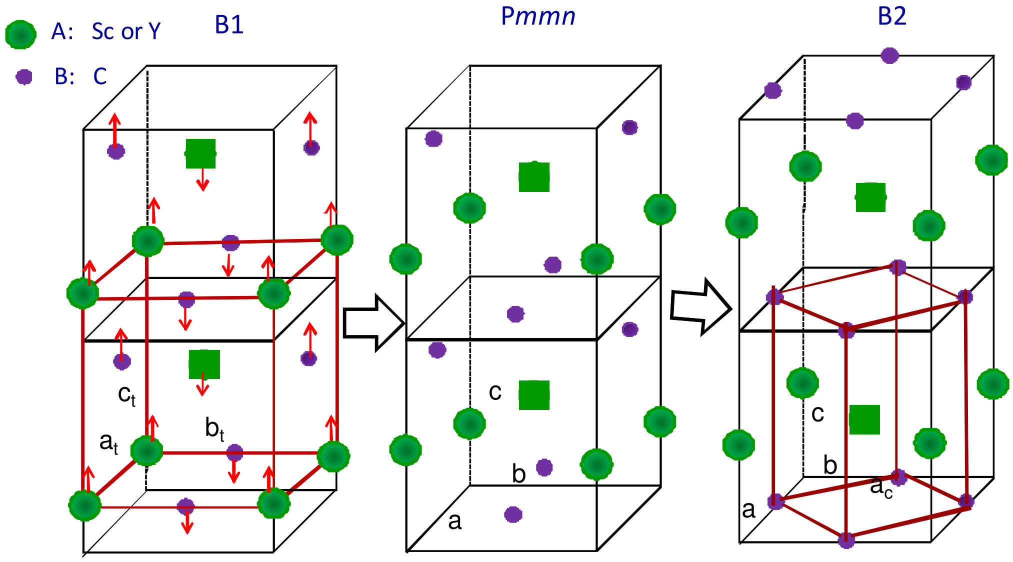

Fig. 3.1 The relation between the Pmmn and B1 structure has been displayed. The Pmmn structure (1×1×2 supercell shown in left figure) has Sc(Y) atom located at 2a (0 0 z_1, ½ ½ -z_1) and C atom located at 2b (0 ½ z_2, ½ 0 –z_2). The big and small filled circles correspond to Sc (Y) and C atom, respectively. The atoms labeled as 1, 2 and 3 represent the atoms lying on front, middle and back planes normal to b axis of Pmmn cell. The arrows display the directions of atomic movement required to convert the Pmmn cell into B1 structure. The right side figure shows the B1 structure (the cell bounded by thick lines) represented as bct cell with the *b/a* and *c/a* ratio is √2 and 1, and z_1 = z_2 = ¼.

For TaC the calculations have been done in five structures where B1, B2 and B3 cubic phases and B4, B8 are hexagonal phases.

Using the total energy calculated at various volumes, the 0 K isotherms has been derived and enthalpies have been calculated for each phase. The structural stability as a function of hydrostatic compression has then been then analyzed by comparing the total enthalpies (H) of different phases as a function of pressure. The 0 K isotherms have been finally converted to 300 K isotherm by adding the thermal corrections. Further the zero pressure bulk modulus (B_0) and its pressure derivative at zero pressure (B_0') are obtained by fitting the isotherm so obtained to the third order Birch-Murnaghan equation of state as described in section 2.2.1 of chapter 2.

Further, the elastic constants of different phases phase in ScC, YC and TaC have been determined as a function of hydrostatic compression following the procedure described in the chapter 2 in section 2.1.

3.3 Results and Discussions

3.3.1 Structural stability and equation of state of ScC and YC

In order to analyze the structural stability of ScC and YC the enthalpies of B1, Pmmn and B2 structures have been calculated and compared as a function of pressure. In case of Pmmn phase, at each compression, optimization of both the axial ratios (*c/a* and *b/a)* and the z_1, z_2 have been performed and total energy of the optimized Pmmn phase as a function of volume is determined. This energy is then used to generate P-V data for Pmmn phase, which finally is utilized to determine the enthalpy of this phase at various pressures.

In Fig.3.2, the optimized axial ratios and z_1 and z_2 parameters of Pmmn structure of ScC and YC is plotted as a function of pressure. As is obvious from the figure, the optimum value of *c/a* and *b/a* ratio at zero pressure are 1.0 and √2, respectively and remain unchanged up to 75 GPa for ScC and up to ≤ 25 GPa for YC. Upon further compression, these ratios first decrease rapidly and achieve a value of ~ 0.67 and ~ 0.99, respectively at ~ 100 GPa for ScC and ~ 0.73

and ~ 0.98, respectively for YC at ~ 70 GPa. Thereafter, for both the materials these ratios show very slow variation with pressure and tend towards the values corresponding to that of primitive tetragonal (P4/nmm) structure. The optimized values of z_1 and z_2 are found to be identical and fixed at ¼ up to the pressure of 75 GPa for ScC and up to 25 GPa for YC. At still higher pressures, for both the material, these parameters start differing from each other and display opposite trend with increasing pressures *i.e.* z_1 increases whereas z_2 decreases with increasing pressure. Again up to ~ 100 GPa in ScC and up to ~ 70 GPa in YC, the z_1 and z_2 vary rapidly with increasing pressure and acquire the values of ~ 0.37 and ~ 0.01 for ScC and ~ 0.38 and ~ 0.005 for YC, at these pressures. Beyond these pressures, the values of z_1 and z_2 vary slowly with increasing pressure and tend towards those corresponding to that of P4/nmm structure. These findings suggest that (i) up to 75 GPa in ScC and up to 25 GPa in YC the B1 phase remains energetically lower than the Pmmn phase, (ii) above 75 GPa in ScC and above 25 GPa in YC the Pmmn structure becomes favourable over B1 phase and (iii) beyond 100 GPa in ScC and beyond 70 GPa in YC the optimized parameters of Pmmn structure vary slowly with increasing pressure and tend to approach values corresponding to that of a primitive tetragonal structure having space group symmetry P_4/nmm with location of Sc (Y) and C atoms to be 2c (0 ½ z, ½ 0 –z) and 2a (0 0 0, ½ ½ 0), respectively.

Further, in Fig.3.3, comparison of the enthalpies of Pmmn and B2 structures relative to B1 phase for ScC and YC have been done. As shown in figure, for ScC, the Pmmn structure emerges as a stable structure for pressures ≥ 80 GPa. In YC, however, B1 phase transforms to the Pmmn structure at ≥ 30 GPa. These values of transition pressures are little off from 75 GPa and 25 GPa (as shown in Fig.3.2 and discussed above) obtained for ScC and YC, respectively, from structural parameter optimization based on minimization of total energy. Results of our static lattice calculations rule out the direct B1 to B2 transition under pressure predicted by Soni *et al.* [25] in these compounds.

The Fig. 3.4 displays the theoretical isotherm for ScC and YC. No comparison could be made with experiments due to non availability of experimental data. It is clear from the figure that the transition is of first order in nature with volume discontinuity at the transition point determined

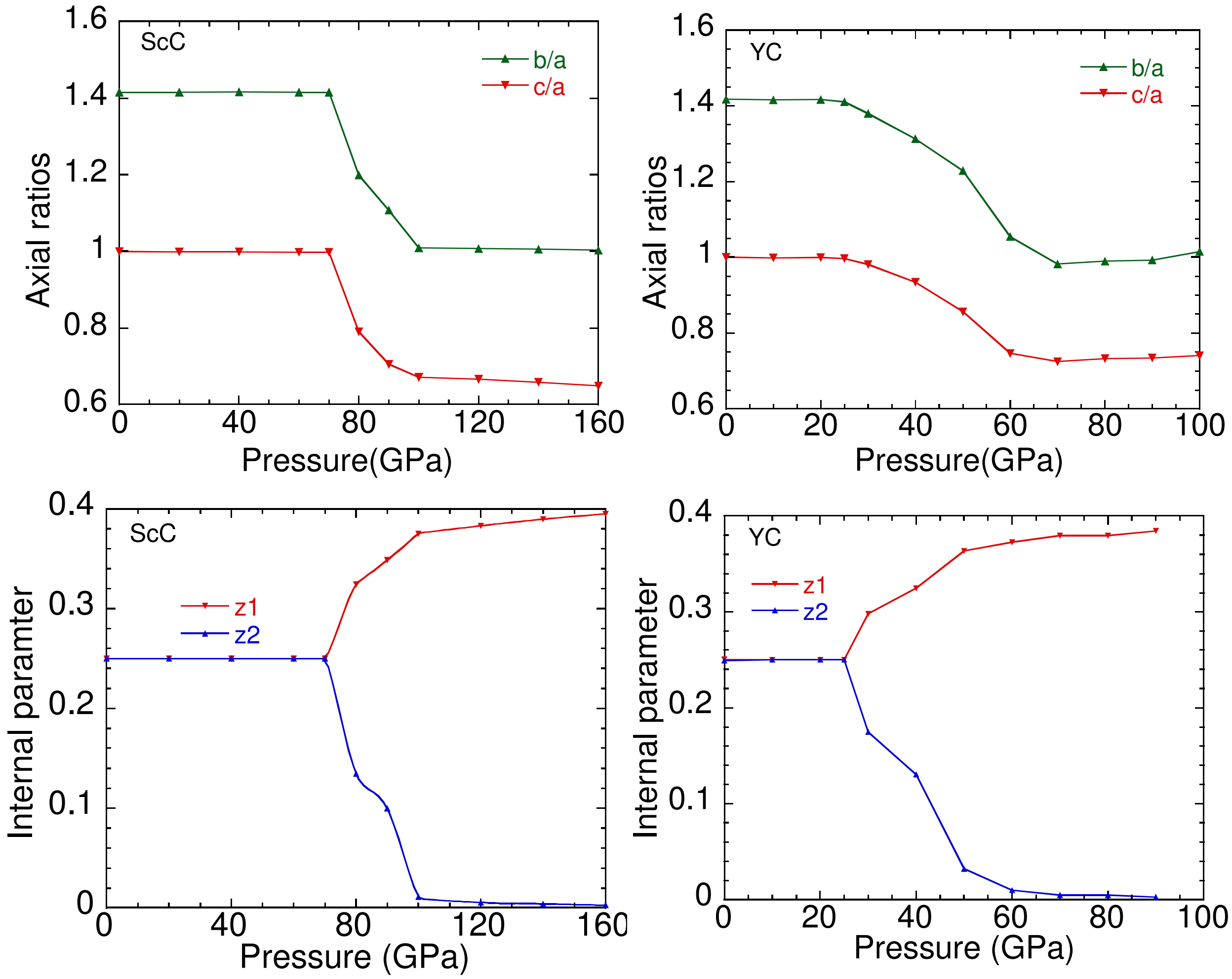

Fig. 3.2 The axial ratios and z_1 and z_2 parameters of Pmmn phase of ScC and YC as a function of pressure**.**

to be ~3.6% in ScC and ~1.6% in YC. Table 3.1, shows various physical properties of ScC and YC at ambient condition derived from our calculations for B1 phase. In ScC, the calculated zero pressure volume (V_0) agrees with experimental data [31] within ~ 2.0% whereas that for YC agrees is within ~0.35% [32]. The zero pressure bulk modulus (B_0) and its pressure derivative (B_0') for both the materials could not be compared with experiments due to non availability of the data, however, our theoretical values compare reasonably well with the other theoretical results [11, 12]. Additionally, in the same Table the elastic constants and Debye temperature (θ_D) determined for B1 phase at zero pressure in the present work have been compared with the theoretical values reported in other source [12].

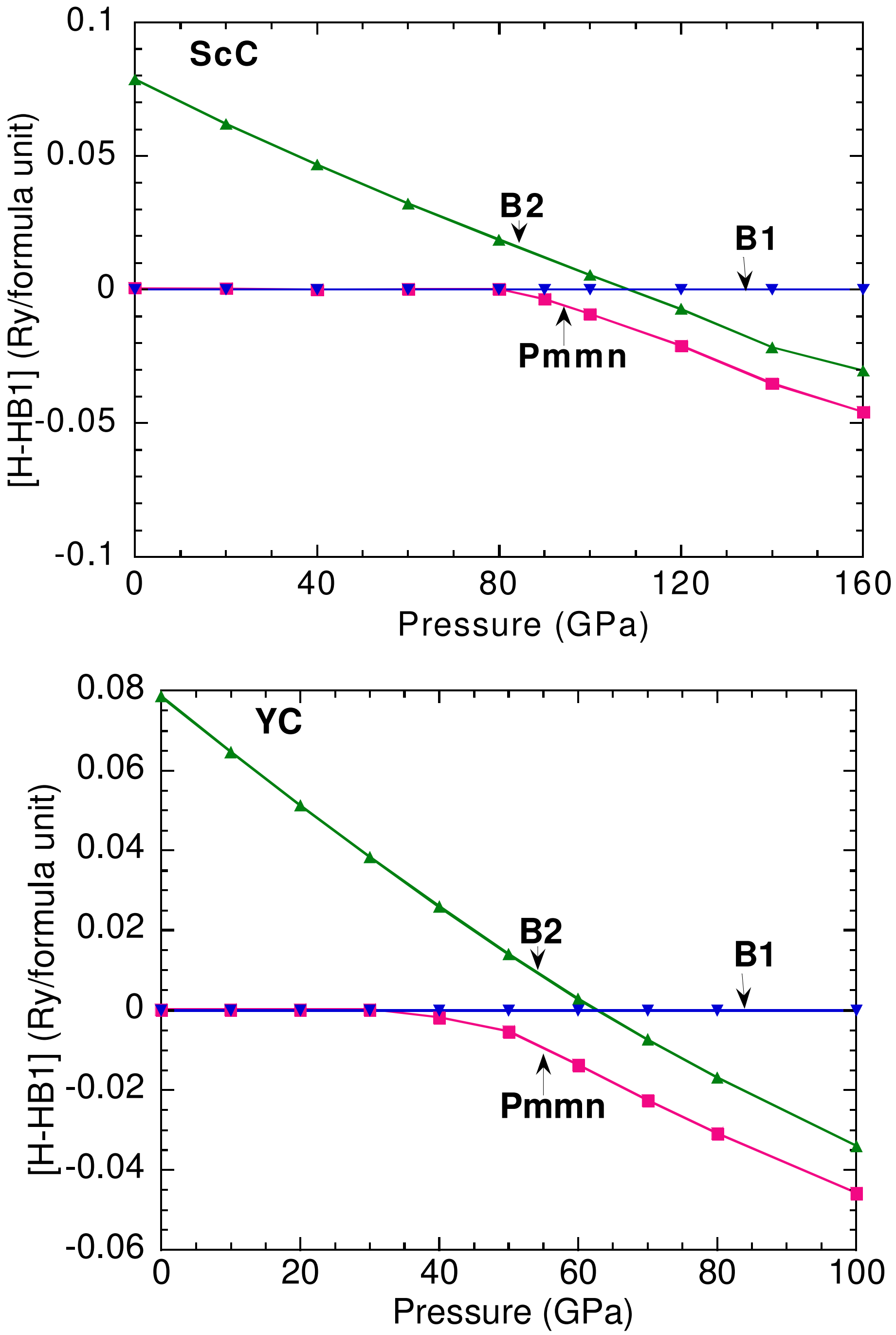

Fig. 3.3 Enthalpy of B1, Pmmn and B2 phases relative to that of B1 phase for ScC and YC at various pressures. For pressures ≤ 80 GPa in ScC and ≤ 30 GPa, the optimum value of *b/*a and *c/a* ratio is √2 and 1, and $z_1 = z_2 = ¼$, indicating that the Pmmn phase is identical to B1 structure up to these pressures.

In ScC, the C_{11} and C_{12} displays good with theoretical value of ref. (12), however, C_{44} is underestimated by ~ 25.5% as compared to those reported in ref. (12). For YC, the C_{11} and C_{44} are underestimated by ~ 5% and ~ 4%, respectively and C_{12} is over estimated by ~ 10% as compared to those reported in ref. (12). The Debye temperature determined in present theoretical work agrees with that of Soni *et al.* [12] within ~3% and ~1% in ScC and YC, respectively.

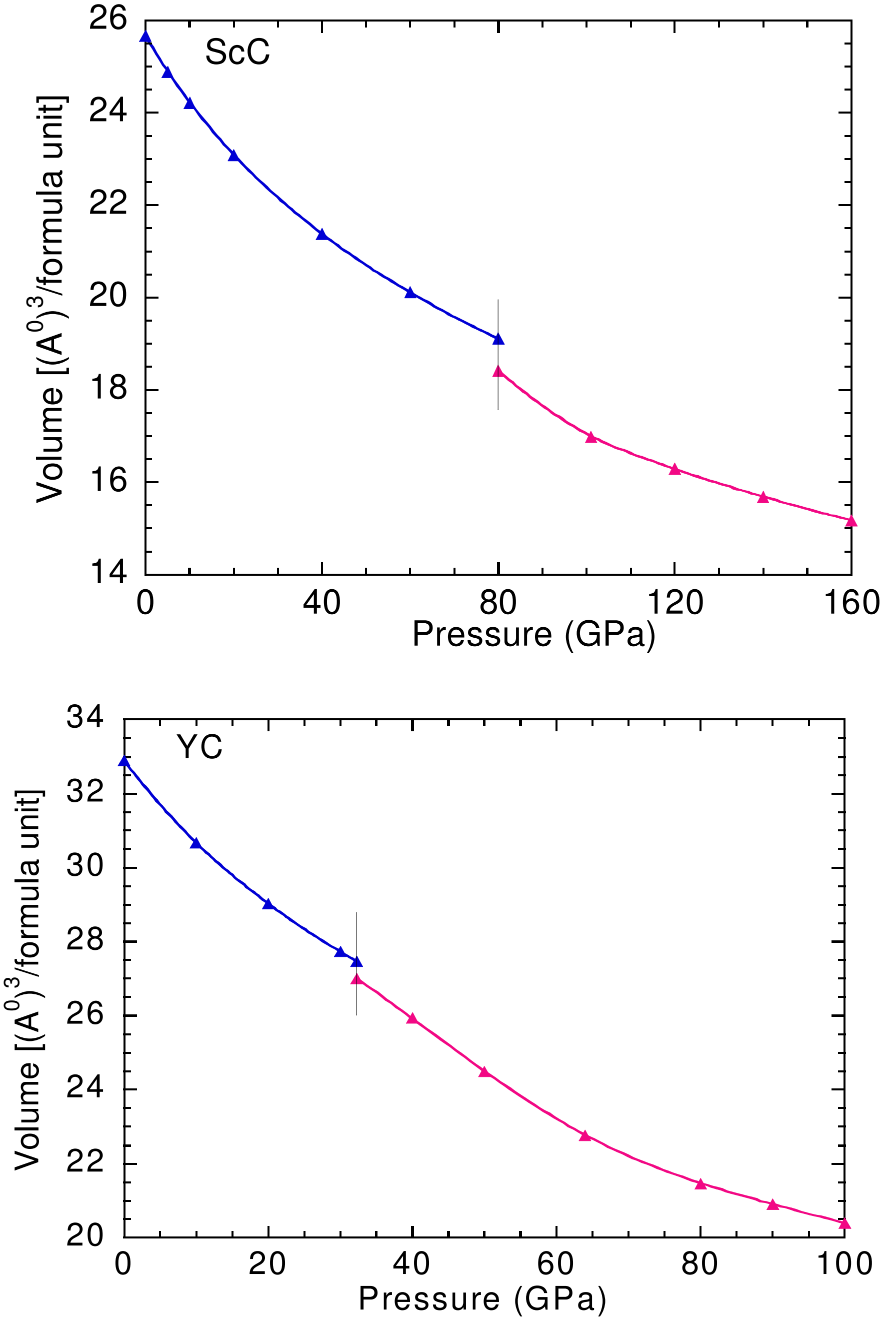

Fig. 3.4 The equation of state of ScC and YC .

Table 3.1 Comparison of various physical and elastic properties of ScC and YC in B1 phase at zero pressure calculated in present work with those available in literature

Properties at Equilibrium Volume	Present Theoretical Work	Theoretical (Other sources)	Experimental
V_0 (Å^3/formula unit)			
ScC	25.43	25.69[1],25.62[11], 25.65 [12]	24.92[31]
YC	33.23	32.77 [11], 32.89[12]	33.35[32]
B_0 (GPa)			
ScC	150	148[1],153[11],154.8[12]	
YC	125.2	128[11], 124.2[12]	
B_0'			
ScC	3.76	4.18[12]	
YC	3.37	4.14[12]	
C_{11} (GPa)			
ScC	305	310[12]	
YC	226	238[12]	
C_{12} (GPa)			
ScC	73	77[12]	
YC	74	67[12]	
C_{44} (GPa)			
ScC	46	62[12]	
YC	54	56[12]	
θ_D (K)			
ScC	665	645[12]	
YC	467	462[12]	

3.3.2 Elastic stability and dynamical stability of ScC and YC under pressure

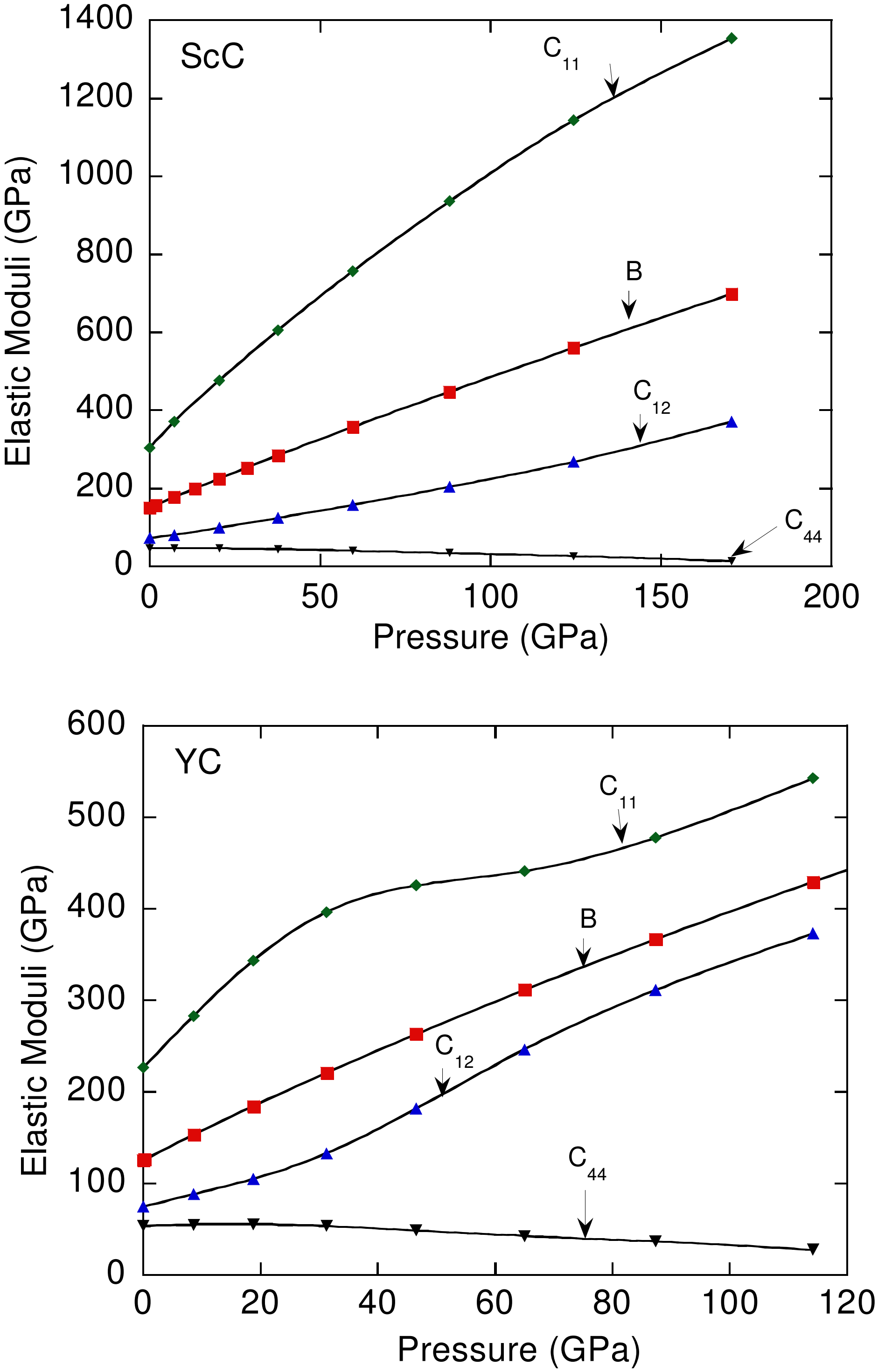

Figure 3.5 The pressure dependent elastic constants of ScC and YC in B1 phase

The elastic stability of B1 phase was analyzed by calculating the elastic moduli as a function of hydrostatic compression and examining the stability conditions throughout the compression path. Fig.3.5 shows the three independent elastic constants of ScC and YC in B1 phase. As is clear from the figure, for both the materials, the elastic constants C_{11} and C_{12} increase monotonically with increasing pressure, however, the shear elastic constant C_{44} displays opposite trend *i.e.* it decreases monotonically with increasing pressure, but remains positive through entire range of pressure up to 160 GPa in ScC and up to 100 GPa in YC. This suggests that the B1 phase remains elastically stable up to highest pressure of investigation in the present work.

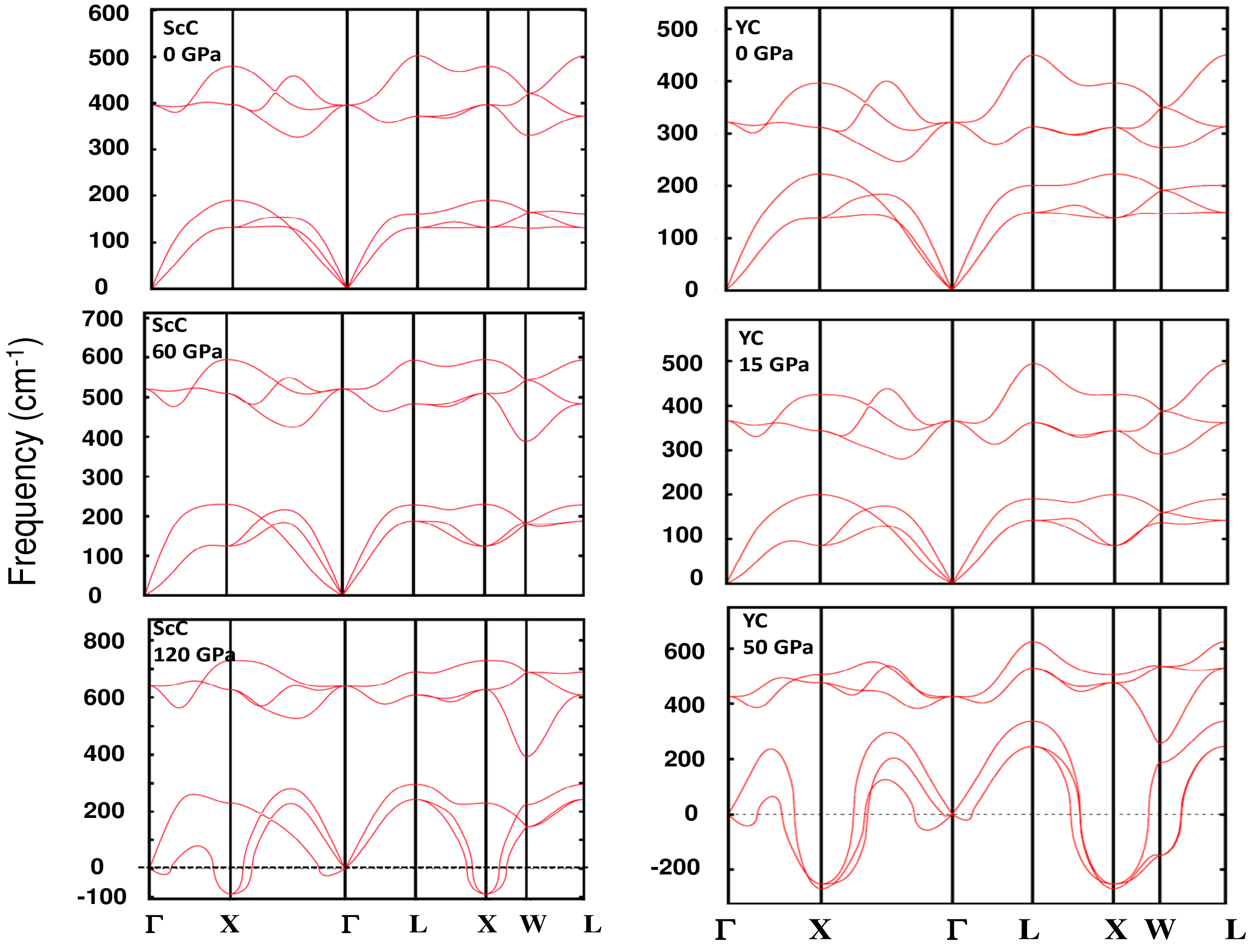

Fig. 3.6 Phonon dispersion relations for ScC and YC in B1 phase at various pressures .

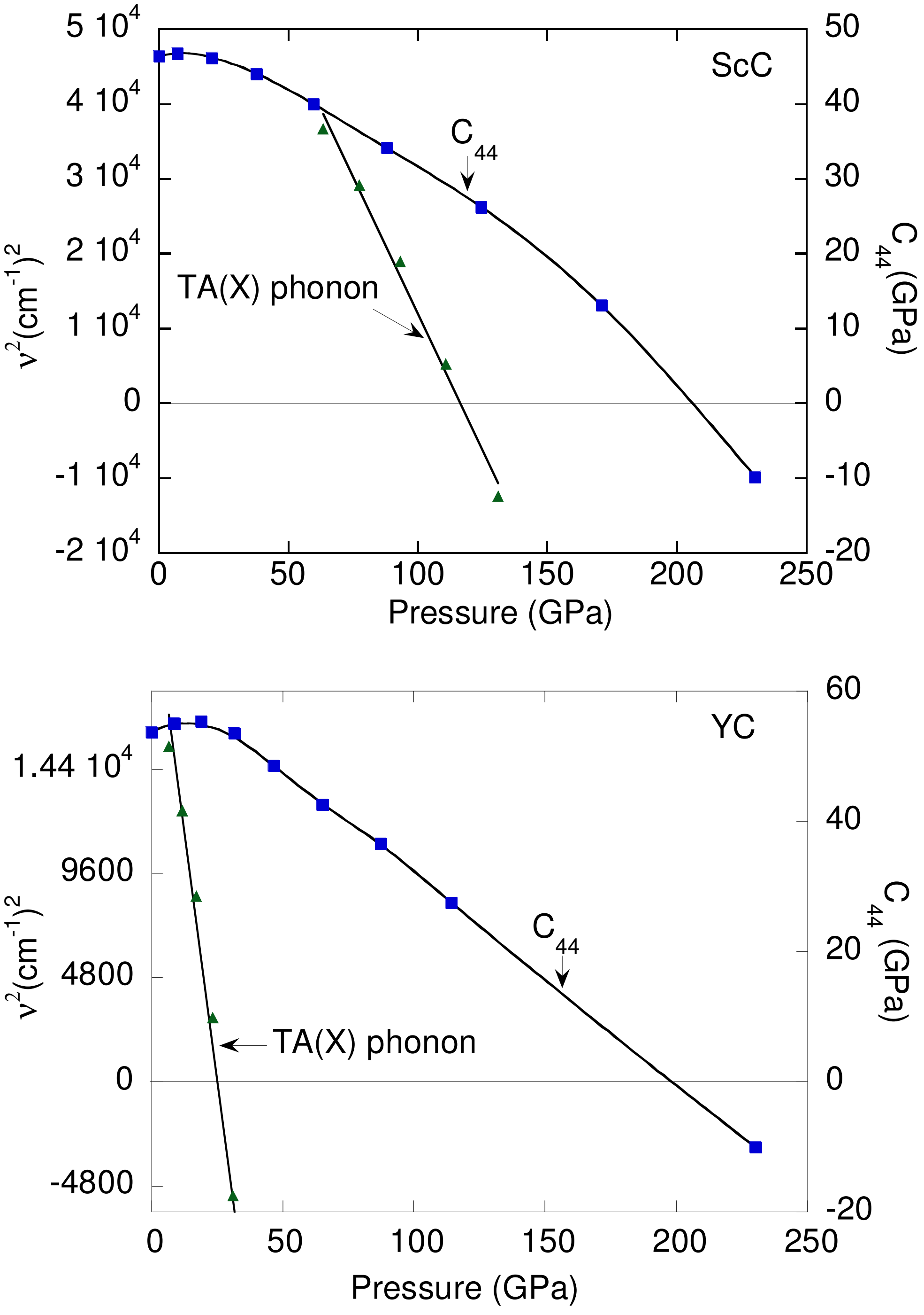

Fig. 3.7 The Square of the transverse acoustic phonon frequency at X point in the Brillouin zone of B1 phase as a function of pressure for ScC and YC. Also plotted is the variation of C_{44} modulus with pressure.

In order to further confirm theoretically obtained B1 → Pmmn phase transition in ScC and YC, lattice dynamic calculations have been performed on B1, Pmmn and B2 structures. The phonon dispersion relations calculated at different pressures for B1 phase are plotted in Fig.3.6. For both ScC and YC, at zero pressure, as expected, the phonon frequencies in all directions are real, demonstrating that the B1 phase is dynamically stable at ambient condition. Further, this phase remains dynamically stable at higher pressures also *e.g.* in ScC it remains stable at 60 GPa but becomes unstable at 120 GPa. Similarly, for YC, B1 is stable at 15 GPa but destabilizes at 50 GPa. In order to find the exact pressures at which the B1 phase becomes unstable dynamically, in Fig.3.7 the square of the frequency of transverse acoustic (TA) phonon at X point has been plotted with pressure. Additionally, the shear elastic modulus C_{44} is also plotted in this figure. As is clear from the figure, for ScC, the phonon frequency ceases to zero at ~ 116 GPa whereas the elastic modulus vanishes at still higher pressure of ~ 207 GPa, indicating that B1 phase becomes dynamically unstable much before it fails elastically. In YC, the B1 phase fails dynamically at ~ 26 GPa which is very close to the ~ 30 GPa, the B1 to Pmmn transition pressure, however, elastically it remains stable even up to ~ 197 GPa. Further, it may be noted that the dynamic instability occurs at points away from the center of the Brillouin zone and much before the elastic instability (the difference between the pressures for the two instabilities is ~ 91 GPa in ScC and ~171 GPa in YC), indicating that the B1 to Pmmn structural phase transition in these carbides is phonon driven.

Table 3.2, lists the phonon frequencies (ω), their pressure derivative coefficients and Gruneisen parameter (γ) of several modes at high symmetry points Γ, X and L of Brillouin zone of B1 phase in ScC and YC. The negative TA Gruneisen parameter at X point for both the materials indicates that the frequency at this point decreases with increasing pressure. Additionally the frequencies of various modes calculated in the present work have been compared with other published data [24]. For ScC the frequencies of all the modes determined in the present work exhibits a good agreement with those reported by Isaev et al. [11]. However, for YC the values obtained in the present work differ from those of Isaev et al. [24] by maximum of ~ 7%. This deviation could be due to the mismatch of the equilibrium volume by ~ 1.4% in YC.

Table 3.2: Phonon frequencies, pressure coefficients and Gruneisen parameters of various modes for B1 structure of ScCand YC at certain high symmetry points of the Brillouin zone. The zero pressure bulk modulus of ScC and YC used for the calculation of Gruneisen parameters is 150 GPa and 125.2 GPa, respectively. Also, compared are the phonon frequencies reported by Isaev et al (ref 24)

Materials	Brillouin zone points	Modes	ω(cm^{-1})	$\frac{\partial \omega}{\partial P}(cm^{-1}/GPa)$	γ
ScC					
	Γ	LTO	420.9,409[11]	4.63	1.65
	X	TA	218.3,222[11]	-0.10	-0.07
		LA	328.4,327[11]	2.46	1.12
		TO	412.9,397[11]	5.27	1.91
		LO	473.6,463[11]	4.57	1.45
	L	TA	225.8,225[11]	2.93	1.95
		LA	279.4,279[11]	3.33	1.79
		TO	366.4,353[11]	4.40	1.81
		LO	494.4,487[11]	3.47	1.06
YC					
	Γ	LTO	324.8,350[11]	4.33	1.67
	X	TA	134.8,130[11]	-10.07	-9.28
		LA	224.3,240[11]	3.03	1.54
		TO	308.3,333[11]	4.10	1.67
		LO	390.7,407[11]	2.70	0.87
	L	TA	150.2,163[11]	2.50	2.09
		LA	200.7,223[11]	3.03	1.90
		TO	308.9,327[11]	4.20	1.71
		LO	444.2,466[11]	3.77	1.06

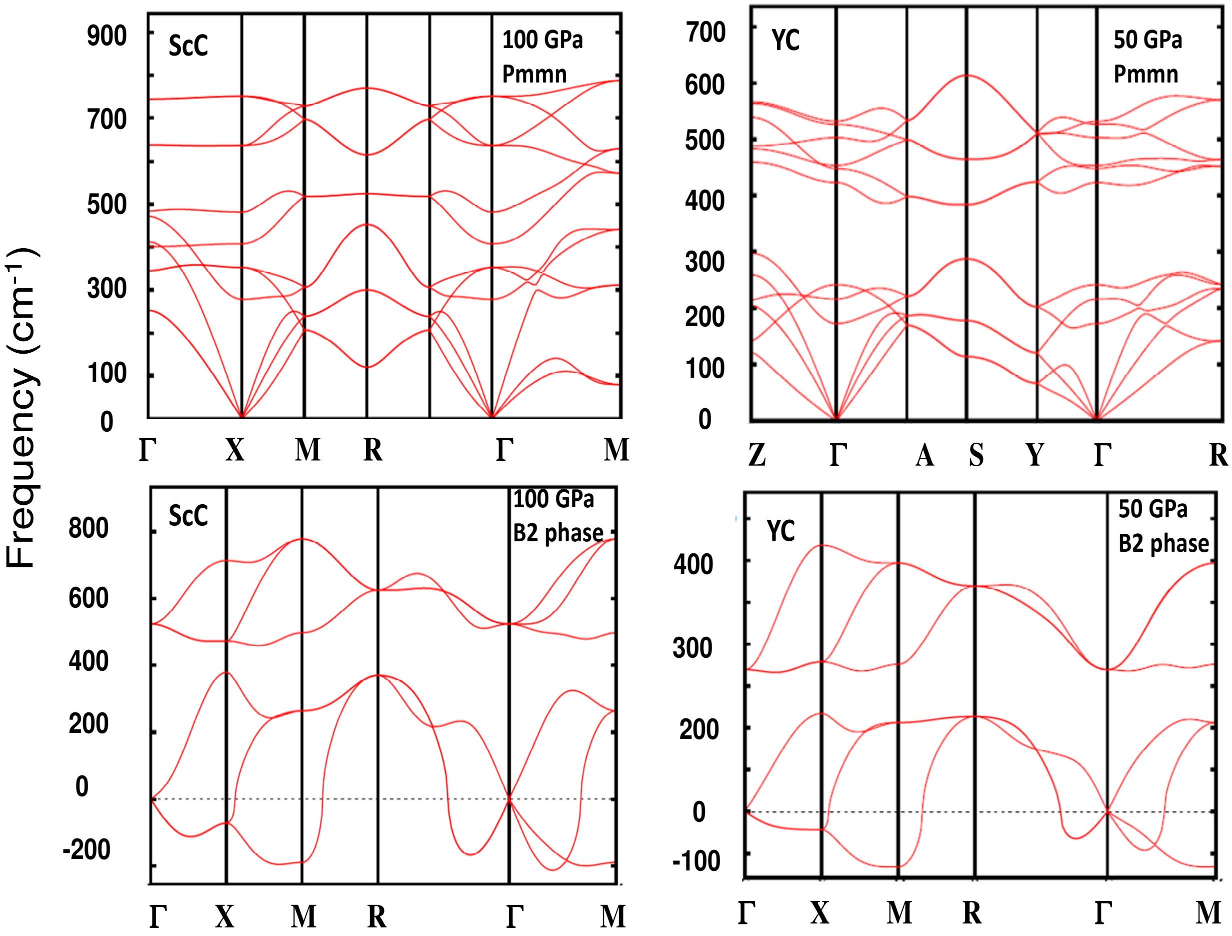

Figure 3.8 Phonon dispersion relations for Pmmn and B2 phases at ~ 100 GPa in ScC and ~ 50 GPa in YC.

The phonon dispersion curve have also been calculated for Pmmn and B2 structures at ~ 100 GPa in ScC and at ~ 50 GPa for YC. As shown in Fig.3.8, the Pmmn structure is dynamically stable whereas the B2 phase still remains as dynamically unstable structure at these pressures in these carbides. Further, it has been found that the dynamical instability of B2 structure persists up to ~200 GPa in both the materials. The results from lattice dynamic calculations substantiate the B1 to Pmmn phase transition predicted from the static lattice calculations in ScC and YC. The results of present static lattice calculations and lattice dynamic calculations predict that under hydrostatic compression B1 phase will transform to Pmmn structure, ruling out the direct B1 to B2 transition predicted by Soni *et al.* [12].

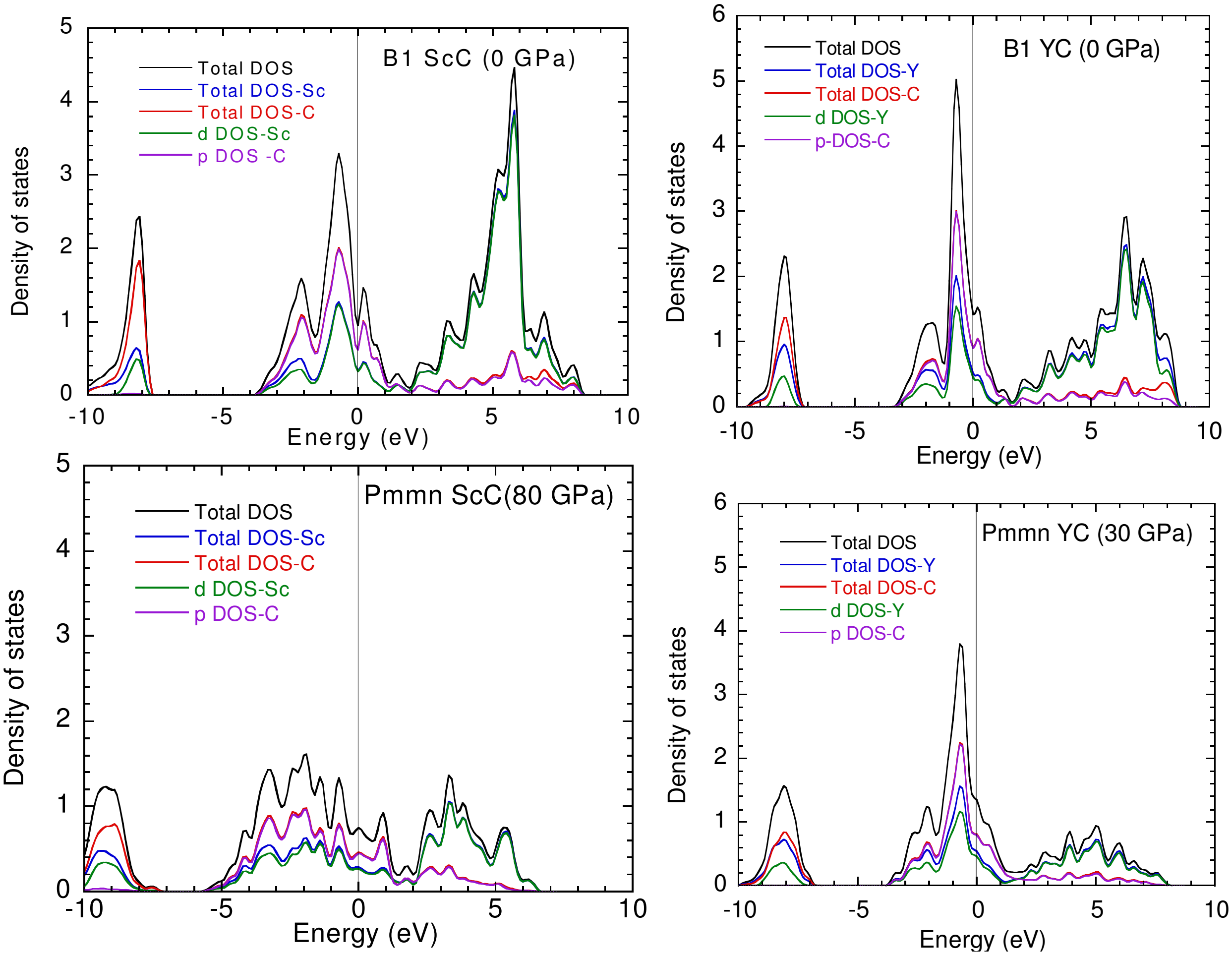

Figure 3.9 Electronic density of states of ScC and YC for B1 and Pmmn phase.

Additionally, the electronic density of states for both the carbides have also been calculated and analyzed. Fig.3.9, displays the theoretically calculated electronic density of states (DOS) of ScC and YC in B1 phase at 0 GPa and in Pmmn structure at transition pressure. For ScC, the major contribution to total density of states around Fermi level comes from the 3d of Sc and 2p of C whereas for YC the same comes from 4d of Y and 2p of C. The density of states at Fermi level for ScC in B1 phase at 0 GPa is found to be ~1.01 states/ev whereas the same for YC has been determined to be 1.45 states/ev. The higher value of DOS at Fermi level for YC as compared to the ScC is in accordance with the higher electron-phonon coupling constant calculated for YC by Isaev et al. [11] theoretically. Further, the DOS at Fermi level decreases with increasing pressure and assumes a value of 0.73 states/ev for ScC and 1.30 states/ev for YC in Pmmn phase. The sufficiently high density of states at Fermi level indicates that both the carbides are metallic in nature at ambient condition. Moreover, the comparatively low density of states at Fermi level for the high pressure Pmmn structure suggests that these carbides in Pmmn phase will exhibit less metallicity.

3.3.3 Structural stability and equation of state of TaC

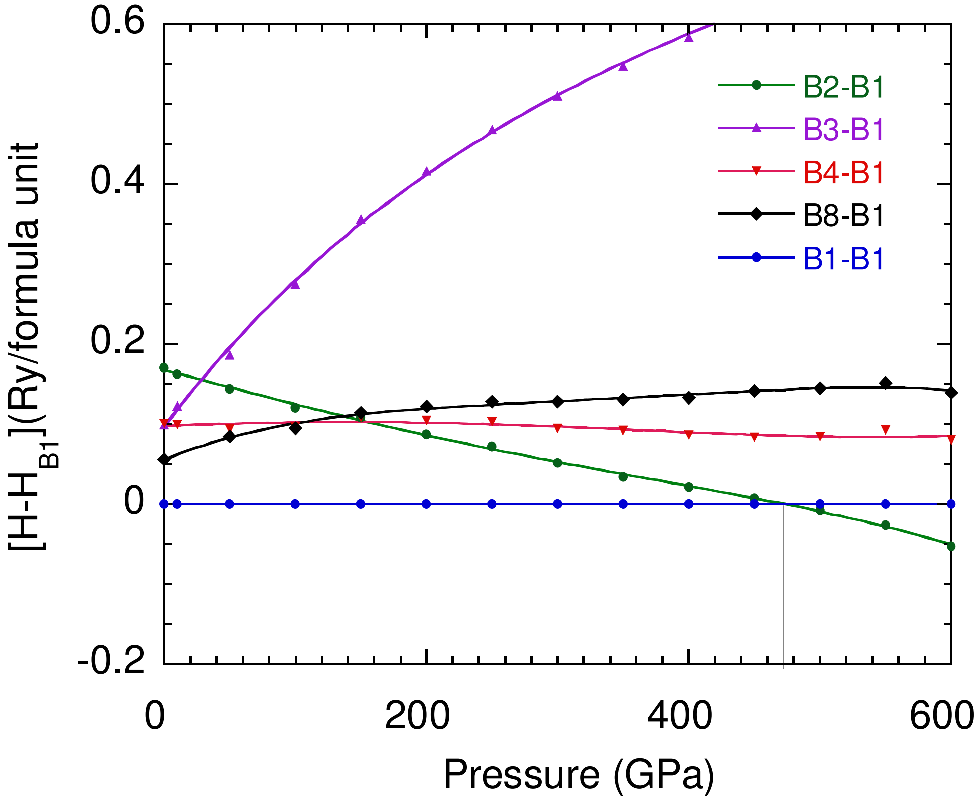

Figure 3.10 Enthalpy difference of B2 , B3 , B4 and B8 with respect to B1 structure .

To examine structural stability of TaC the total energy calculations have been carried out at several unit cell volumes for B1, B2, B3, B4 and B8 structures. The P-V data have been generated from this volume dependent total energy, which then is utilized to calculate the enthalpies of B1, B2, B3, B4 and B8 phases at various pressures. The comparison of enthalpies of these phases as a function of pressure is displayed in Fig. 3.10. As is obvious from the figure, the B1 phase transforms to B2 phase at ~ 472 GPa as compared to 660 GPa that predicted by Srivastva *et al.* [25] from pseudopotential calculations carried out within GGA using SIESTA code. The equation of state of TaC have been plotted in Fig.3.11 along with experimental data [19]. The theoretical isotherm agrees well with the experimental data. Further, the volume discontinuity determined at the transition pressure is ~ 5.4%. In Table 3.3 listed are the various physical quantities for B1 phase at ambient conditions derived from equation of state. The zero pressure equilibrium volume (V_0) agrees within ~ 1.3%, with experimental data [13]. The zero pressure theoretical bulk modulus (B_0) is more close to the experimental values reported in ref. (13 and19) than to that reported in ref. 14. The pressure derivative (B_0') agrees within 2% with experimental value [19]. It may be noted that in view of the Pmmn phase found to be stable phase at high pressure in ScC and YC, the stability of the same has been tested in TaC also but did not find it to be stable.

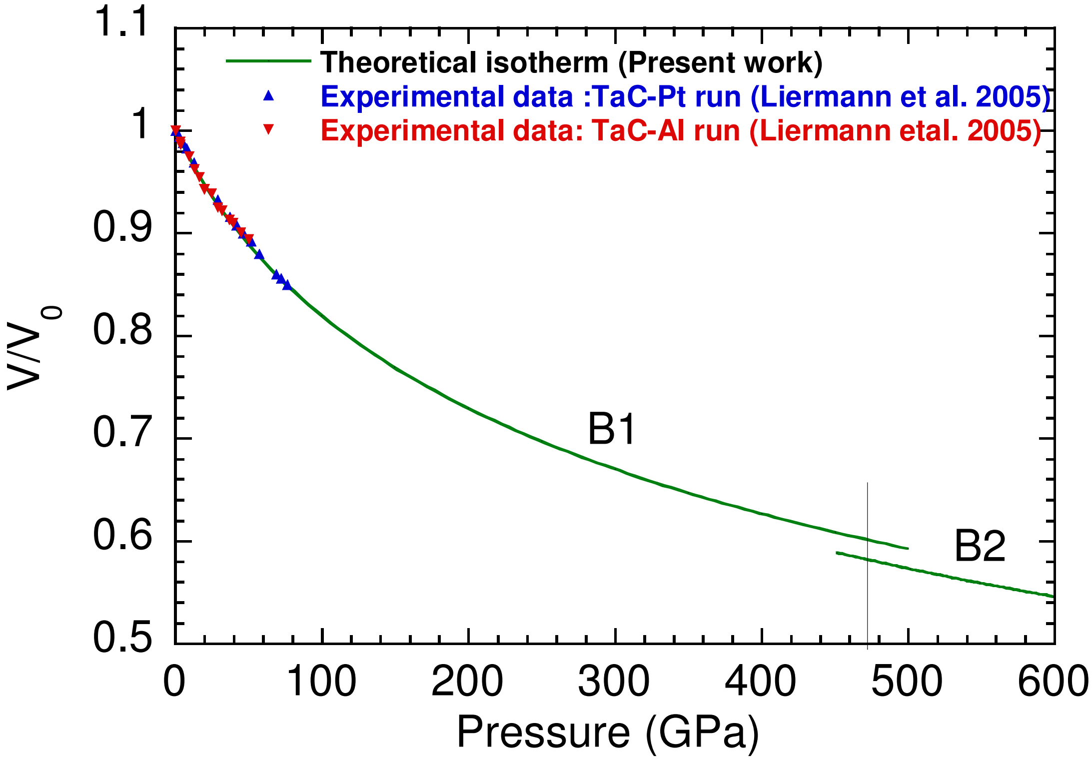

Fig. 3.11 Equation of state of TaC with experimental data of Liermann *et al.*

Table 3.3: Various physical quantities at zero pressure for TaC

Properties at Equilibrium Volume	Present Theoretical Work	Theoretical (Other sources)	Experimental
V_0 (Å^3/formula unit)	22.4	23.1[15],22.3[11] 22.4[1], 21.7[21] 21.6[22],23.7[24] 23.3[25]	22.1[13]
B_0 (GPa)	342	318[12], 324[11] 321[1] 370[22] 356[23], 311[24] 391[25]	344[13], 332[14], 345[19]
B_0'	3.93	4.58[22], 3.03[25]	4.0[19]
C_{11} (GPa)	723	621[12], 740[23] 641[24]	595[15] ,631[13]
C_{12} (GPa)	151	155[12], 165[23] 146[24]	155[12], 165[23] 146[24]
C_{44}(GPa)	178	167[12], 176[23] 156[24]	193[15]
Y(GPa)	534	550[24]	537[13] 567[14]
G(GPa)	215	188[24]	216[13] 234[14]
α (K^{-1})	1.8×10^{-5}	1.6×10^{-5}[21] 2.1×10^{-5}[24]	1.6×10^{-5}[33]
θ_D (K)	516	538[24]	556[13] 593[14]

3.3.4 Elastic stability and dynamical stability of TaC under pressure

Further, to understand the B1 to B2 phase transition in terms of elastic instability, the elastic moduli of B1 and B2 phase as a function of pressure have been determined. As expected, the elastic constants C_{11}, C_{12} and C_{44} of B1 phase at zero pressure (Table 3.3) are positive and agree with experimental data within ~ 21%, 10% and 7.7%, respectively. Additionally, the zero pressure elastic constants have been utilized to determine the Debye temperature (θ_D), polycrystalline Young's modulus (Y) and shear modulus (G) at ambient condition. As listed in Table 3.3, the θ_D determined in the present work agrees with experimental data within ~ 13%. The values of Y and G calculated in the present work agree better with the experimental data of Jun and Shaffer [13].

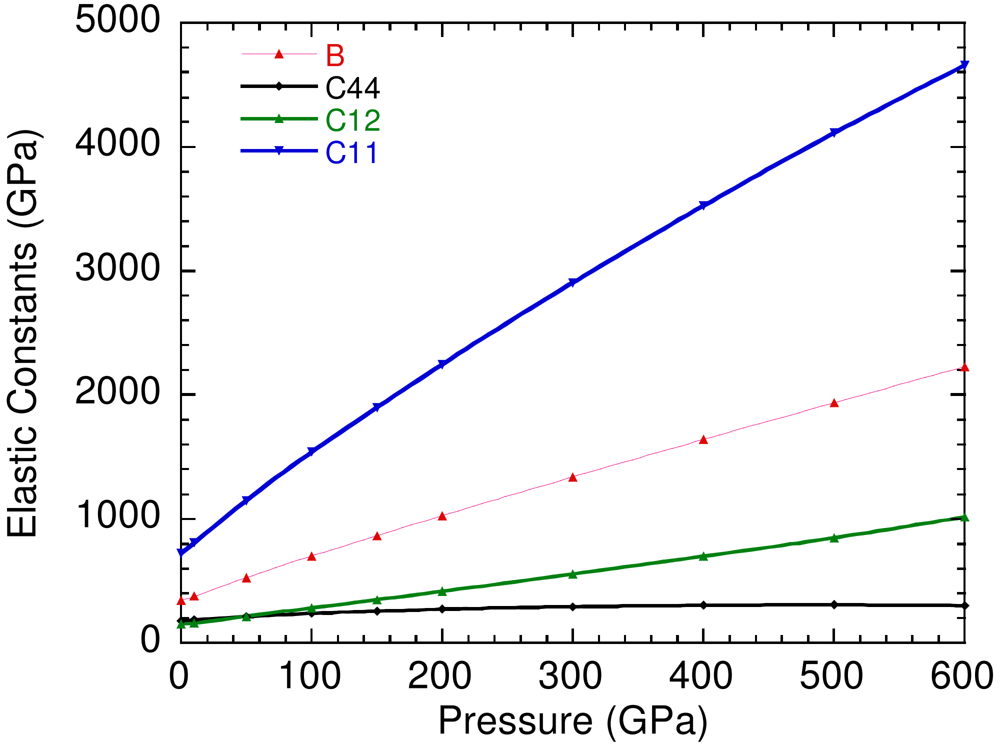

Fig. 3.12 Pressure dependent elastic constants of B1 phase

For B1 phase, as shown in Fig. 3.12, the C_{11} and C_{12} increase monotonically with increasing pressure whereas the C_{44} modulus displays different behavior. Initially, it increases with increasing pressure and reaches to a maximum value of ~ 308 GPa around the B1 to B2 transition pressure. Thereafter though it starts softening, it still remains positive even at 600 GPa.

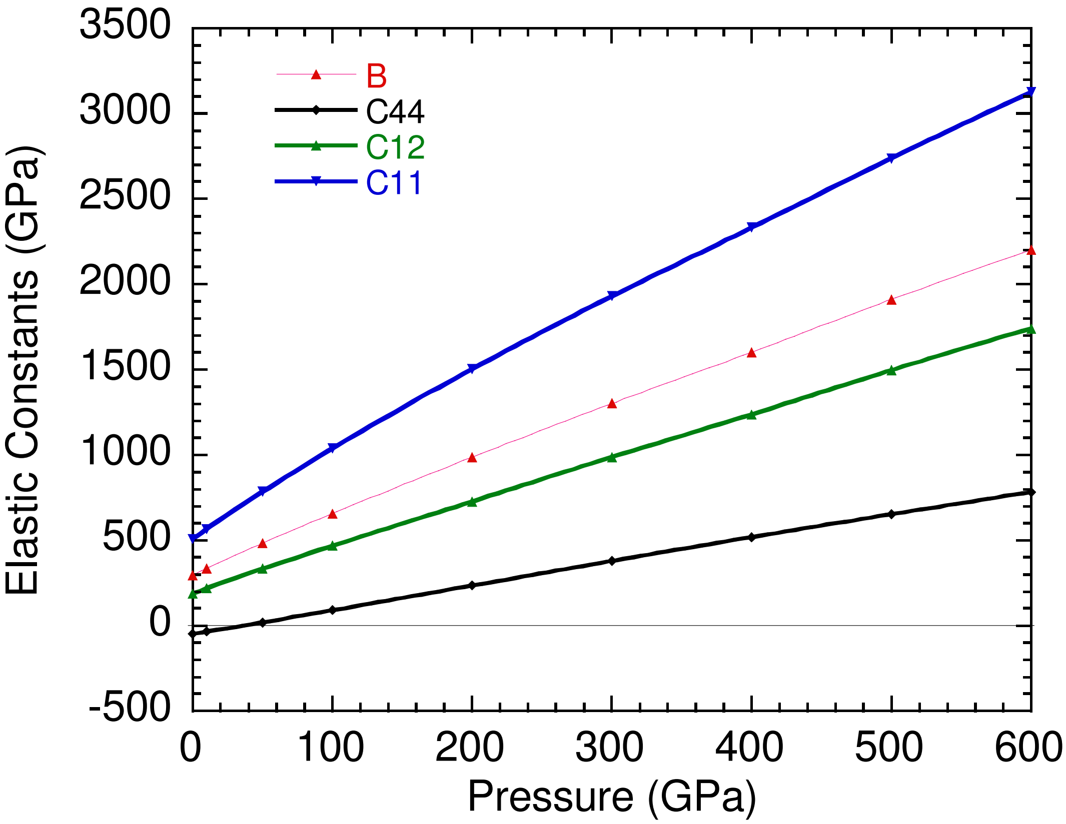

Figure 3.13 Pressure dependent elastic constants of B2 phase

The elastic constants as a function of pressure have also been calculated for B2 phase. As shown in Fig. 3.13, for B2 phase the C_{11} and C_{12} elastic constants are positive but C_{44} is negative (-55 GPa) at zero pressure. With increasing pressure all the elastic constants increase monotonically and the C_{44} modulus acquires a positive value for pressures ≥ 40 GPa, suggesting that this phase will be stable elastically only beyond this pressure.

In addition to the static lattice calculations, the lattice dynamics of the two phases has also been studied. In Fig. 3.14, the phonon spectra and density of states of B1 phase is displayed at zero pressure, 200 GPa and 500 GPa, respectively. The same for B2 phase is depicted in Fig. 3.15. As can be seen from the figures the phonon spectra of the B1 phase display positive frequencies in all the directions of Brillouin zone not only at ambient pressure but also beyond the B1 to B2 transition pressure indicating that this phase is stable lattice dynamically even at pressures higher than the transition pressure. The elastic and lattice dynamic stability of B1

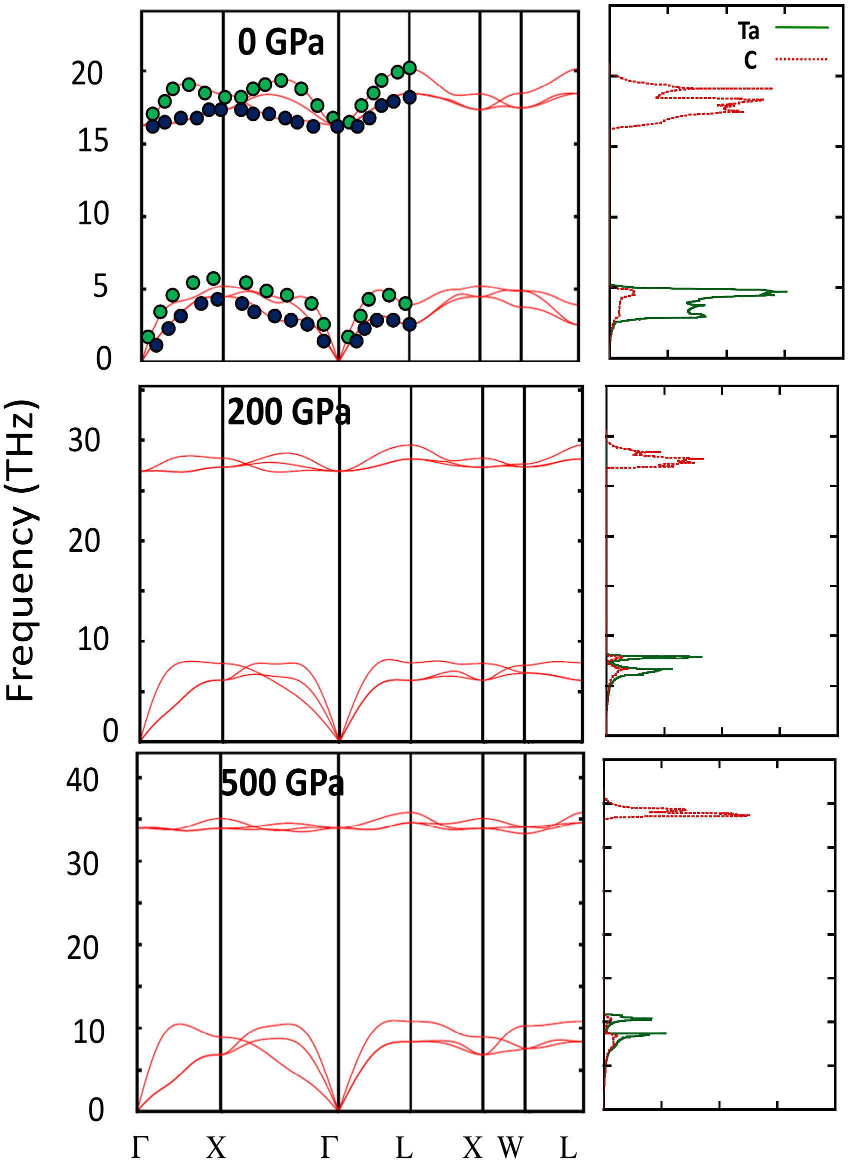

Fig.3.14: The Phonon spectra and density of states of B1 phase

phase even beyond the transition pressure suggests that this structure remains as metastable phase even after B1 to B2 structural transition. Further, the theoretical dispersion relations at zero pressure compare well with the experimental values [16]. As far as B2 phase is concerned it is clear from the figure 3.15 that this structure is unstable lattice dynamically at zero pressure but becomes stable at 200 GPa as well as 500 GPa. To get the exact value of pressure at which the onset of lattice dynamical stability occurs, the frequency of longitudinal acoustic (LA) and TA phonons at M point of the Brillouin zone of B2 phase have been calculated and plotted in Fig.

3.16. It is clear from the figure that for pressures of ≥ 83 GPa the frequency of TA phonons at M point becomes real, indicating lattice dynamic stability of B2 phase beyond this pressure.

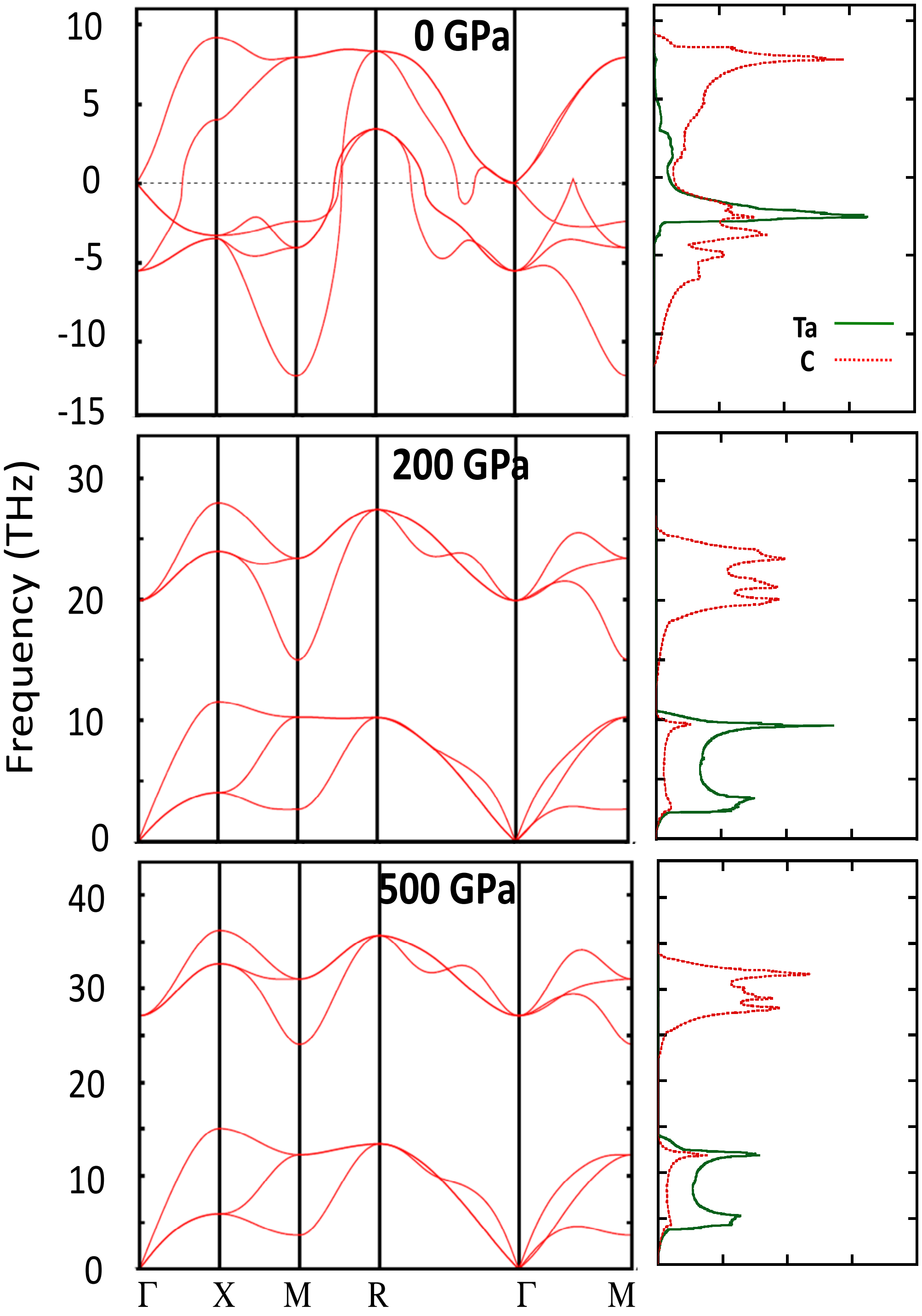

Fig. 3.15 The Phonon spectra and density of states of B1 phase

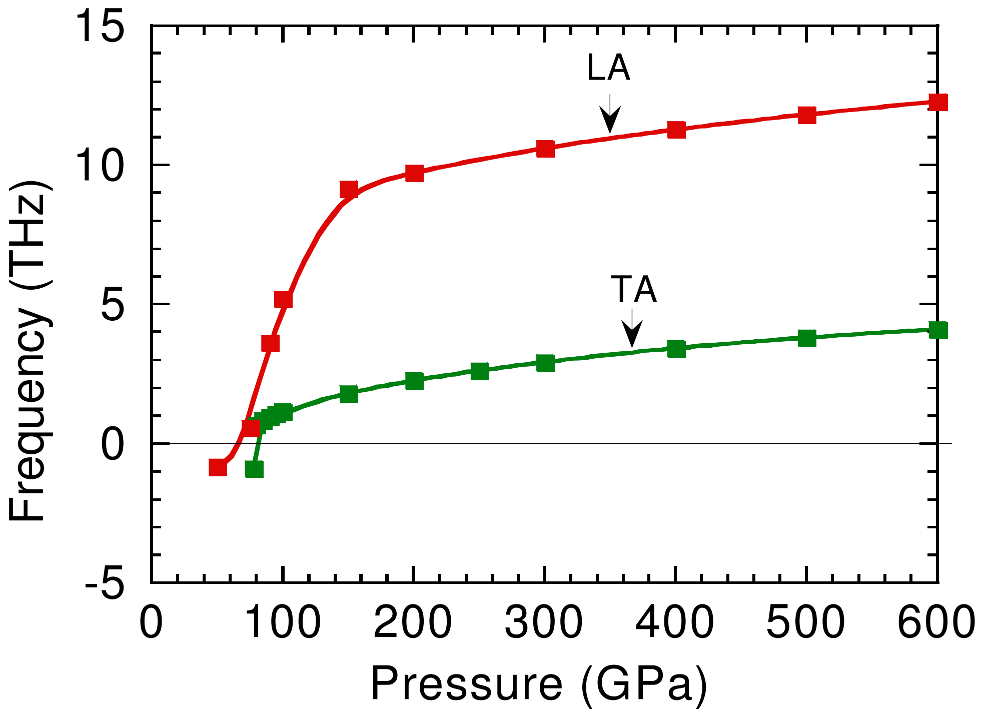

Fig. 3.16 Frequency of LA and TA phonons as a function of pressure at M point of Brillouin of B2 phase.

3.3.5 Effect of temperature on Thermo physical properties of TaC

The calculations have been further extended to determine the temperature effect on volume and bulk modulus of B1 phase of TaC. For this purpose the Helmholtz free energy (F) has been calculated as a function volume at a fixed temperature and the minimum in free energy is determined. This along with F(V) is then used to determine the volume V and bulk modulus B corresponding to the minimum free energy at that temperature. This process has been repeated at various temperatures, and volume and bulk modulus as a function of temperature has been determined. In fig. 3.17, the free energy as a function of volume at various temperatures ranging from 0K to 3000K has been displayed. As obvious from the figure, the free energy decreases with increasing temperature and this effect is more pronounced at higher temperatures as the increase in TS term becomes larger and larger due to increase in both the T and S.

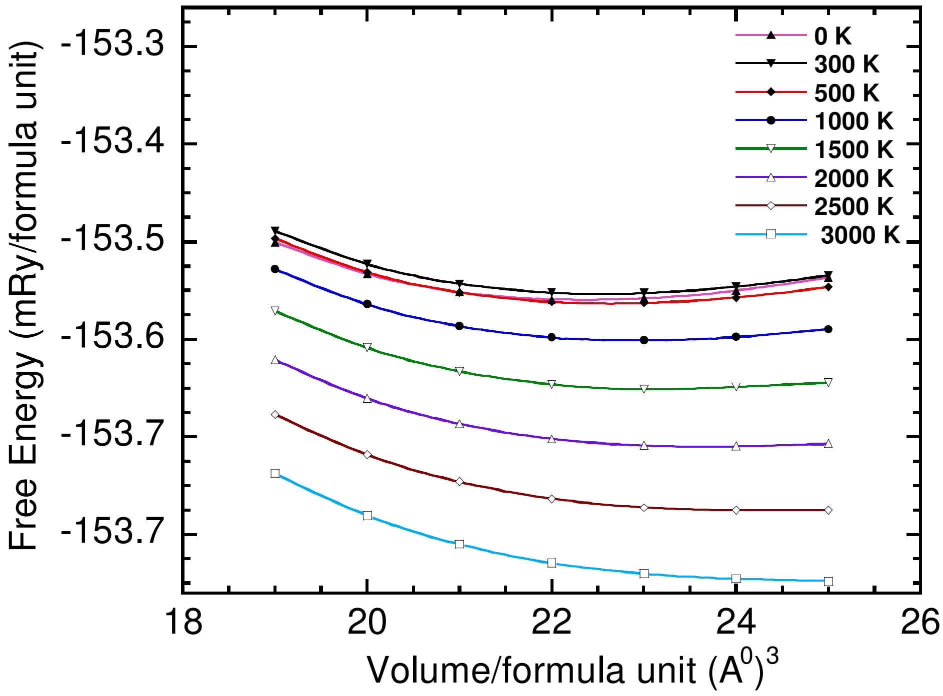

Fig.3.17 Helmholtz free energy of B1 phase of TaC as function volume for various temperatures

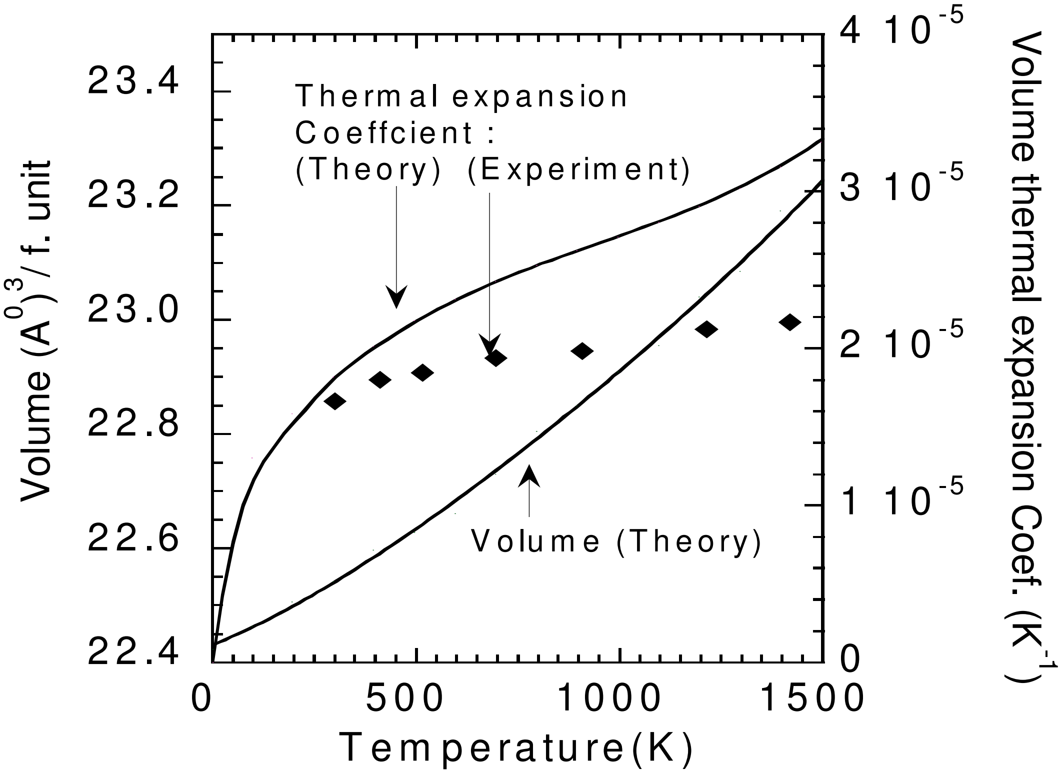

Fig. 3.18 The volume/f.unit and volume thermal expansion coefficient of B1 phase of TaC as a function of temperature with thermal expansion data of [32].

The temperature dependence of zero pressure volume of TaC in B1 phase determined from the free energies calculated as a function of volume at different temperature is displayed in Fig. 3.18. Also plotted is the volume thermal expansion coefficient derived from this along with the experimental data [33]. The zero pressure volume/formula unit increases from 22.4 $(A^0)^3$ at 0K to 22.5 $(A^0)^3$ at 300 K. As the zero pressure volume was already overestimated by ~ 1.3% at 0K, the overestimation further increases to ~ 1.8% at 300K. Further, for temperatures << 500K *i.e.* (T/θ) << 1, the thermal expansion coefficient falls rapidly with decreasing temperature. At higher temperatures it displays a softer dependence upon temperature. As shown in figure, the theoretically determined thermal expansion coefficient for TaC deviates from experimental data [33] significantly at temperatures above 400K and the deviation increases with increasing temperature. The reason for this could be the large anharmonic effects (especially due to the intrinsic anharmonicity *e.g.* significant phonon-phonon interactions) in reality as compared to that calculated by theory within QHA. The temperature dependence of the bulk modulus is plotted in Fig.3.19. As expected, the bulk modulus decreases monotonically with increasing temperature. The value of bulk modulus at 300K is obtained to be ~ 341 GPa as compared to its 0K value of 342 GPa *i.e.* a decrease of ~ 0.3 % and deviation from experimental value is within 2.7%.

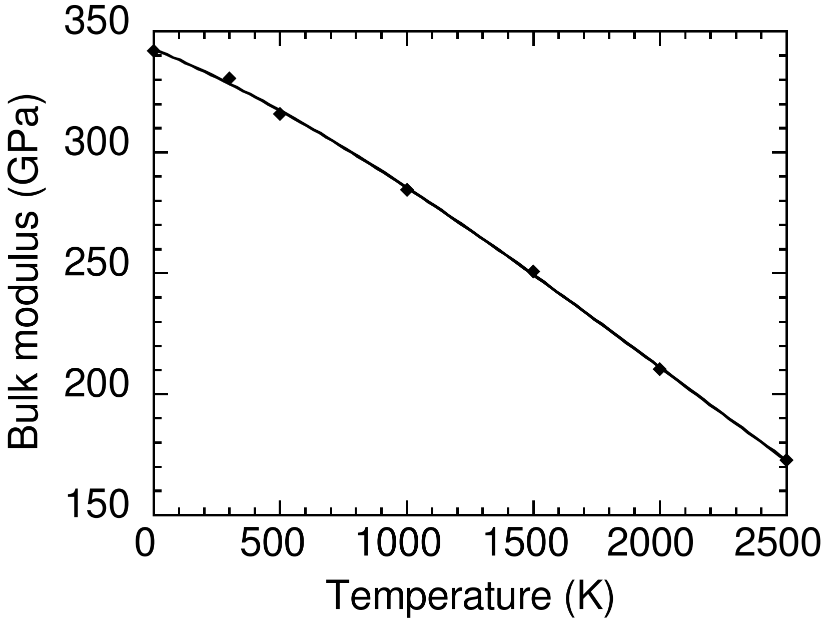

Fig. 3.19 The bulk modulus of B1 phase of TaC as a function of pressure

3.4 Summary

The structural stability analysis has been carried out on ScC and YC. The comparison of enthalpies of B1, Pmmn and B2 phase determined as a function of pressure from static lattice calculations predict the B1 to Pmmn structural phase transition in these carbides, ruling out the possibility of direct B1 to B2 phase transition under hydrostatic compression. The pressures for B1 to Pmmn phase transition have been determined to be ~ 80 GPa in ScC and ~ 30 GPa in YC. The theoretically predicted pressure induced B1 → Pmmn phase transition from static lattice calculations in the present work is also supported by present lattice dynamic calculations performed on these phases. The current theoretical work emphasizes that the phonons play dominant role in deciding the structural stability of these carbides.

In TaC, the present calculations predicted the B1 to B2 structural transition at a pressure of ~ 472 GPa. This structural phase transition has been substantiated further by examining the elastic and lattice dynamic stability of B1 and B2 structures as a function of pressure up to ~ 600 GPa. Apart from high pressure investigations, the temperature effect on volume and bulk modulus has been also determined. Various thermo physical quantities derived from present theoretical calculations agree reasonably with the available experimental data.

References

1. Aleksandra Vojvodic and Carlo Ruberto, *J. Phys. Cond. Matter* **22**, 3755011 (2010).
2. Zengtao Lv, HaiquanHu, Cheng Wu, Shouxin Cui, Guiqing Zhang and Wenxia Feng, *Physica B* **406**, 2750 (2011).
3. Hui Li, Litong Zhang, Qingfeng Zeng, Haitao Ren, Kang Guan, Qiaomu Liu, Laifei Cheng , *Solid. State Comm*. **151**, 61(2011).
4. H. G. Smith and W. Gläzer, *Phys. Rev. Lett.* **25**,1611 (1970).
5. H. G. Smith, *Phys. Rev. Lett*. **29**, 353 (1972).
6. H. G. Smith and W. Gläzer, in Proceedings of the International Conference on Phonons, Rennes, France, July 1971, edited by M. A. Nusimovici, Flammaron Sciences, Paris, (1971).
7. A. Krajewski, L. D'Alessio and G. De Maria, *Cryst.ResTechnol*.**33**,341(1998).
8. M. Khusainov, G. Demyshav, and M. Myshlyaev, *Russ. Metall*. **5**, 144, (1990).
9. D. J. Rowcliffe and W. J. Warren, *J. Mater. Sci.,* **5** 345, (1970).
10. B.D. Sahoo, D. Mukherjee, K.D. Joshi and Satish C. Gupta, *J. Phys.: Conf. Series* **3,77,** 012087 (2012).
11. E. I. Isaev, S. I. Simak, I. A. Abrikosov, R. Ahuja., Yu. Kh. Vekilov, M. I. Katsnelson, A. I. Lichtenstein and B. Johansson, *J. Appl. Phys*. **101**, 123519 (2007).
12. Pooja Soni, Gitanjali Pagare, Sankar P. Sanyal, *J. Phys. and Chem. Solids* **72**, 810 (2011).
13. C. K. Jun and P. T. B. Shaffer, *J. Less-Common Metals*, **23** 367, (1971).
14. S.P. Dodd, M. Cankurtaran and B. James, *J. Materials Sci*., **38** , 1107(2003).
15. Laura Lo´pez-de-la-Torre, Bjo¨rn Winkler, Ju¨rgen Schreuer, Karsten Knorr, Miguel Avalos-Borja , *Solid State Comu*., **134**, 245 (2005).
16. H. G. Smith and W. Gläzer, *Phys. Rev. Lett*. **25**, 1611 (1970).
17. H. G. Smith, *Phys. Rev. Lett.* **29**, 353 (1972).
18. W. Weber, H. Bilz, and U. Schroder, *Phys. Rev. Lett*. **28**, 600 (1972).
19. .H.P. Liermann, A.K. Singh, B. Manoun, S.K. Saxena, C.S. Zha, *Int. J. Refractory Metals & Hard Materials* **23**, 109 (2005).
20. Tanmoy Das, Sudipta Deb, Abhijit Mookerjee, *Physica B*, **367**, 6 (2005).
21. Satoshi Iikubo, Hiroshi Ohtani and Mitsuhiro Hasebe, *Materials Transactions*, **51**, 574 (2010).

22. M. Sahnoun, C. Daul, J.C. Parlebas, C. Demangeat and M. Driz, *Eur. Phys. J. B* **44**, 281 (2005).
23. Zhigang Wu, Xiao-Jia Chen, Viktor V. Struzhkin, and Ronald E. Cohen, *Phys. Rev. B* **71**, 214103(2005).
24. Feng Peng, Ligang Han, Hongzhi Fu, and Xinlu Cheng, *Phys. Status Solidi B* **246**, 1590 (2009).
25. Anurag Srivastava , Mamta Chauhan and R.K. Singh, *Phase Transitions* **84**, 58 (2011)
26. S. Baroni, P. Giannozzi and A. Testa, *Phys. Rev. Lett*. **58,** 1861 (1987).
27. Baroni, A. Corso Dal, S. de Gironcoli, P. Giannozzi, C. Cavazzoni, G. Ballabio, S. Scandolo, G. Chiarotti, P. Focher, A. Pasquarello, K. Laasonen, A. Trave, R. Car, N. Marzari and A. Kokalj, http://www.pwscf.org
28. J.P. Perdew and Y. Wang, *Phys. Rev. B* **45**, 13244 (1992).
29. H J Monkhorst and J D Pack, *Phys. Rev. B* **13**, 5188 (1976).
30. P. Giannozzi, S. de Gironcoli, P. Pavone and S. Baroni, *Phys. Rev. B* **43** 7231(1991).
31. E.Toth, Transition Metal Carbides and Nitrides, Academic, NewYork, (1971).
32. P.Villars, L.D. Calvet, Pearson's Handbook of Crystallographic Data for Intermetallic Phases, American Society for Metals, Metals Park, OH, (1985).
33. Y. S. Touloukian, R. K. Kirky, R. E. Taylor and T. Y. R. Lee, (ed.): Thermal properties of matter, TPRC data books, vol. 13. New York, Plenum Press; 1975.

Chapter 4

Structural Stability Analysis of CeN under High Pressure

4.1 Introduction

The physical properties of f-block elements (4f-lanthanides, 5f-actinides) and their compounds are mainly governed by the f electrons. The main difference between the two f electron series can be ascribed to the degree of hybridization of the f orbitals with the conduction electron orbitals. The f electrons in the lanthanides are believed to displays localized nature, whereas, in actinides the f electrons are itinerant and the degree of the itinerancy increases upon traversing from Th to Pu in the light actinide series. Further, the increasing distortion in ambient structure from fcc for Th to monoclinic for Pu is associated to this successively increasing delocalization. Various binary compounds are formed by combination of the lanthanides with simple elements such as C, O, N and S. Among them the mono-nitrides of lanthanides have received much attention due to their unique electronic and magnetic properties, and their use in the potential applications in spintronics [1-17]. The CeN is one of the interesting nitrides among them, which has been classified to be a mixed valence compound in previous studies [1-17]. The common situation found in most of the lanthanides is that the occupied 4f states are well localized and contain integer number of electrons. When such localized 4f states lie very close to or even degenerate with the Fermi level then mixed valance picture comes into existence as these states may start to hybridize with the conduction band states and acquire a width in the meV range. In such conditions also the 4f states may be treated as localized and hybridization can be treated as a perturbation. The CeN, the mononitride of the first member of the lanthanide elements, which crystallizes in the rock salt (B1) crystal structure at ambient conditions, is different in several aspects in the series of rare earth nitrides. For example, the mixed valence picture which is believed to exist in CeN suggests that the state of the Ce ion in CeN fluctuates between the trivalent $4f^1[5d6s6p]^3$ configuration and tetravalent $4f^0[5d6s6p]^4$ configuration. The lattice constant of CeN is significantly smaller than that for the other rare earth mono-nitrides.

Additionally the thermal expansion shows an unusual increase in lattice constants at higher temperatures as compared to that for other rare earth mononitrides. Furthermore, the magnetic susceptibility also displays an unusual dip at higher temperature [12]. Though various above unusual physical properties could be interpreted satisfactorily using the mixed valence model the large difference between the trivalent and tetravalent configurations does not support this model. Therefore the other picture, *i.e.* itinerant 4f picture, is more widely accepted in this compound in which 4f states can be described within band theory as ordinary Bloch states

As far as high pressure behavior of CeN is concerned Rukmangad *et al.* [11] from their theoretical calculations based on two body inter ionic potential model predicted B1 to B2 (CsCl type) structural phase transition at ~ 88 GPa. The recent energy dispersive x-ray diffraction (EDXRD) measurements [18] carried out on CeN sample compressed statically in diamond anvil cell report B1 to B2 structural phase transition at ~ 65 GPa with relative volume change of ~ 10.9% at this pressure. This structural transition has been further supported by *ab-initio* calculations carried out using full potential linear muffin-tin orbital method by the same authors [18]. The B1 to B2 transition pressure reported by this theoretical study is ~ 68 GPa with volume discontinuity of ~ 10.8% at the transition pressure. This high pressure B1 to B2 structural phase transition seen in CeN is in contrast to that observed in mononitrides of its left and right nearest neighbors in periodic Table *i.e.* LaN and PrN which have been reported undergo B1 to a primitive tetragonal structural phase transition at ~ 22.8 GPa and ~ 40 GPa, respectively [15, 12]. This tetragonal structure (B10) having space group symmetry of P4/nmm can be viewed as a distortion of CsCl structure with action in the 2c(0, 1/2, z) and anion at 2a(0, 0, 0) positions. The value of z for LaN is reported to be 0.345 whereas that for PrN is obtained to be 0.3546.

This chapter of the thesis presents theoretical investigation on structural satiability, elastic stability and dynamic stability of B1 phase of CeN under hydrostatic compression. The structural stability has been examined by calculating and comparing the total energy as a function of hydrostatic compression at 0 K for B1, B10 and B2 structures. The transition pressure has been determined by comparing the enthalpies of all the structures. The 0 K isotherm has been determined from the theoretically calculated total energy as a function of volume, and finally converted to 300 K isotherm after adding finite temperature contributions. The mechanical properties have been determined from the theoretically derived single crystal elastic constants. The lattice dynamic stability of B1 and B10 and B2 phases has also been analyzed as a function of pressure.

4.2 Methodology Employed for Present Calculations

To analyze the structural stability of CeN the theoretical investigations have been performed on three phases namely B1, B10 and B2. The detailed analysis of structural stability included both the static lattice calculations and lattice dynamic calculations. All the calculations have been performed employing plane wave pseudopotential method within the framework of Density Functional Theory (DFT) [19] implemented in Quantum ESPRESSO package[20].The first step towards the structural stability analysis was to calculate the total energy of B1, B10 and B2 phases as a function of hydrostatic compression. The total energy calculations have been performed within generalized gradient approximation (GGA)[21] for the exchange correlation potential. The ultrasoft pseudopotential having valence configurations of $4f^1 5s^2 5p^6 5d^1 6s^2$ and $2s^2 2p^3$ has been used for Ce and N respectively. For generation of pseudopotential, the cut off radius in Ce are taken to be 1.8 Bohr for 4f, 5p and 5d, and 1.6 Bohr for 5s and 6s orbitals whereas these in N are taken to be 1.1 Bohr for both 2s and 2p orbitals. Also, non-linear core correction to the exchange-correlation energy functional for Ce has been added. For GGA, we have used PW91 [21] potential for both the atoms. Electronic wave functions are expanded in a plane wave basis set (PWs) with energy cut off of 90 Ry and charge density is represented in PWs with energy cut off of 1000 Ry. Energy convergence of 10^{-6} Ry has been met by using the 12x12x12, 6x6x9, 16x16x16 Monkhorst–Pack (MP) [22] grid of k-points in the full Brillouin zone (BZ) of B1, B10 and B2 structures. The dynamic stability of B1, B10 and B2 phase has been analyzed from the phonon spectra determined from self consistent density functional perturbation theory using linear response method [23]. For phonon dispersion calculations a 4×4×4, 3×3×5 and 4×4×4 q mesh in the first BZ of B1, B10 and B2 structure has been used. The elastic moduli of B1 phase at a given volume are determined using the total energy computed as a function of appropriate strain [24-26]. The elastic moduli are finally extracted by expressing the energy of the strained lattice as described in chapter 2 in section 2.1.

4.2.1 Structural stability analysis and determination of equation of state

To analyze the structural stability under hydrostatic compression, the total energy for B1, B2 and B10 phases of CeN at 0 K have been computed as a function of volume up to about 250 GPa. The B10 structure is a primitive tetragonal cell with space group P_4/nmm. As shown in the Fig. 4.1, the atomic species Ce and N of the two units of CeN contained in the cell are located at 2c (0 ½ z, ½ 0 -z) and 2a (0 0 0, ½ ½ 0) sites (international table of Crystallography, Vol. 2). It may be noted that the B10 structure becomes identical to B2 phase for $c/a = 1/\sqrt{2}$ and z = ½ (Fig. 4.1). In present calculations both the *c/a* ratio and the z in B10 structure have been optimized for all volumes. For this purpose, at each volume, several *c/a* ratios ranging from ~ 0.81 to 0.69 (which include the *c/a* corresponding to B2 structure also) have been chosen and optimized the value of *z* for each *c/a.* The optimum *c/a* and *z* at a given volume is the one for which the total energy is minimum. This procedure was repeated at various volumes and optimum *c/a* and *z* as a function of volume has been obtained. Using the total energy calculated at various volumes the 0 K isotherms has been derived and enthalpies have been calculated for each phase. The structural stability as a function of hydrostatic compression has then been analyzed by comparing the total enthalpies (H) of B1, B10 and B2 phases as a function of pressure.

The 0 K isotherms for B1, B10 and B2 phases of CeN determined from calculated total energy as a function of volume. The 300 K isotherm is derived by adding the thermal contributions to the 0 K isotherm. The zero pressure bulk modulus (B_0) and its pressure derivative at zero pressure (B_0') were obtained by fitting the isotherm so obtained to the third order Birch-Murnaghan equation of state as described in the chapter 2 in section 2.1.

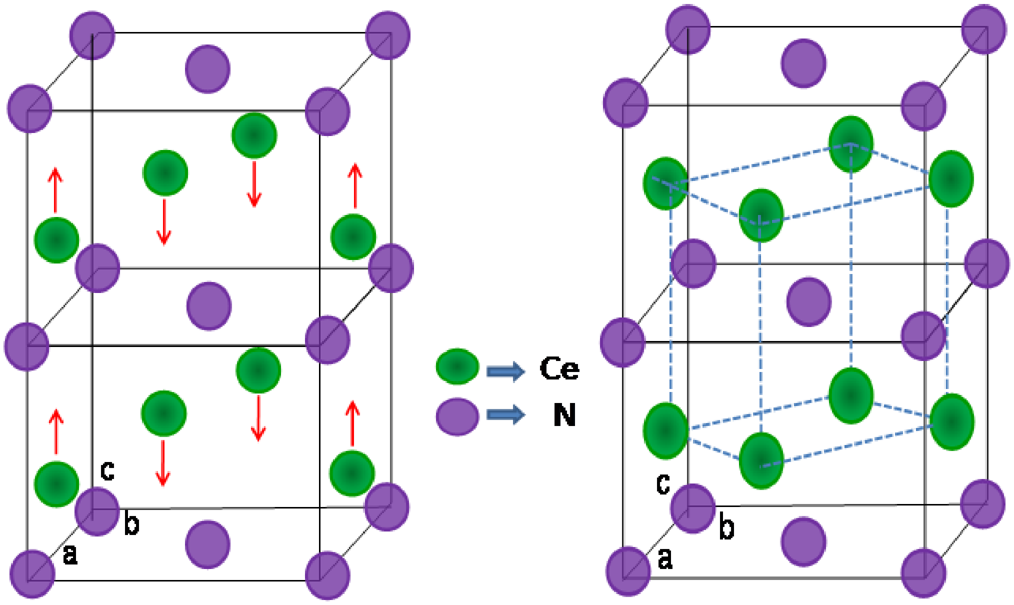

Primitive Tetragonal (B10) structure

Simple cubic (B2) structure

Fig. 4.1 A relationship between B10 (tetragonal with space group P_4/nmm) and B2 structure in CeN. The atomic shuffle needed for B10 structure to transform to B2 structure. In the B10 structure, the nitrogen atoms occupy the 2a (0 0 0, ½ ½ 0) site and cerium atoms occupy the 2c (0 ½ z, ½ 0 -z) location (for B10 structure, z is a free internal parameter). The B10 structure becomes identical to the B2 phase for z = 0.5 and $c/a = 1/\sqrt{2}$. The cell formed by dotted lines in the right hand side figure is the B2 unit cell formed from the B10 structure

4.3 Results and Discussions

4.3.1 Structural Phase Transition Sequence and the EOS

In order to analyze the structural stability of CeN the enthalpies of B1, B10 and B2 structures have been calculated as a function of pressure. The B10 phase is distorted B2 structure and becomes identical to B2 phase for $c/a = 1/\sqrt{2}$ and z = ½. At each compression, we have optimized both the c/a ratio and the z for B10 structure and total energy of the optimized B10 phase is utilized to determine the enthalpy of B10 phase at various pressures. In Fig.4.2, the equilibrium *c/a* and *z* parameter of B10 phase has been plotted as a function of pressure. As can be seen from the figure the *c/a* decreases monotonically with increasing pressure and adopts a value of 0.746 at 53 GPa *i.e.* at B1 to B10 transition pressure; it further decreases to a value of ~ 1/√2 (the value corresponding to B2 structure) at the pressure of ~ 200 GPa and saturates at this value upon further compression. The trend shown by *z* with increasing pressure is opposite to that of *c/a*. It increases with increasing pressure and achieves a value of 0.415 at 53 GPa. Upon further compression it reaches to a value of 0.5 (the value corresponding to B2 structure) at ~ 200 GPa and remains fixed at this value for still higher compressions. These results suggest that for pressures ≥ 200 GPa the B10 phase reduces to B2 structure. Further, Fig. 4.3, displays the enthalpy of the B1 and B10 phase relative to that of the B2 phase as a function of hydrostatic pressure. As shown in the figure, the B10 phase emerges as a structure of lowest enthalpy phase at a pressure of ~ 53 GPa and remains lowest till ~ 200 GPa. For pressures of ≥ 200 GPa, as already discussed, the B10 structure reduces to B2 structure. This structural sequence of B1 → B10 → B2 predicted from the present theoretical calculations is different than direct B1 → B2 transition reported in the static compression experiment by Olsen et al [18].

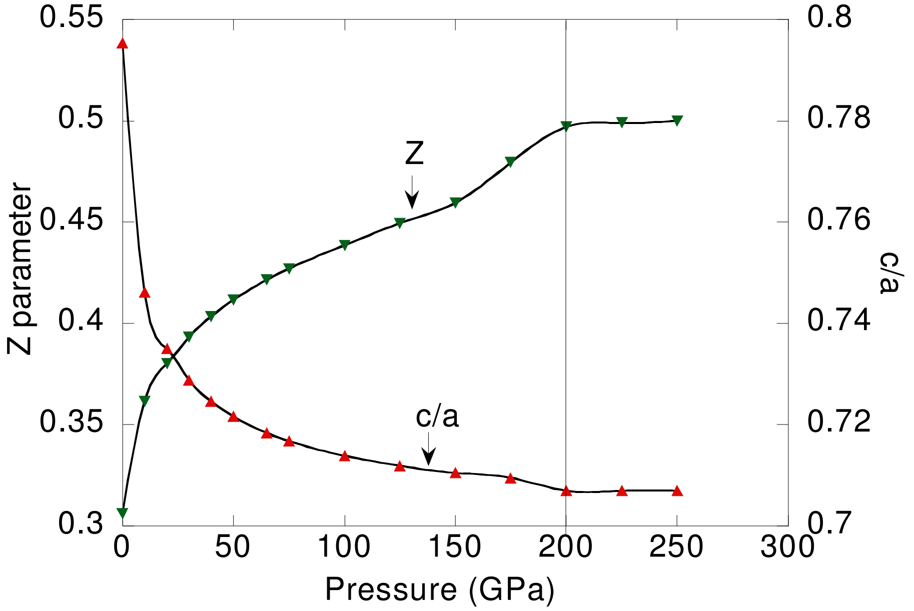

Fig. 4.2 The c/a ratio and z-parameter of B10 phase of CeN as a function of pressure. The vertical line indicates that for pressures ≥ 200 GPa the optimum value of *c/a* ratio and the z parameter of B10 phase become 1/√2 and 0.5, respectively.

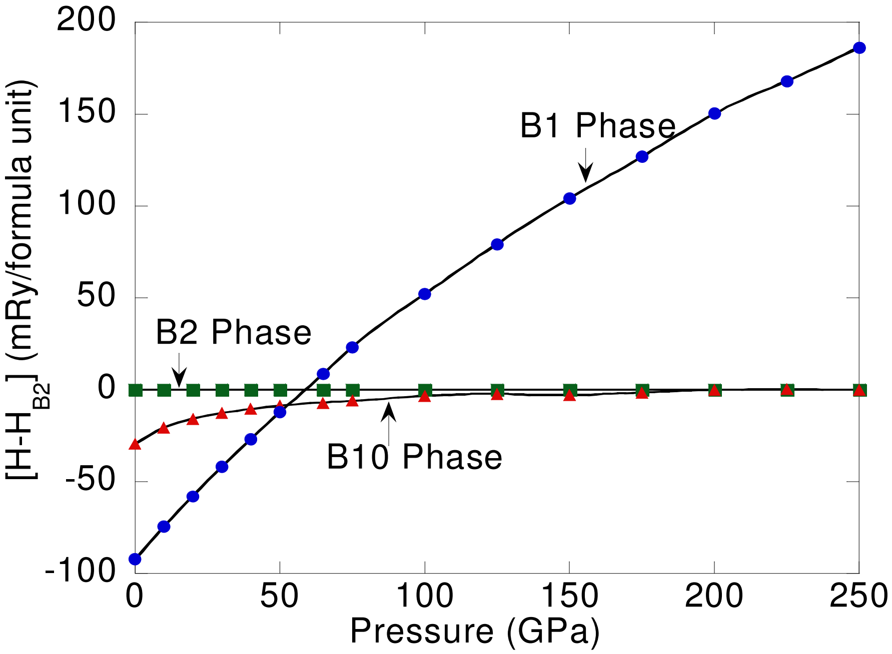

Fig. 4.3 Enthalpy of B1 and B10 phases relative to that of B2 phase for CeN at various pressures. For pressures ≥ 200 GPa, the optimum value of axial ratio and z parameter of B10 phase become 1/√2 and 0.5, respectively, indicating that the B10 phase reduces to B2 structure.

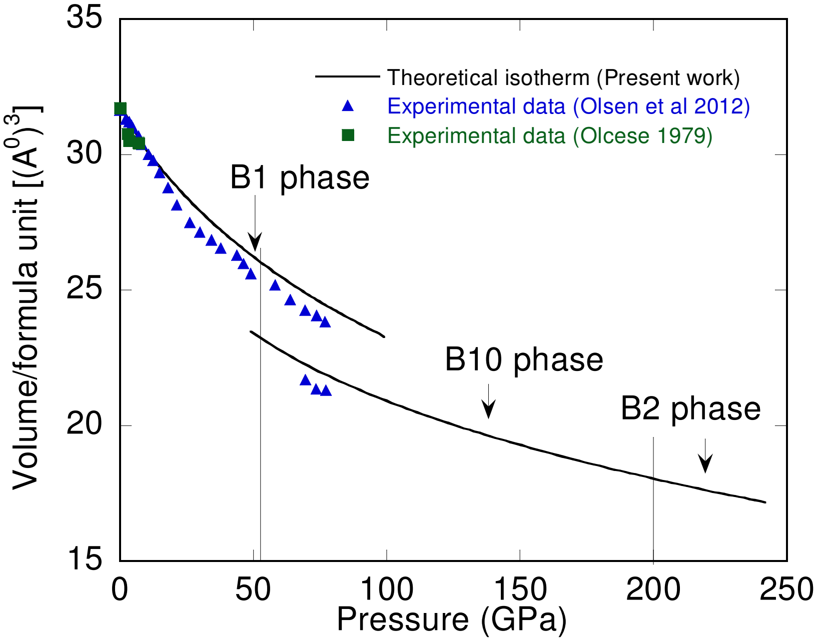

Fig. 4.4: Theoretically determined isotherm of CeN. Also shown are experimental data for comparison**.**

Table 4.1: Comparison of theoretical and experimental values of equation of state parameters of B1, B10 and B2 phases of CeN at zero pressure.

Properties at Equilibrium Volume	Present Theoretical Work	Theoretical (Other sources)	Experimental
B1 Phase:			
V_0 (Å^3/formula unit)	31.85	31.62[9], 32.23[13] 31.70[18] 28.87[27]	31.71[28], 31.64[18] 31.38 [29]
B_0 (GPa)	168.2	158.1[9], 140.02[11] 158.1[18] , 159[27]	156 [18]
B_0'	4.02	3.3[9] , 3.3[18]	4.0 [18]
B10 Phase:			
V_0 (Å^3/formula unit)	30.55		
B_0 (GPa)	99.1		
B_0'	4.90		
B2 Phase:			
V_0 (Å^3/atom)	28.39		
B_0 (GPa)	159.3		
B_0'	4.47		

The Fig. 4.4 compares the theoretical isotherms with the experimental data [18]. The theoretical isotherm at 300 K agrees with the experimental data within ~ 13%. Further as is clear from the figure, the B1 to B10 transition is first order in nature with volume discontinuity of ~ 11% at the transition pressure. Whereas, as obvious from enthalpy plot and the isotherm, the B10 to B2 transition in CeN is second order in nature. Additionally, in Table 4.1, various physical properties derived from total energy calculations are listed for B1, B10 and B2 phases at zero pressure and compared with available experimental data [18, 28, 29] and other theoretical values [9, 11, 13, 18, 27]. The calculated zero pressure volume of B1 phase agrees with experimental data within ~ 1.5%. The bulk modulus and its pressure derivative at this volume for B1 phase are overestimated by ~ 7.8% and ~ 5%, respectively as compared to the experimental values [18]. These quantities for B10 and B2 phases could not be compared with literature due to unavailability of data.

4.3.2 Elastic and dynamic stability under pressure.

Table 4.2, compares the elastic constants for B1 phase at zero pressure derived theoretically in the present work with the theoretical values reported in other sources [9, 11]. Due to non availability of the experimental data, no comparison of these theoretically determined elastic constants of CeN could be done with the experiments. The present theoretical value of elastic constant C_{11} is more close to that of ref. 11 whereas C_{12} and C_{44} agree better with ref. 9. The Debye temperature (θ_D) calculated for B1 phase from elastic constants turns out to be 337 K as compared to the theoretical value of 437 K determined by Kanchana et al.[9] using FP-LMTO method. Further, the elastic stability of B1 phase was analyzed by calculating the elastic moduli as a function of hydrostatic compression and examining the stability conditions throughout the compression path. Fig. 4.5 shows the three independent elastic constants of CeN in B1 phase. As is clear from the figure, the elastic constants C_{11} and C_{12} increase monotonically with increasing pressure, however, the shear elastic constant C_{44} displays opposite trend *i.e.* it decreases monotonically with increasing pressure and vanishes at ~ 110 GPa. It may be noted that though C_{44} in B1 phase decreases monotonically with increasing compression, it does not soften completely at the B1 to B10 transition pressure.

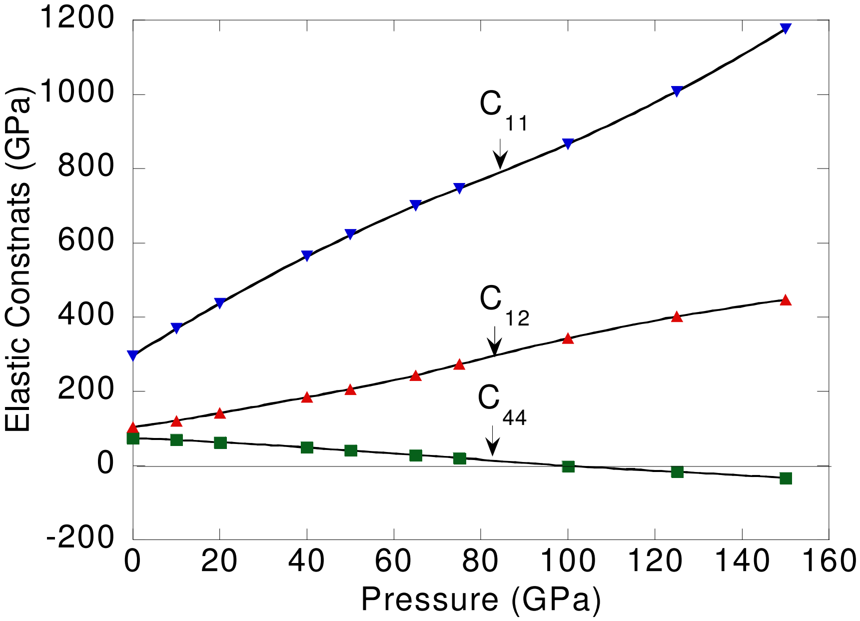

Fig. 4.5 Theoretically calculated elastic constants of CeN single crystal in B1 phase as a function of pressure.

Table 4.2: Elastic Constants of CeN for B1 phase at zero pressure.

Properties at Equilibrium Volume	Present Theoretical Work	Theoretical (Other sources)	Experimental
C_{11}(GPa)	296.6	310[9] , 299[11]	--
C_{12}(GPa)	104	83.2[9], 60.8[11]	--
C_{44} (GPa)	74.9	72.6[9] , 63[11]	--
(θ_D)(K)	337	437[9]	--

In order to confirm the theoretically obtained B1 → B10 → B2 structural sequence in CeN under pressure, further examination of the dynamic stability of B1, B10 and B2 phases has been carried out. The phonon dispersion relations and vibrational density of states calculated at ambient condition for B1 phase are plotted in Fig. 4.6. As expected, the phonon frequencies in all directions are real, demonstrating that the B1 phase is dynamically stable at ambient condition. Just above the theoretically predicted B1 to B10 transition pressure (at 60 GPa); the phonon spectra for the B1 phase (Fig. 4.7) shows that some of the transverse acoustic (TA) phonon frequencies midway of the Γ-X direction become imaginary, thereby making this phase dynamically unstable. However, the B10 phase emerges as dynamically stable structure at this pressure. The B2 phase having imaginary phonon frequencies around M point remains dynamically unstable at 60 GPa. In order to test the dynamic stability of B2 phase at still higher pressures, the phonon spectra have been calculated at higher pressures also. One such spectrum calculated at ~ 225 GPa is plotted in Fig.4.8. As is clear from the figure, the phonon frequencies of B2 phase are positive in all directions suggesting that this phase is dynamically stable at this pressure. The outcomes of lattice dynamic stability analysis further support the high pressure structural sequence of B1 → B10 → B2 suggested by the present static lattice calculations.

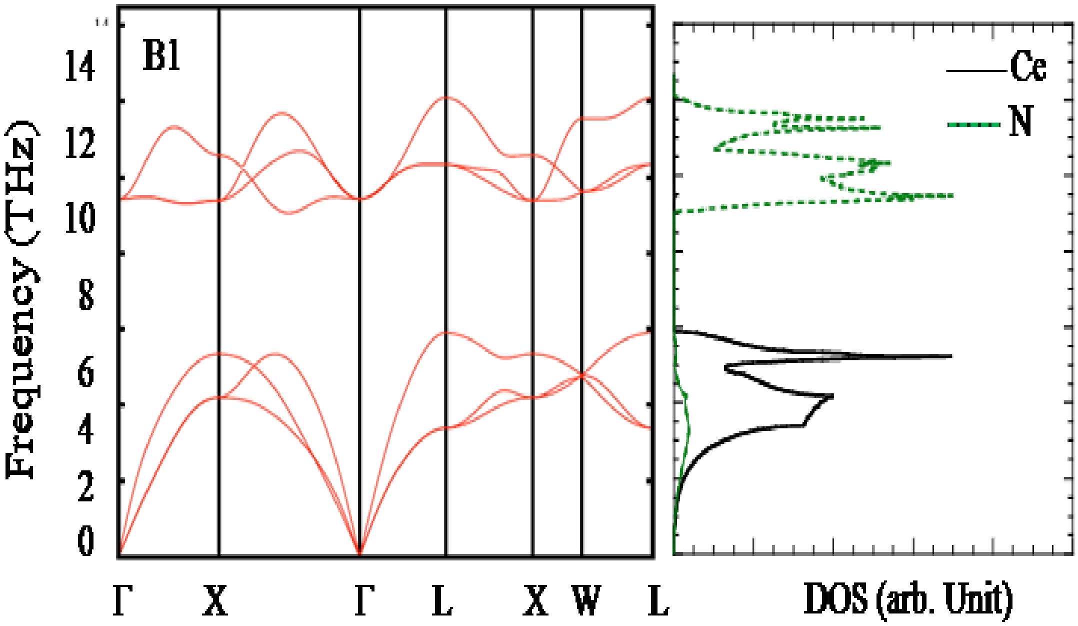

Figure 4.6 Theoretically determined phonon spectra of CeN in B1 phase at zero pressure. The projected phonon density of states is also plotted in the right side.

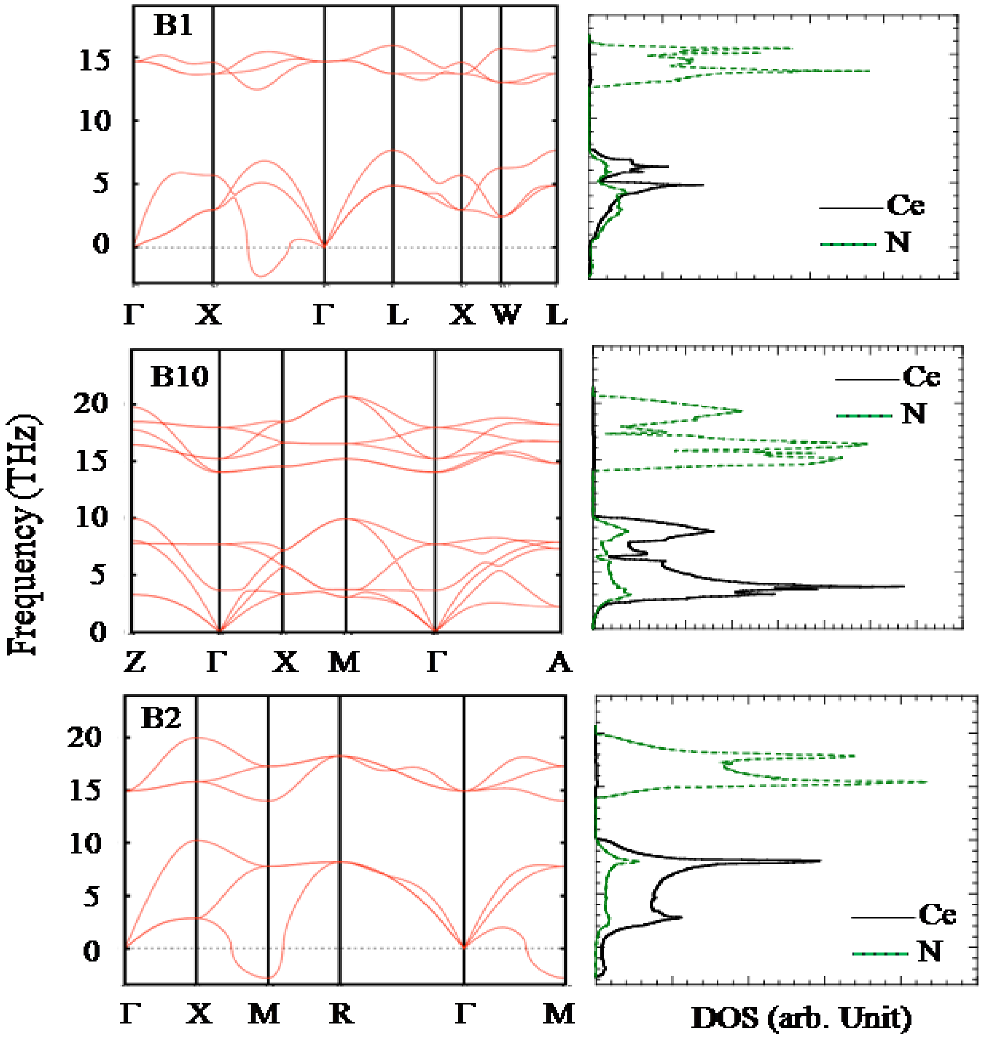

Fig. 4.7 Theoretically calculated phonon spectra and projected phonon density of states of CeN in B1, B10 and B2 phases at ~ 60 GPa *i.e.* around the theoretical B1 → B10 transition pressure.

As expected, irrespective of crystal structure, the projected phonon density of states, plotted in the Fig. 4.6, 4.7 and 4.8 show that the high frequency vibrations are dominated by the N atom due to its relatively lower atomic mass whereas the low frequency vibrations are dominated by Ce atom due to its higher mass.

In order to find the exact pressure at which the B1 phase becomes dynamically unstable, the frequency of transverse acoustic (TA) phonons at X point and at (½, 0, ½) point and longitudinal acoustic (LA) phonons at X point has been plotted as a function of pressure in Fig. 4.9. As can be seen the TA phonon frequency at (½, 0, ½) decreases to zero around ~ 60 GPa. Further, in the same figure, the TA phonon frequency at M point for B2 phase has also been plotted. Figure clearly shows that the B2 structure emerges as a dynamically stable phase at ~ 200 GPa.

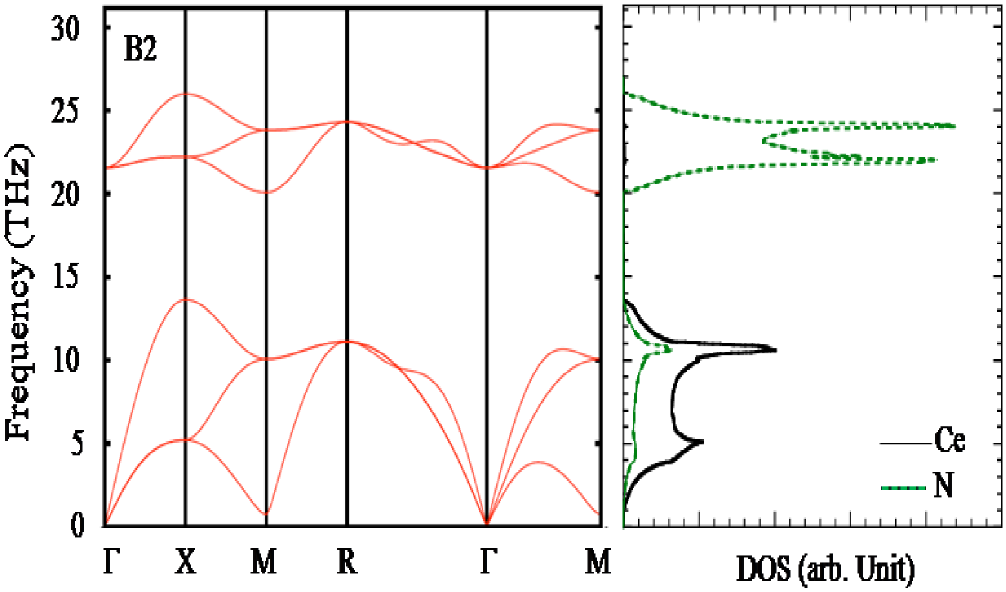

Fig. 4.8 Theoretically calculated phonon spectra and projected phonon density of states of CeN in B2 phase at ~ 225 GPa *i.e.* just above the theoretical B10 → B2 transition pressure

Additionally to substantiate our theoretically predicted high pressure structural sequence, we have calculated the angle dispersive x-ray diffraction (ADXRD) pattern of B1, B10 and B2 structures at 75 GPa *i.e.* around the experimentally reported B1 to B2 phase transition pressure using powder cell 1.0 software. As displayed in Fig. 4.10, except few weak peaks *e.g.* (211), (301), most of the diffraction peaks of B10 structure in the calculated pattern coincide either with B1 or with B2 phase. In the experimental EDXRD pattern [18] recorded at ~ 77 GPa, many peaks *e.g.* (222) and (400) of B1 phase and (210) of B2, which display a good strength in our calculated pattern, are hardly visible. This suggests that in order to unambiguously identify whether the high pressure phase is B2 or B10, it is essential to conduct the experiments at still higher pressures so that the weak peaks, if present, are developed significantly to be visible clearly.

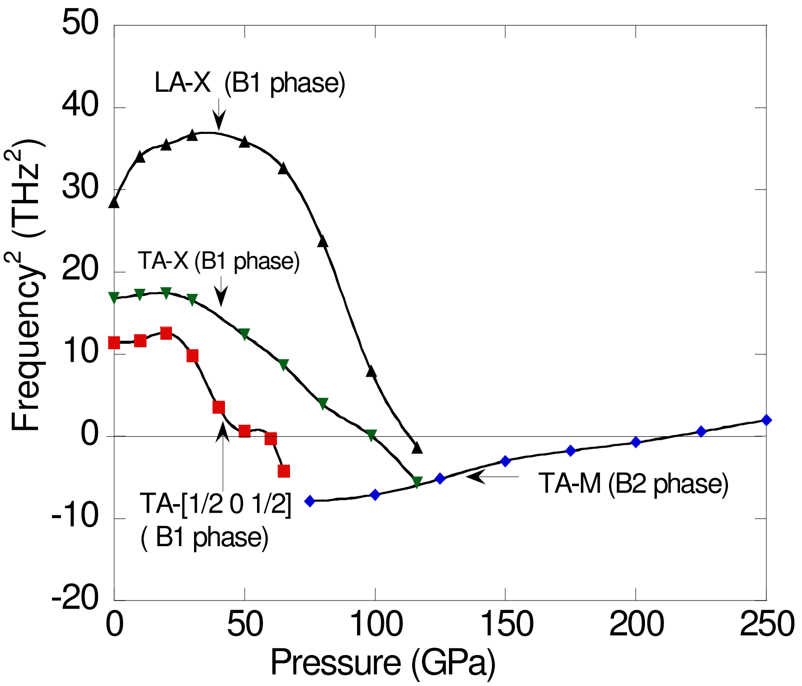

Fig. 4.9 The square of the acoustic phonon frequency at X and (1/2 0 1/2) point in the Brilouin zone of B1 phase and at M point in the Brillouin zone of B2 phase as function of pressure.

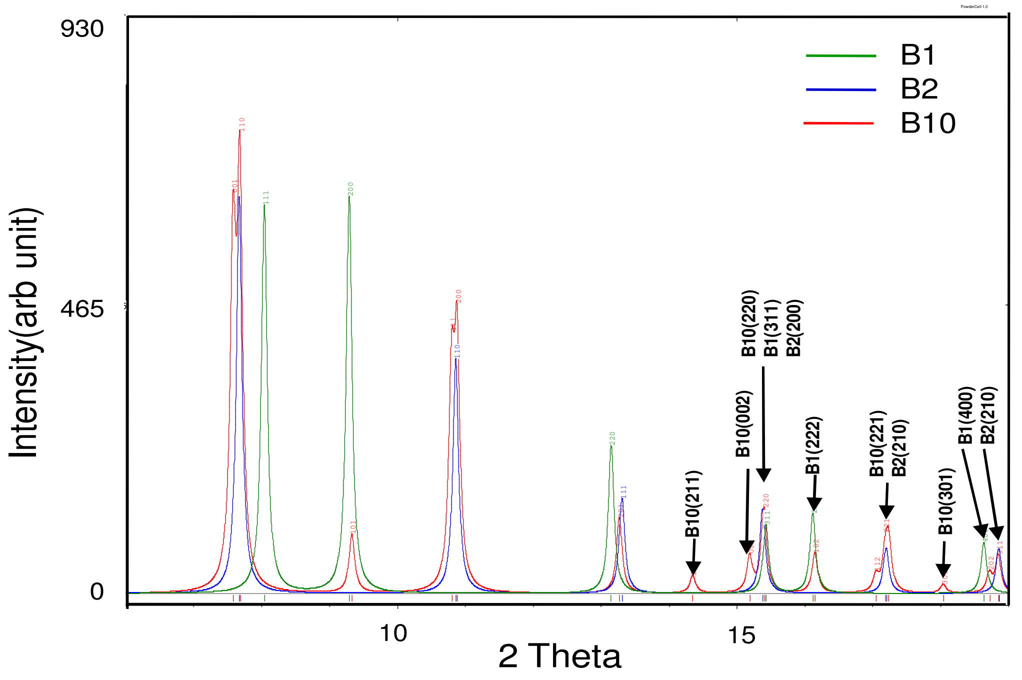

Fig. 4.10 The calculated angle dispersive x-ray diffraction of B1, B2 and B10 Phases of CeN at ~ 75 GPa.

4.3.3 Reproduction of phase transition in LaN

Finally to test whether the calculations carried out using present theoretical method can reproduce the experimental observations of Schneider et al [15] on statically compressed LaN, the total energy calculations on B1, B10 and B2 structures of this materials has also been carried out. The theoretically determined enthalpy is compared for these three phases at various pressures in LaN (Fig. 4.11). As is clear from the figure in case of LaN also present calculations suggest that the B1 transforms to B10 structure at ~ 20 GPa, which is close to the experimental value of 22.8 GPa [15]. Additionally, this work predicted that upon further compression the B10 phase will transform to B2 structure at ~ 165 GPa. Finally, in Fig. 4.12, the theoretically optimized values of *c/a* ratio and internal parameter z along have been plotted along with the experimental data [15] for LaN. Present theoretical *c/a* ratio and z parameter agree with experimental data within ~ 8% and ~ 2.8%, respectively demonstrating that the theoretical calculations correctly reproduce the experimental data of LaN[15], thereby supporting findings of present work on CeN.

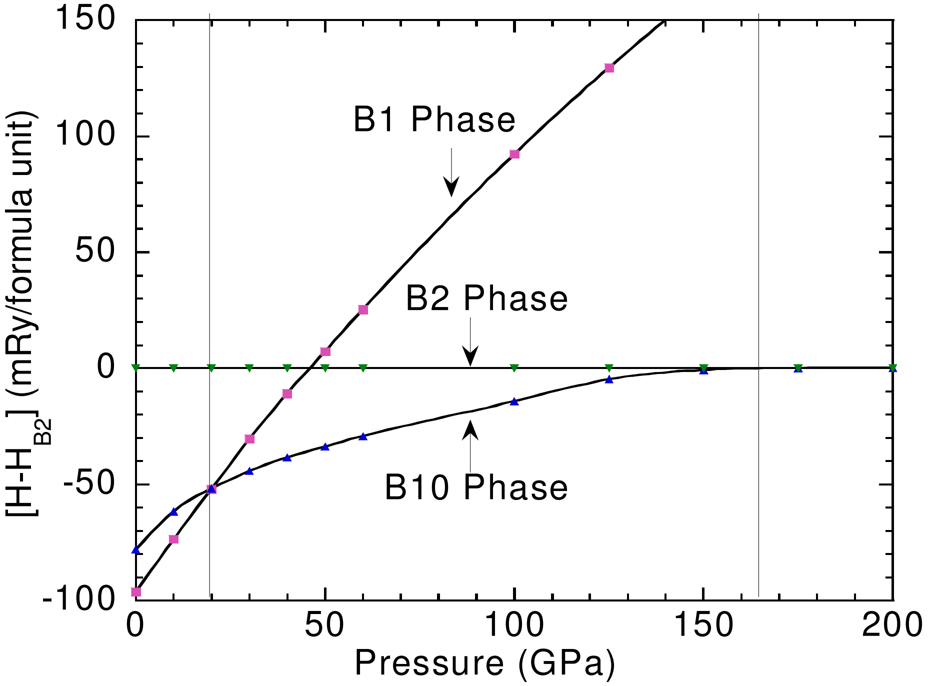

Fig. 4.11 Enthalpy of B1 and B10 phases relative to that of B2 phase for LaN at various pressures.

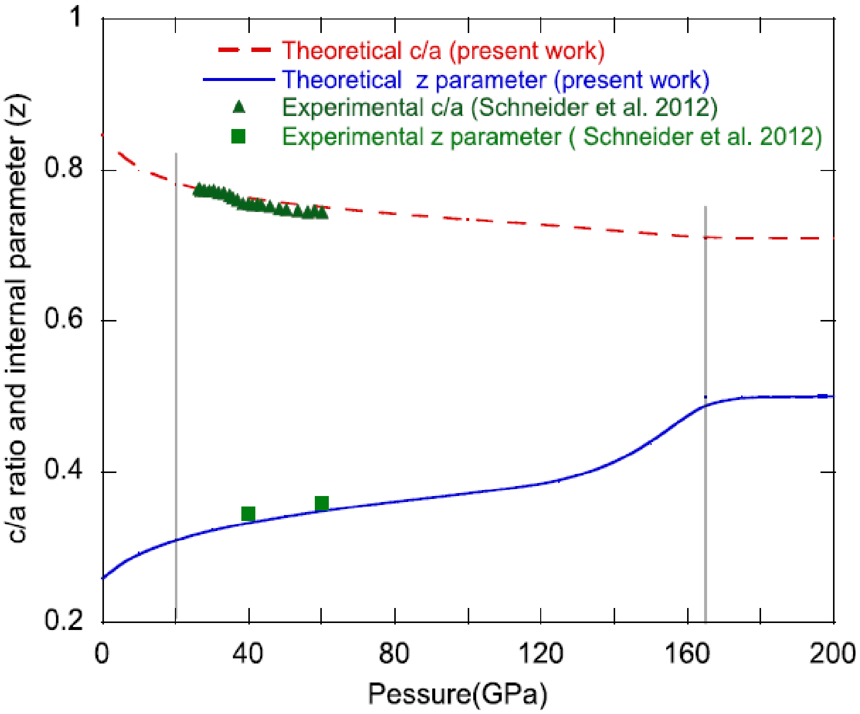

Fig. 4.12 Optimized c/a ratio and z parameter of B10 Phase in LaN. Also plotted the experimental data [15]

4.4 Summary

The structural stability analysis carried out on CeN suggests that B1 phase will transform to B10 structure at ~ 53 GPa which upon further compression will transform to B2 phase at ~ 200 GPa. This theoretical finding does not agree with experimentally reported direct B1 to B2 phase transition at ~ 65 GPa [18]. The present theoretically predicted high pressure structural sequence of B1 → B10 → B2 is also supported by lattice dynamic calculations performed on these phases. The current theoretical work emphasizes that the phonon play dominant role in deciding the structural stability of CeN. Additionally, the theoretically calculated x-ray diffraction pattern of B1, B10 and B2 structures at ~ 75 GPa suggest that more experiments at still high pressures are needed to be conducted to confirm whether the high pressure phase is B2 or B10. Finally, the outcomes of the present work on CeN have been substantiated by reproducing the experimentally reported B1 to B10 transition in LaN.

References

1. A. Jayaraman, W. Lowe and L.D. Longinotti, *Phys. Rev. Lett.* **36**, 366 (1976).
2. A. Werner, H.D. Hochcheimer, R.L. Meng and E. Butcher, *Phys. Lett. A* **97A**, 207 (1983).
3. J.M. Leger, D. Ravot and J. Rossat-Mignod, *J. Phys. C.* **17,** 4935 (1984).
4. J.M. Legger, K. Oki, J. Rossat-Mignod and O. Vogt, *J. Phys.* **46**, 889 (1985).
5. I. Vedel, A.M. Redon, J. Rossat-Mignod, O. Vogt and J. Leger, *J. Phys. C* **20**, 3439 (1987).
6. J.M. Leger, I. Vedel, A.M. Redon, J. Rossat-Mignod and J. Mago, *Magn. Mater* **63**, 49 (1987).
7. N. Mori, Y. Okayama,H. Takahashi, Y Haga and T. Suzuki, *Physica B* **186**, 444 (1993).
8. Anna Delin, P. M. Oppeneer, M. S. S. Brooks, T. Kraft, J. M. Wills, Bo¨rje Johansson and Olle Eriksson, *Phys. Rev. B* **55**, R10173 (1997).
9. V. Kanchana, G. Vaitheeswaran, Xinxin Zhang, Yanming Ma, A. Svane, and O. Eriksson, *Phys. Rev.B* **84**, 205135(2011).
10. S.K. De and S. Chatterjee, *J. Phys. C: Solid State Phys.* **21**, 3261 (1988).
11. Aditi Rukmangad, Mahendra Aynyas and Sankar P. Sanyal, *Indian J. Pure & Appl. Phys* **47**, 114 (2009).
12. Hyunchae Cynn, Magnus Lipp, William Evans and Yasuo Ohishi, *J. Phys.: Conference Series* **215,** 012010 (2010).
13. Mikhail S. Litsarev, Igor Di Marco, Patrik Thunstr¨om, and Olle Eriksson, *Phys. Rev.B* **86,** 115116 (2012).
14. Mohamed Ghezali, Bouhalouane Amrani, Youcef Cherchab, Nadir Sekkal, *Materials Chem. and Phys.* **112**, 774 (2008).
15. Sebastian B. Schneider, Dominik Baumann, Ashkan Salamat and Wolfgang Schnick, *J. Appl. Phys*. **111**, 093503 (2012).
16. G. Vaitheeswaran, V. Kanchana, M. Rajagopalan, *Solid State Commun*. **124**, 97(2002).
17. Sanjay D. Gupta, Sanjeev K. Gupta, Prafulla K. Jha, *Computational Materials Sci*. **49**, 910 (2010).
18. J. Staun Olsen, J.-E. Jørgensen, L. Gerward, G. Vaitheeswaran, V. Kanchana, A. Svane, *J. Alloys and Compounds*, **533**, 29 (2012).

19. S. Baroni, A. Corso Dal, S. de Gironcoli, P. Giannozzi, C. Cavazzoni, G. Ballabio, S. Scandolo, G. Chiarotti, P. Focher, A. Pasquarello, K. Laasonen, A. Trave, R. Car, N. Marzari and A. Kokalj, http://www.pwscf.org
20. J.P. Perdew and Y. Wang, *Phys. Rev. B* **45**, 13244 (1992
21. N. Troullier and J.L. Martins, *Phys. Rev. B* **43**, 1991(1993).
22. H J Monkhorst and J D Pack, *Phys. Rev. B* **13**, 5188 (1976).
23. P. Giannozzi, S. de Gironcoli, P. Pavone and S. Baroni, *Phys. Rev. B* **43** 7231(1991)
24. R. E. Cohen, L. Stixrude, and E. Wasserman, *Phys. Rev. B* **56**, 8575 (1997).
25. S. C. Gupta, K. D. Joshi, and S. Banerjee, *Metall. Mater. Trans*. **39A**, 1593 (2008).
26. J. F. Nye, Physical Properties of Crystals (Oxford University Press, Oxford, 1957).
27. A. Savane, Z. Szotek, W.M. Temmerman and H. Winter, *Sold State Commun*. **102,** 473 (1997).
28. G.I. Olcese, *J. Phys. F: Metal Physics* **9**, 569 (1979).
29. J. Danan, C. de Novion and R. Lallement, *Solid State Commu*. **7**, 1103 (1969).
30. Powder Cell

Chapter 5

Structural Stability Analysis of ThC and UC under High Pressure

5.1 Introduction

The knowledge of various aspects of the electronic structures, mechanical and dynamical properties of actinide carbides is of importance not only due to their applications in the nuclear industry but also from the basic science point of view. The binary compounds of actinide metals, having rocksalt structure (B1 phase), formed by combining with light elements like C, N and O have attracted the attention of both the theoretician and experimentalists since long [1-12]. The *5f* electrons of the actinide metal behaving intermittent to highly localized *4f* electrons in lanthanides and itinerant *d* electrons in transition metals are believed to be responsible for varying physical and chemical properties of these compounds [1, 4, 5, 9, 11]. Among these materials, the good conductivity, high melting point, high metal density combined with the high burn up of the carbides and nitrides as compared to that of the oxides makes them preferable candidates for fuel in generation IV advanced reactors [12]. Among the carbides of thorium and uranium several soichiometries such as the thorium monocarbide (ThC), thorium dicarbide (ThC_2) [3], uranium monocarbide (UC), uranium dicarbide (UC_2) and diuranium tricarbide (U_2C_3) [6-8] are stable compounds at ambient condition. Among the actinide carbides, the thorium monocarbide (ThC) is one of the suitable candidates as an alternative fertile material in advanced fast reactors [5] whereas, the uranium monocarbide (UC) has great potential for applications in nuclear powered rockets for a better power density and in future nuclear reactors [12]. Further, the thorium carbide mixed with uranium-plutonium carbides are potential candidates for use as fuel in generation IV reactors [6, 7]. For such applications the understanding of structural and elastic stability under high pressure and knowledge of various thermophysical properties such as its thermal expansion behavior, heat capacity, bulk modulus etc as a function of temperature is important.

In ThC, Gerward *et al.*[4] carried out the first static high pressure x-ray diffraction measurements using diamond anvil cell and reported that this material remains stable in the rocksalt type structure up to 36 GPa, the maximum pressure achieved in the experiment [4]. The experiment has been repeated further by the same authors [13] up to still higher pressure of ~ 50 GPa and no structural transition has been observed. It may be noted that the samples used in these experimental studies are substoichiometric with carbon deficiency of ~20%.

After this experimental work, a few theoretical investigations have also been reported in this material. For example, in a theoretical study performed by Lim and Scuseria [14] on B1 phase of ThC, authors have reported that unlike that for actinide oxides, the screened hybrid functional produces the structural parameters and band structure as accurate as that calculated by local density approximation (LDA) or generalized gradient approximation (GGA). In a subsequent theoretical work on B1 phase of this compound using the full-potential linearized augmented–plane wave (FP-LPW) method within GGA, Shein and Ivanovskii [15] have reported that the spin orbit coupling (SOC) has negligible effect on the structural parameters and hence can be ignored while modeling the structural properties of ThC. Apart from these theoretical studies carried out to understand the ground state properties, a few investigations to examine the high pressure behaviour of ThC have also been reported. Aydin *et al.*[16] have calculated the thermodynamic properties and pressure and temperature dependence of elastic constants of B1 phase using CASTEP code within three different exchange correlation approximations i.e. LDA, GGA and LDA+U. The study shows that various physical properties *e.g.* zero pressure equilibrium volume, zero pressure bulk modulus and its pressure derivative, derived from GGA calculations display better agreement with the experiments. Recently, Daroca *et al.* [17] have also reported the theoretical investigation on the phonon spectrum and, mechanical and thermophysical properties of ThC in B1 phase.

For UC, several experimental and theoretical studies have been reported [6, 18-22] in the past. For example, Jackman *et al.* [18] have measured the phonon spectra of UC at ambient conditions employing the inelastic thermal neutron scattering and utilized these to determine the U-C and U-U force constants. Graham *et al.* [19] have determined the adiabatic elastic constants of single crystals of this material using acoustic wave velocities measured along various crystallographic directions employing ultrasonic technique. Similar experimental study has been reported by Routbort also [20].

In theoretical front, various studies pertaining to ground state structural and elastic stability of UC have been published [6, 21, 22]. In *ab-initio* study using full-potential linear muffin-tin-orbital (FP-LMTO) technique within local spin density approximation (LSDA), Trygg et al. [6] have calculated electronic structure and elastic constants of ground state structure *i.e.* B1 phase of UC. Their calculated elastic constants at ambient conditions agree well with the experiments [19, 20], however, the zero pressure equilibrium volume of 27.15 $(A^0)^3$/formula unit is underestimated by ~ 11% as compared to the experimental value of 30.5$(A^0)^3$/formula unit [23]. From first principles electronic band structure calculations within generalized gradient approximation (GGA) implemented in the VASP code, Freyss [21] has determined bulk properties of UC and found a good agreement with the experimental data. Based on this, it is suggested that GGA can satisfactorily describe this class of compounds [21]. Apart from these studies at ambient condition, a high pressure energy dispersive x-ray diffraction study has also been reported in this material by Olsen *et al.* [23]. According to this experimental study, the B1 phase of UC transforms to an orthorhombic phase at ~ 27 GPa. This high pressure phase has been reported to be slightly different from the body centre orthorhombic (bco) structure and named as pseudo body centered orthorhombic phase by the authors [23]. The deviation of the high pressure phase from bco structure could not be quantified in the experiment.

With the aim to explore the possible high pressure phase transitions, two monocarbide systems ThC and UC have been investigated by us in detail employing *ab-initio* theoretical methods. The studies include (i) the prediction of structural phase transitions in ThC and reproduction of experimentally observed phase transition in UC under hydrostatic pressure; (ii) the calculation and analysis of phonon dispersion relations to further support the results of our static lattice calculations. In ThC, for prediction of high pressure phase transition the evolutionary structure search method has been used. This method has the capability to predict the stable as well as metastable structures at any pressure without using any priori information, For this purpose USPEX code [24-26] has been used. Apart from the high pressure study, the effect of temperature on thermal expansivity and bulk modulus of ThC has also been examined within quasiharmonic approximations (QHA). All these theoretical investigations have been discussed in this chapter.

5.2 Methodology Employed for Present Calculations

5.2.1 Thorium carbide

As a first step towards the analysis of the structural stability of the ThC, the search for lowest enthalpy structure has been carried out at pressures of 0 GPa, 25 GPa, 60 GPa and 225 GPa using evolutionary structure search method implemented in the USPEX code [24-26]. The calculations required for structure relaxations for this purpose are carried out employing density functional theory based projector augmented wave (PAW) method [27, 28] implemented in the Vienna Ab-Initio Simulation Package (VASP) [29-32]. The exchange and correlation part of the total energy has been calculated using GGA [33]. The structure search at each pressure is carried out using three simulation cells of 4, 8 and 12 atoms, respectively. The PAW (PBE) pseudopotential having valence configurations of $6s^2 6p^6 6d^1 5f^1 7s^2$ for Th and $2s^2 2p^2$ for C has been used. In Th, the cut off radius of the PAW is chosen to be 2.8 Bohr for 7s, 6s, 6d and 5f orbitals and 2.5 Bohr for 6p orbitals. The cut off radius is taken to be 1.2 Bohr for 2s and 1.5 Bohr for 2p orbitals of C. The energy cutoff of 600 eV is used in plane wave expansion of electronic wave functions. The evolutionary structure search method suggested that the B1 phase is the lowest enthalpy structure at 0 GPa, however, at 25 GPa the primitive orthorhombic structure has been found to be of lowest enthalpy. This structure has space group *Pnma* with four atoms of Th and four atoms of C occupying the 4c Wyckoff positions (International Table of Crystallography, Vol. 2) *i.e.* (x,1/4,z) (-x+1/2,3/4,z+1/2) (-x,3/4,-z) and (x+1/2,1/4,-z+1/2). At still higher pressure of 60 GPa, another orthorhombic structure of eight formula units per cell with space group symmetry of *Cmcm* has been found to exhibit lowest enthalpy. In this structure, the eight atoms of Th occupy two crystallographically inequivalent 4c sites, *i.e.* $(0,y_1,1/4)$ $(0,-y_1,3/4)$ $(1/2,1/2+y_1,1/4)$, $(1/2,1/2-y_1,3/4)$ and $(0,y_2,1/4)$ $(0,-y_2,3/4)$ $(1/2,1/2+y_2,1/4)$, $(1/2,1/2-y_2,3/4)$, respectively. The eight atoms of C have been located at the 8f sites *i.e.* (0,y,z) (0,-y,z+1/2) (0,y,-z+1/2) (0,-y,-z) (1/2,1/2+y,z) (1/2,1/2-y,z+1/2) (1/2,1/2+y,-z+1/2) and (1/2,1/2-y,-z), respectively. The two orthorhombic structures are displayed in Fig.5.1. Further, at 225 GPa, it has been found that the B2 structure has lowest enthalpy.

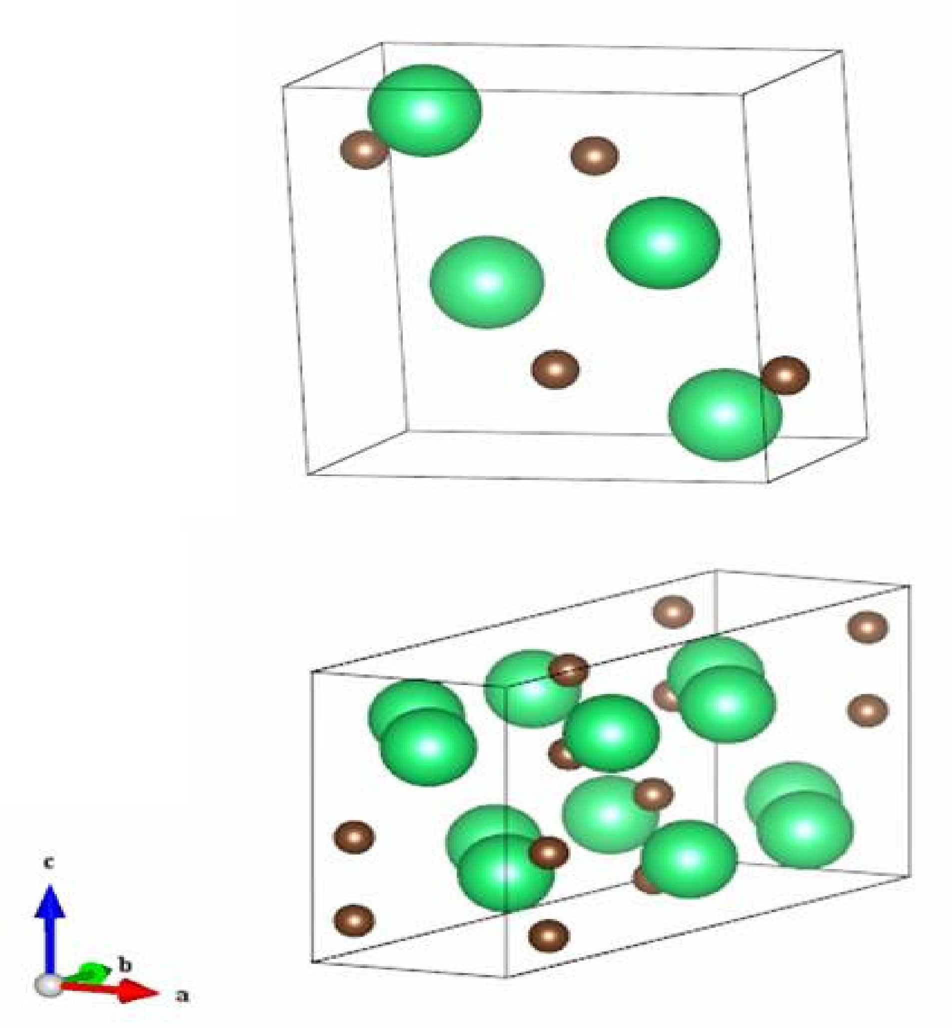

Fig. 5.1 The unit cell of *Pnma* structure (top) and *Cmcm* structure (bottom) of ThC. The large spheres represent the thorium atoms and small spheres show the carbon atoms.

After identifying the lowest enthalpy structures at few pressures, the calculations of total energy have been carried out on these structures, *i.e.* on B1, *Pnma*, *Cmcm* and B2 structures, at several hydrostatic compressions. The aim of these refined calculations was to determine the exact transition pressures. At each compression, we have optimized the axial ratios and free internal parameters for both the orthorhombic structure. The Monkhorst–Pack (MP) [34] grid of 12x12x12 k-points and 16x16x16 k points in the full Brillouin zone (BZ) have been chosen for B1 and B2 phase, respectively, to achieve the energy convergence of criteria of 10^{-6} Ry. The k point grids used in full BZ of Pnma and Cmcm structures is 8x12x8 and 9x5x6, respectively.

Further, the elastic constants of ThC in B1 phase have been determined as a function of pressure. As the B1 phase is a cubic structure, it has only three independent elastic moduli namely bulk modulus B = $(C_{11}+2C_{12})/3$ and two shear moduli $C' = (C_{11}-C_{12})/2$ and C_{44}. To determine all these moduli, the stress-strain approach has been used as implemented in the VASP code. In this approach these elastic moduli can be expressed as [35, 36]:

$$B=\frac{1}{3}\left(C_{11}+2C_{12}\right)=\frac{\partial\sigma_{11}}{\partial\varepsilon_{11}}\ ;\ C'=\frac{1}{2}\left(C_{11}-C_{12}\right)=-\frac{\partial\sigma_{11}}{\partial\varepsilon_{33}};\ C_{44}=\frac{1}{2}\frac{\partial\sigma_{12}}{\partial\varepsilon_{12}} \tag{5.1}$$

In order to analyze the dynamic stability of B1, *Pnma*, *Cmcm* and B2 phase at a given volume the phonon dispersion relations have been determined using lattice dynamical calculations carried out employing the small displacement method within the supercell approach implemented in Phonopy code [37]. The diagonalization of the dynamical matrix constructed from the force constant matrix yielded the phonon frequencies. To determine the displacement pattern and to solve the dynamical matrix, a 3 × 3 × 3 supercell has been used. Forces induced by small atomic displacements were calculated using the VASP program using 4 × 4 × 4 Monkhorst–Pack mesh [34] for BZ integrations.

5.2.2 Uranium carbide

The analysis of structural stability and determination of equation of state of UC has been carried out from total energy calculations within static lattice approximation. These calculations have been performed using two *ab-initio* methods namely plane wave pseudopotential method implemented in Quantum Espresso package [38] and full potential linearized augmented plane wave (FP-LAPW) method implemented in WIEN2K [39, 40] software. For the calculations using plane wave pseudopotential method the electronic wave functions and charge density have been expanded in a plane wave basis set with energy cut off of 150 Ry and 600 Ry, respectively. Energy convergence of 10^{-6} Ry has been met by using 8×8×8 Monkhorst–Pack (MP) [34] grid of k-points for sampling of the full Brillouin zone (BZ). The exchange correlation interaction is treated within generalized gradient approximation (GGA) generated using atomic code by Dal Corso. Troullier-Martins [41] norm conserving pseudopotential having valence configurations of $6s^2 6p^6 5f^3 6d^1$ and $2s^2 2p^2$ has been used for U and C, respectively. For generation of pseudopotential, the cut off radius in U are taken to be 1.52 Bohr for 6p, 1.26 Bohr for 6s, 1.26 Bohr for 5f and 2.2 Bohr for 6d orbitals. For C atom the cut off radius of 1.5 Bohr has been used for both the 2s and 2p orbitals. Also, non-linear core correction to the exchange-correlation energy functional for U has been added. Elastic constants and dynamical stability have determined as described in the chapter 2 of the thesis.

For the calculations based on FP-LAPW method the unit cell has been divided into two regions, the one, non overlapping atomic spheres centered at the atomic sites and the other an interstitial region. The muffin tin radius used for atomic sphere of uranium was 2.2 a.u. while the same for carbon was kept at 1.4 a.u. The parameter $R_{MT}K_{MAX}$ that determines the number of basis functions (size of matrices) is chosen to be 7. Here R_{MT} is muffin tin radius and K_{MAX} is the magnitude of the largest K vector (reciprocal lattice vector) used in plane wave expansion. The dimension of K^2_{max} is that of energy *i.e.* Rydberg. The magnitude of the largest vector (G_{max}) used in charge density Fourier expansion was set to be 14. A grid of 3000 k points was used for sampling of the Brillouin zone. The exchange correlation interaction was treated within generalized gradient approximation (GGA) [33] for all the calculations.

5.3 Results and Discussions

5.3.1 Structural stability, equation of state and electronic density of states of ThC

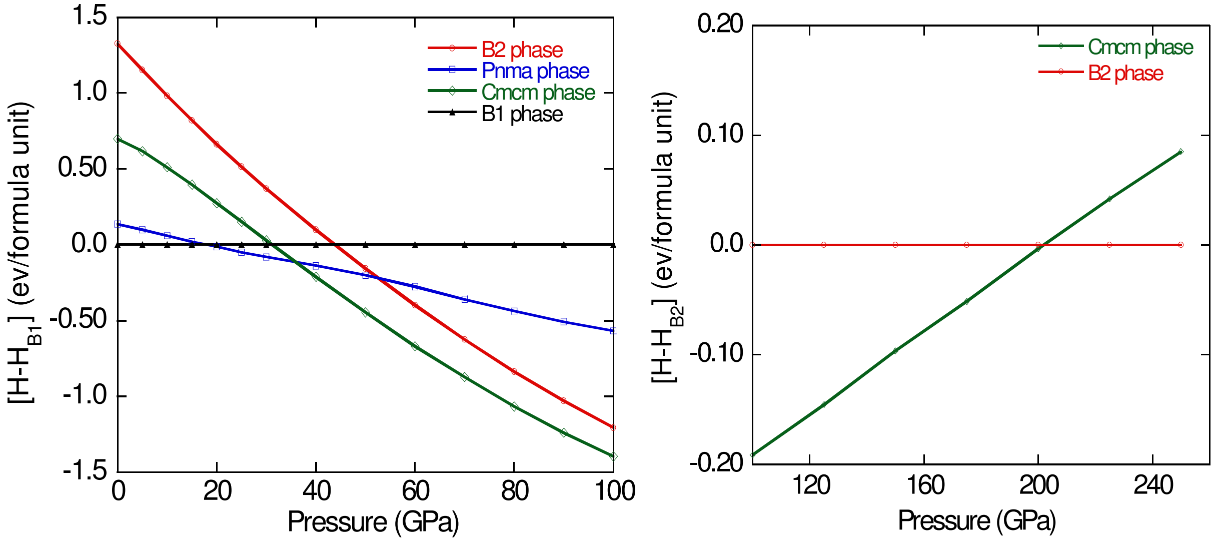

Fig. 5.2 Enthalpies of *Pnma*, *Cmcm*, and B2 phase with respect to that of B1 phase as a function of pressure (left figure) for ThC. The enthalpy of B2 structure relative to that of *Cmcm* phase at various pressures (right figure).

In order to analyze the structural stability of ThC under pressure, first, the search for lowest enthalpy structure at pressures of 0 GPa, 25 GPa, 60 GPa and 225 GPa has been carried out using evolutionary structure search method implemented in the USPEX code [24-26]. Based on this search it has been found that at 0 GPa the B1 phase has lowest enthalpy, whereas at 25 GPa a lower symmetry primitive orthorhombic phase with space group *Pnma* appears as a lowest enthalpy phase. At 60 GPa, it is the *Cmcm* structure which has lowest enthalpy and at still higher pressure of 225 GPa the B2 phase exhibits the lowest enthalpy. Having identified the lowest enthalpy structures at different pressures, refined total energy calculations have been carried out as a function of volume on B1, *Pnma*, *Cmcm* and B2 structures only and derived the enthalpies as a function of pressure. In Fig 5.2, the enthalpies of these phases are compared as a function of pressure. The comparison suggests that the ambient condition stable phase B1 transforms to an orthorhombic phase (space group symmetry *Pnma*) at ~ 19 GPa, which further undergoes a transition to another orthorhombic phase (space group symmetry *Cmcm*) at ~ 36 GPa. Upon further compression, the *Cmcm* phase transforms to B2 structure at ~200 GPa. While performing calculations on the lower symmetry *Pnma* and *Cmcm* structures, the axial ratios as well as internal parameter have been optimized at each volume. In Table 5.1, these have been listed at zero pressure and at transition pressure for *Pnma* and *Cmcm* phases. As is clear from the Table 5.1, for the *Pnma* structure, at zero pressure, the optimum value of b/a and c/a ratio is 0.580 and 1.005, respectively, with the value of free parameter x and z for the Th atom calculated to be 0.250 and 0.916 and for C atom as 0.998 and 0.247, respectively. Further, as depicted in Fig.5.3, both the axial ratios and internal parameters remain more or less constant with increasing pressure.

For *Cmcm* structure, however, as listed in the Table 5.1 and displayed in Fig5.3, the value of b/a at zero pressure is 4.403, which decreases monotonically with increasing pressure and approaches a value of ~ 3.662 at ~ 36 GPa, thereafter, it shows a gradually increasing trend with pressure and acquires a value of ~ 3.843 at ~ 200 GPa. Additionally, the c/a ratio with zero pressure value of 1.609 initially shows a small dip with increasing pressure up to ~ 7 GPa, thereafter it increases gradually with increasing pressure and reaches a value of 1.631 at ~ 36 GPa (Table 5.1) and further increases to ~1.684 at ~ 200 GPa. The value of the internal free parameters y_1 and y_2 for Th atoms at two inequivalent 4c sites are 0.446 and 0.693, respectively, at zero pressure and increases slightly to ~ 0.458 and ~ 0.742 at ~ 36 GPa. Thereafter it remains almost fixed for the entire range of pressure up to ~200 GPa. The free parameters y and z for C atoms have been calculated to be 0.924 and 0.876, respectively, at zero pressure. As shown in Fig. 5.3, the y parameter increase with increasing pressure whereas the z parameter displays opposite trend. At a pressure of ~ 36 GPa these parameters acquire a saturated value of ~ 0.895 and 0.891, respectively (Table 5.1) Thereafter, they remain almost fixed at these values upon further compression.

Table 5.1 Transition pressures and optimized axial ratios and internal parameters of *Pnma* and *Cmcm* phase at zero pressure and at transition pressures.

Parameters	***Pnma* phase**	***Cmcm* phase**
	At P= 0 GPa	**At P= 0 GPa**
a(Å)	6.342	3.506
b(Å)	3.680	15.439
c(Å)	6.373	5.644
b/a	0.580	4.403
c/a	1.005	1.609
Internal parameters	Th: x=0.250, z= 0.916 C: x=0.998, z=0.247	Th: y_1= 0.446, y_2= 0.693 C: y = 0.924, z = 0.876
	At P = 19 GPa	**At P= 36 GPa**
a(Å)	6.131	3.307
b(Å)	3.512	12.114
c(Å)	6.083	5.395
b/a	0.573	3.662
c/a	0.992	1.631
Internal parameters	Th: x=0.250, z= 0.916 C: x=0.998, z=0.247	Th: y_1= 0.458, y_2= 0.742 C: y = 0.895, z = 0.891

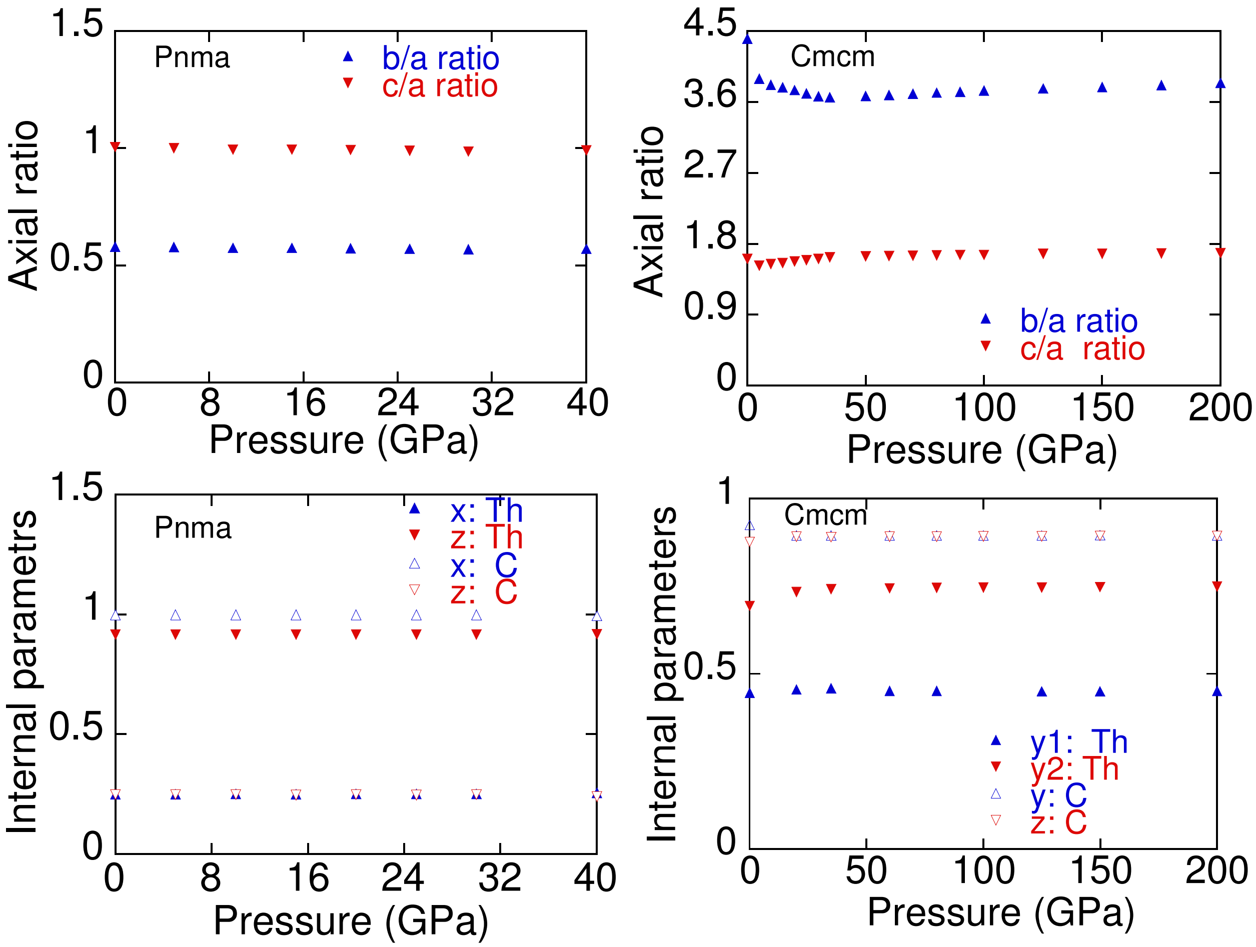

Fig. 5.3 Optimized axial ratios and free internal parameters for *Pnma* structure and *Cmcm* phase of ThC as a function of pressure.

The structural transitions of B1 → *Pnma* → *Cmcm* → B2 with corresponding transition pressures of ~ 19 GPa, 36 GPa and 200 GPa, predicted for ThC in the present theoretical work differs from the results of static high pressure experimental works [4, 13], where ThC is reported to remain stable in B1 phase up to 50 GPa, the maximum pressure of the experiments. However, it may be noted that the samples used in these experiments were not stoichiometric and there was a carbon deficit of ~20%. It has been further reported by these authors [4, 13] that the effect of reducing the carbon content is to reduce the unit cell volume or equivalently the interatomic spacing. This reduction in interatomic spacing due to removal of carbon from lattice sites may have influence on the stability of ThC under pressure. For example, the complete removal of carbon makes the thorium metal to remain stable in fcc phase up to the pressures of ~ 70 GPa (Ref. 42). In light of the discrepancy between the theory and experiment, it will be interesting to perform the high pressure experimental studies for other substoichiometric cases also as it will give more insight on the effect of carbon content on the structural stability of ThC under high pressure.

In Fig.5.4, the theoretically derived isotherm of ThC has been plotted along with the experimental data of Gerward *et al.* [4, 13]. Up to the pressure range of ~ 20 GPa, the two experimentally measured isotherms, *i.e.* those reported by Gerward *et al.* [4, 13] in two separate studies, display fairly good agreement with theoretical isotherm of B1 phase. At higher pressures, the experimental data [4, 13] exhibit a good agreement with the theoretical isotherm of ThC in *Pnma* phase. The volume discontinuities determined at B1 to Pnma transition pressure is ~ 3.3% and at Pnma to Cmcm transition pressure is ~ 9.5% whereas at Cmcm to B2 transition pressure it is ~1.4%. The existence of volume discontinuities at transition pressures suggest that these transitions are of first order in nature.

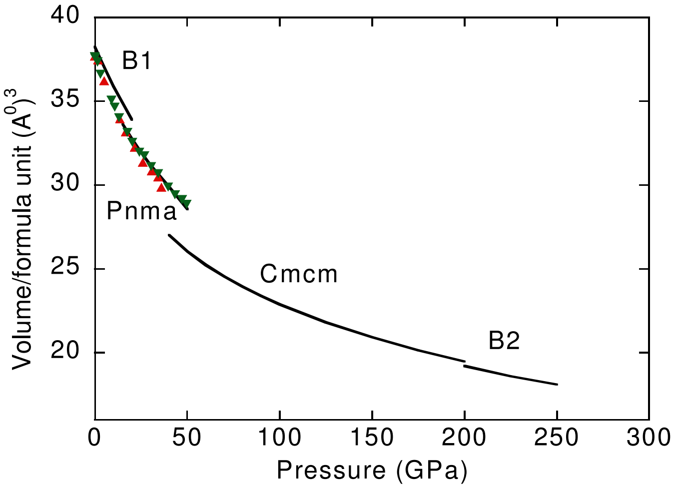

Fig. 5.4 The isotherm of ThC. The solid lines correspond to the theoretical isotherm at 0K. The symbols ▲ and ▼ show experimental data from Ref. (4) and Ref. (13).

Table 5.2, compares the zero pressure equilibrium volume/formula unit (V_0), zero pressure bulk modulus (B_0) and its pressure derivative (B_0') derived from present theoretical calculations at 0K with the experimental data [4, 13] and theoretical values from other sources [5, 14, 16, 17, 43]. As listed in the Table 5.2, the V_0 of 38.24 Å^3 obtained without adding the zero point energy contribution is underestimated by ~ 0.47% from that obtained by including the zero point correction calculated within QHA. Further, this theoretical value agrees with the experimental values [4, 13] within ~ 1.5%. Similarly, the B_0 value of 137 GPa, obtained from isotherm derived from 0K calculations without including zero point energy correction is overestimated by ~ 2.2% as compared to that obtained after adding zero point energy correction. As far as the comparison of B_0 with experimental data is concerned, the theoretical values are overestimated by maximum of ~ 26% and correspondingly its pressure derivative B_0' is underestimated by maximum of ~ 4.8%.

TABLE 5.2. Various physical quantities at zero pressure and 0K

Physical quantities	**Present work**	**Experimental**	**Theory other sources**
V_0 (Å^3/f. unit)	38.24, 38.42[a]	37.68[4] 37.66[13]	39.10[5], 38.06[14], 38.08[16], 37.96[17], 38.75[43]
B_0(GPa)	137, 134[a],131[b]	109 [4,13]	132[5],132[14] 134[16],135[17],121[43]
B_0'	3.09, 2.95[a]	3.1[4]	2.88[14], 3.0[17], 3.31[43]
C_{11}(GPa)	216		276[16], 222[17], 211[43]
C_{12}(GPa)	89		99[16] , 86[17], 76[43]
C_{44}(GPa)	80		87[16], 66[17], 80[43]
θ_D(K)	258	262 [45]	458[16], 311[17]

[a] Quantities obtained from 0K isotherm derived after adding the zero point energy calculated using QHA.
[b]Bulk modulus derived from elastic constants.

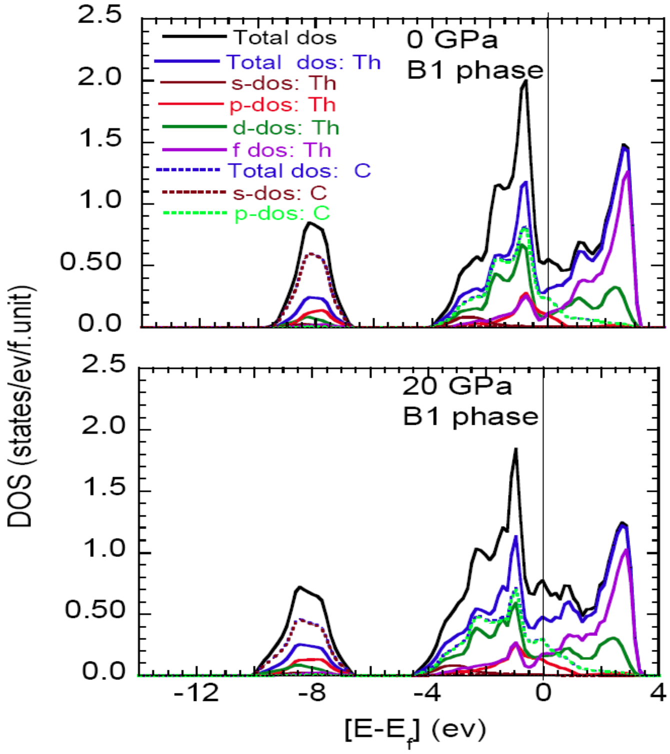

Figure 5.5 Electronic density of states of ThC in B1 phase at 0 GPa and 20GPa, respectively.

As the electronic density of states (DOS) can provide important piece of information related to the orbital character of the states and extent of mixing of various orbitals, it is worth to calculate and analyze these. In Fig.5.5, the electronic density of states of ThC have been displayed for B1 phase at zero as well as 20 GPa *i.e.* around the B1 to *Pnma* transition pressure. Apart from the total DOS and individual contribution of Th and C atom to the total DOS, the partial DOS have been plotted from different orbitals for each atom. As can be seen from the figure, at 0 GPa, the lowest valence band with its peak centered at ~-8 eV from the Fermi energy is separated from the next one by ~ 2.8 eV causing an opening of a pseudogap in the energy range of ~ -6.5 eV to -4.5 eV. Further, there is a significant overlapping between the higher valence band and conduction band, causing DOS at Fermi energy to be sufficiently high ~ 0.52 states/eV/formula unit to make ThC metallic in character at ambient conditions. Further, the total DOS at the lowest valence band are mainly comprised of s-states of C with a small contribution from the *p* and *d*-states of the thorium atom, whereas, the total DOS near the Fermi level at next valence band, dominantly consist of p-states of C and d-states of Th with a small contribution from the Th-*f* and Th-*p* states. The contribution of the Th-5*f* states to the total DOS in conduction bands becomes increasingly significant as one move away from the Fermi level and at ~ 3.1 eV the total DOS of the conduction band is mainly comprised of *f*-states. These results are in agreement with previous studies [14, 16]. As expected, upon compression, at ~ 20 GPa the electronic bands of B1 phase of Th get broaden causing the pseudogap between the lowest valence band and the next one to decrease to ~ 1.9 eV. The Fermi level now lies at a small but sharp hill in total DOS with the DOS at Fermi energy increased to ~ 0.76 states/eV/formula unit. This indicates that the DOS plot of B1 phase develops a typical signature of structural instability at ~ 20 GPa.

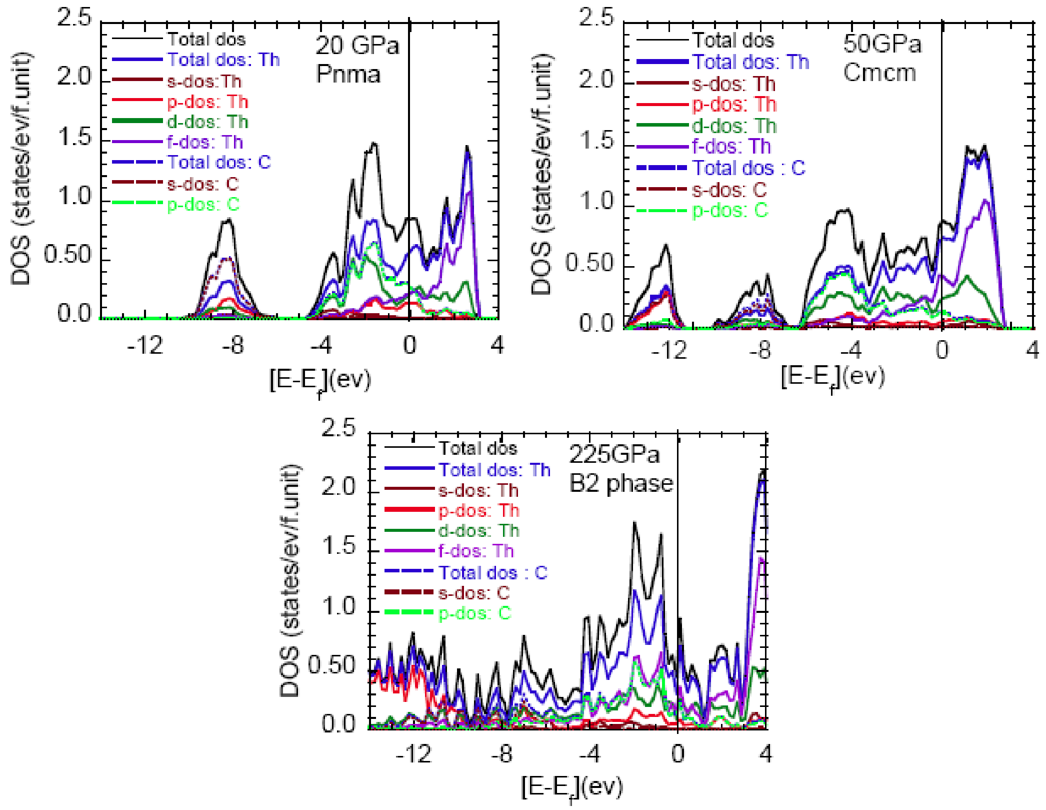

Figure 5.6 Electronic density of states of ThC in *Pnma*, *Cmcm* and B2 phase at 20 GPa, 50 GPa and 225 GPa, respectively.

For further understanding, the electronic DOS have been calculated for the predicted high pressure phases at the transition pressures. The calculated total DOS and various component

DOS are plotted in the Fig. 5.6. At 20 GPa, the major difference between DOS plots of ThC in *Pnma* phase and in B1 phase is that for *Pnma* structure apart from the main peak a small shoulder has also been developed in the lowest valence band and the peaks of higher energy bands have become more distinct. Additionally, the gap between the valance bands is reduced to ~ 1.6 eV as compared to 1.9 eV that for the B1 phase. Further, though, the Fermi level for *Pnma* phase also lies at a small peak in DOS plot, the top of the peak is flat as compared to that for the B1 phase, causing relatively a small variation in the DOS at Fermi energy upon shifting the Fermi level. This enhances the possibility of the *Pnma* structure to be stable relative to the B1 phase at this pressure. As far as metalicity is concerned the nature of DOS suggests that the conductivity of this phase is as good as that of the B1 phase.

For the *Cmcm* structure, DOS have been plotted at ~ 50 GPa *i.e.* in the regime of the stability of the *Cmcm* phase. As can be seen from the figure, for the *Cmcm* phase, the lowest valence band displaying a shoulder at 20 GPa in *Pnma* phase has clearly split into two separate bands with one centered at ~ -8 eV and other centered around -12.1 eV. Further, the total DOS in the former still consists of the *s*-states of C and *d*-states of Th, whereas, the *p*-states of Th have shifted to lower energy, constituting the lower band. To some extent, this splitting of the band may have effect of lowering the energy of the structure as *p*-states of Th have been pushed down in energy. Further, the higher energy edge of the conduction band has been reduced to ~ 2.7 eV as compared to ~ 3.1 eV that in *Pnma* phase at 20 GPa. This could have further caused shifting of various states to lower energy. The metallic character of ThC is still preserved in this phase also.

Finally, as displayed in Fig.5.6, the density of state plot for B2 structure at 225 GPa shows that Fermi level now lies close to a valley with DOS at Fermi energy ~ 0.6 states/eV/f. unit. The extent of the broadening of bands is so large that all the pseudogaps have been closed.

5.3.2 Elastic stability and dynamical stability of ThC

The calculations have also been carried out to determine the elastic constants of the B1 phase of ThC. Table 5.2 compares present theoretical values at zero pressure with those available from other sources [16, 17, 43]. No comparison with the experiments could be done due to non availability of experimental data. Further, these elastic constants have been utilized to determine the zero pressure Debye temperature (θ_D) following the procedure described in the Ref (44). As listed in the Table, the θ_D value of 258 K determined in the present work displays better agreement with the experimental value of 262 K (ref. 45) than those reported in other theoretical studies [16, 17].The calculations of elastic constants are further extended to high pressures. Fig 5.7 displays elastic constants of B1 phase as a function pressure. Further, for comparison, these quantities calculated using energy-strain approach in FP-LAPW calculations in previous work [43] have also been plotted. The C_{11} and C_{44} display good agreement with the data [43], whereas the C_{12} constant in the present calculations is somewhat overestimated as compared to that reported in previous study [43].

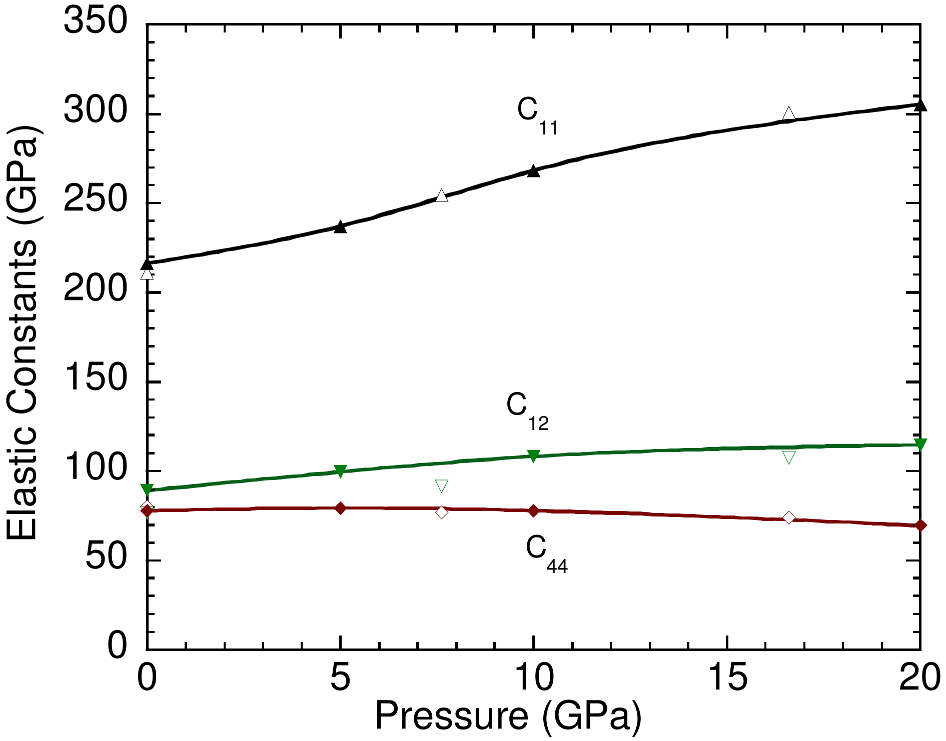

Fig. 5.7 Elastic constants of B1 phase of ThC as a function of pressure. The filled symbols and solid lines represent the values determined in the present work. The open symbol display the elastic constants calculated from FP-LAPW calculations (Ref. 43).

The phonon dispersion relations have also been determined for ThC as a function of pressure to substantiate the outcomes of our static lattice calculations. For this purpose, the lattice dynamic calculations have been performed on B1, *Pnma*, *Cmcm* and B2 phases of ThC at different pressures. Fig.5.8 shows the phonon dispersion relation for B1 phase of ThC at 0 GPa, 25 GPa (just above the B1 to *Pnma* transition pressure) and 35 GPa. As expected, at zero pressure, all the phonon branches along all the Brillouin zone (BZ) directions have positive frequencies. Further, at 25 GPa also, the phonon spectrum suggests that the B1 phase is dynamically stable. Upon further compression, at ~ 35 GPa, some transverse acoustic (TA) phonon frequencies at X-point become imaginary causing the lattice dynamical instability in the B1 phase. The close examination of the phonon spectrum of B1 phase shows that at all pressures the longitudinal optical (LO) branch displays larger dispersion as compared to the transverse optic (TO) branch. Further, as is clear from the figure, there is almost no gap between the optical and acoustic branch at ambient pressure but a gap of ~ 2THz opens up at ~ 25 GPa. The reason for opening of this gap is associated to the increased stiffening of the optical branch at this pressure. It may be noted that the acoustic branch at this pressure remains more or less similar to that at zero pressure. Upon further compression, to ~ 35 GPa, this gap reduces to ~ 1THz due to the softening of one of the TO branch along KX direction caused by a significantly large splitting in this direction.

In order to pin point the pressure corresponding to the failure of TA(X) phonon, this phonon frequency has been plotted as a function of pressure in Fig. 5.9. The exact pressure corresponding to the TA(X) phonon failure obtained from this figure is ~34 GPa.

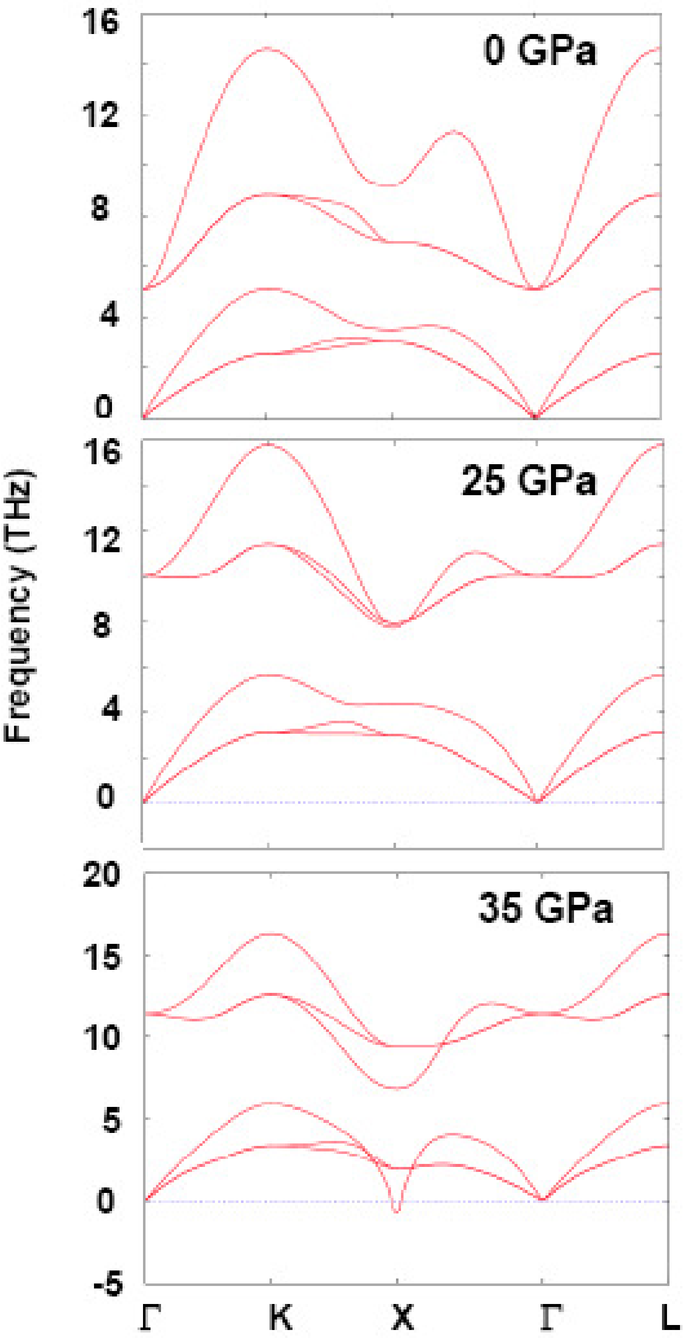

Fig. 5.8 Theoretically determined phonon spectra of ThC in B1 phase at 0, 25 and 35 GPa, respectively.

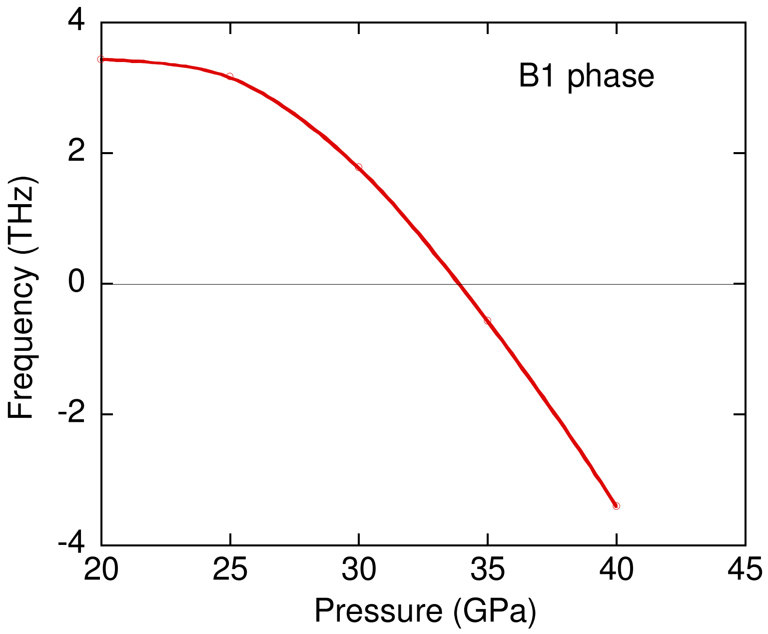

Fig. 5.9 TA (X) phonon frequency as a function of pressure for B1 phase of ThC.

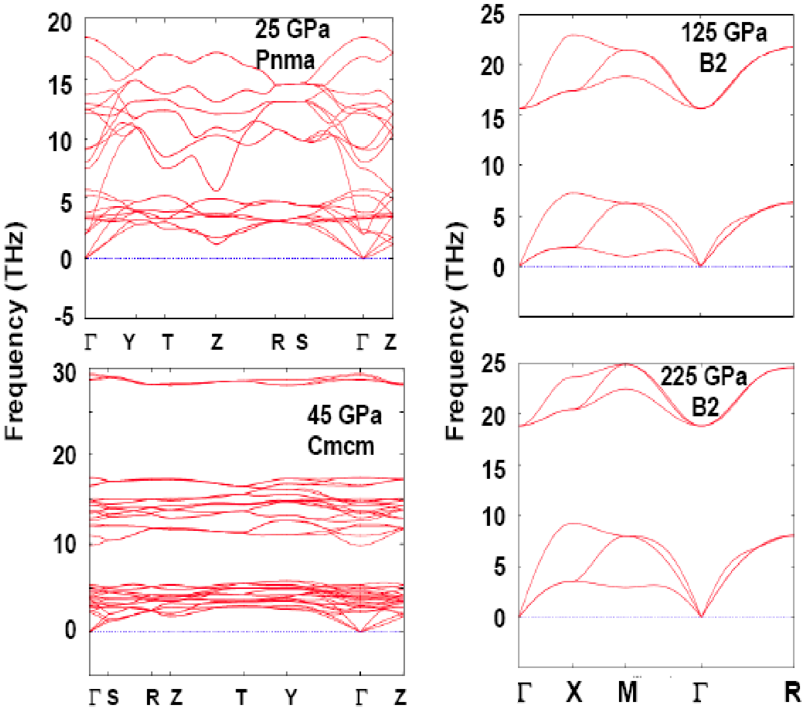

Fig. 5.10 Theoretically determined phonon spectra of ThC for *Pnma* phase at 25 GPa, for *Cmcm* phase at 45 GPa, and for B2 phase at 125 GPa and 225 GPa, respectively.

In Fig. 5.10, the phonon dispersion relations have been shown for *Pnma* structure at ~ 25 GPa, for *Cmcm* phase at ~ 45 GPa and for B2 phase at ~ 125 GPa and 225 GPa. The phonon spectrum for *Pnma* phase at 25 GPa and that for *Cmcm* phase at ~ 45 GPa in this figure display that the phonon frequencies for all modes in all the BZ directions have real values, indicating the lattice dynamic stability of *Pnma* and *Cmcm* phases around 25 GPa and 45 GPa, respectively. Unlike that for *Pnma* structure, for the *Cmcm* phase the phonon spectrum forms three sets of well separated bands. The first set consists of overlapping optical as well as three acoustic branches, whereas reaming two sets are formed of optical branches. Finally, at 125 GPa and 225 GPa, for B2 structure, the phonon frequencies corresponding to different modes are real along all the BZ directions.

5.3.2 Zero pressure thermophysical properties of ThC at high temperature

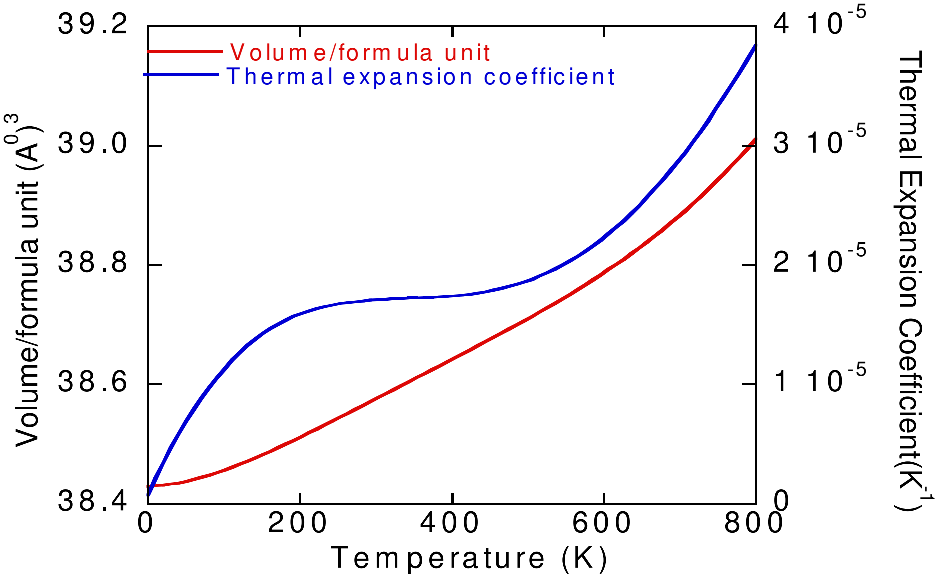

Fig. 5.11 Theoretically calculated zero pressure equilibrium volume and volume thermal expansion coefficient of B1 phase of ThC as a function of temperature.

The lattice dynamic calculations have also been utilized to derive various physical quantities such as equilibrium volume, thermal expansion coefficient, bulk modulus and Helmholtz free energy as a function of temperature at zero pressure for B1 phase of ThC. Fig. 5.11 displays the variation of zero pressure equilibrium volume and corresponding volume thermal expansion coefficient as a function of temperature. As expected, the zero pressure equilibrium volume increases monotonically with increasing temperature and acquires a value of 38.57 $Å^3$ at 300K (Table 5.3), which is higher by ~ 0.4% from its 0K value of 38.42 $Å^3$. This increase in zero pressure equilibrium volume further enhances the overestimation to ~ 2.4% from the experimental value [13]. Here it is worth to mention that the lower value of experimentally measured volume as compared to the theoretical one could be associated to the substoichiometry of the samples used in the experiments [13]. The volume thermal expansion coefficient of 1.7×10^{-5}/K (Table 5.3) calculated at 300 K in the present work, shows better agreement with experimental data [46, 47] as compared to those reported in other theoretical works[16, 17]. Further, as displayed in the figure, there are various features in the plot of thermal expansion coefficient as a function of temperature. For example, at lower temperatures ($T/\theta_D << 1$) it shows a strong dependence upon temperature (rapid increase with increasing temperature) whereas, a weaker dependence upon temperature at higher temperatures *e.g.* from ~ 200K to 430K. At still higher temperatures, the behavior again changes with exhibiting a rapid increase with increasing temperature. This strong temperature dependence at very high temperatures shown by theoretical thermal expansion coefficient may be due to the negligence of the higher order anharmonic effects such as phonon-phonon interaction in QHA. As it is well known that the phonon-phonon interaction becomes significant at high temperatures and increases with increasing temperature, the neglect of this effect at high temperatures might be the cause for the overestimation of the thermal expansion coefficient in ThC.

TABLE 5.3. Various physical quantities at zero pressure and 300K

Physical quantities	Present work	Experimental	Theory other sources
V_0 (Å^3/f. unit)	38.57	37.68[4],37.66[13]	38.30[16],38.25[17]
B_0(GPa)	128	109[4,13]	132[16]
$\alpha(\times 10^{-5}K^{-1})$	1.7	1.95[46],1.38[47]	2.5[16], 2.72[17]
C_v (J/K/mol)	44.98		46.29[16],45.11[17]
γ	1.132		1.562[16]
C_P (J/K/mol)	45.24	45.1[45]	45.69 [17]
$S_{vibration}$(J/K/mol)	60.89	58.3[45]	

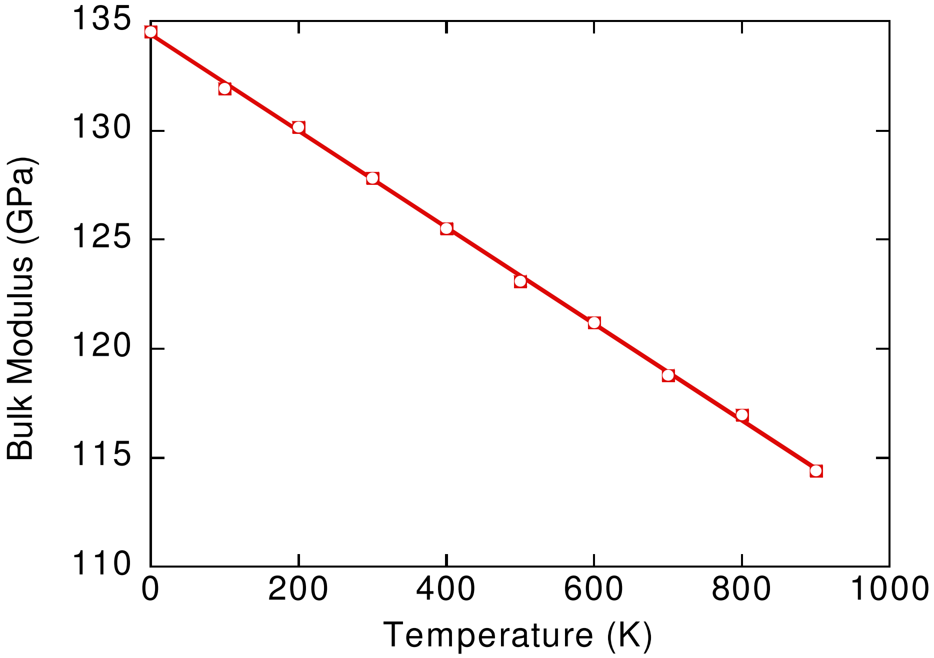

Fig. 5.12 Theoretically calculated zero pressure bulk modulus of B1 phase of ThC as a function of temperature

Fig. 5.12 shows the temperature dependence of the zero pressure bulk modulus of ThC in B1 phase. As observed in general, the bulk modulus decreases monotonically with increasing temperature and reaches a value of ~ 128 GPa (Table 5.3) at 300K which is lower by ~ 4.4% from its 0K value of 134 GPa. This shifts the theoretical value more close to the experimental data [4, 13].

Further, the zero pressure constant volume heat capacity C_V as a function of temperature has also been calculated. The value of C_V calculated at 300K is compared with the other theoretical values [16, 17] in Table 5.3. The agreement is quite good. Now, as one measures the constant pressure specific heat (C_P) in experiments instead of C_V, so to have a comparison with experimental data, C_P has been determined employing the theoretically derived C_V in the following expression:

$$C_p(T) = C_v[1+\alpha(T)\gamma\ (T)T]$$

Where, the Gruneisen parameter (γ) as a function of temperature is evaluated using the expression:

$$\gamma(T) = \alpha(T)B_0(T)V_0(T)/C_v$$

In Table 5.3, the value of γ so obtained at 300 K is compared with the available theoretical value from other source [16]. Finally, in Fig. 5.13, the presently calculated C_V and C_P have been plotted as a function of temperature, also, plotted are the experimental data [45] and other theoretical values [17, 45] for comparison. As expected, the C_V starts approaching the Dulong-Petit limit asymptotically at the temperature T ~ θ_D. As far as comparison with experimental data is concerned, the present theoretical values display an excellent matching with experiment. The present theoretical C_V and C_P agree with the theoretical values of Daroca *et al.* [17] at least up to 675 K, thereafter, these quantities, especially, the C_P deviates systematically. The 300 K value of C_P determined in the present work (Table 5.2) agrees with the experimental data[45] within ~ 0.3%.

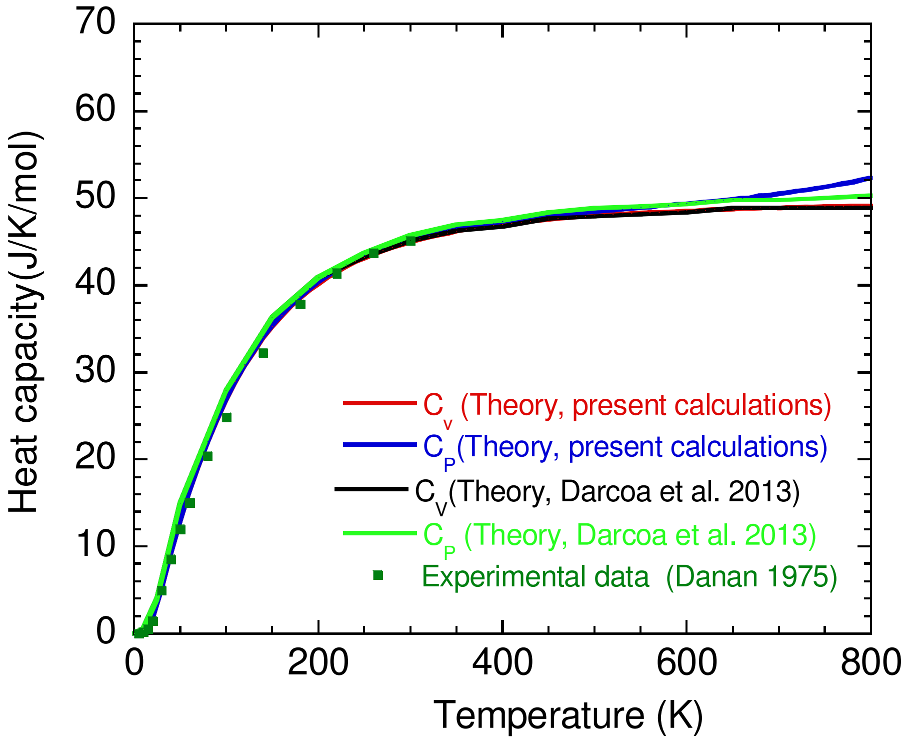

Fig. 5.13 Theoretically calculated zero pressure heat capacity of ThC in B1 phase as a function of temperature.

Finally, Fig. 5.14 shows the temperature dependence of the vibrational free energy $F_{vibration}$, along with its components $E_{vibration}$ and $TS_{vibration}$ for B1 phase at zero pressure. Also, plotted are the experimentally measured data [46] for comparison. As is obvious from the figure, although both the term $TS_{vibration}$ and $E_{vibration}$ increase monotonically with increasing temperature, the increase in former is more rapid as compared to that in latter, causing $F_{vibration}$ to decrease the with increasing temperature. The theoretically determined variation of $TS_{vibration}$ with temperature shows excellent agreement with the experimental data [45]. Further, Table 5.3, compares the present theoretical vibrational entropy $S_{vibration}$ at 300 K with the experimental data [45]. The agreement with experiment is within ~ 4.4%.

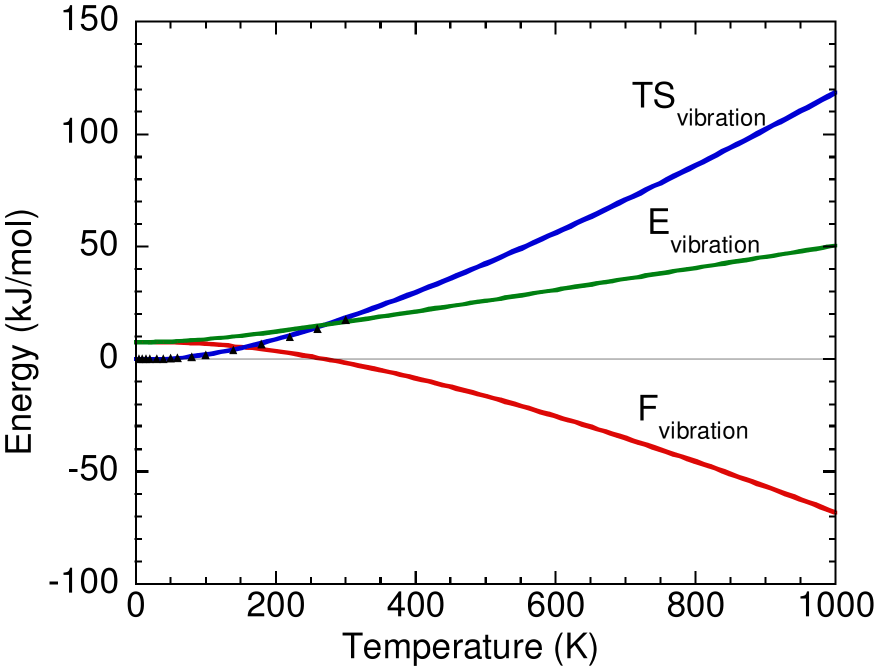

Fig. 5.14 Theoretically calculated zero pressure Helmholtz free energy of ThC in B1 phase as a function of temperature. Also plotted are various components of the free energy. The solid curves represent the theoretical values and symbols correspond to the experimental data (Ref. 45).

5.3.4 Structural stability and equation of state of UC

As a first step towards the analysis of structural stability of UC, the relative stability of non magnetic and antiferromagnetic orderings in B1 phase of UC has been examined. For this purpose the total energy of B1 phase at various volumes has been calculated for non magnetic as well as antiferromagnetic case using FP-LAPW method. For the antiferromagnetic case the B1 structure has been represented as tetragonal cell having $c/a = \sqrt{2}$ with U atoms located at (0,0,0) and (1/2,1/2,1/2), and C atoms situated at (0,0,1/2) and (0,1/2,1/2). At all volumes the non magnetic structure was found to be lower in energy by ~ 0.1 mRy/formula unit than the antiferromagnetic one as shown in Fig. 5.15. Though this value of energy difference between antiferromagnetic and non magnetic structure is within the error limit of the present theoretical method, it suggests that there is no significant difference in total energy for the two configurations. Further, the equation state derived for both the ordering in B1 phase is displays in Fig. 5.16. As is clear from the figure the isotherm derived from the calculations for non magnetic case shows better agreement with the experimental data than that for the antiferromagnetic case. Therefore, further calculations to understand the structural, elastic and dynamical stability of UC under pressure have been performed for non magnetic case within GGA only.

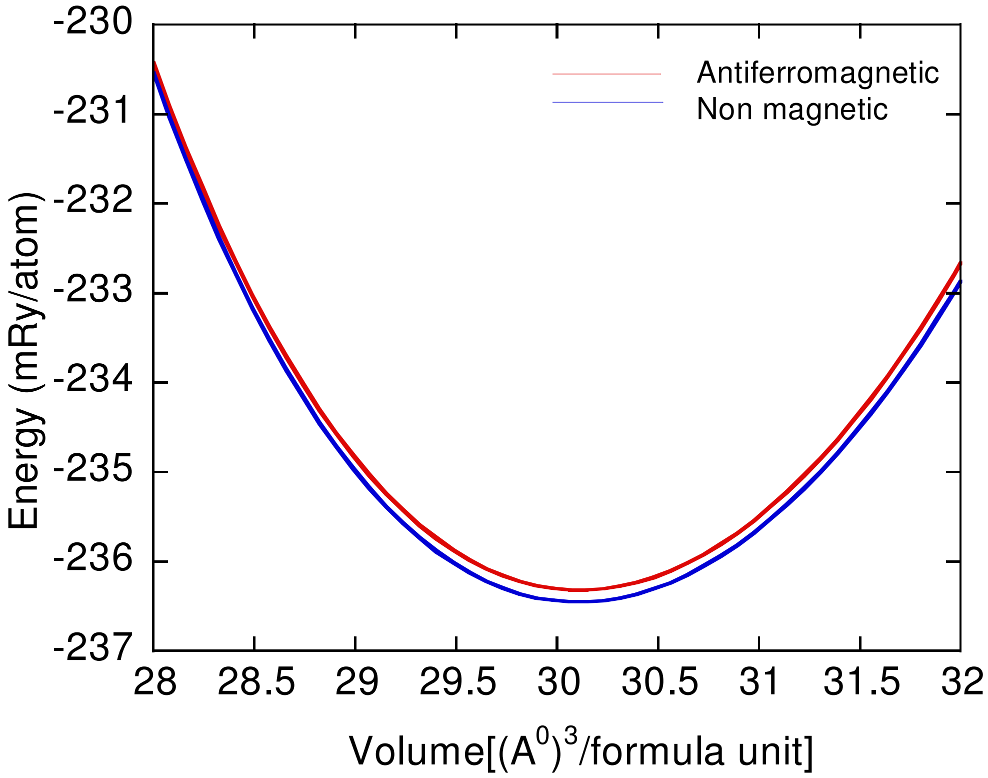

Fig. 5.15 Comparison of energy of B1 phase of UC calculated for non magnetic and antiferromagnetic case using FP-LAPW method.

To analyze the structural stability under hydrostatic compression, the total energy for B1, Pmmn and Immm phases at 0 K have been computed as a function of volume up to about 50 GPa. In the Pmmn structure, which has a primitive orthorhombic cell, the atomic species U is located at 2a (0 0 z_1, ½ ½ -z_1) and C is located at 2b (0 ½ z_2, ½ 0 –z_2) (international table of Crystallography, Vol. 2). It may be noted that the Pmmn structure is a distorted B1 phase (Fig.5.17) which for *b/a* =√2, *c/a* =1 and z_1=z_2=1/4 becomes identical to B1 phase. In other words, the B1 and Pmmn structure are related by group-subgroup relation. Further, if the internal parameters of Pmmn cell are changed such that z_1=z_2=1/4 the Pmmn Structure reduces to Immm structure. In present calculations, the optimization of both the axial ratios (*c/a* and *b/a*) and the z_1, z_2 of Pmmn structure has been carried out at all pressures. The optimum *c/a, b/a,* z_1 and z_2 at a given volume is the one for which the total energy is minimum. In order to analyze the structural stability of UC the enthalpies of B1, Pmmn and Immm structures have been calculated and compared as a function of pressure. In case of Pmmn phase, at each compression, optimization of both the axial ratios (*c/a* and *b/a)* and the z_1, z_2 have been performed and total energy of the optimized Pmmn phase as a function of pressure is determined. This energy is then used to generate P-V data for Pmmn phase, which finally is utilized to determine the enthalpy of this phase at various pressures.

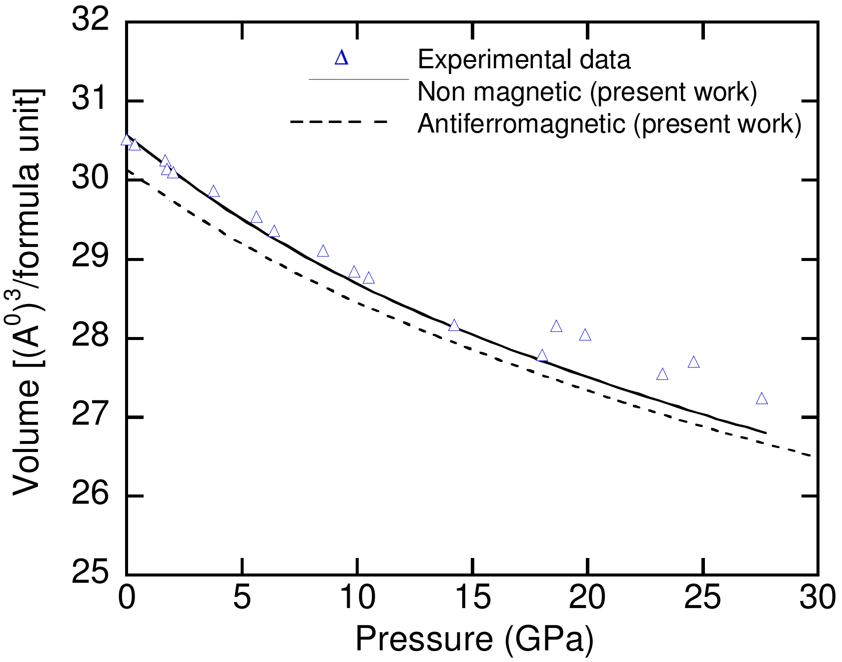

Fig. 5.16 Comparison of equation of state of B1 phase of UC calculated for non magnetic and antiferromagnetic case using FP-LAPW method also plotted are experimental data [10]

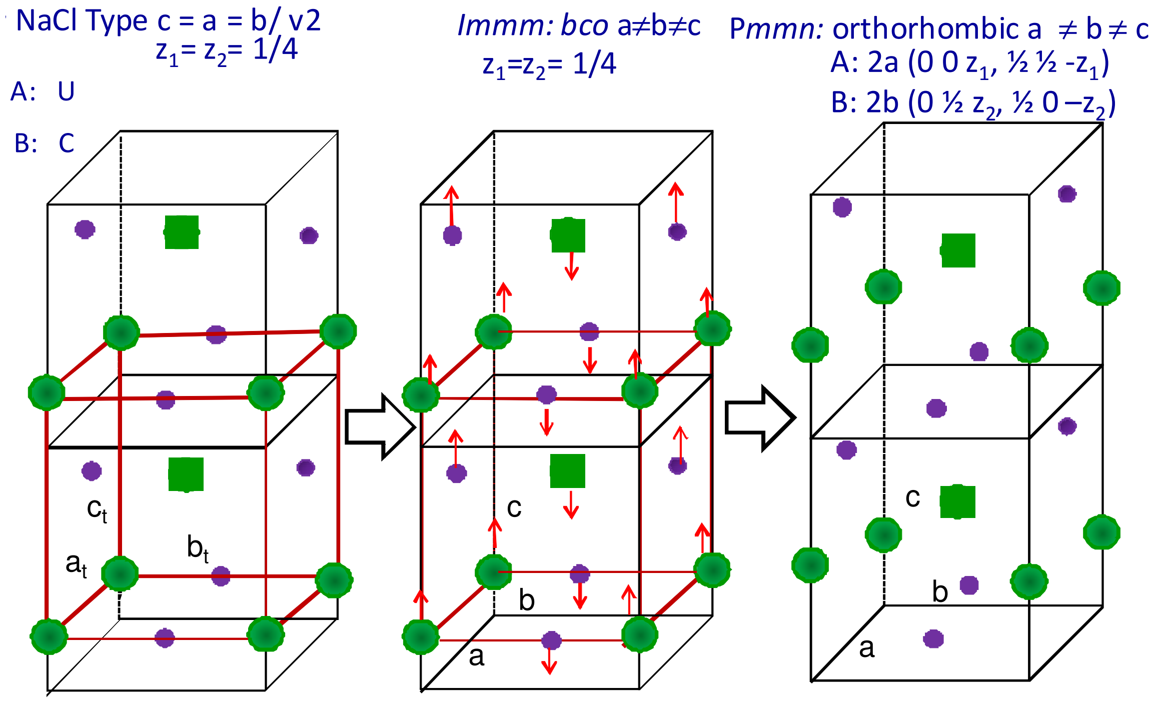

Fig. 5.17 The relation between the Pmmn,B1 and Immm structure. The Pmmn structure (1×1×2 supercell shown in left figure) has U atom located at 2a (0 0 z_1, ½ ½ -z_1) and C atom located at 2b (0 ½ z_2, ½ 0 –z_2). The big and small filled circles correspond to U and C atom, respectively.

In Fig. 5.18 the optimized axial ratios parameters of Pmmn structure of UC is plotted as a function of pressure. As is obvious from the figure, the optimum value of *c/a* and *b/a* ratio at zero pressure are 1.0 and √2, respectively and remain unchanged up to the pressure 20 GPa. Upon further compression, these ratios start increasing with pressure and almost saturate at a value of ~ 1.19 and ~ 1.45, at ~25 GPa. The optimized values of z_1 and z_2 are found to be identical and fixed at ¼ up to the pressure of ≤ 20 GPa as shown in Fig.5.19. At still higher pressures, these parameters start differing from each other and display opposite trend with increasing pressures *i.e.* z_1 increases whereas z_2 decreases with increasing pressure. This change in z_1 and z_2 continues with increasing pressure and acquire the values of ~ 0.31 and ~ 0.19 at 25GPa which remain more or less fixed at these values at still higher pressures. This behavior of axial ratios and the internal free parameters with pressure indicates that the B1 to Pmmn phase change occurs at ~ 20 GPa.

Further, in Fig.5.20, a comparison of the enthalpies of Pmmn and Immm structures relative to B1 phase for UC has been presented. As shown in Fig.5.20, the onset of B1 to Pmmn transition takes place at ~ 20 GPa as compared to the experimental value of 27 GPa [10]. Further, it is clear from the Fig.5.20 that around the B1 to Pmmn transition pressure the enthalpy of Immm phase is very close to that of Pmmn phase.

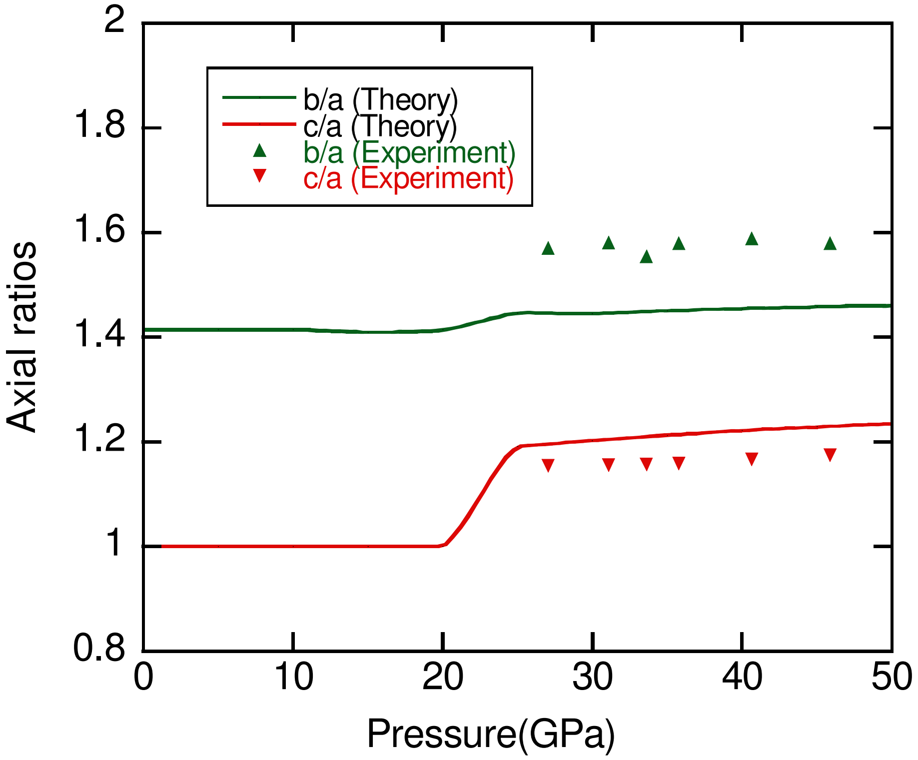

Fig. 5.18 The axial ratios of Pmmn phase of UC as a function of pressure with experimental data [10]

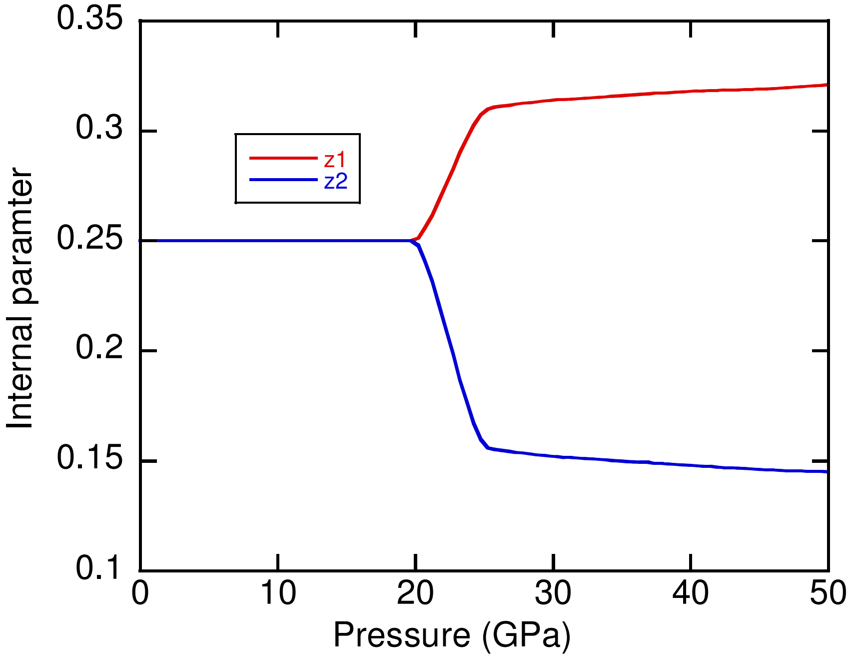

Fig. 5.19 The internal parameters (z_1 and z_2) of Pmmn phase of UC as a function of pressure.

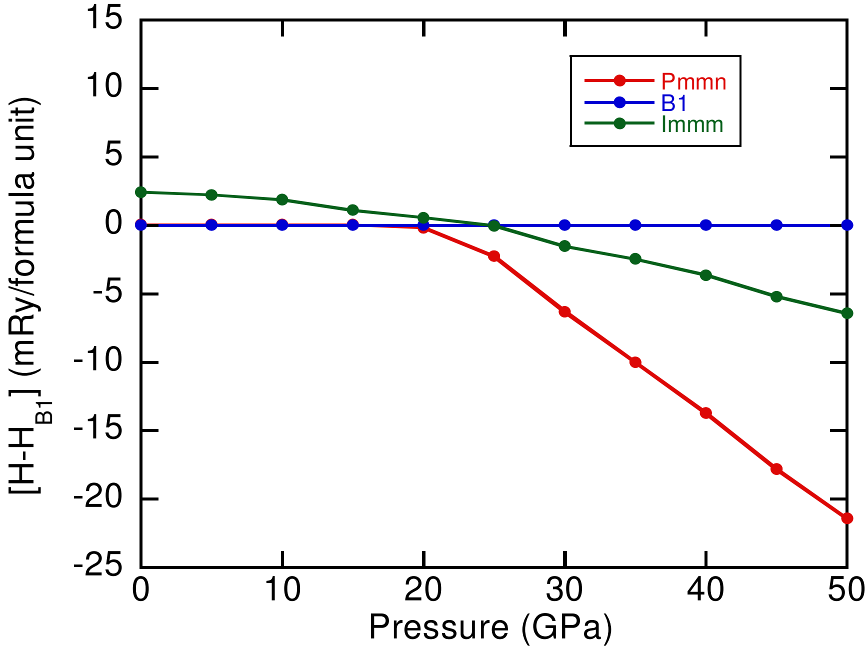

Fig. 5.20 Enthalpies of Pmmn and Immm phase with respect to that of B1 phase as a function of UC.

In Fig. 5.21, the equation of state determined from these calculations along with the experimental data [23] has been displayed. At a given pressure, the maximum deviation of theoretical volume from the experimental one is within ~ 5% and the transition is of first order having volume discontinuity ~2.5% at 20 GPa. Table 5.4 compares the zero pressure equilibrium volume, bulk modulus and its derivative derived from present theoretical calculations to the available experimental data [23] and theoretical values from other sources [9, 22]. The zero pressure equilibrium volume and bulk modulus derived from FP-LAPW calculations show a good agreement with experimental values [10], however, the pressure derivative of bulk modulus is overestimated by ~ 37%. The pesudopotential calculations underestimate the V_0 by ~ 2.4% and overestimate the B_0 by ~ 16%, whereas the B_0' compares well with the experiment [23]. It may be noted that the orthorhombic phase reported to occur at high pressure in the experimental study differs slightly from the body centered orthorhombic (bco) structure as two small intensity Bragg peaks present in the EDXRD pattern at pressure > 27 GPa could not be indexed as reflections from bco and the new structure is termed as the pseudo body centred orthorhombic structure [23]. Further, as shown in Fig. 5.21, the XRD pattern of Pmmn and Immm(bco) phases have also been calculated at ~30 GPa. It is clear from the figure that most of the intense peaks of Pmmn structure except few match with that of Immm structure.

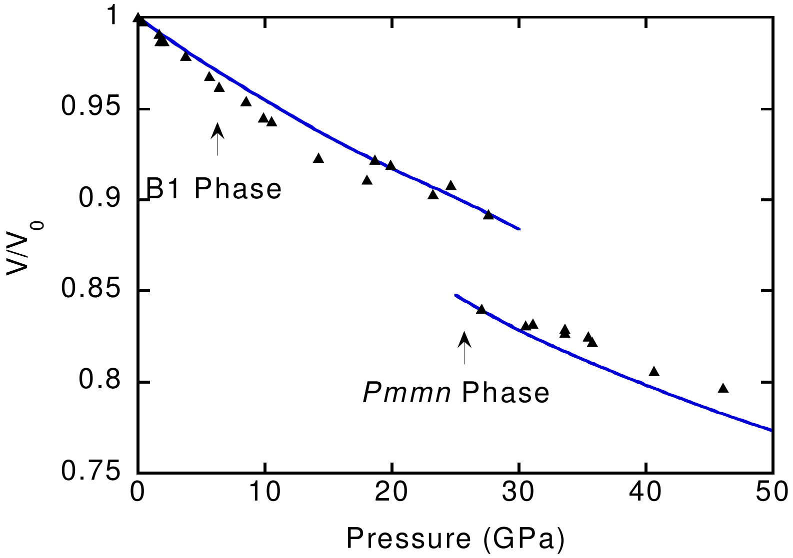

Fig. 5.21 Comparison of equation of state of B1 and Pmmn phase of UC with experimental data [10].

TABLE 5.4. Various physical quantities at zero pressure and 0K for UC

Physical quantities	Present work	Experimental	Theory other sources
V_0 (Å^3/f. unit)	29.7, 30.56[a]	30.5[9]	29.9 [6], 27.1[9]
B_0(GPa)	185.2, 158.3[a]	160[23], 159[20],164[19]	185[6], 168[9] 204[22]
B_0'	3.59, 4.94 [a]	3.6[23]	
C_{11}(GPa)	273	318[20], 320[19]	350[9], 264[22]
C_{12}(GPa)	141	79[20], 86[19]	79 [9], 175[22]
C_{44}(GPa)	37	67 [20], 65[19]	65[9], 80[22]
θ_D(K)	206	366 [48]	
γ	1.6		

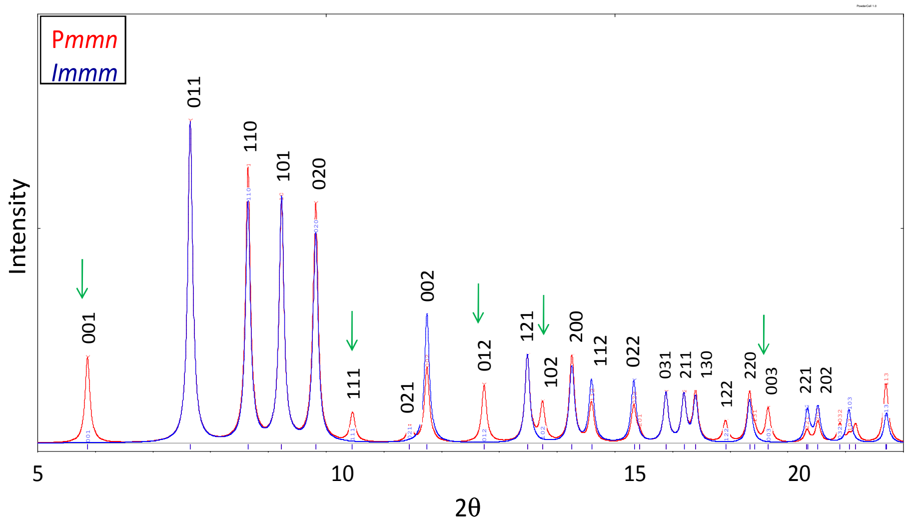

Fig. 5.22 The calculated angle dispersive x-ray diffraction of Pmmn and Immm(bco) Phases of UC at ~ 30 GPa. Arrows in XRD plot are the peaks which are not present in Immm (bco) phase

5.3.5 Elastic stability and Dynamical stability of UC in B1 phase

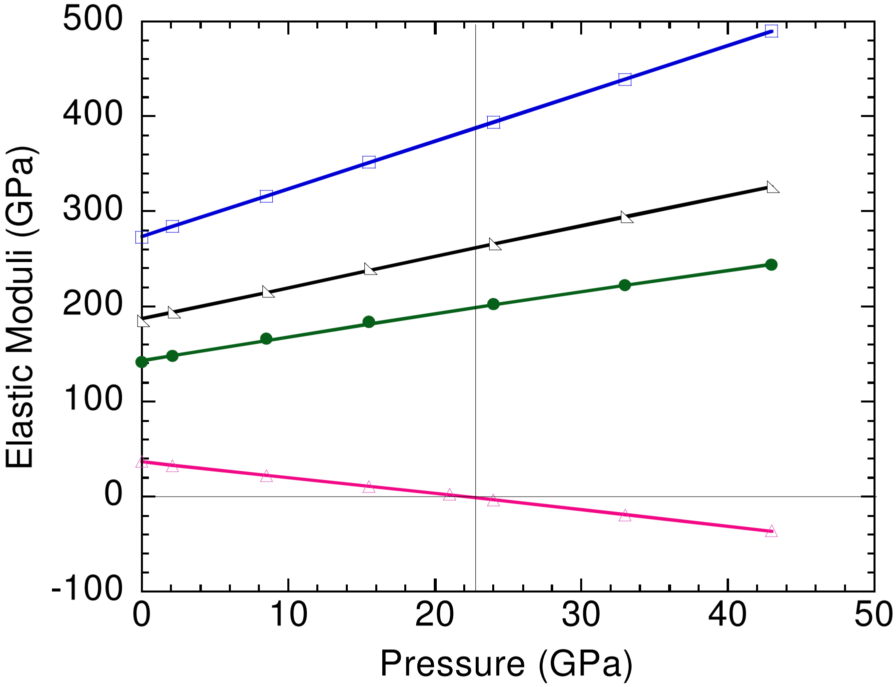

Fig. 5.23 Elastic constants as a function of pressure for B1 phase of UC determined from static lattice calculations.

Further, to understand this phase transition from mechanical instability point of view, the elastic constants of B1 phase have been calculated as a function of pressure using both pseudopotential method (quantum espresso) and all electron method (wien2K). In Table 5.4, elastic constant of B1 phase have been compared at zero pressure calculated in the present work with the available experimental values [19, 20] and those reported by other theoretical works [4, 9]. The values of elastic constants deviate significantly from the experiment. The pseudopotential calculations underestimate the C_{11} and C_{44} by ~ 14% and ~ 43%, respectively, however, overestimate the C_{12} by ~ 64%. It may be noted that the deviation of C_{12} and C_{44} from experimental values is much large as compared to that of C_{11}. As it is well known that the C_{12} and C_{44} depend largely on long range forces, however, the C_{11} depends more on nearest neighbour interactions [49, 50], it appears that GGA is not able describe the long range interactions properly in this compound. Also, listed in the Table 1 are the zero pressure Debye temperature (θ_D) determined from theoretical elastic constants using the procedure followed in the ref. (48, 51, 52) and Gruneisen parameter (γ) obtained by applying the Slater's [53] definition. The theoretical value of θ obtained as 206 K from pseudopotential calculation is significantly lower than the experimental value of 366 K [54]. The lower value of θ obtained in the present theoretical calculations is due to the underestimation of shear elastic moduli $C' = (C_{11}-C_{12})/2$ and C_{44}. Fig.5.23 displays the behaviour of theoretically determined elastic constants as a function of hydrostatic pressure. As can be seen from the figure the C_{44} modulus determined from pseudopotential calculations vanishes ~ 22 GPa which is just above the ~ 20 GPa, the transition pressure calculated for the onset of B1 to Pmmn transition. This is expected as the calculation of elastic constants involves total energy and not the enthalpy. The vanishing of the C_{44} modulus near the B1 $\rightarrow$ Pmmn transition point indicates that this structural transition is driven by elastic failure.

Finally, the lattice dynamic calculations have been carried out to understand the dynamical stability of B1 phase under hydrostatic compression. The phonon spectra and corresponding phonon density of states of B1 phase determined at zero pressure and around the transition pressure are displayed in Fig. 5.24 along with the available experimental data [33]. The calculated phonon spectra at ambient conditions agree well with the experimental data [33]. As expected, the projected phonon density of states plotted in this figure, show that the high frequency vibrations are dominated by the C atom due to its lower atomic mass whereas the low frequency vibrations are dominated by U atom due to its higher mass. Further, it is clear from the Fig. 5.24, at ambient conditions the phonon frequencies of B1 phase in all the directions of Brillouin zone are real, supporting the experimentally observed dynamical stability at ambient conditions. However, around the transition point the transverse acoustic phonon branch along Γ-X direction becomes imaginary causing dynamic instability in B1 phase. Additionally, the phonon instability around transition pressure is of long wavelength nature as it occurs near the Brillouin zone centre. This long wavelength phonon instability near the transition point further confirms that the B1 → Pmmn transition is driven by elastic failure (the vanishing of C_{44} modulus).

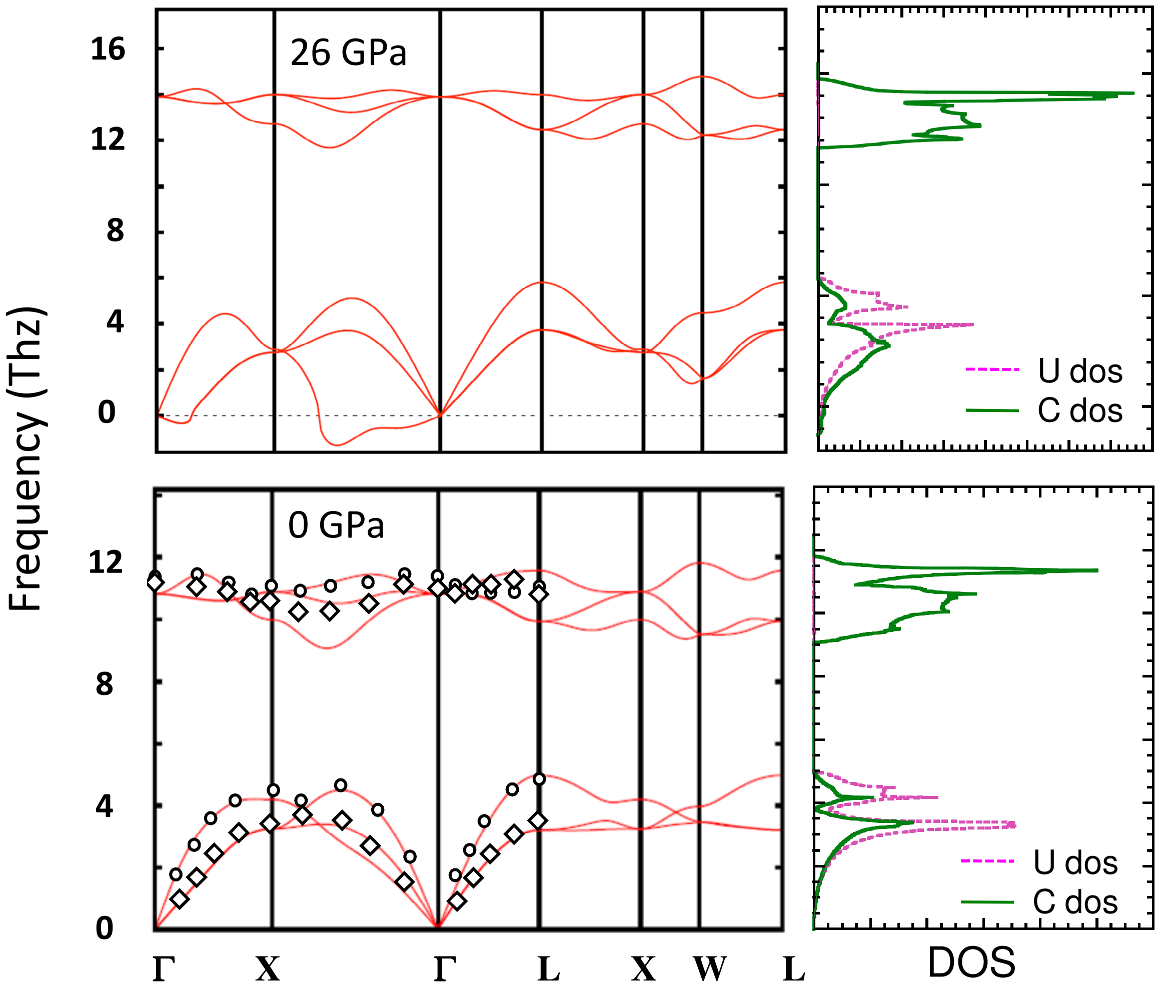

Fig. 5.24: Phonon spectra and phonon density of states of UC at ambient pressure and above transition pressure for B1 phase. Also plotted are the experimental data at zero pressure. The circles and diamonds correspond to the experimentally measured longitudinal and transverse phonons, respectively.

5.4 Summary

To summarize, detailed first principles electronic band structure calculations have been carried out in ThC and UC as a function of hydrostatic compression. For ThC, the evolutionary structure search method has been used as a first step to search for the stable structures at few pressures. The method suggested the B1 phase to be of lowest enthalpy at 0 GPa. At ~25 GPa, however, the *Pnma* structure was found to have lowest enthalpy. At still higher pressure of ~ 60 GPa the *Cmcm* phase showed to have lowest enthalpy and at a very high pressure of ~ 225 GPa, the B2 structure displayed the lowest enthalpy. After identifying the possible stable structures at different pressures, detailed total energy calculations have been performed on these structures as a function of hydrostatic compression and the enthalpies have been derived at various pressures. The comparison of enthalpies derived from these static lattice calculations suggested that ThC will transform from B1 phase to *Pnma* structure at ~ 19 GPa, which upon further compression will transform to another orthorhombic phase with space group symmetry *Cmcm* at ~ 36 GPa. The *Cmcm* structure will remain stable up to ~ 200 GPa and will transform to B2 phase upon further compression. This high pressure structural sequence predicted in the present work differs significantly from the experimental works [4, 13], which report that the ThC remains stable in B1 phase up to 50 GPa (the maximum pressure of the experiment). It has been speculated that the substoichiomerty of the samples which had the effect of reducing the interatomic spacing could be the reason for enhanced stability of B1 phase in experiments [4, 13]. It will be interesting to investigate this material experimentally for other various substoichiometries also, as it will add a new understanding on the effect of changing the carbon content on the structural stability of B1 phase under hydrostatic pressure.

Further, to substantiate the findings of static lattice calculations, the lattice dynamic calculations have also been performed on these structures. It has been found that the B1 structure remains dynamically stable for pressures < 34 GPa and fails at this pressure as TA(X) phonon frequency ceases to zero. For *Pnma* structure, the phonon spectrum has been calculated just above the transition pressure (~ 25 GPa) and it was found that the structure is stable dynamically also. Similar calculations on *Cmcm* phase around 45 GPa, demonstrated that this phase is dynamically stable at this pressure. The B2 structure, however, stabilized dynamically at ~ 125 GPa *i.e.* much before the *Cmcm* to B2 transition pressure. These results of the lattice dynamic calculations further support predictions of the static lattice calculations. Finally, various thermophysical properties of B1 phase have been derived at ambient pressure and compared with the available experimental as well as theoretical data. The temperature dependence of zero pressure heat capacity and entropy displays good agreement with the experimental data [45].

In UC the first principles electronic band structure calculations have been performed using plane wave pseudo potential method and FP-LAPW method. The structural and elastic stability of UC has been examined under hydrostatic compression. The FP-LAPW calculations demonstrated that the lattice parameters and equation of state for non-magnetic ordering in B1 phase displays good agreement with the experimental data indicating that it is sufficient to perform the calculations for non-magnetic case. The plane wave pseudo potential calculations suggested that B1 phase to Pmmn phase transition occurs at ~ 20 GPa as compared to the experimental value of 27 GPa [23]. Present calculations suggest that the high pressure phase of UC is a primitive orthorhombic (also named as pseudo bco in the experimental study [23]). The examination of elastic moduli of B1 phase along the hydrostatic compression path shows that the C_{44} shear modulus vanishes near the B1 to Pmmn transition point, indicating that this transition is driven by elastic instability. This argument is further supported by the lattice dynamical calculations performed on B1 phase of UC, which shows that the long wavelength TA phonon frequencies become imaginary around the transition point. Various physical quantities such as zero pressure equilibrium volume, bulk modulus, its pressure derivative, Debye temperature, Gruneisen parameter and elastic constants determined from the present calculations have been compared with the available data from experiments and other theoretical sources.

References

1. C.P. Mallett, *J. Phys. C.* **15**, 6361 (1982).
2. D.J. Lam, J.B. Darby and M.V. Nevitt, The Actinides: Electronic Structure and Related Properties (Ed: A.J. Freeman and J.B. Darby (Academic Press, New York, 1974), Vol II, P. 119.
3. Handbook of the Physics and Chemistry of the Actinides (Ed: A.J. Freeman and G.H. Lander, North Holand, Amsterdam 1985).
4. L. Gerward, J. Stalin Olsen, U. Benedict, J.-R. Itie and J.C. Spirlet, *J.Appl.Cryst.***19**, 308 (1986).
5. I.R. Shein, K.I. Shein, A.L. Ivanovskii, *J. Nucl. Mater* **353**, 19 (2006).
6. A.E. Austin, Acta Cryst. 12, 159 (1959).
7. D. Petti, D. Crawford, and N. Chauvin, *MRS Bull*. **34**, 40 (2009).
8. D. C. Crawford, D. L. Porter, and S. L. Hayes*, J. Nucl. Mater*. **371**, 202 (2007).
9. J. Trygg, J.M. Wills, M.S.S. Brooks, B. Johansson and O. Eriksson, *Phys. Rev. B* **52**, 2496 (1995).
10. P. Modak and Ashok K. Verma, *Phys. Rev. B* **84**, 024108 (2011).
11. B.D. Sahoo, K.D. Joshi and Satish C. Gupta, *J. Nucl. Mater.* **81**, 437 (2013).
12. Massoud T. Simnad and John P. Howe, Material Science in Energy Technology (Ed: G. Libowitz and M.S. Whittingham, Academic Press, New York, 1979) p. 105.
13. L. Gerward, J. Stalin Olsen, U. Benedict and H. Luo, *J. Less Common Metals* **161**, L11 (1990).
14. I.S. Lim, G.E. Scuseria, *Chem. Phys. Lett*. **460**, 137 (2008).
15. I.R. Shein and A.L. Ivanovskii, *Phys. Solid State* **52**, 2039 (2010).
16. S. Aydin, A.Tatar, Y.O. Ciftci, *J. Nucl. Matter* **429**, 55 (2012).
17. D. Pérez Daroca, S. Jaroszewicz, A.M. Llois, H.O. Mosca, *J. Nucl. Mater*. **437**, 135 (2013).
18. J.A. Jackman, T. M. Holden, and W.J.I. Buyers, P. de V. DuPlessis, O. Vogt and J. Genossar*, Phys. Rev. B* **33**, 7144 (1986).
19. L. J. Graham. H. Nadler and R. Chang, *J. Appl. Phys*. **34**, 1572 (1963).

20. J. L. Routbort, *J. Nuclear Mater.* **40**,17 (1971).
21. Michel Freyss, *Phys. Rev. B.* **81**, 0141011 (2010).
22. Hongliang Shi, Ping Zhang, Shu-Shen Li, Bo Sun, Baotian Wang*, Phys. Lett. A* **373**, 3577 (2009).
23. J. S. Olsen, L. Gerward, U. Benedict, J.P. ITIE and K. Richter, *J. Less Comn. Metals* **121**, 445 (1986).
24. C.W. Glass, A.R. Oganov and N. Hansen, *Comput. Phys. Comun.* **175,** 713 (2006)
25. A.R. Oganov, C.W. Glass and S.Ono, *Earth Planet. Sci. Lett.* **241** 95 (2006)
26. A.R. Oganov and C.W. Glass*, J. Chem. Phys*. **124,** 244704 (2006)
27. P.E. Blochl, *Phys. Rev. B* **50**, 17953 (1994)
28. Carsten Rostgaard, arXiv:0910.1921v2 [Cond. Mat. Mtrl Sci] 2009
29. G. Kresse and J. Hafner, *J. Phys.: Condens. Matter* **6**, 8245 (1994)
30. G. Kresse and J. Furthmuller, *Comput. Mater. Sci*. **6**, 15 (1996)
31. P. E. Bl¨ochl, *Phys. Rev. B* **50**, 17953 (1994)
32. G. Kresse and D. Joubert, *Phys. Rev. B* **59**, 1758 (1999)
33. J.P. Perdew, K. Burke and M. Ernzerhof, *Phys. Rev. Lett*., **77**, 3865 (1996)
34. H.J. Monkhorst and J D Pack, *Phys. Rev. B* **13**, 5188 (1976)
35. G. Kresse and J. Furthmuller, *Europhys. Lett*. **32**, 729 (1995); A. van de Walle and G. Ceder, *Rev. Mod. Phys*. **74**, 11 (2002)
36. Y von Le Page and Paul Saxe*, Phys. Rev. B* **65**, 104104 (2002)
37. A. Togo, *Phys. Rev. B* 78, 134106 (2008)
38. S. Baroni, A. Corso Dal, S. de Gironcoli, P. Giannozzi, C. Cavazzoni, G. Ballabio, S. Scandolo, G. Chiarotti, P. Focher, A. Pasquarello, K. Laasonen, A. Trave, R. Car, N. Marzari and A. Kokalj, http://www.pwscf.org
39. P. Blaha, K. Schwarz, P. Sorantin and S.B. Trickey, *Comput. Phys. Commun*. **59**,399 (1990).
40. P. Blaha, K. Schwarz and J. Luitz, WIEN2K (Technical University of Vienna).
41. N. Troullier and J.L. Martins, *Phys. Rev. B* ,**43** ,1993, (1991).
42. Y.K. Vohra and W.B. Holzapfel, *High Press. Res.,* **11**, 223 (1993)
43. B.D. Sahoo, K.D. Joshi and Satish C. Gupta, AIP Conference Proceedings **1536**, 937 (2013).
44. B. D. Sahoo, K. D. Joshi, and Satish C. Gupta, *J. Appl. Phys*. **116**, 193504 (2014)

45. J. Danan, *J. Nucl. Mater* **57**, 280 (1975)
46. R.S. Street, T.N. Water, *The Thermal Expansion of the ThC and ThN*, UKAEA Report AERE-1115, (1962)
47. P. Chiotti and R.W. White*, J. Nucl. Mater*. **23**, 37 (1967)
48. P. Ravindran, Lars Fast, P. A. Korzhavyi, B. Johansson, J. Wills and O. Eriksson, *J. Appl. Phys*. **84**, 4891 (1998).
49. M.D. Salleh, J.E. Macdonald, G.A. Saunders and P. De V. DuPlessis, *J. Matter. Sci*. **21 ,** 2577 (1986).
50. P.A. Wedgwood*, J. Phys. C: Solid State Phys*. **7,** 3203(1974).
51. O. L. Anderson, *J. Phys. Chem. Solids* **24** ,909 (1963).
52. E. Schreiber, O. L. Anderson, and N. Soga, Elastic Constants and their Measurements (McGraw-Hill, New York, 1973).
53. J.C. Slater, Introduction to Chemical Physics (MCGraw-Hill, New York, 1939)
54. R. Colella, D. Dragone and A. Merilini, *Phys. Stat. Sol. B* **36**,135(1969).

Chapter 6

Summary and Future Scope

The atomistic computational technologies (computational quantum mechanics and molecular dynamic simulations) have played an important role in the field of condensed matter. The advent of these theoretical tools has bridged the gap between fundamental materials science and materials engineering. Looking to this aspect, the present thesis attempts to understand the theoretical investigations of physical properties of several binary compounds using pseudopotentials and density functional theory (DFT) under extreme conditions of high pressure. Particularly, this final and concluding chapter of the thesis summarizes the entire work of the present thesis along with the important general conclusions from each chapter. Also the important discussions regarding the applicability and advantage of the present version of density functional theory has been highlighted.

The first chapter has provided a brief description of the basic concepts and scopes of the high pressure research, and outlines the research work to be presented in the successive chapters of the thesis. Besides this, it also describes the different methods used to generate high pressure in materials and various characterization techniques utilized to understand the behavior of materials under high pressure. A brief description of modern DFT based *ab-initio* electronic band structure methods employed for understanding the material response under high pressures is presented in the first chapter of the thesis. Apart from this, a brief account of the algorithm used for the prediction of pressure induced phase transformations on various materials has also been provided in the thesis. An outline of the methodology used for examination of elastic stability and lattice dynamic stability has been provided in the same chapter.

The second chapter has dealt with the theoretical calculations carried out on CdO. In CdO, the first principle *ab-initio* calculations at 0 K have been performed to analyze structural stability under pressure. The structural stability analysis carried out on NaCl type

(B1) and CsCl type (B2) structures suggests that the B1 phase will transforms to B2 phase at ~87 GPa in good agreement with experimental value of 90.6 GPa [1]. Additionally, employing the theoretically determined thermal equation of state in conjunction with Rankine Hugoniot relation, the Hugoniot of B1 phase of this material has been derived. The pressure dependent elastic constants have been determined for both B1 and B2 phases. The examination of behavior of elastic moduli as a function of pressure demonstrates that the C_{44} shear modulus of CdO in B1 phase fails at ~126GPa, suggesting the development of elastic instability in B1 phase around this pressure. In contrast the B2 phase remains elastically unstable up to a pressure of ~ 38GPa and emerges as an elastically stable structure beyond this pressure. To test the dynamical stability of B1 and B2 phase, the lattice dynamical calculations have been performed for both the phases at ambient conditions as well as at high pressures. The phonon dispersion for B1 phase shows imaginary frequencies around ~116 GPa. For the B2 phase the imaginary frequencies persist up to 56 GPa and thereafter all the frequencies became positive making the structure dynamically stable beyond this pressure. The analysis of elastic and dynamic stability as a function of hydrostatic compression suggests that the pressure induced B1 to B2 transition in CdO is driven by soft transverse acoustic phonon mode at the Brillouin zone boundary.

The third chapter of the thesis has reported the detailed theoretical investigations carried out in transition metal carbides ScC, YC and TaC. The comparison of enthalpies of B1 , Pmmn and B2 phases in ScC and YC determined as a function of pressure from static lattice calculations has predicted the B1 to Pmmn structural phase transition in these carbides, ruling out the possibility of direct B1 to B2 phase transition under hydrostatic compression. The pressures for B1 to Pmmn phase transition has been determined to be ~ 80 GPa in ScC and ~ 30 GPa in YC. Present theoretically predicted B1 → Pmmn phase transition under high pressure has been further substantiated by present lattice dynamic calculations performed on these phases. The current theoretical work emphasizes that the phonons play dominant role in deciding the structural stability of these carbides, and rules out the previously proposed high pressure B2 phase by Soni et al [2]. The electronic band structure calculations performed on various plausible structures of TaC as a function of hydrostatic compression suggest that the B1 phase of this material will transform to B2 structure at a pressure of ~ 472 GPa. This structural phase transition has been substantiated further by examining the elastic and lattice dynamic stability of B1 and B2 structures as a function of pressure up to ~ 600 GPa. Apart from high pressure investigations, the high temperature behavior of this material in B1 phase has also been examined and the temperature effect on various physical quantities such as volume and bulk modulus has been determined. The present theoretical calculations have been further utilized to derive various thermophysical quantities.

The fourth chapter has presented the theoretical high pressure investigations on CeN. The structural stability analysis carried out on rare earth nitride CeN has suggested that B1 phase will transform to B10 structure at ~ 53 GPa, which upon further compression will transform to B2 phase at ~200 GPa. This theoretical finding does not agree with experimentally reported direct B1 to B2 phase transition at ~ 65 GPa [3]. Further, the high pressure structural sequence of B1 → B10 → B2 predicted from present static lattice calculations has been supported by present lattice dynamic calculations. Additionally, the analysis of the theoretically calculated x-ray diffraction pattern of B1, B10 and B2 structures at ~ 75 GPa suggests that more experiments at still high pressures are needed to be conducted to confirm whether the high pressure phase is B2 or B10. Finally, these theoretical predictions in CeN have been further substantiated by the outcomes of our theoretical calculations on LaN, in which we are able to reproduce the experimentally observed B1 → B10 transition [4].

The theoretical investigation on carbides has been extended to monocarbides of light actinides *i.e.* UC and ThC and presented in the fifth chapter of the thesis. The detailed first principles electronic band structure calculations carried out in ThC as a function of hydrostatic compression in conjugation with evolutionary structure search method implemented in the USPEX code [7] suggests that the B1 phase has lowest enthalpy at 0 GPa. At ~25 GPa, however, the *Pnma* structure emerges as lowest enthalpy phase. At still higher pressure of ~ 60 GPa the *Cmcm* phase shows to have lowest enthalpy and at a very high pressure of ~ 225 GPa, the B2 structure shows the lowest enthalpy. After identifying the possible stable structures at few pressures, detailed total energy calculations have been performed on these structures at several hydrostatic compressions and the enthalpies as a function of pressure have been derived. The comparison of enthalpies derived from these static lattice calculations suggests that ThC transforms from B1 phase to *Pnma* structure at ~19 GPa, which upon further compression transforms to another orthorhombic phase with space group symmetry *Cmcm* at ~ 36 GPa. The *Cmcm* structure remains stable up to ~ 200 GPa and transforms to B2 phase upon further compression. This high pressure structural sequence predicted in the present work is in sharp contrast with the experimental work [5], which reports that the ThC remains stable in B1 phase up to 50 GPa, the maximum pressure of the experiment. Further, to substantiate these theoretical findings of static lattice calculations, the lattice dynamic calculations have been performed on these structures. It has been found that the B1 structure remain dynamically stable for pressures < 33.8 GPa and fails at this pressure as TA(X) phonon frequency ceases to zero. For *Pnma* structure, the phonon spectrum calculated just above the transition pressure (~ 25 GPa) demonstrates the dynamic stability of this structure at this pressure. Similar calculations on *Cmcm* phase around 45 GPa, demonstrates that this phase is dynamically stable at this pressure. The B2 structure, however, has been stabilized dynamically at ~ 125 GPa *i.e.* much before the *Cmcm* to B2 transition pressure. These results of present lattice dynamic calculations are in favour of the present predictions of static lattice calculations. In the present scenario it is essential to re-examine the structural stability of ThC under high pressure experimentally to either reconcile with the theory or rule out the existence of these high pressure phases.

The calculations on UC suggest that the onset of B1 to Pmmn phase transition occur at ~ 20 GPa as compared to the experimental value of 27 GPa. In the present work the fractional coordinates of the U and C atoms in the high pressure phase could be quantified which otherwise in the experiment could not be determined. The examination of elastic moduli of B1 phase along the hydrostatic compression path shows that the C_{44} shear modulus vanishes near the B1 to Pmmn transition pressure, indicating that this transition is driven by elastic instability. This argument is further supported by the lattice dynamical calculations performed on B1 phase of UC, which shows that the long wavelength TA phonon frequencies become imaginary around the transition point. Various physical quantities such as zero pressure equilibrium volume, bulk modulus, its pressure derivative, Debye temperature, Gruneisen parameter and elastic constants determined from the present calculations have been compared with the available data from experiments and other theoretical sources.

As far as prediction of crystal structure at high pressures in these binary solids is concerned only three structures B1, B2 and Pmmn have been examined in ScC, and YC, and only five phases B1, B2, B3, B4 and B8 have been investigated in TaC. The possibility of any other high pressure structures may require testing of still more phases, specially for ScC ,YC and TaC, as there are no high pressure experiments on these materials up to the predicted B1 to Pmmn or B2 transition pressures. It is quite challenging to guess and perform total energy calculations for all the plausible structures to predict the high pressure phases of materials theoretically. For a new material, in order to find the stable structure, one has to carry out the total energy calculations as a function of compression for all the possible candidate structures which may be the structures of analogous system or new structures guessed from chemical intuition. The plot of total energy versus volume for all the structures is then used to find the energetically stable structures at different compressions or equivalently at different pressures among the tested ones. But problem arises when some unexpected structure or hitherto unknown structure gets stabilized at high pressure; as is the case for the high pressure B10 phase in LaN system. So, here, reliable structure prediction capabilities of computer simulation are necessary which will work without any prior knowledge, assumption or intuition of the system [6]. Simulated annealing [8-10], minima hopping [11], metadynamics [12-14], evolutionary algorithm USPEX (Universal Structure Predictor: Evolutionary Xtallography) [15-17] etc. are some of the methods which have been applied in recent past to explore the stable crystal structures in many materials by relaxing the randomly produced structures. These methods are implemented in the sophisticated simulation computer codes such as USPEX [18], CALYPSO [19], XtalOpt [20], to predict crystal structure.

Further, all these theoretical calculations are based on the DFT. Despite the improvements in various approximations in DFT, it has its own limitations. There are difficulties in using DFT to properly describe intermolecular interactions, charge transfer excitations; transition states, global potential energy surfaces, some other strongly correlated systems and in calculations of the band gap of some semiconductors. The exchange-correlation potentials which are used in DFT calculations such as GGA and LDA are not exact. This produces some inherent error in these calculations. For example, the transition metals, lanthanides and actinides have partially filled inner orbitals with narrow energy bands which pose difficulty in simulating these materials and sometime the results are away from the experimental observations. For example, the simple material NiO has a partially filled 3*d*-band and therefore would be expected to be a good conductor. However, strong coulomb repulsion (a correlation effect) between *d*-electrons makes NiO a wide-band gap insulator. Thus, strongly correlated materials have electronic structures that are neither simply free-electron-like nor completely ionic, but a mixture of both. Hence in many cases one has to go beyond GGA and LDA approximations. The development of better approximations for the coulomb correlation and exchange correlation terms in such systems is still an area of active research.

In DFT the use of pseudopotentials gives benefits in terms of computational speed and memory requirement for computations but still it has its drawbacks. In principle, the shape of the pseudopotential should not affect the chemical behaviour of a system, this happens only when the cut off radius of pseudopotential is very small. Often in DFT larger cut off radius are chosen to use lower plane wave cut off energy. The shape of the potential is then chosen so as to give results in a reasonably good agreement with experiments. The "transferability" of the pseudopotential *i.e.* how it will behave under different chemical environments, plays an important role when one generates a pseudopotential and it can only be improved by reducing its cut-off radius. It should also be noted that ultrasoft pseudopotentials tend to be more transferable than the norm-conserving ones. There are other issues related to pseudopotentials, which may or may not be of importance depending on the system under study and the properties one wishes to calculate. For example, deciding which electrons to be treated as 'core' and which to be treated as 'valence' or whether or not relativistic effects should be included is fully dependent on the kind of atoms involved in making the system under consideration. So the results of pseudopotential calculation have to be checked with all electron calculations. Developing better pseudopotentials is still an area of active research.

The high pressure phase transitions investigated in the present thesis encourage us to study the multi component system under high pressure and high temperature as a future work. The molecular dynamics simulations of metals and binary systems could be the promising future scope of our research. The band structure of metallic complexes having large number of atoms in the unit cell is also an interesting problem to deal with in future. The work will also be extended for semiconducting materials in solid and liquid phase. Finally, the future experimental studies on the systems theoretical investigated in the present work will be of great importance as these will either confirm or rule out the existence of theoretically predicted phase transitions.

References

1. Haozhe Liu, Ho-kwang Mao, Maddury Somayazulu, Yang Ding, Yue Meng, and Daniel Häusermann, *Phys. Rev.* **B 70**, 0941141 (2004).
2. Pooja Soni, Gitanjali Pagare, Sankar P. Sanyal, J. Phys. and Chem. Solids **72**, 810 (2011).
3. J. Staun Olsen, J.-E. Jørgensen, L. Gerward, G. Vaitheeswaran, V. Kanchana, A. Svane, J. Alloys and Compounds, **533**, 29 (2012).
4. S. B. Schneider, D. Baumann, A. Salamat and W. Schnick, *J. Appl. Phys.* **111**, 093503-1 (2012).
5. J. S. Olsen, L. Gerward, U. Benedict, J.P. ITIE and K. Richter, *J. Less Comn. Metals* 121 (1986), 445-453
6. Anurag Srivastava , Mamta Chauhan and R.K. Singh, *Phase Transitions* **84**, 58 (2011).
7. A. R. Oganov *et al.*, "Evolutionary Crystal Structure Prediction and Novel High-Pressure Phases." *High-Pressure Crystallography*. Springer Netherlands (2010), 293-323.
8. M. W. Deem, J. M. Newsam, *Nature* **342**, 260 (1989)..
9. J. Pannetier, J. Bassasalsina, J. Rodriguez-Carva jal, and V. Caignaert, *Nature* **346**, 343 (1990).
10. M. B. Boisen, G. V. Gibbs, M. S. T. Bukowinski, *Phys. Chem. Minerals* **21**, 269 (1994).
11. S. Gödecker, *J. Chem. Phys.* **120**, 9911 (2004).
12. R. Martonak, A. Laio, and M. Parrinello, *Phys. Rev. Lett.* **90**, 075503 (2003).
13. R. Martonak, A. Laio, M. Bernasconi, C. Ceriani, P. Raiteri, F. Zipoli, and M. Parrinello, *Z. Krist.* **220**, 489 (2005).
14. R. Martoňák, D. Donadio, A. R. Oganov, M. Parrinello, *Nature Materials* **5**, 623 (2006).
15. A. R. Oganov, C. W. Glass, S. Ono, *Earth Planet. Sci. Lett.* **241**, 95 (2006).
16. A. R. Oganov, C. W. Glass, *J. Chem. Phys.* **124**, 244704 (2006).
17. C. W. Glass, A. R. Oganov, N. Hansen, *Comp. Phys. Comm.* **175**, 713 (2006).
18. http://uspex.stonybrook.edu/
19. http://www.calypso.cn/

20. http://xtalopt.openmolecules.net/wiki/index.fcgi/